

Quantum Dots Genosensor for Her2/Neu Oncogene - A Breast Cancer Biomarker



By

Xolile Godfrey Fuku

A thesis submitted in fulfillment of the requirements for the degree of

**UNIVERSITY of the
WESTERN CAPE
Philosophiae Doctor**

In the

Department of Chemistry, Faculty of Science

University of the Western Cape

Bellville, Cape Town, South Africa

Supervisors: Prof Priscilla Baker and Prof Emmanuel Iwuoha

November 2014

KEY WORDS

Breast cancer

Gold electrodes

Biomarkers

Amphiphilic bifunctional molecules

DNA sensors

Human epidermal growth factor receptor 2

Quantum dots

Electrochemical impedance spectroscopy

Excitation/Emission matrix (EEM) fluorescence

Square wave voltammetry

Fourier transform infrared spectroscopy

UV/vis spectroscopy

Cytotoxicity

Chronocoulometry

Electrochemical quartz microbalance spectroscopy

Micro-fluidics

Raman spectroscopy

Contact angle



Quantum dots genosensor for Her2/neu oncogene - a breast cancer biomarker

Xolile Godfrey Fuku

PhD Thesis, Department of Chemistry, University of the Western Cape, November 2014.

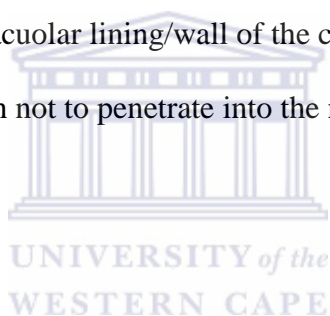
ABSTRACT

The human epidermal growth factor receptor (HER)-family of receptor tyrosine kinases; human epidermal growth factor receptor 1, human epidermal growth factor receptor 2, human epidermal growth factor receptor 3 and human epidermal growth factor receptor 4 (EGFR/HER1, ErbB2/HER2, ErbB3/HER3, and ErbB4/HER4) plays a major role in the pathogenesis of many solid tumours, in approximately 25 - 30% of breast cancers. Breast cancer is the second most common type of cancer and affects around 3000 women annually in South Africa alone. While the benefits of treatment and cancer progress to enhance therapeutic effectiveness for the patient are well documented, it is also important to employ or fabricate methods in which cancer can be screened at an early stage. A number of gene and protein based biomarkers have shown potential in the early screening of cancer. One specific biomarker that is over-expressed in 20 - 30% of human breast cancers is the human epidermal growth factor receptor 2 (Her2/neu). Several methods have been developed for detection of Her2/neu oncogene including immunohistochemistry (IHC), enzyme-linked immunosorbant assay (ELISA), fluorescent in situ hybridisation (FISH) and polymerase chain reaction (PCR). However, these methods are subjected to interference problem. For these reasons an ultrasensitive, cheap and easy to use genosensor has been developed for early detection of the Her2/neu oncogene using electrochemical and spectroscopic methods. Due to their high surface-to-volume ratio, electro-catalytic activity as well as good biocompatibility and novel electron transport properties quantum dots are highly attractive materials for ultra-sensitive

detection of biological macromolecules via bio-electronic or bio-optic devices. In this study a quantum dots (QDs)-based genosensor was developed in which Ga₂Te₃-based quantum dots were synthesised using a novel aqueous solution approach by mixing 3-mercaptopropionic acid (3MPA)-capped gallium metal precursor with reduced tellurium metal. The morphological, compositional and structural characterisation of the QDs was investigated prior to their utilization in DNA sensor construction. High resolution-transmission electron microscopy (HR-TEM) images confirmed the spherical nature and average particle size (5 nm), while x-ray photoelectron spectroscopy (XPS) and energy dispersive x-ray spectroscopy EDX analysis confirmed the presence of gallium and tellurium in the material. X-ray diffraction (XRD) studies confirmed crystallinity and size (6 nm) in agreement with transmission electron microscopy (TEM) analysis. An amphiphilic bifunctional molecule, 3MPA and 3-mercaptosuccinic acid (3MSA) were used as capping agents for all quantum dots. It was found that 3-MPA/3MSA improved the solubility, stability, biocompatibility, affinity for gold and the electron transfer kinetics of the QDs, and prevented their agglomeration. Retention of the capping agent on the quantum dots surface was verified by Fourier transform infrared spectroscopy (FTIR) which gave scissor-type bending vibrations of C-H groups in the region 1365 cm⁻¹ to 1475 cm⁻¹, stretching vibrations of C=O at 1640 cm⁻¹, symmetric and asymmetric vibrations of the C-H and -SH in the region 2850 cm⁻¹ to 3000 cm⁻¹ as well as stretching vibrations of -O-H group at 3435 cm⁻¹. Raman analysis also confirmed these vibrational stretches. Only the 3MPA-Ga₂Te₃ QDs were used to study the optical and electrochemical properties, and were also used in genosensor preparation. Optical examination by UV-visible and fluorescence confirmed the semi-conducting nature of the QDs with the calculated band gap energies of 3.30 - 3.50 eV. Cyclic voltammetry (CV), square wave voltammetry (SWV), electrochemical quartz crystal microbalance (EQCM) and electrochemical impedance spectroscopy (EIS) enabled electrochemical interrogation of the

surface confined materials and their extension to HER2/neu oncogene complimentary DNA detection using a Ga₂Te₃ modified electrode surface - sensitivity ($2-10 \times 10^{-2} \mu\text{A ng}^{-1} \text{mL}^{-1}$) and limit of detection (*LOD*: 0.20 - 0.70 pg mL⁻¹) as calculated from SWV, CV and EQCM measurements and the dynamic linear range (*DLR*) of the sensor was found to range from 0.1 - 4 nM. The *LOD* calculated in this study was lower than the required values of Her2/neu in blood. The calculated parameters suggest that the sensor could be used to detected Her2/neu at physiologically relevant concentrations, owing to ultrasensitive sensor and thus allow smaller and low cost sampling. The other sensing platforms were prepared by bioconjugation of amine-terminated 21 base oligonucleotide probe-DNA (NH₂-5'-AAT TCC AGT GGC CAT CAA-3') onto the quantum dots-modified electrodes with the aid of 1-ethyl-3-(3-dimethylaminopropyl) carbodiimide hydrochloride (EDC) and N-hydroxysuccinimide (NHS). The prepared DNA electrodes were electrostatically tested with different DNA sequences of Her2/neu oncogene which included 5'-GAA CAT GAA GGA CCG GTG GGC-3' (complementary target), 5'-CAT AGT TGC AGC TGC CAC TGG-3' (non-complementary target), 5'-GAT CAT GAA GCA CCG GAG GGC-3' (3-base mismatched target) and 5'-GAT CAT GAA GCA CCG GAG GGT-3' (1-base mismatched target) to determine the specificity of the genosensor. The hybridisation events were monitored cyclic voltammetrically by monitoring the guanine oxidation signal. The QDs-based genosensor was found to be specific to complementary DNA, evident by current decrease and showing that the surface was fully bound. The 3MSA-Ga₂Te₃ QDs were used to study the cytotoxicity in cancer cells since the MSA quantum dots were more soluble than the 3MPA. From the MTT assay (UV-vis spectroscopy) - a colorimetric assay for assessing cell viability; using A549 human bronchial lung epithelial cells, the 3MSA-Ga₂Te₃ QDs were found to have no cytotoxicity at QDs concentration range of 0 - 1000 $\mu\text{g mL}^{-1}$ after 24 h. However, the cytotoxicity was observed at a concentration of 1000 $\mu\text{g mL}^{-1}$ from chronocoulometry (CC) measurements.

The reason for the cytotoxicity at this concentration was due to QDs coming out of suspension and settling on the cells. The overall data obtained from CC and MTT techniques suggests that the stability of the coating ligands on the QDs did not affect their cytotoxicity, therefore confirming that the 3MSA-coated Ga₂Te₃ QDs are more stable meaning that there was no leaching of metal ions compared to previously studied nanomaterials. 3MSA-Ga₂Te₃ QDs internalisation or transport into the cell was assessed using A549 human bronchial lung epithelial. Confocal microscope showed images of the cell incubated at higher concentration (1000 µg mL⁻¹) and from the observed images it was clear that the cells were dead. Evidence of particle internalization was obtained by using TEM technique. TEM confirmed that the 3MSA-Ga₂Te₃ QDs were not internalised by the cells but they were rather aligned on the vacuolar lining/wall of the cells. The TEM results suggest that the quantum dots were big enough not to penetrate into the nucleus.



DECLARATION

I declare that Quantum dots genosensor for Her2/neu oncogene - a breast cancer biomarker.

Is my own work, **that it has not been submitted for any degree or examination in any other university, and that all sources I have used or quoted have been indicated and acknowledged by means of complete references.**

Xolile Godfrey Fuku

November 2014

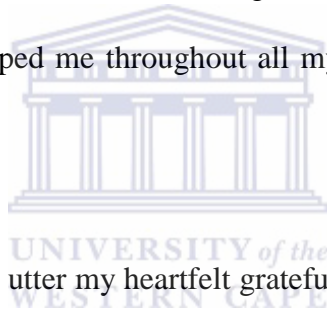


ACKNOWLEDGEMENTS

The LORD is my shepherd, I lack nothing, and He guides me along the right paths. To the Almighty God; thank You for giving me the strength, hope, wisdom, dedication and courage to finish this work. Thank You in your name and the Holy Spirit

“Bakusondela kum abenzi bobubi ukuba badle inyama yam, Bakuza ababandezeli bam neentshaba zam kum, bakhubeka bawa bona. Ndicele nto-nye kuYehova, ndifuna yona: Ukuba ndihlale endlwini kaYehova yonke imihla yobomi bam, ndiphicothe etempileni yakhe”.

The research presented in this thesis was the fruit of working with many talented scientists. It is with great humility and gratitude that I acknowledge the kindness, wisdom and generosity of so many people who have helped me throughout all my trials and tribulation during this research period.



First and foremost I would like to utter my heartfelt gratefulness to my supervisors: Professor Priscilla G.L Baker and Professor Emmanuel Iwuoha, who guided me and gave me valuable suggestions regarding the project. Your enthusiasm and creativity is matched by your vast scientific knowledge and uncanny ability to find meaning in even the worst-looking data. Thank you for your excellent supervision and support during this period. I have enjoyed each day as your student.

To Dr. Jahed Nazeem thank you, for your continuous support throughout this research period. My SensorLab post-doctors Dr Waryo, Dr Baleg and Dr Masikini who shared their opinions and experience through which I received the required information crucial for my project. To MINTEK-DST and Marie Curie Smartcancersens for their financial support.

To Chemistry Department: Mrs Wilhelma Jackson, all the Academic and Technical staff for your willingness to assist. The support of my colleagues past and present in SensorLab; Dr Peter Ndagili, Dr Fanelwa Ajayi, Dr Stephen Mailu, Dr Euodia Hess, Kerileng Molapo, Gcineka Mbambisa, Dr Nolubabalo Matinise, Dr Chinwe Ikpo, Dr Natasha Ross, Dr Mawethu Bilibana, Dr Abebaw Tsegaye, Abongili Jijana, Hlamolo Makelani, Lindsay Wilson, Candice Rassie, Christopher Sunday, Noluthando Myedi, thank you for being such good colleagues and friends. I wish to express my deep sense of gratitude to Prof Dempsey, Dr Seddom, Dr Kumar-Pillai, Dr Singh, Dr Padmanabhan, for their assistance and insightful information during my stay at ITT Dublin, Ireland.

To my friends: Thabiso, Molantwa, Mduduzi, Lerato and Euodia. Thank you for your assistance and having faith in me. You are true friends.

To the Fuku family: for their love and support. To my sisters and brothers: Karabo, Monica, Lucky, Patrick, Zamile (R.I.P), Vuyisile, Nomasonto, Micheal, Ndabeni, Thamsanqa, Ntsizi, Lindiwe, Smanga and Bongani. To my uncles and aunts: Micheal, Kleinbooi (R.I.P), Fanana, Nzimeni (R.I.P), Noluthando, thank you for giving me hope, courage and most of all making me believe. To My special and true friend Mamokoena, for her consistent support, believe and encouragement.

Finally, yet importantly, I would like to express my heartfelt thanks to my beloved parents: Nontembiso Emily Fuku and Nozililo Finie Fuku for their blessings, and wishes for the successful completion of this project. Thank you for believing, pushing and guiding me to succeed and most importantly for your love. You have always been there for me, and I am forever in your debt.

“If there is effort, there is always accomplishment”

By Jigoro Kano

DEDICATION

This project is dedicated to

The

Almighty God

And

My Mom

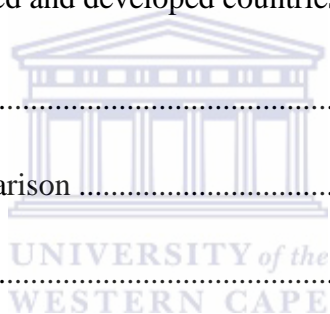
Mrs. Nozililo Madillo Fenie Fuku (R.I.P)



TABLE OF CONTENTS

THESIS TITLE	i
KEY WORDS.....	ii
ABSTRACT.....	iii
DECLARATION	vii
ACKNOWLEDGEMENTS.....	viii
DEDICATION.....	x
TABLE OF CONTENTS.....	xi
LIST OF FIGURES	xxii
LIST OF TABLES.....	xxxiii
LIST OF SCHEMES.....	xxxiv
LIST OF PUBLICATIONS	xxxv
LIST OF ABBREVIATIONS.....	xxxvi
CHAPTER 1	1
General Introduction	1
1.1 Background and Introduction.....	2
1.2 Problem statement.....	8
1.3 Motivation or rationale of the study	10
1.4 Aim and Objectives of the study	11

General objectives.....	11
1.5 Thesis layout	13
CHAPTER 2	16
Literature review	16
2.1 Cancer and biomarkers.....	17
2.1.1 Breast Cancer in Women.....	19
2.1.2 Breast cancer in men.....	20
2.1.3 Statistics (non-developed and developed countries)	23
2.1.3.1 Comparison	23
2.1.3.2 International comparison	23
2.2 DNA and its functions.....	26
2.3 Nanoscience, Nanotechnology and Quantum dots.....	33
2.3.1 Quantum dots and their applications:	36
2.3.1.1 Quantum dots:.....	36
2.3.1.2 Semiconductors.....	36
2.3.1.3 Advantages of quantum dots over conventional methods	41
2.3.1.4 Challenges/disadvantages facing quantum dots on their applications.....	42
2.3.1.4.1 The toxicity of quantum dots	42
2.3.1.4.2 Insolubility of quantum dots	44

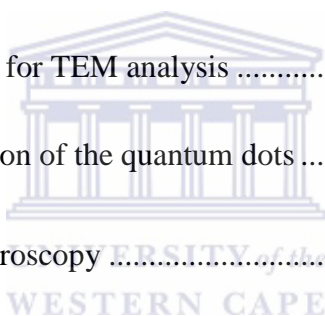


2.3.1.4.3 Intermittent blinking.....	44
2.3.1.4.4 Photo bleaching.....	45
2.3.1.4.5 Non specific binding.....	45
2.3.1.4.6 Agglomeration of quantum dots.....	45
2.4 Properties of quantum dots.....	46
2.4.1 Quantum confinement.....	46
2.4.2 Radiative Relaxation.....	47
2.4.3 Band edge emission.....	47
2.4.4 Defect emission.....	48
2.4.5 Activator emission.....	48
2.4.6 Non-radiative relaxation.....	48
2.4.7 Surface Passivation.....	49
2.5 Quantum dots synthesis processes.....	50
2.5.1 Top-down synthesis.....	52
2.5.2 Bottom-up approach.....	52
2.5.3 Chemical methods.....	53
2.5.4 Physical methods.....	53
2.6 Surface modification and functionalisation of Quantum dots with biomolecules.....	54
2.7 Applications of quantum dots.....	55



2.7.1 Bio-imaging application of quantum dots	57
2.8 Electrochemical sensors based on quantum dots and their functions	59
2.8.1 Biosensing applications based on quantum dots	62
CHAPTER 3	66
Methodology	66
Experimental procedures	67
3.1 Reagents and materials.....	67
3.2 Instrumentation and electrochemical measurements.....	68
3.2.1 Instrumentation.....	68
3.2.2 Synthesis of quantum dots using mercaptopropionic acid (3-MPA) and 3- mercaptosuccinic acid (3-MSA) as a capping agent (stability).....	69
3.2.2.1 Two-pot synthesis of Ga ₂ Te ₃ capped with 3-mercaptopropionic acid.....	69
3.2.2.2 One-pot synthesis of Ga ₂ Te ₃ capped with 3-mercaptopropionic acid	71
3.3 Preparation of Ga ₂ Te ₃ -MPA/Au and Ga ₂ Te ₃ -MPA/GCE electrodes.	73
3.4 DNA genosensor fabrication (dsDNA/Ga ₂ Te ₃ -MPA/Au)	73
3.5 Reaction mechanism electrostatic and covalent bonding between EDC/NHS and Mercapto Acids (3MPA and 3MSA)	76
3.6 Methodology for genosensor-cation interaction (Mechanism)	78
3.7 Sample preparation for cytotoxicity studies of 3MSA/Ga ₂ Te ₃ on lung cancer cells	79

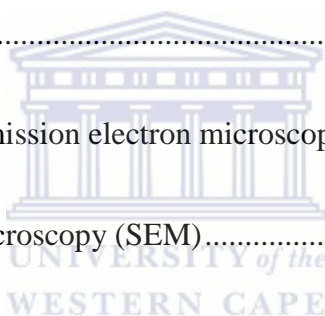
3.7.1 Experimental.....	79
3.7.1.1 Apparatus	79
3.7.1.2 Reagents and materials	79
3.7.1.3 Sample preparation for electrochemical cytotoxicity assay.....	80
3.7.1.4 MTT cell viability assay	80
3.7.1.5 Design and fabrication of a TOXOR prototype for cellular enzyme measurement	81
3.7.1.5.1 Design and fabrication of prototype TOXOR device and GenoDot microanalyzer (GDMA)	81
3.7.1.6 Sample preparation for TEM analysis	83
3.8 Spectroscopic characterisation of the quantum dots	83
3.8.1 Ultraviolet–visible spectroscopy	83
3.8.2 Fluorescence spectroscopy	84
3.8.3 Fourier transforms infra red spectroscopy (FTIR).	84
3.8.4 X-ray diffraction spectroscopy (XRD) and X-ray photoelectron spectroscopy (XPS).	84
3.8.5 Raman spectroscopy	85
3.9 Microscopic characterization of the quantum dots and nanocrystals.....	85
3.9 .1 High resolution transmission electron microscopy (HRTEM).....	85
3.9 .2 Atomic Force microscopy (AFM).	85



3.10 Parameters used for our techniques.....	86
Electrochemical spectroscopy and microscopy techniques used.....	88
3.11 Electrochemical techniques.....	89
3.11.1 Electroanalytical techniques.....	89
3.11.2 Basic components of an electroanalytical system	89
3.11.2.1 Cyclic voltammetry (CV)	91
3.11.2.2 Square wave voltammetry (SWV).....	94
3.11.2.3 Chronocoulometry	97
3.11.2.4 Electrochemical quartz micro-balance (EQCM)	100
3.12 Spectroscopic Methods	102
3.12.1 UV/vis spectroscopy.....	102
3.12.2 Fluorescence spectroscopy	104
3.12.2.1 Absorption and Fluorescence relaxation pathways.....	106
3.12.2.2. Fluorescence emission	106
3.12.2.3 Stokes's shift.....	106
3.12.2.4 Nonradiative relaxation.....	107
3.12.2.5 Intersystem crossing and phosphorescence and/or the radiative transition of an excited molecule.	108
3.12.2.6 Quantum yield.....	110
3.12.3 Electrochemical Impedance Spectroscopy (EIS)	111



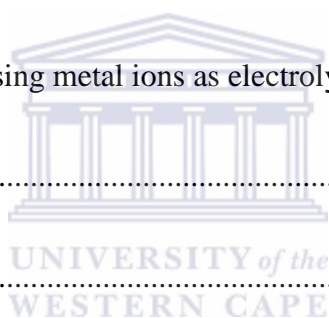
3.12.3.1 Electrical circuit elements.....	116
3.12.4 Fourier Transform Infrared Spectroscopy (FTIR).....	119
3.12.5 Raman spectroscopy	119
3.12.6 X-ray diffraction spectroscopy (XRD)	122
3.12.6.1 Applications of XRD	125
3.12.7 X-Ray Photoelectron Spectroscopy (XPS)	127
3.12.7.1 The Photoemission Process	128
3.12.7.2 Spectroscopy	130
3.13 Microscopic techniques.....	132
3.13.1 High resolution transmission electron microscopy	132
3.13.2 Scanning Electron Microscopy (SEM).....	133
3.13.3 Atomic force microscopy (AFM).....	134
3.14 Drop shape analyser	135
3.14.1 Thermodynamics	136
3.14.2 Applications.....	137
CHAPTER 4	138
Results and discussion 1	138
Characterisation of 3MPA-Ga ₂ Te ₃ quantum dots.....	138
4.1 Introduction	139



4.2 Atomic force and electron microscopy (AFM, HR-TEM, TEM, STEM and SEM)....	140
4.2.1 Characterisation of 3MPA-Ga ₂ Te ₃ quantum dots	140
4.3 Atomic force microscopy (AFM).....	146
4.3.1 Characterisation of 3MPA-Ga ₂ Te ₃ using AFM	146
4.4 X-ray diffraction analysis of 3MPA-Ga ₂ Te ₃ quantum dots	149
4.5 Fourier Transform Infra-Red spectroscopy (FTIR) analysis of 3MPA-Ga ₂ Te ₃ quantum dots	151
4.6 Raman spectra of 3MPA-Ga ₂ Te ₃ quantum dots, 3MPA and the naked substrate	153
4.7 X-ray photo-electron spectroscopy (XPS) analysis of 3MPA-Ga ₂ Te ₃ quantum dots..	155
4.8 Hydrophilic and hydrophobic nature of the quantum dots (capped and uncapped Ga ₂ Te ₃).....	158
4.9 UV/vis and Fluorescence Spectroscopy	160
4.10 Quantum yield Comparison between 3MPA-Ga ₂ Te ₃ quantum dots with Rhodamine 6G	165
4.11 Genosensor response using, electrochemical impedance spectroscopy (EIS)	167
4.12 Sub-conclusion	171
CHAPTER 5	172
Results and discussion 2	172
Genosensor responses	172

5.1 Introduction	173
5.2 Electrochemical responses of Her2/neu Oncogene genosensor	173
5.2.1 Detection mechanism	173
5.2.2 Cyclic and square wave voltammetry responses	183
5.2.3 Stability of the probe-modified electrode and Sequence-specific hybridisation studies	190
5.2.4 Impedimetric responses	193
5.2.5 Chronocoulometric responses.....	196
5.2.6 Time-based Amperometry responses	199
5.3 Spectroscopic genosensor response	202
5.3.1 UV-vis responses of Her2/neu oncogene genosensor	202
5.4 Sub conclusion	205
CHAPTER 6	207
Results and discussion 3	207
EQCM and micro-fluidic responses of Her2/Neu Oncogene genosensor	207
6.1 EQCM of genosensor	208
6.1.1 Genosensor response of 3MPA-Ga ₂ Te ₃ /ssDNA.....	208
6.2 Micro-Fluidics of genosensor	214

6.2.1 Scan rate dependence of 3MPA-Ga ₂ Te ₃ and genosensor response of 3MPA-Ga ₂ Te ₃ /ssDNA.....	214
6.3 Sub-conclusion.....	217
CHAPTER 7	219
Results and discussion 4	219
Mechanism of DNA-QDs interaction	219
7.1 Introduction	220
7.2 Electrochemical genosensor mechanism.....	220
7.2.1 Genosensor response using metal ions as electrolytes	220
7.3 Sub-conclusion.....	229
CHAPTER 8	230
Results and discussion 5	230
Cytotoxicity of quantum dots.....	230
8.1 Introduction	231
8.2 Cytotoxicity of quantum dots using 3 MSA-Ga ₂ Te ₃ in cancer cells.....	231
8.2.1 Characterisation of 3 MSA-Ga ₂ Te ₃ using electron microscopy and spectroscopy.....	231
8.2.1.1 Atomic force and electron microscopy of 3 MSA-Ga ₂ Te ₃	231
8.2.1.2 AFM of 3 MSA-Ga ₂ Te ₃	234
8.2.1.3 XRD analysis of 3 MSA-Ga ₂ Te ₃	237



8.2.1.4 Structural analysis of 3 MSA-Ga ₂ Te ₃	239
8.2.1.6 Toxicity tests of 3 MSA-Ga ₂ Te ₃	244
8.3 Sub-conclusion.....	250
CHAPTER 9.....	251
Conclusion and recommendation.....	251
9.1 Conclusion.....	252
9.2 Recommendations.....	257
References.....	258



LIST OF FIGURES

Figures	Title	Page no
Figure 1	Schematic representation for cancer occurrence.	18
Figure 2	Image of an infected breast (amplification/overexpression of cells).	20
Figure 3	Structure of the (A) Her/neu family and (B) Her2/neu [64].	22
Figure 4	Rate of cancer incidents. (B) Race distribution of breast cancer and (C) Pie chart of cancer mortality.	24
Figure 5	Cell structure representing the home of DNA (Nucleus) [97].	27
Figure 6	(A) Chemical structure of the DNA bases and (B) Pieces of DNA that contains the information for making a particular biochemical, usually a protein [98; 101].	28
Figure 7	Canonical Watson-Crick DNA base paring through G-C and T-A intermolecular.	29
Figure 8	Simplified mechanistic pathway for the oxidation of guanine.	32
Figure 9	Semiconductor Energies.	38
Figure 10	Schematic representation QDs, atoms and bulk materials.	39
Figure 11	Schematic representation of quantum dots and bulk materials.	41
Figure 12	(A) Defines shells and core shells of different quantum dots, (B)	51

Quantum dot (TGA-CdTe/ZnS) with two II-VI layers (Core and shell) capped with TGA and (C) Quantum dots (3MSA-Ga₂Te₃) with only the core capped with MSA and MPA.

Figure 13	The versatility of quantum dots application in different branches of science.	56
Figure 14	Application of quantum dots in tumour cells.	58
Figure 15	Schematics of genosensing process.	60
Figure 16	Schematic representation of QDs – DNA interactions.	63
Figure 17	Two-pot synthesis of Ga ₂ Te ₃ capped with 3-mercaptopropionic acid.	71
Figure 18	One-pot synthesis of Ga ₂ Te ₃ capped with 3-mercaptopropionic acid.	72
Figure 19	Schematic representation of quantum dots-DNA with common DNA (Hybridisation).	74
Figure 20	Schematic representation of genosensor fabrication.	75
Figure 21	Fully assembled A) GDMA and B) TOXOR sensing devices. Displayed is the reagent cavity, microwell with immobilised cells, sink-overflow device and printed sensor for enzyme activity and ssDNA/3MPA- Ga ₂ Te ₃ measurements.	82
Figure 22	Representation of an electrochemical cell consisting of three	90

electrodes.

Figure 23	A cyclic voltammogram of 5 mM ferricyanide using boron-doped diamond (BDD) electrode at a scan rate of 25 mV s^{-1} .	92
Figure 24	Square-wave waveform showing the amplitude, E_{sw} ; step height, E ; square-wave period, delay time, T_d ; and current measurement times, 1 (forward pulse) and 2 (reverse pulse).	95
Figure 25	Square-wave voltammograms for reversible electron transfer. Curve A; forward current. Curve B: reverse current. Curve C: net current.	96
Figure 26	Typical chronocoulometry of 3MPA- Ga_2Te_3 .	98
Figure 27	A Jablonski diagram representing the energy levels for a fluorescent molecule and several important transitions.	105
Figure 28	Overlaying of absorbance and fluorescence spectra showing the Stoke's shift.	107
Figure 29	Nyquist plot.	113
Figure 30	A typical Nyquist plot.	113
Figure 31	Typical Bode plot of bare Au and Au/3MPA- Ga_2Te_3 in PBS showing variation of impedance and phase angle with changes in frequency.	115
Figure 32	Equivalent circuit of a capacitor and a resistor in parallel at one	115

time constant.

Figure 33	Energy-level diagram showing the states involved in Raman signal. The line thickness is roughly proportional to the signal strength from the different transitions.	120
Figure 34	X-ray diffraction pattern schematic.	123
Figure 35	XRD spectra of 3MPA- Ga ₂ Te ₃ showing lattice patterns and phase angles.	124
Figure 36	Ejection of photoelectrons.	127
Figure 37	The photoemission process involved for XPS surface analysis.	129
Figure 38	Spectrum from 3 MPA- Ga ₂ Te ₃ showing various sulphur, gallium, oxygen and a carbon peaks.	130
Figure 39	The C 1s region of the XPS spectrum from spin-cast and sheet 3MPA- Ga ₂ Te ₃ . Carbon is present in three distinct chemical states.	131
Figure 40	AFM schematic system with sample topography.	134
Figure 41	Hydrophobic surface (left) and hydrophilic surface (right).	135
Figure 42	Demonstration of the $\theta/2$ method (Young's modulus).	137
Figure 43	TEM (i), HRTEM (ii) (FFT: insert), image of 3MPA- Ga ₂ Te ₃ .	141

Figure 44	STEM (i) and SEM (ii) image of 3MPA- Ga ₂ Te ₃ quantum dots.	143
Figure 45	EDS (i) and mapping (ii-iv) images of 3MPA-Ga ₂ Te ₃ quantum dots.	145
Figure 46	AFM images of 3MPA-Ga ₂ Te ₃ quantum dots.	147
Figure 47	AFM images of 3MPA-Ga ₂ Te ₃ quantum dots.	148
Figure 48	AFM images of 3MPA-Ga ₂ Te ₃ quantum dots.	149
Figure 49	X-ray diffraction pattern of 3MPA-Ga ₂ Te ₃ quantum dots.	150
Figure 50	FTIR spectra of A) 3 MPA and B) 3MPA-Ga ₂ Te ₃ .	152
Figure 51	Raman spectra of A) 3 MPA, Ga ₂ Te ₃ -3 MPA, tape and B) Chemical structure of 3MPA and 3 MPA-Ga ₂ Te ₃ (Abbreviations: ν , stretching; δ , in-plane bending; G , out-of-plane bending; T , rocking, wagging).	154
Figure 52	XPS spectra of 3MPA-Ga ₂ Te ₃ .	156
Figure 53	XPS spectra of 3MPA-Ga ₂ Te ₃ .	157
Figure 54	Hydrophobic surface and hydrophilic surface of A) Solid surface (blank), B) Ga ₂ Te ₃ and C) 3 MPA-Ga ₂ Te ₃ .	159
Figure 55	UV/vis of 3MPA-Ga ₂ Te ₃ in solution (before and after refluxing).	160
Figure 56	(A) Fluorescence spectra of 3MPA-Ga ₂ Te ₃ showing and (B) Both emission and excitation in solution (before and after	163

refluxing).

- Figure 57 (A) 3D-Mesh and (B) Contour plots of 3MPA-Ga₂Te₃ in solution. 164
- Figure 58 Comparison between rhodamine 6G and 3 MPA-Ga₂Te₃. 166
- Figure 59 A) Nyquist plots of bare Au, Au/Ga₂Te₃-3MPA and Au/Ga₂Te₃-3MPA/ssDNA modified electrodes in 0.1 M PBS (pH = 7.4). (B) Bode plots and exploration of (A). 169
- Figure 60 (A) Voltammetric plots of (a) bare GCE (b) GCE/3MPA (c) GCE/Ga₂Te₃ and (d) GCE/Ga₂Te₃-3MPA and (B) Cyclic voltammetry data of ssDNA on bare glassy carbon electrode (GCE/ssDNA), all the measurements were performed in PBS, pH 7.4 at a scan rate of 25 mV s⁻¹. 174
- Figure 61 (A) Voltammetric plots of (a) GCE/Te, (b) GCE/Ga₂Te₃-3MPA and (c) GCE/Ga₂Te₃-3MPA /ssDNA and (d) bare GCE and. (B) Cyclic voltammetry response for Bare (Au) and Au/Ga₂Te₃-3MPA/ssDNA modified electrodes at a scan rate of 25 mV s⁻¹. All the measurements were performed in PBS, pH 7.4. 176
- Figure 62 Voltammetric plots of (A) Au/Ga₂Te₃-3MPA and (B) GC/Ga₂Te₃-3MPA. All measurements were performed in PBs pH = 7.4 at a scan rate of 5-30 mV s⁻¹. 180
- Figure 63 Voltammetric plots of (A) Au/Ga₂Te₃-3MPA/ssDNA and (B) Randel-Sevčik plot of data from 'A'. All measurements were 182

performed in PBs pH = 7.4 at a scan rate of 5-30 mV s⁻¹.

- Figure 64 Voltammetric plots of Au/3MPA-Ga₂Te₃/ssDNA at different concentration of Her2/neu oncogene (0.1→1), (A) CV responses to Her2/oncogene and (B) Calibration curves of Her2/oncogene genosensor in 'A'. 184
- Figure 65 Calibration curve of Her2/oncogene with data from '64 B'. 186
- Figure 66 Voltammetric plots of Au/3MPA-Ga₂Te₃/ssDNA at different concentration of Her2/neu oncogene (0.1→1), (A) SWV responses to Her2/oncogene and (B) Calibration curves of Her2/oncogene genosensor in 'A'. 188
- Figure 67 Calibration curves of Her2/oncogene with data from '66 B'. 189
- Figure 68 Voltammetric plots of Au/3MPA-Ga₂Te₃/ssDNA in 0.1M PBS pH = 7: at different analytes (0.5 nM) of Her2/oncogene, (Complimentary, 1-Base mis-match, non-complimentary and 3-Base mis-match) (A) Responses to Her2/oncogene. 191
- Figure 69 The stability of the genosensor (3MPA-Ga₂Te₃/ssDNA) in 0.1 M PBS pH = 7: at a scan rate of 25 mV s⁻¹. 192
- Figure 70 EIS/Nyquist plots of Au/3MPA-Ga₂Te₃/ssDNA in 0.1M PBS pH = 7: at different concentration of Her2/oncogene (A) Responses to Her2/oncogene and (B) Calibration curve of Her2/oncogene in 'A'. 194

Figure 71	Calibration curve of Her2/oncogene with data from '70B'.	195
Figure 72	Chronocoulometric plots of Au/3MPA-Ga ₂ Te ₃ /ssDNA in 0.1 M PBs pH = 7.4: at different concentration of Her2/oncogene (A) Responses to Her2/oncogene and (B) Calibration curve of Her2/oncogene in 'A'.	197
Figure 73	Calibration curve of Her2/oncogene with data from '72B'.	198
Figure 74	Time-based chronoamperometric plots of Au/3MPA-Ga ₂ Te ₃ /ssDNA in 0.1 M PBS pH = 7: at different concentration of Her2/oncogene (A) Responses to Her2/oncogene and (B) Calibration curve of Her2/oncogene in 'A'.	200
Figure 75	Calibration curve of Her2/oncogene with data from '74B'.	201
Figure 76	UV/vis plots of (A) DNA, 3MPA- Ga ₂ Te ₃ and Au/3MPA-Ga ₂ Te ₃ /ssDNA.	202
Figure 77	(A) UV/vis plots of 3MPA-Ga ₂ Te ₃ /ssDNA at different concentrations of Her2/oncogene (0.5-8 nM) and (B) Calibration curve of Her2/oncogene in 'A'.	204
Figure 78	Calibration curve of Her2/oncogene with data from '77 B'.	205
Figure 79	Voltammetric plots of CE/3MPA-Ga ₂ Te ₃ /ssDNA at different concentration of Her2/neu oncogene (0.1→1), (A) CV responses to Her2/oncogene and (B) Calibration curves of Her2/oncogene genosensor in 'A'.	209

Figure 80	Calibration curves of Her2/oncogene with data from '79 B'.	210
Figure 81	EQCM voltammetric plots of CE/3MPA-Ga ₂ Te ₃ /ssDNA at different concentration of Her2/neu oncogene (0.1→1), (A) EQCM responses to Her2/oncogene and (B) Calibration curves of Her2/oncogene genosensor in 'A'.	212
Figure 82	Calibration curves of Her2/oncogene with data from '81B'.	213
Figure 83	Micro-fluidics voltammetric plots of 3MPA-Ga ₂ Te ₃ /ssDNA in 0.1M PBS pH = 7: (A) CV plots for 5-30 mV s ⁻¹ and (B) Randel-Sevčík plot of data from 'A'.	215
Figure 84	Micro-fluidics voltammetric plots of 3MPA-Ga ₂ Te ₃ /ssDNA in 0.1M PBS pH = 7: (A) Responses to Her2/oncogen and (B) Bar-chart of the genosensor peak current from 'A'.	216
Figure 85	Voltammetric plots of A) GCE/3MPA-Ga ₂ Te ₃ /ssDNA at different potential windows (-1.0 V to 1.0 V) and B) Calibration curve of potential windows in 'A'.	221
Figure 86	Genosensor response of A) CV of GCE/3MPA-Ga ₂ Te ₃ /ssDNA with different cations but same concentrations (0.1M) and B) Table showing the electronegativity of different cations together with a periodic table with elements from group 1 and 2.	223
Figure 87	Effect of electrolytes on genosensor responses: (A) CsCl and Calibration curves of Her2/oncogene genosensor in (B) CsCl	224

	electrolyte.	
Figure 88	Calibration curve of Her2/oncogene with data from '87B' CsCl electrolyte.	225
Figure 89	Effect of electrolytes on genosensor responses: (A) LiCl and Calibration curves of Her2/oncogene genosensor in (B) LiCl electrolyte.	226
Figure 90	Calibration curve of Her2/oncogene with data from '89 B' LiCl electrolyte.	227
Figure 91	TEM (A), STEM (B) and HRTEM (C:insert) image of Ga ₂ Te ₃ -3MSA.	233
Figure 92	AFM images of 3MSA-Ga ₂ Te ₃ quantum dots.	235
Figure 93	AFM images of 3MSA-Ga ₂ Te ₃ quantum dots.	236
Figure 94	FFT crystallinity of A,B) 3MSA-Ga ₂ Te ₃ and C) X-ray diffraction pattern of 3MSA-Ga ₂ Te ₃ quantum dots.	237
Figure 95	EDS spectra of Ga ₂ Te ₃ -3 MSA.	239
Figure 96	FTIR spectra of a) 3 MPA, b) uncapped Ga ₂ Te ₃ and c) Ga ₂ Te ₃ -3 MSA.	240
Figure 97	XPS spectra of 3MSA-Ga ₂ Te ₃ .	241
Figure 98	XPS spectra of 3MSA-Ga ₂ Te ₃ .	243
Figure 99	Electrochemical AP cytotoxicity assay.	245

Figure 100	Light microscopy (X100) image of cells after 24 h exposure to (A) medium plus PBS and (B) $1000 \mu\text{g mL}^{-1}$ Ga_2Te_3 3 MSA quantum dots.	247
Figure 101	26500 X TEM images of A549 human lung epithelial cells: (A) in PBS only.	248
Figure 102	26500 X TEM images of A549 human lung epithelial cells: (B and C) in PBS solution of 3MSA- Ga_2Te_3 .	249



LIST OF TABLES

Tables	Title	Page no
Table 1	Parameters used for CV at different scan rates and EQCM at different additions of analytes.	86
Table 2	Parameters used for CV and SWV for different additions of Analytes.	86
Table 3	Parameters used UV/vis and EIS Spectroscopy for characterisation and different additions of Analytes.	87
Table 4	Parameters used chronocoulometry and chronoamperometry for different additions of analytes.	87
Table 5	The seven crystal systems and the restrictions placed on the lattice parameters of the unit cell.	126
Table 6	Comparison of different systems for detection of HER2/neu oncogene (The original values are all converted to ng mL ⁻¹).	190
Table 7	Difference in frequency and mass as we introduce target HER2/neu oncogene.	213
Table 8.	Analytical parameters of the genosensor obtained by various techniques.	218

LIST OF SCHEMES

Schemes	Title	Page no
Scheme 1.	MPA interaction with Ga ₂ Te ₃ quantum dots.	69
Scheme 2.	MSA interaction with Ga ₂ Te ₃ quantum dots.	71
Scheme 3.	Reaction mechanisms for the formation of amide bonds with (A) EDC and (B) NHS.	77
Scheme 4	Reaction mechanism of: (A) 3MPA-Ga ₂ Te ₃ with linkers (EDC/NHS) and (B) Molecular structure of Au/3MPA- Ga ₂ Te ₃ /DNA–DNA assembly/interaction.	178
Scheme 5.	Reaction mechanism of GC/3 MSA/Ga ₂ Te ₃ /dsDNA with cationic species i.e Li ⁺ and Cs ⁺ .	228

LIST OF PUBLICATIONS

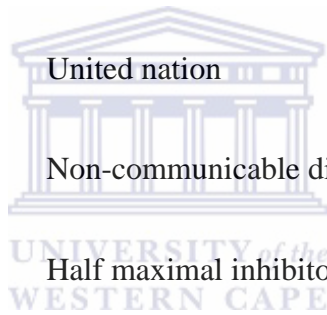
1. **Xolile G Fuku**, Faiza j Iftikhar, Euodia H Hess, Priscilla PGL Baker, Emmanuel I Iwuoha, Cytochrome c biosensor for determination of trace levels of cyanide and arsenic compounds, *Anal chim acta*, 2012, 730, 49-59.
2. **Xolile G Fuku**, Priscilla PGL Baker, Emmanuel I Iwuoha, Spectroscopic evaluation of cytochrome c interaction to arsenic and cyanide ligands and its structural changes on the electrode interface 2014, **50**(5),58–66.
3. Abd Almonam Baleg, Nazeem Jahed, Anne L. Djoumessi Yonkeu, Njagi Njomo, Gcineka Mbambisa, Kerileng M. Molapo, **Xolile G. Fuku**, Gertrude Fomo, Hlamulo Makelane, Abebaw Tsegaye, Tesfaye T. Waryo, Priscilla Baker, Sibulelo Vilakazi, Robert Tshikhudo, Emmanuel I. Iwuoha, Impedimetry and microscopy of electrosynthetic poly(propylene imine)-co-polypyrrole conducting dendrimeric star copolymers, *Electrochimica Acta*, 2014, 128, 448-457
4. Rachel F. Ajayi, Unathi Sidwaba, Usisipho Feleni, Samantha F. Douman, Oluwakemi Tovide, Subelia Botha, Priscilla Baker, **Xolile G. Fuku**, Sara Hamid, Tesfaye T. Waryo, Sibulelo Vilakazi, Robert Tshihkudo, Emmanuel I. Iwuoha, Chemically amplified cytochrome P450-2E1 drug metabolism nanobiosensor for rifampicin anti-tuberculosis drug, *Electrochimica Acta*, 2014, 128, 149-155
5. **Xolile Fuku**, Baljit Singh, Rachel Ajayi, Abongile Jijana, Priscilla Baker, Eithne Dempsey, Emmanuel Iwuoha, Electrochemical HER2/neu oncogene detection using Ga₂Te₃ quantum dots based genosensor (*Analyst*, Submitted).

LIST OF ABBREVIATIONS

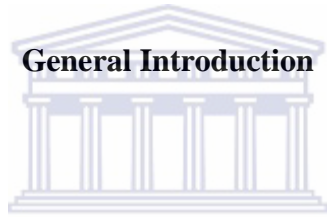
Her2/neu	Human epidermal growth factor receptor 2
BC	Breast cancer
MMPs	Matrix metalloproteinases
EGFR	Epidermal growth factor receptor
DNA	Deoxyribonucleic acid
EDC	1-ethyl-3-(3-dimethylaminopropyl) carbodiimide hydrochloride
NHS	N-hydroxysuccinimide
3-MPA	3-mercaptopropionic acid
3-MSA	3-mercaptosuccinic acid
Au	Gold
GCE	Glassy carbon electrode
QDs	Quantum dots
DCIS	Ductal carcinoma in situ
IDC	Infiltrating ductal carcinoma
ILC	Infiltrating lobular carcinoma
LCIS	Lobular carcinoma in situ
Neu	Neuroglioblastoma
HOMO	Highest occupied molecular orbital
LUMO	Lowest unoccupied molecular orbital
LOD	Limit of detection

LDR	Linear dynamic range
NIL	Nanoimprint lithography
PVD	Physical vapour disposition
CVD	Chemical vapour disposition
MBE	Molecular beam epitaxy
PL	Photoluminescence
TOP	Trioctylphospine
TOPO	Ttrioctylphosphine oxide
GDMA	GenoDot microanalyzer
HRTEM	High resolution transmission electron microscopy
XRD	X -ray diffraction
FTIR	Fourier transform infra-red
CC	Chronocoulometry
CV	Cyclic voltammetry
SWV	Square wave voltammetry
EIS	Electrochemical impedance spectroscopy
EQCM	Electrochemical quartz microbalance
FFT	Fast Fourier transform
AFM	Atomic force microscopy
EEM	Excitation/emission matrix
UV-vis	Ultraviolet visible

IHC	Immunohistochemistry
FISH	Fluorescent in situ hybridisation
PCR	Polymerase chain reaction
ELISA	Enzyme linked immunoabsorbant essay
FDA	Food and drug administration
EPA	Environmental protection agency
WHO	World health organisation
CANSA	Cancer association of South Africa
UN	United nation
NCD	Non-communicable diseases
IC ₅₀	Half maximal inhibitory concentration
HIV	Immunodeficiency virus
TB	Tuberculosis
NNI	National nanotechnology initiative
SANi	South African nanotechnology initiative
AMTS	Africa's advanced manufacturing technology strategy
SAMES	South African micro-economic strategy



CHAPTER 1



General Introduction
UNIVERSITY *of the*
WESTERN CAPE

1.1 Background and Introduction

Cancer which is expressed as a disorder of chaos and causes an impairment of biochemical pathways in living metabolisms or an abnormal and uncontrolled cell growth due to an accumulation of specific genetic and epigenetic defects, both environmental and hereditary in origin [1]; is an emerging health problem in South Africa, with breast cancer being one of the leading cancers killers in women over the world. Breast cancer (BC) is a disease in which malignant (cancerous) cells form in the tissues of the breast, usually in the ducts and lobules. Invasion and metastasis are the root causes of cancer death with the initial step being the breakdown of extracellular matrix by invading cancer cells via a concerted action of proteolytic enzymes (such as matrix metalloproteinases, MMPs), particularly the gelatinases MMP2 and MMP9 [4; 5]. The secretion and activity of these enzymes are partially dependent on the human epidermal growth factor receptor 2 (HER2) pathway. BC is caused by a gene called HER2. HER2 which is also called *cerbB-2*, was first cloned and verified from the rat neuro/glioblastomas that were induced by ethylnitrosourea [2; 3]. It is located in the chromosome 17q21 Her-2 receptor molecules on the cell surface [4]. Her-2/neu proto-oncogene encodes the 1,255 amino acid transmembrane Her-2 glycoprotein of 185 kDa molecular weight [4; 5]. The HER2 gene is responsible for making HER2 protein. This gene is the second member of the epidermal growth factor receptor (EGFR) family [6]. A previous study has demonstrated that the physiological function of the HER2/neu gene is related to the neural and cardiac development from gene knockout experiments in mice [6]. Since it has no specific ligands, HER2/neu typically heterodimerises with other members of the EGFR family [5; 7]. This gene has also been linked to neoplastic transformation. Extensive studies have shown that the amplification and/or over-expression of the HER2/neu proto-oncogene-

are associated with a wide range of human cancers including, breast, stomach, lung, ovary and oral cavity [8]. About 30% in breast carcinoma is associated with overexpression of HER2/neu [6; 9]. When two copies of the gene are present in normal amounts, the protein plays an important role in normal cell growth and development. The HER2 protein transmits signals directing cell growth from the outside of the cell to the nucleus inside the cell. Growth factors — chemicals that carry growth-regulating orders — attach to the HER2 protein and signal normal cell growth [10; 11]. In approximately 25 percent of women with breast cancer, there is a genetic alteration in the HER2 gene that produces an increased amount of the growth factor receptor protein on the tumour cell surface[10; 12]. This overexpression can cause cells to divide, multiply, and grow more rapidly than normal, thus cancerous breast cells develop [13; 14]. HER2/neu which causes breast cancer tissue to be cancerous will be used as the biomarker, since detection of cancer infers that certain characteristics of the tumour are different from corresponding normal tissue and can be measured as biomarkers. Biomarkers, also called molecular markers or biochemical marker; are biological molecules found in body fluids or tissues [15; 16; 17]. In cancer, molecular biomarkers are often genes or gene products such as proteins. Appropriate markers maybe able to define risks and identify the early stages of tumor development, assist in tumour detection and diagnosis verify stratification of patients for treatment, predict outcomes of the disease and also assist in surveillance of disease recurrence[16; 18]. The disadvantages of biomarkers includes: expensive (costs for analyses), Ethical responsibility, laboratory error and less storage (longevity of samples) [16; 17]. However, apart from their draw back biomarkers have several advantages such as objective assessment, precision of measurement, reliable; validity can be established and biased than questionnaires[16; 17], hence the use of biomarkers for screening.

HER2/neu oncogene will be used as a marker in the early detection of breast cancer. Breast cancer remains a major public health problem worldwide. Screening of the tumour at an early stage is considered vital in South Africa if not the world. According to statistics one in six South African men and one in seven South African women will get cancer during their lives. Over 3000 women die each year due to breast cancer. Based on cancer association of South Africa (CANSA) statistics, early diagnosis is one of the most important strategies to reduce BC morbidity rate and to improve the survival rate since there are no clear prevention methods or strategies. Thus researchers have and still are trying to develop a method which will overcome the stigma. Some of the developed methods includes: western blots, mass spectroscopy, near infrared spectroscopy, southern blots, lateral flow strips, polymerase chain reactions (PCR), enzyme linked immunoabsorbant assay (ELISA) or PCR-ELISA and recently electrochemical methods [19; 20]. Apart from electrochemical methods, all these methods are always expensive, time consuming labour intensive and also harmful to the patients. Hence many researchers propose electrochemical sensor methods in our case a DNA quantum based electrochemical sensing technique which is less expensive, less time consuming, user friendly and without multiplexing capabilities. Developing a quantum based technique requires quantum dots synthesis. In recent years researchers have used organic and inorganic synthesis of materials for nature imitation, giving rise to, among others, synthesis of colloidal nanocrystals with tailored physical and chemical properties [21]. In particular, synthesis of nanostructured inorganic compounds has led to the development of a variety of approaches that mimic the recognition and nucleation capabilities found in biomolecules for ample range of applications [22]. These nanomaterials present a hierarchical self-assembly of topologically complex and multifunctional architectures with properties tuneable at each level of the ladder [23]; an element that broadens the scope of their purpose.

Compared with traditional organic fluorophores and fluorescent proteins, QDs are superior in fluorescence brightness, emission tuneability and photobleaching resistance. In addition, QDs have broad absorptions with narrow emission spectra, and are multi-colour. They can be excited simultaneously by a single-light source, with minimal spectral overlapping. These unique optical properties make QDs ideal candidates for multi-colour imaging of molecules in order to investigate the dynamic cellular processes of cancer progression, such as continual cell migration, invasion and metastasis. However, the clinical application of QDs-based probes *in vivo* has been limited by potential cytotoxicity effects, and clinical application should firstly involve *in vitro* studies, especially in molecular pathology. The advances of QD-based probes for breast cancer have demonstrated a promising preclinical application in recent studies.

Quantum dots also known as zero-dimensional material are very, very tiny particles on the order of a nanometer in size (1-20 nm) and are composed of a hundred to a thousand atoms. They comprise elements from groups II-VI, III-V or IV-VI. Their size and shape are well known to have vital influence on their widely varying electrical, optical properties and bio-imaging. This is due to their potential applications in several areas, including catalysis, coatings, textiles, data storage, biotechnology, health care, biomedical, pharmaceutical industries and most recently, in bioanalytical chemistry [24]. In bioanalytical chemistry, particular applications of quantum dots include their use as fluorescent labels, fluorescent probes, immunosensors and oligodeoxyribonucleotide (ODN) labels for deoxyribonucleic acid (DNA) sensors or genosensors [25]. Tuning the size of quantum dots leads to quantum confinement effects, which permits modulation of optical and electrochemical properties of the nanocrystals [26].

The optical properties of quantum dots can as well be influenced by changing their chemical composition through alloying [27], which can be controlled at the synthesis stage. Another strategy to modulate the optical properties of quantum dots may involve substitution of host cations with metals like manganese, copper, or rare-earth elements [28]. By the incorporation of impurity atoms into the lattice of the host semiconductor, the dominant recombination route can be transferred to the impurity related trap states [27], providing an alternative pathway to the band-edge emission, which involves the highest occupied and the lowest unoccupied quantum-confined orbitals. Further modulation of their electronic properties involve suitable functionalisation with amphiphilic bifunctional molecules such as mercapto carboxylic acids [29] [30]. These molecules permeate rapid transfer of electrons between the small sizes of quantum dots and the surface of the target particles, resulting to a higher charge detaching efficiency [31]. Short chained capping agents such as mercaptopropionic acid (MPA) and/or mercaptosuccinic acid (MSA) have been used for self assembly on gold electrodes [32] and are associated with enhanced electrochemical signals of the quantum dots towards target analytes [33]. The power and scope of electrochemically and optically modulated quantum dots can be greatly enhanced by coupling them with biological recognition reactions and electrical processes, to form nanobioelectronics [34]. This coupling also requires proper surface tailoring and functionalisation of the quantum dots, to make them biocompatible. Besides improving the nanocrystal electrochemistry, the mercapto acids leave free carboxylic acid groups on the surface of the quantum dots, which can covalently link favourably with amine groups of biomolecules, thus conferring biocompatibility properties on the quantum dots. Quantum dots have a great potential for DNA diagnostics and can have profound impact in analysis of DNA in clinical diagnostics and anti-cancer therapy. Additionally they can also play a vital role in drug deliver.

Quantum based DNA sensors for an early screening of cancer and/or BC has been vastly studied, while other researchers have devoted their time in drug delivery and cytotoxicity of the quantum dots. Huang *et al.*, developed a sensitive quantum dots-based “OFF-ON” fluorescent sensor for ruthenium anticancer drugs and ctDNA [35], meanwhile Johns Hopkins University engineers have developed a new method of finding specific sequences of DNA by making them light up beneath a microscope by using tiny semiconductor crystals, biological probes and a laser [36]. The researchers, who say the technique will have important uses in medical research, demonstrated its potential in their lab by detecting a sample of DNA containing a mutation linked to ovarian cancer [36]. Morten *et al.*, develop a quantum dot based DNA nanosensor specifically targeting the cleavage–religation activity of an essential DNA-modifying enzyme, human topoisomerase I [37]. DNA nanosensor based on biocompatible graphene quantum dots and carbon nanotubes was developed by Zhao *et al.*, [38]. Wang, an assistant professor in the Department of Mechanical Engineering and the Whitaker Biomedical Engineering Institute at Johns Hopkins, led his team in exploiting an important property of quantum dots: They can easily transfer energy. When a laser shines on a quantum dot, it can pass the energy on to a nearby molecule, which in turn emits a fluorescent glow that is visible under a microscope. All these sensors have a common goal which is an early screening of cancer but far-better compared to traditional techniques. The assays have shown great promise in biological crude samples and thus are expected to contribute in clinical diagnostic and may help in identify people at risk of developing cancer, so that treatment can begin at a very early stage. Based on those findings we propose a more efficient quantum based electrochemical DNA sensor or an electrochemical nanobiosensor that will be ultrasensitive, have a very low detection limit, quick and relatively simple. This approach opens up development of DNA-based genosensors for the detection of transgenes or biomarkers for breast cancer.

1.2 Problem statement

The burden of breast cancer (BC) involves not only the affected patients and their loved ones, who suffer physically, emotionally and financially, but the society in general. Hence, early screening of BC at a nano-scale is of utmost importance. According to statistics from the cancer association of South Africa (CANSAs), breast cancer is the most common cancer among South African women. Cancer cells produce deoxyribonucleic acids (DNA), ribonucleic acids (RNA), proteins and metabolites as potential biomarkers. Breast cancer is signified by over expression of the human epidermal growth factor receptor 2 (HER2) protein which is encoded by the ERBB2 gene. Detection of this gene is therefore an important clinical procedure in cancer screening practise. Cancer screening for detection, risk assessment diagnosis and prognosis are based on three main assay platforms (genomic, proteomic and metabolic/metabolomic profiles). Genomic technologies including DNA microarrays, polymerase chain reaction (PCR)-based assays, and fluorescence in situ hybridization (FISH) permit the determination of genetic materials associated with cancers and tumours. DNA-based biomarkers originate from genetic mutations, loss of heterozygosity (LOH), microsatellite instability (MSA), and DNA methylation. RNA-based biomarkers are mostly mRNAs found in tissues and bodily fluids. Using DNA microarrays, it is possible to identify biomarkers that are differentially expressed in malignant tissues including breast tumours. The challenge for medical diagnostics industries is how to translate the DNA microarrays technology into reliable tools for clinical applications. This work will focus on synthesis of mercaptopropionic and mercaptosuccinic – capped chalcogenic binary quantum dots of Gallium. These capped quantum dots will be used for fabrication of reliable, ultrasensitive, cheap and less time wasting genosensor, for detection of human epidermal growth factor Receptor 2. In the synthesis of the quantum dots gallium will be used as

cationic precursors, while tellurium will be used as chalcogenic anion. Mercapto acids will confer bio conjugation properties on the quantum dots as well as solubilise and non-agglomerate them. Transmission electron microscopy (TEM) will be used to infer the size and mono-dispersity of the quantum dots while Atomic force microscopy will infer their morphology. Fourier transform infra-red (FTIR) and subtractively normalized FTIR (SNFTIR) spectroscopy will be used to confirm retention of the capping agent and its voltage dependent vibrations on the surface of the quantum dot. Further studies of Raman active molecules within the quantum dots will be done using Raman spectroscopy. Optical properties of the quantum dots will be studied by ultra-violet visible (UV-vis) as well as fluorescence spectroscopy. Electrochemical studies will be done using cyclic voltammetry (CV), square wave voltammetry (SWV) and electrochemical impedance spectroscopy (EIS). Genosensors for HER2 will be prepared by immobilizing amine terminated single strand DNA (ssDNA) of the sequence $\text{NH}_2\text{-}5'\text{-TTG ATG GCC ACT GGA ATT-}3'$ onto a quantum dot modified gold electrode followed by hybridization with different concentrations of the target sequence $5'\text{-AAT TCC AGT GGC CAT CAA-}3'$. The hybridization events will be monitored by EIS to obtain response profiles.

1.3 Motivation or rationale of the study

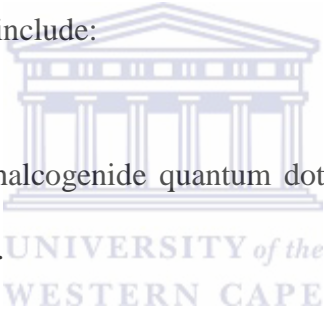
The United Nation (UN) declaration on non-communicable diseases (NCD's) which are also recognised by the World Health Organisation (WHO) ratified in September 2011, acknowledged that of the 36 million global deaths due to NCD's, nearly 80% occurred in developing countries. It also recognised that by 2030, NCD's would become the most common cause of death, even in Africa. While previously in South Africa NCD's, including cancer, were relegated to a lower priority behind communicable diseases such as human immunodeficiency virus (HIV) and tuberculosis (TB). The changing epidemiology of NCD's has suddenly propelled cancer into the spotlight. Cancer, once perceived as a problem of developed countries and the socio-economically advantaged communities in South Africa, is now the fourth leading cause of death in South Africa accounting for 7% of mortality. Thus the National Advisory Committee on the prevention and control of cancer in line with section 91(1) of the national health act was established by the minister of health due to reasons mentioned above. This act shows that it is vitally important that cancer be prevented at all cost. The importance of screening and early detection of breast cancer in determining the survival rate is only matched by the numerous methods already developed for diagnosing the disease. Among the methods are digital mammogram, magnetic resonance imaging, optical imaging and molecular diagnostic techniques. These methods are very expensive, time consuming and require expertise in instrumentation and techniques for sample analysis. The BCB-SensorTek project proposes an easy to use DNA genosensors technology to determine breast cancer biomarker of genetic origin and/or DNA genosensors to determine metabolomic biomarkers. The biosensor fabrication will be based on QDs technology. Binary telluride QDs of Ga, will be made biocompatible and used for the development of DNA-based genosensors for the detection of transgenes or biomarkers for breast cancer.

1.4 Aim and Objectives of the study

General objectives

The aim of the proposed research project is the development of binary chalcogenic quantum dots genosensors for breast cancer biomarkers. The intent is to use polymeric materials and/or ligands as platforms for attachment of the probe DNA with quantum dots and to specifically detect an oligonucleotide sequence related to 5-human receptor factor growth 2-3-phosphate kinase. Not only detecting the oligos but also uses these nanomaterials in cancer cell in order to determine their toxicity and fluorescent properties.

The main objectives of this study include:

- 
- To synthesis binary Ga-chalcogenide quantum dots capped with mercaptopropionic and mercaptosuccinic acid.
 - Electroanalysis of quantum dots by atomic force microscopy (AFM), electrochemical impedimetry spectroscopy (EIS) and voltammetry of quantum dots.
 - Determination of the high resolution microscopic (SEM, HRTEM), optical (UV-Vis, luminescence) and spectroscopic (Raman and FTIR) properties of the quantum dots.
 - Determination of suitable signal transduction technique for the sensor system.
 - Development, optimisation, evaluation and testing of the telluride and selenide quantum dots DNA and DNA aptamer genosensors.
 - Design a microfluidic device for the detection of breast cancer.
 - Determine the hydrophobicity, hydrophilicity and fluorescent properties of quantum dots using contact angle and confocal microscope.

- Determine the cytotoxicity of the quantum dots in cancer cell using electrochemical and spectroscopic assays.
- Determine the mechanism of the DNA sensor/genosensor



1.5 Thesis layout

This thesis is structured into 9 chapters

Chapter 1 gives the background and introduction information with a brief discussion on semiconducting nanomaterials, screening of breast cancer, specifically detection of HER2/neu oncogene – a biomarker which cause cancer tumours, traditional and present methods of detecting breast cancer. Additionally it explains the rational and how to address the problem at hand.

Chapter 2 focuses on the importance of cancer in general and breast cancer, detailing the cause and methods of detection. Introduction of quantum dots discussing their current composition, their advantages over classical dyes. Discuss the properties of quantum dots, which are reportedly superior to traditional dyes. A review of the progress made in the synthesis (methods) and functionalisation (strategies) of quantum dots is also described in this chapter. This chapter also features a review of the applications of quantum dots, with specific attention given to optical and electrochemical biosensor applications. A further description of the applications of quantum dots in electrochemical detection of DNA hybridisation is given, since it is one of the interests in this study. Various methods of electrode modification/immobilization of the probe DNA, as well as different electrochemical and spectroscopic techniques used for detection of DNA hybridisation are also described in this chapter. Lastly describes the effect of size bio-imaging and cytotoxicity of quantum dots in biological molecules, specifically cells.

Chapter 3 covers all reagents used in this study and their particular sources. A description of all procedures for synthesis and characterisation of the telluride quantum dots also features in this chapter. Also give descriptive information on hybridisation phenomena. Procedures for the fabrication, characterisation and application of voltammetric and impedimetric sensors and genosensors for detection of selected analytes; oligonucleotide sequence related to 5-human epidermal growth factor receptor 2-3-phosphate kinase oncogene were also highlighted. The fabrication of microfluidic sensor and toxicity assays. The last part of this chapter describes the techniques used in this study and the principles underlying each technique.

Chapter 4 discusses the electrochemical, microscopic and optical properties of telluride binary quantum dots.

Chapter 5 discusses the electrochemical properties, applications of the 3 MPA- Ga₂Te₃ quantum dots by evaluating their catalytic properties and fabrication and genosensor (3 MPA-Ga₂Te₃/ssDNA) response towards target analytes, i.e. common DNA, non-common DNA, 3-base mismatch and 1-base mismatch.

Chapter 6 Entails genosensor response using a very sensitive electrochemical quartz crystal micro-balance (EQCM) and GenoDot microanalyzer (GDMA)-micro-fluidics. The effective mass change and frequency will be monitored during hybridisation.

Chapter 7 discusses the mechanism of the DNA sensor while interacting with the target analytes.

Chapter 8 discusses the cytotoxicity of quantum dots and their fluorescent properties using electrochemical and microscopic techniques.

Chapter 9 presents the conclusions and recommendations.





2.1 Cancer and biomarkers

Cancer is one of the major killers throughout both the developed and developing world, including South Africa [39; 40]. Cancer is expressed as a disorder of chaos which causes an impairment of biochemical pathways in living metabolisms or an abnormal and uncontrolled cell growth due to an accumulation of specific genetic and epigenetic defects, both hereditary in origin and environmentally [41; 42; 43]. Unregulated cell growth leads to the formation of a tumour mass that over time becomes independent of normal homeostatic checks and balances. Tumour cells in essence become resistant to apoptosis and other antigrowth defences within the body [43], Figure 1. As the cancer progresses, the tumour begins to spread beyond the site of origin and metastasize to other body organs and systems, at which point, the cancer is essentially incurable [44; 45; 46]. In particular, malfunctioning of the controls of cells through the human body is mostly observed breakdown in cancer. Cancer can take over 200 distinct forms, including lung, prostate, breast, ovarian, ematologic, skin, and colon cancer, and leukemia, and both environmental factors (e.g., tobacco smoke, alcohol, radiation, and chemicals) and genetic factors (e.g., inherited mutations and autoimmune dysfunction) are associated with an increased risk of developing cancer [47; 48]. 1 in 29 women in South Africa are diagnosed with cancer [49]. Bacterial and viral infections are also strongly associated with some types of cancer (i.e., stomach cancers and cervical cancer, respectively). The most common type of cancer in men and women is prostate and breast cancer, respectively, with 192,000 new cases of each reported annually [43]. Although cancer is most commonly diagnosed later in life (77% of cases are diagnosed in individuals aged 55 years and older) [50; 51].

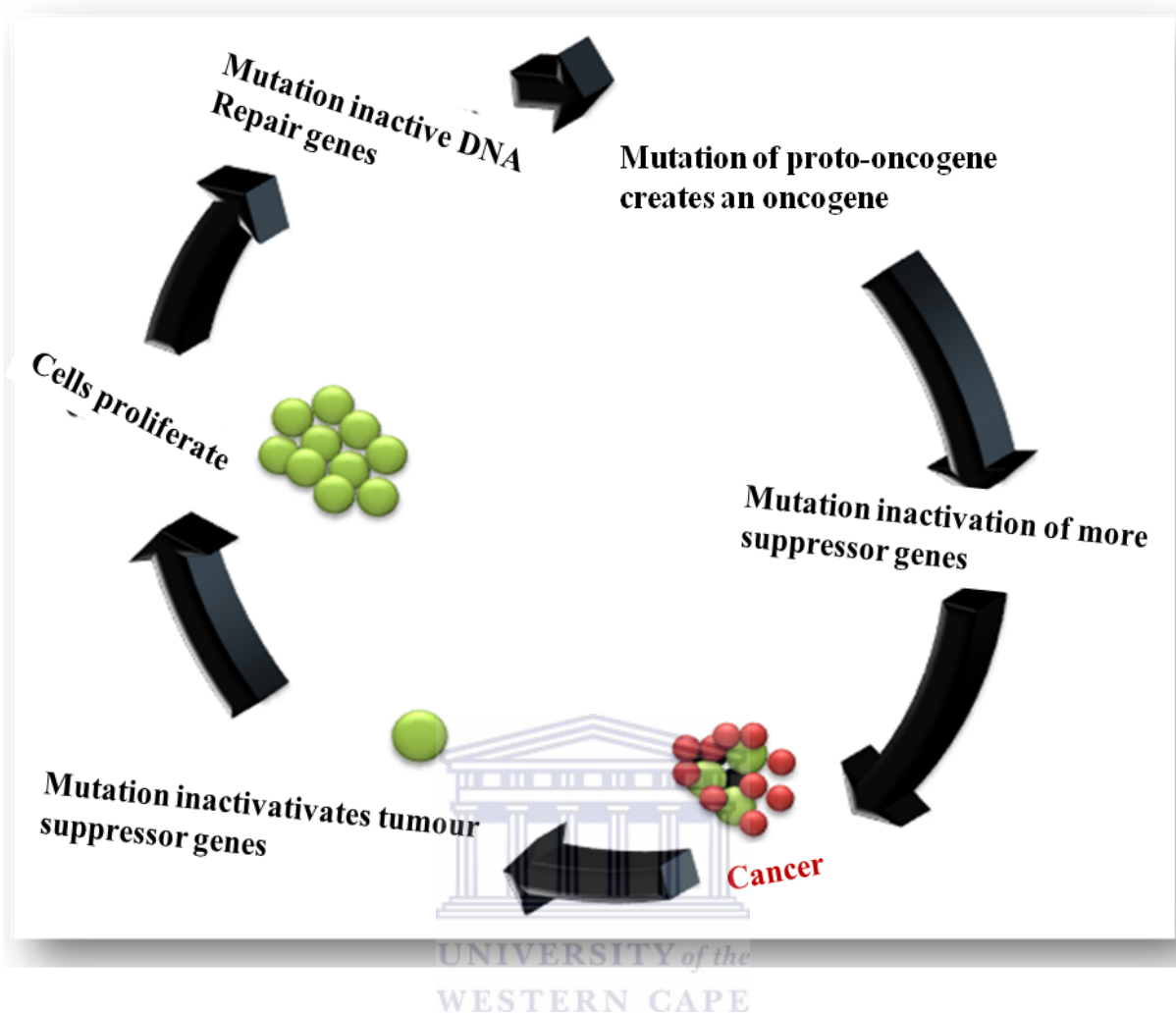


Figure 1. Schematic representation for cancer occurrence.

Breast cancer (BC) is the second leading cause of cancer-related deaths in women worldwide after lung cancer and is the most frequently diagnosed form of cancer among women [1; 52]

It is a disease in which malignant (cancerous) cells form in the tissues of the breast. It is considered a heterogeneous disease because it differs by individual, age group, and even the kinds of cells within the tumours itself [1]. It is the most common cancer among South African women.

According to the National Cancer Registry (2003) breast cancer (excluding cancer of the skin) is the number one cancer among all females except for Black females where it is the number two cancer [53; 54]. Although breast cancer is mainly a disease of women, some men also develop breast cancer. It is about 100 times less common among men than among women. For men, the lifetime risk of getting breast cancer is about 1 in 794. The prognosis for men with breast cancer was once thought to be worse than that for women, but recent studies have not found this to be true. In fact, men and women with the same stage of breast cancer have a fairly similar outlook for survival (American Cancer Society; National Cancer Registry). According to the National Cancer Registry (2003) the lifetime risk of all females developing breast cancer is 1: 31. In breast cancer, abnormal cells in the breast become malignant (cancerous) and may invade and destroy nearby tissue (Figure 2).

2.1.1 Breast Cancer in Women

There are two main categories of breast cancer and are named depending on where in the breast the cancer originates (Figure 2):

- Ductal carcinoma – where the cancer starts in the ducts (tubes) that move milk from the breast to the nipple (most breast cancers are of this type).
- Lobular carcinoma – where the cancer starts in the parts of the breast called lobules that produce milk.

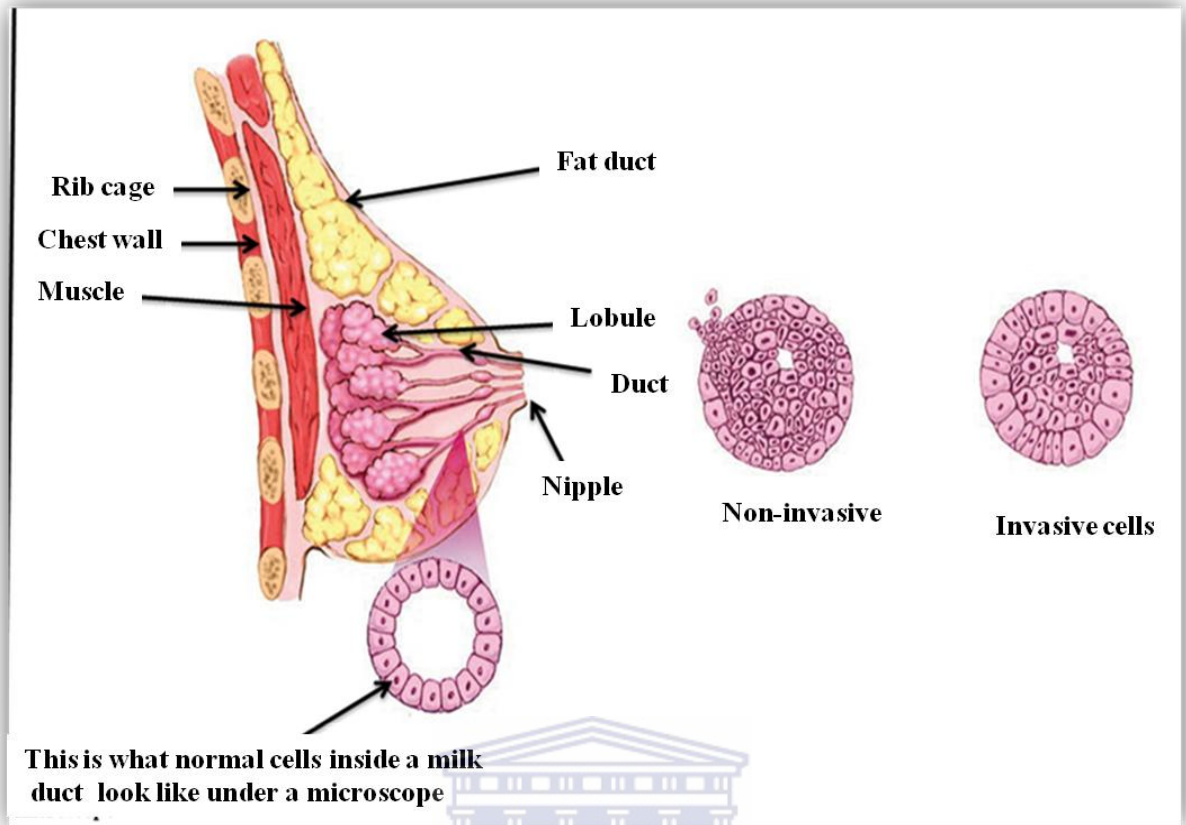


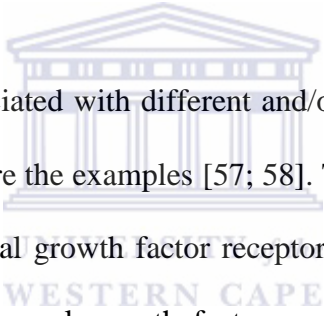
Figure 2. Image of an infected breast (amplification/overexpression of cells).

2.1.2 Breast cancer in men

Not only does breast cancer affect women but it also encroach on men, although is very rare. Male cancer can occur at any age, this cancer can cause more deadly diseases which can lead to death, even though it can be easily cured [55]. Like in women, men also have different categories of breast cancer types which occur in the breast. The categories are as follows i.e.

Ductal carcinoma in situ (DCIS) – which is also known as intraductal carcinoma, where cancer cells form in the breast ducts but do not grow through the walls of the ducts into the fatty tissue. **Infiltrating ductal carcinoma (IDC)** – is a type of breast cancer where the

cancer breaks through the wall of the duct and grows through the fatty tissue of the breast. At this point, it can spread to other parts of the body. At least 8 out of 10 male breast cancers are IDC's, **Infiltrating lobular carcinoma (ILC)** – where the cancer starts in the breast lobules and grows into the fatty tissue of the breast. ILC is very rare in men, accounting for only about 2% of male breast cancers, **Lobular carcinoma in situ (LCIS)** – where abnormal cells form in the lobules, but they do not grow into the fatty tissue of the breast or spread outside the breast. As with invasive lobular carcinoma, **Paget disease of the nipple** – this type of breast cancer starts in the breast ducts and spreads to the nipple, it may be associated with DCIS or with infiltrating ductal carcinoma. It accounts for about 1% of female breast cancers but a higher percentage of male breast cancers [56].



There are many risk factors associated with different and/or that can cause cancer e.g. food, smoking, genetic and pesticides are the examples [57; 58]. The main cause of breast cancer is the kinase protein called epidermal growth factor receptor 2 (HER2) [59; 60; 61; 62]. This onco-protein belongs to the epidermal growth factor receptor (EGFR/ErbB) HER Family (HER1, HER3 and HER4) [63; 64; 65], Figure 4. The HER2 gene which is also known as neuroglioblastoma (Neu) cell line, ErbB-2, CD340 or p185 is a protein that in humans is encoded by the ErbB2 gene [66; 67; 68]. ErbB2 is located on the long arm of chromosome 17. Normal cells contain two copies of the HER2 gene, which encodes a protein comprising 1255 amino acids of molecular weight 185 kDa (Figure 4) [64; 69; 70]. This protein has homology to, and conforms to the general structure of the HER proteins, Figure 3. Studies of human cancers have demonstrated that HER2 gene amplification- generation of more than the normal two gene copies [71; 72]; (On 17q12 chromosome) and/or HER2 receptor over-expression are observed in a variety of tumour types i.e. breast, ovarian, pancreatic and lung cancer[62;63].

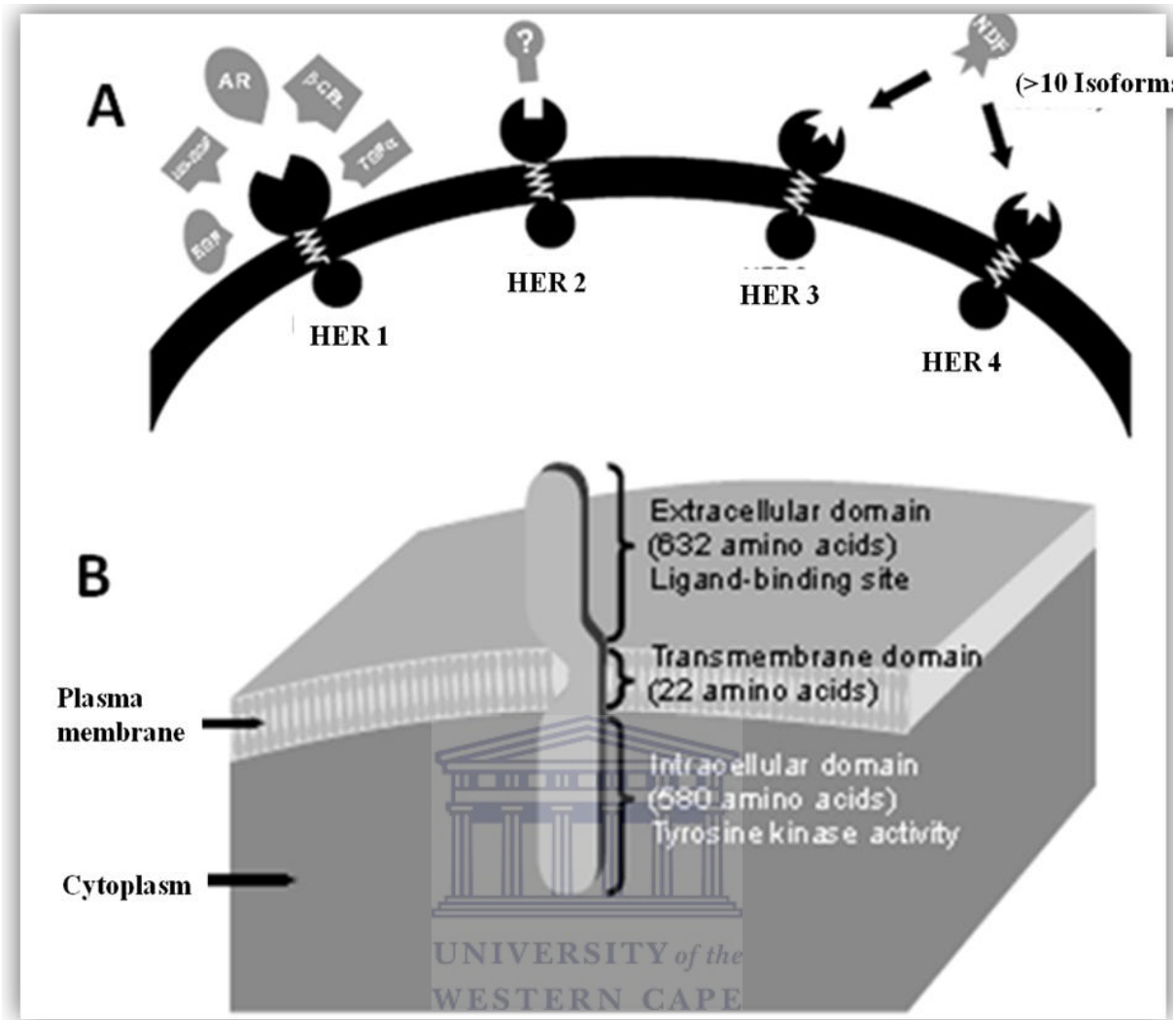


Figure 3. Structure of the (A) Her/neu family and (B) Her2/neu [64].

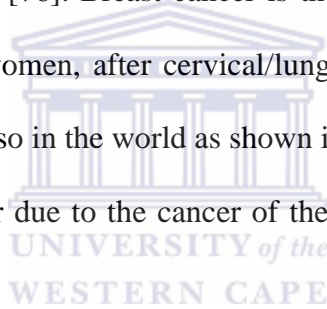
Amplification of these gene leads to overexpression of the receptor and disrupts normal control mechanisms and potentially leading to the formation of aggressive tumour cells [63; 71; 73]. The percentage of tumours in which the HER2 gene is amplified is usually lower than the percentage in which the protein is overexpressed. The incidence of HER2 gene amplification is $25\pm 30\%$ for breast and $15\pm 30\%$ for ovarian carcinomas [49], with the incidence of HER2 protein overexpression being slightly higher [61; 74; 75].

2.1.3 Statistics (non-developed and developed countries)

2.1.3.1 Comparison

The current prevalence (the number of cancer cases) and incidence (the rate at which new cancer cases are growing) in South Africa are not known, because the country's cancer registry has not been updated since 1999. Figure 4 A, B and C, indicates the incident rates of cancers and rates of death between different races which are caused by the cancer of the breast and it also indicates the mortality in which the breast cancer carcinoma spreads.

According to statistics one in six South African men and one in seven South African women will get cancer during their lives [76]. Breast cancer is the second leading cause of cancer-related death among SA black women, after cervical/lung cancer and is the leading cancer killer among white women and also in the world as shown in the pie-chart (Figure 4) [76; 77]. Over 3 000 women die each year due to the cancer of the breast (National Cancer Registry (2003)[76]



2.1.3.2 International comparison

Breast cancer was found to be less common in black women than in other population races [76; 78]. The age-standardised rates of 11.30 per 100000.00 compare well with the rates from central Africa (Harare age-standard rate 20.40 per 100000.00; Kampala 164 per 100000.00) and BC is rare in countries like Gambia (3.40 per 100000.00) [78; 79]. By disparity, the rate for black women in the United states is 65.00 in 100000.00 [78; 80]. In white women the rates in South Africa (70.20 per 100000.00) are comparable to those of the developed countries such as United Kingdom (56.10 per 100000.00) and the United States (89.20 per 100000.00) countries [76; 77; 81].

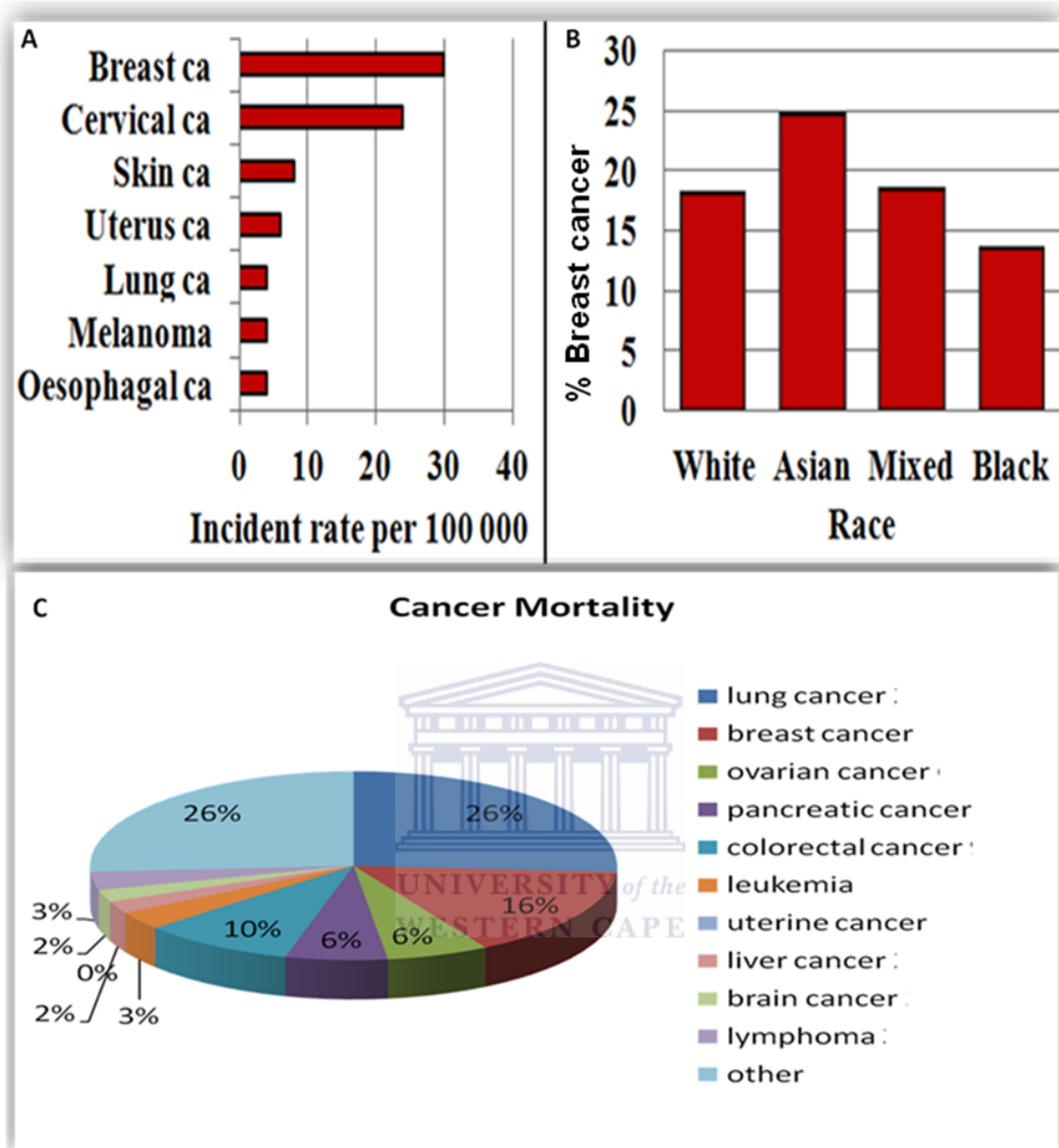
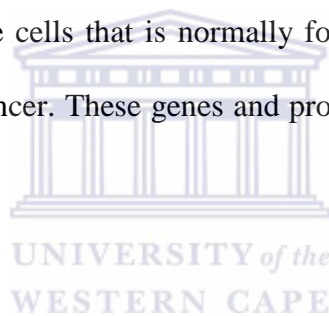


Figure 4. (A) Rate of cancer incidents. (B) Race distribution of breast cancer and (C) Pie chart of cancer mortality.

This statistics show or confirms the need of early screening assays for the detection of breast tumour, especially in under-developed countries such as Southern Africa and its counterparts[81]. Screening for this cancer of the breast in its early stage necessitates highly sensitive assays to detect biomarkers of carcinogenesis, thus serving as an excellent chance of

recovery. Biomarkers are used to detect this cancer [82]. There is no standard definition for “biomarker” that is universally used. In 1999, the US National Institutes of Health/Food and Drug Administration Working Group drafted a definition of a biomarker; as a characteristic that is objectively measured and evaluated as an indicator of normal biological processes, pathogenic processes or pharmacological response to a therapeutic intervention [83; 84]. Biomarkers could be found in the body and they are quantifiable molecules such as proteins, metabolites, DNA, or RNA [85]. The abnormal concentrations of such biomarkers are indicator for a pathological condition in the body, such as cancer [86]. A biomarker could also be a molecule that occurs as a specific response of the metabolism to the presence of cancer [85]. Every type of cancer could be associated with gene modifications and alterations in protein function [87]. These gene modifications and protein changes can be useful. They are like a map that doctors may use to guide how to treat some cancers. Biomarkers can take a wide variety of forms namely: some markers can be used to indicate the presence of certain organisms, including a history of their presence even if they no longer exist [85; 88]. Cancer biomarkers can be used for prognosis: to predict the natural course of a tumour, indicating whether the outcome for the patient is likely to be good or poor [88; 89]. They can also help doctors to decide which patients are likely to respond to a given drug (prediction) and at what dose it might be most effective (pharmacodynamics) [90; 91]. Cancer biomarkers are present in tumour tissues or serum and encompass a wide variety of molecules, including DNA, mRNA, transcription factors, cell surface receptors, and secreted proteins and their also rigorously being explored [91]. The most frequently used and best known biomarker is Her2; this oncoprotein is cell-membrane bound by its extracellular domain and is shed into circulation making it a potent biomarker used to monitor the response to treatment [91; 92], and to detect re-urrences in patients with diagnosed breast carcinoma.

Amplification of HER2 was first noted in human breast cancer and in other types of cancers [93]. The HER2 gene is amplified in approximately 20-30% of breast cancer as mentioned earlier and it is associated with aggressive tumour behaviour [93; 94]. A final note about biomarkers is that they may be referred to by several different names, especially in cancer medicine and research. The National Cancer Institute notes that biomarkers in cancer may also be called molecular markers and signature molecules, although, as we have seen, not all biomarkers fit into these categories. Molecular biomarkers, also called molecular markers, tumour markers or biochemical markers, are one of the most common types, these are biological molecules found in body fluids or tissues [95]. In cancer, molecular biomarkers are often genes or gene products such as proteins. An example is prostate specific antigen which is a protein produced by prostate cells that is normally found in low levels in the blood of men and HER-2/neu in breast cancer. These genes and proteins are made up of thousands or millions of DNA molecules.



2.2 DNA and its functions

DNA, short for deoxyribonucleic acid, has been the focus of much attention since its double-helix structure or twisted ladder shape was first discovered by James Watson and Francis Crick in 1953 [96; 97; 98]. The discovery revealed what many researchers had long believed, which is that DNA actually carries the genetic information for the development and functioning of living organisms. DNA holds within it the information that instructs cells to develop specific features that enable them to perform specific roles in the body [97]. For instance, muscle cells are designed to contract, nerve cells are designed to communicate information, and cancer cells are designed to grow and replicate, it also carries the genes that make up the hereditary information that is passed from generation to generation.

DNA is found within the nucleus of nearly every cell in our bodies, Figure 5. The nucleus is a round or oval-shaped structure within the cell known mainly for its role as the home of DNA. In the cell nucleus, DNA is found tightly bound with proteins in structures called chromosomes [99; 100].

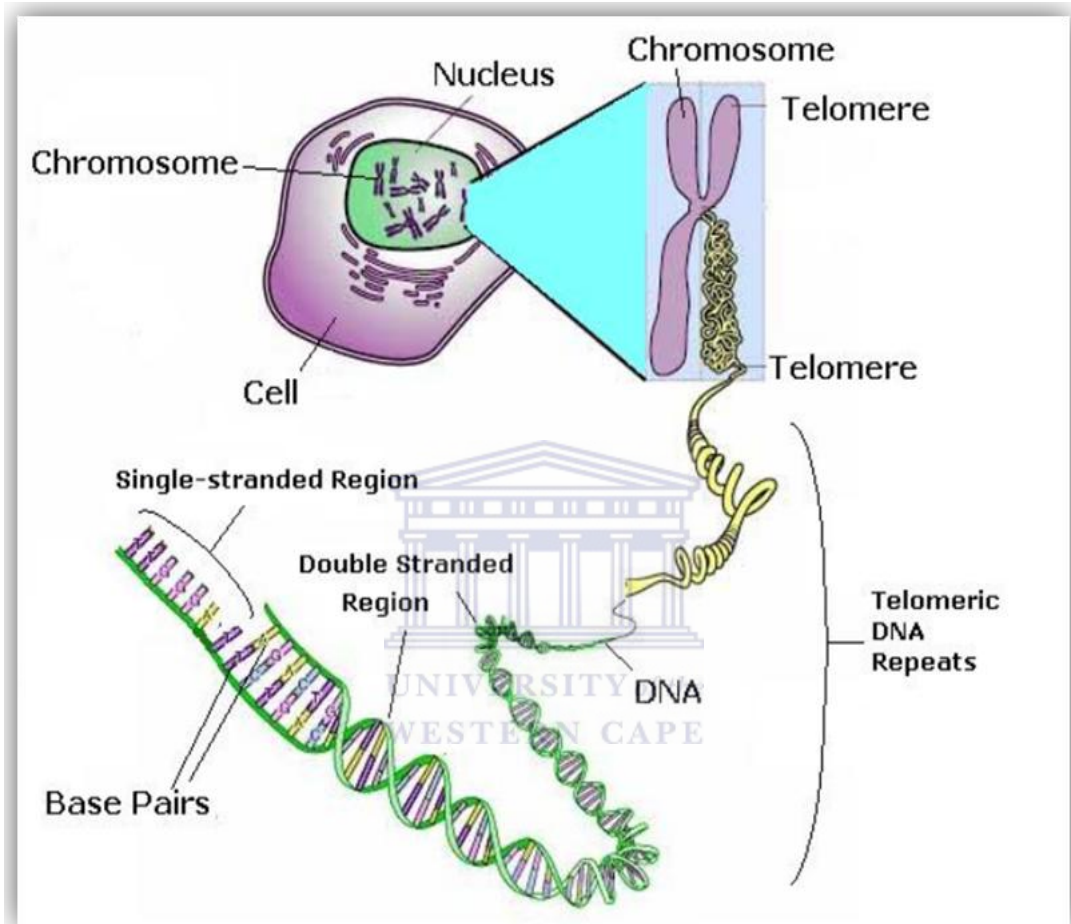


Figure 5. Cell structure representing the home of DNA (Nucleus) [97].

As noted previously, DNA is made up of chemical building (that form a double helix, a complex structure that could be compared to a twisted ladder) or subunits called oligonucleotides, each made up of a sugar, a phosphate and a base blocks (Figure 6) [97; 98]. The steps of the twisted ladder are pairs of chemicals. It is the order of these chemicals that makes humans different from cats and makes one person susceptible to cancer and another to Alzheimer disease.

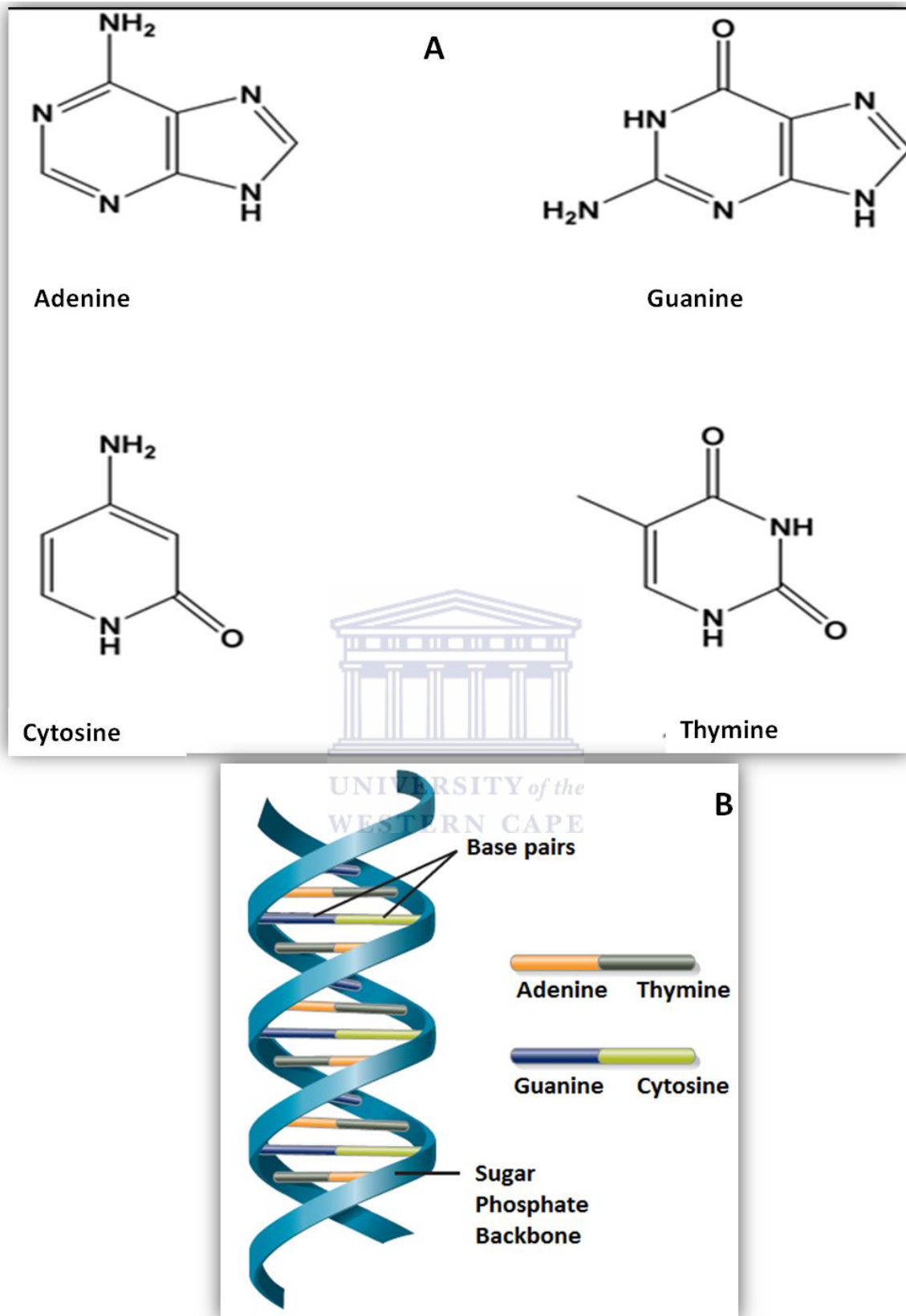


Figure 6. (A) Chemical structure of the DNA bases and (B) Pieces of DNA that contains the information for making a particular biochemical, usually a protein [98; 101].

The four chemicals that pair up in DNA are known as nucleotides or nucleotidebases [98]. These are adenine (A) and guanine (G) (purine bases) as well as cytosine (C) and thymine (T) (pyrimidine bases). The rule of base pairing is that A must pair with T, and C must pair with G. Note that either letter of the pair can be “first” in the pairing, such that A pairs with T and T pairs with A; C pairs with G and G pairs with C[98; 101]. The chemical structure of each of these bases given above is shown below (Figure 6A). In a normal DNA structure, a Watson-Crick base pairing occurs whereby guanine forms hydrogen bonds with cytosine and while adenine forms hydrogen bonding with thymine. This process is commonly called hybridization (Figure 7) and gives rise to double stranded oligonucleotides [101; 102] whose structure is given in the Figure 6B.

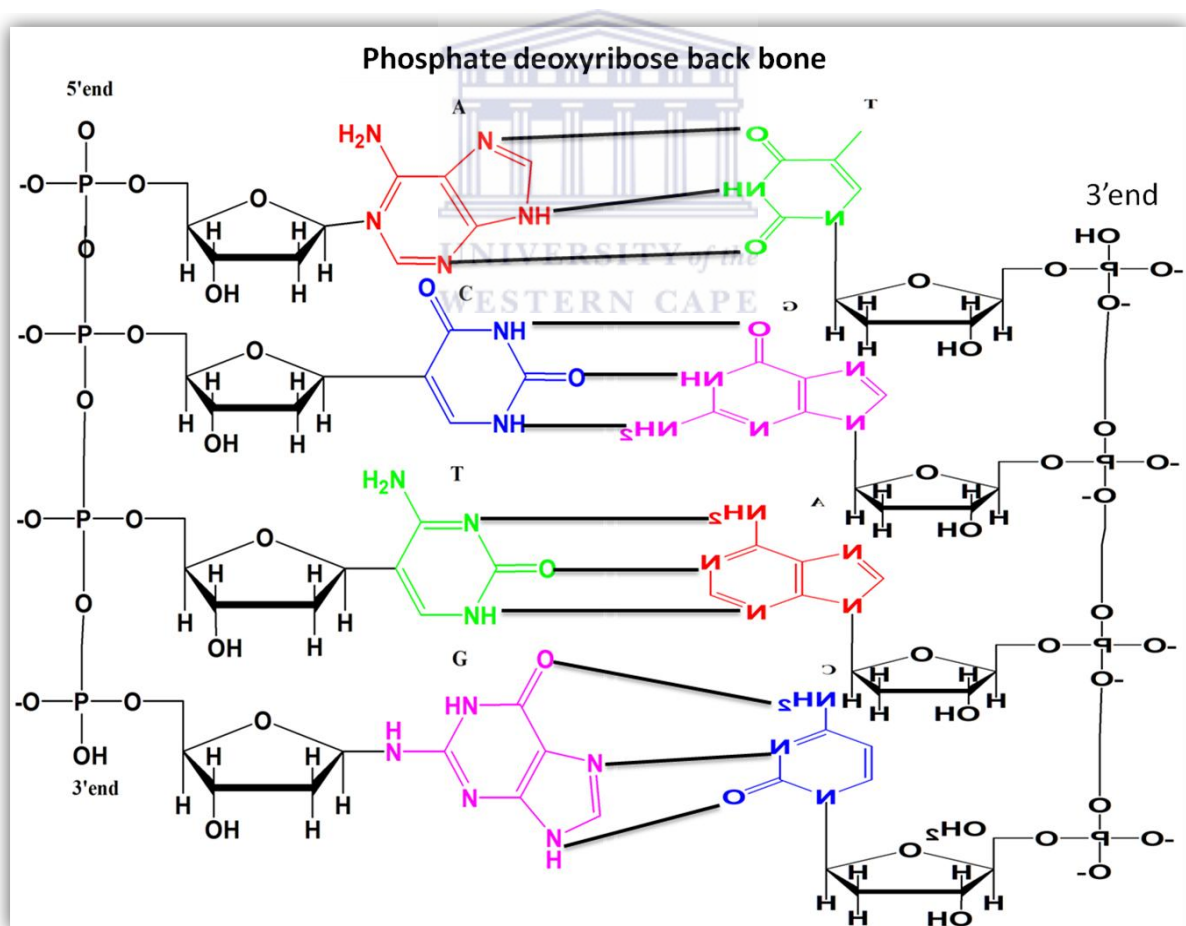


Figure 7. Canonical Watson-Crick DNA base pairing through G-C and T-A intermolecular hydrogen bonds.

Hybridization is the process of establishing a non-covalent, sequence-specific interaction between two or more complementary strands of nucleic acids into a single complex, which in the case of two strands is referred to as a duplex [103; 104]. Oligonucleotides, DNA, or RNA will bind to their complement under normal conditions, so two perfectly complementary strands will bind to each other readily [105; 106]. DNA–DNA hybridisation generally refers to a molecular biology technique that measures the degree of genetic similarity between pools of DNA sequences[104]. It is usually used to determine the genetic distance between two species. When several species are compared that way, the similarity values allow the species to be arranged in a phylogenetic tree; it is therefore one possible approach to carrying out molecular systematics [103; 104]. From the four bases/amino acids, guanine and adenine have attracted great research interest due to crucial roles that they play in metabolic and analytical processes. They participate in fundamental functions such as energy transduction, metabolic co-factors and cell signalling. They are essential building blocks of nucleic acids and determination of their individual concentrations in an organism is an important practice in biomedical analysis, molecular pathology, environmental and forensic science. This is because; deficiency of these purine bases is a key indicator of possible mutation of the immune system and aging[103; 104].

The development of electrochemical transducer based devices for determining nucleotide sequences and measuring DNA hybridization began with the discovery of the electroactivity of nucleic acids about 50 years ago [106]. When nucleic acids interact with solid electrodes, they are strongly adsorbed and undergo charge transfer reactions, producing signals that can provide information about their type, concentration, their structural changes as well as their interaction with various compounds.

Moreover, strongly adsorbed nucleic acids on solid electrodes can be the basis for fast response DNA detectors. At physiological and alkaline pH, the potential window of most solid electrodes is about 1000 mV more positive than that of the mercury electrode, which usually operates within the range 0 to -2000 mV versus saturated calomel electrode. Solid electrodes are therefore best suited for studying nucleic acids oxidation while mercury electrodes would suit studies involving reduction of nucleic acids. Amongst the components of nucleic acids, only the bases undergo reduction at mercury electrodes and oxidation at other solid electrodes such as carbon (GC) and gold (Au). There are however some reports of oxidation of the nucleic acids sugar residues at copper electrodes using sinusoidal voltammetry. Of the oxidisable nucleic acid bases, the purine bases (guanine and adenine) are of particular interest to electrochemists since they undergo oxidation with relative ease and can allow for quantification of a DNA sample. The oxidation of guanine is a complex mechanism and is thought to be a $4e^-$, $4H^+$ system. The first step is a $2e^-$, $2H^+$ electrochemical reaction (EE) whereby, the guanine forms 8-oxoguanine. The loss of the first electron gives an intermediate radical species. This species may dimerise to form an electroactive product which can undergo oxidation at potentials higher than those of the radical formation. The 8-oxoguanine formed in step one can further undergo a reversible $2e^-$, $2H^+$ to give highly hydrolysable products. This simplified mechanism of guanine oxidation is illustrated in the Figure 8. The negatively charged phosphate backbone of the DNA also possesses electrochemical properties that can be used for detection of DNA upon hybridization. The detection methods for electrochemical DNA hybridization are classified into two major protocols; direct and indirect detections[107]. In direct electrochemical detection of DNA hybridization, the signal monitored arises from oxidation of the purine nucleobases, adenine and guanine [108]. The oxidation of adenine and guanine at mercury electrodes has been reported [109].

However oxidation signals of these nucleobases at other solid electrodes such as gold, copper, carbon have limited use in analytical purposes since they are poorly developed with very high over potential and often merge into background discharge current. To overcome this, modified electrodes have been explored to enhance the oxidation signals of these bases. For this reason nanomaterials such as quantum dots are employed (3MSA/MPA-Ga₂Te₃) in our system.

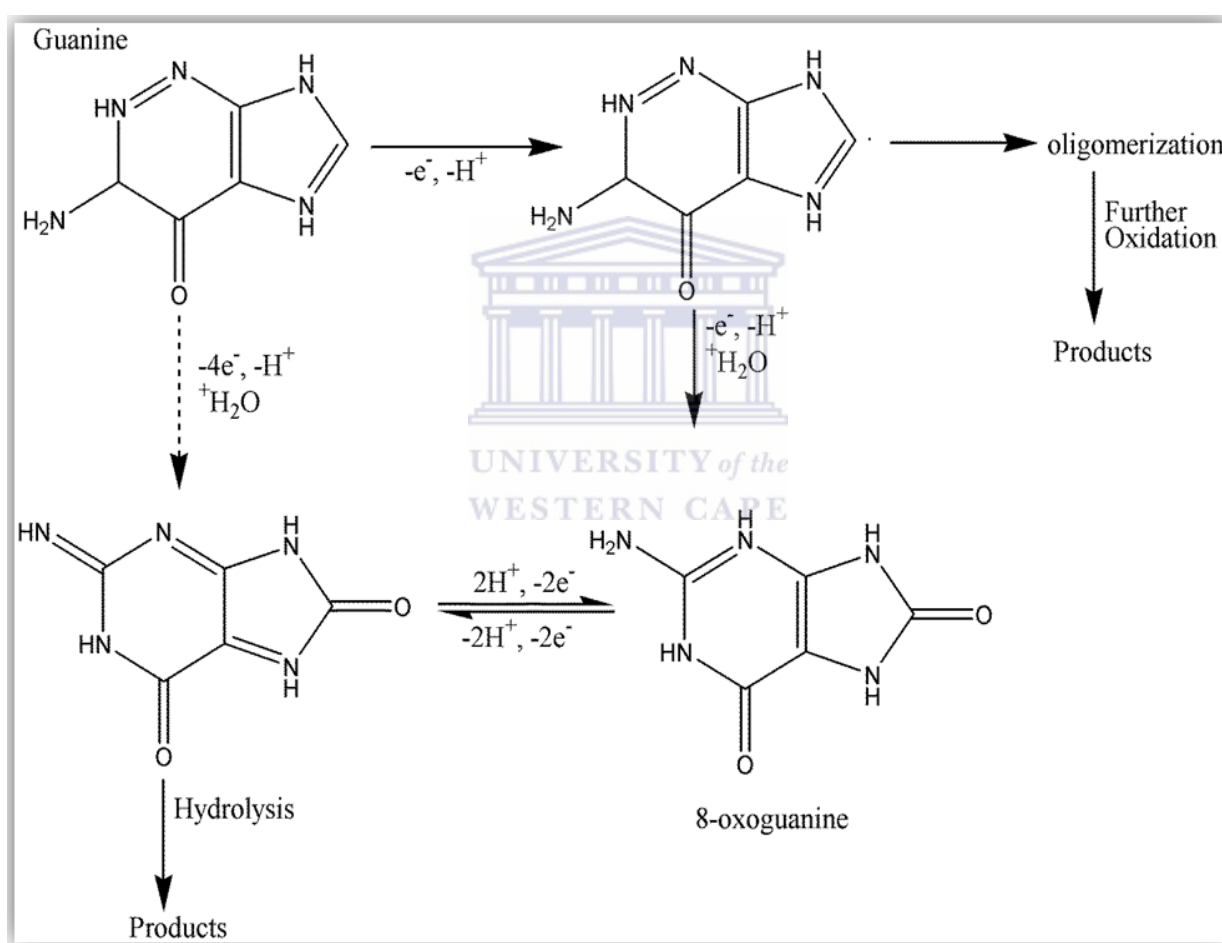


Figure 8. Simplified mechanistic pathway for the oxidation of guanine.

2.3 Nanoscience, Nanotechnology and Quantum dots

Nanoscience has shown itself to be one of the most exciting areas in science, with experimental developments being driven by pressing demands for new technological applications. It is a highly multidisciplinary research field and the experimental and theoretical challenges for researchers in different fields are substantial. Nowadays, scientists and research scholars have been developing new kinds of nano materials which could be used for forensic science, biology, electronic technology, environmental science, computer manufacturing, sports facility production as well as food industries. In 21 January 2000 California Institute of Technology, President Bill Clinton advocated nanotechnology development and raised it to the level of a federal initiative, officially referring to it as the National Nanotechnology Initiative (NNI). While the South African Nanotechnology Initiative (SANi) and South Africa's Advanced Manufacturing Technology Strategy (AMTS) were launched between 2002- 2003. The minister of science and technology in South Africa Mr Musibudi Mangena together with other groups placed the first nanotechnology strategic plan in 20 April 2006. The main areas of focus included the following: **(a)** The establishment of characterisation centres which are geographically distributed and contain multi-user facilities multi to provide researchers with– advanced instruments for design, synthesis, characterisation, modelling and fabrication **(b)** The creation of research and innovation networks that will serve to enhance collaboration among traditional disciplines, research teams and institutions **(c)** Capacity building initiatives that are aimed at developing human capital resources and **(d)** A number of Flagship Projects that are aimed at demonstrating the benefits of nanotechnology towards an enhanced quality of life and increased economic growth. These will initially focus on – Water, energy, health, chemical and bio-processing,

mining and minerals as well as advanced manufacturing. This strategy was referred to as South African Micro-Economic Strategy (SAMÉS).

Nanoscience and nanotechnology are referred to as a type of applied science, studying the ability to observe, measure, manipulate and manufacture materials at the nanometer scale [110]. The prefix nano in the word nanometer (nm) is an SI unit of length, namely 10^{-9} or a distance of one-billionth of a meter [110; 111]. As a comparison, a head of a pin is about one million nanometers wide or it would take about 10 hydrogen atoms end-to-end to align in series in order to span the length of one nanometer [112]. Because the matter it deals with is smaller than the macroscopic scale which could be seen by our naked eye, but larger than the microscopic scale of the electrons and protons and that could only be sensed by cloud chambers, it dwells in a new realm called mesoscopic scale which contains the domain of 10^{-7} to 10^{-9} nm. In other words, whenever a macroscopic device is scaled down to mesoscopic scale, it starts revealing quantum mechanical properties. While macroscopic scale could be studied by Classical Mechanics and microscopic scale could be expressed by Quantum Mechanics, mesoscopic scale is somewhere in between and our knowledge about this field is quite limited. This has stimulated the scientists to start a new territory dealing with the “bridge” which connects the macro and micro, this “bridge” being the so called nanoscience. Why should this be emphasized that often? Because making products at the nanometer scale is and will become a big economy for many countries. By 2015, nanotechnology could be a \$1 trillion industry and meanwhile, according to National Nanotechnology Initiative, scientists will create new ways of making structural materials that will be used to build products and devices atom-by-atom and molecule-by-molecule. These nanotechnology materials are expected to bring about lighter, stronger, smarter, cheaper, cleaner, and more durable products.

One of the main reasons why there is a lot more activities in producing nanotechnology products today than before is because there are now many new kinds of facilities that can handle nanomaterials. Including, but not limited to, transmission electron microscopy (TEM) which could directly see the atoms clusters; and atom force microscopy (AFM) which can measure, see, and manipulate nanometer-sized particles; nanoimprint lithography (NIL) which is equipped with high-precision alignment system with accuracy within 500nm and fine alignment up to 50 nm; Physical Vapour Disposition (PVD) and Chemical Vapour Disposition (CVD) as well as Molecular Beam Epitaxy (MBE) systems which allow the scientists to accurately control the ingredients of the nanodevices when manufacturing them. With more and more nanotechnologies emerging into our lives and the benefits it provided after been manufactured and become commercially available, it will also bring some ethical, legal, social and moral issues as well. Most of them are not new problems but because of nanotechnology their importance and urgency have been emphasized to a new level. From technology perspective, nanotechnology has stimulated its application in national defence and weapons, e.g. the materials with high stiffness and high strength made of carbon nanotubes, so that weapons made from these materials could hardly been identified by probes which are only suited for detection of metal based weapons. On the other hand this would bring a lot of problems for the TSA (Transportation Security Administration) to detect criminals who want to get on planes or enter security areas. Potentially, whether it is still safe to use nanotechnology in cosmetics, food and apparel industry is still under investigation. Because nanoparticles are so small, they could easily permeate into living body without being noticed, and while there is not enough knowledge about the interaction of these nanoparticles with our body organs and systems. They could be involved in cancer development or in certain kind of new diseases which could not be cured. By far not only scientists are involved in solving these problems because nanotechnology is already, intrinsically, a multidisciplinary science.

2.3.1 Quantum dots and their applications:

2.3.1.1 Quantum dots:

From the end of last century, researchers in many different disciplines tend to pay attention to nano-scale materials and related applications. The term “nanoparticle” came into frequent use in the early 1990s together with the related concepts, “nanoscaled” or “nanosised” particle. Until then, the more general terms submicron and ultrafine particles were used [68]. From a scientific point of view, nanoparticles are of great scientific interest as they are effectively a bridge between bulk materials and atomic or molecular structures. A bulk material should have constant physical properties regardless of its size, but at the nano-scale this is often not the case. Size-dependent properties are observed such as quantum confinement in semiconductor particles, surface plasmon resonance in some metal particles and superparamagnetism in magnetic materials. Nanoparticles have been suggested recently for various potential applications in electronics where quantum confinement effects may be of advantage. When electrons are confined to a small domain such as a nanoparticle the system is called a “quantum dot” or zero-dimensional structure, which is a semiconductor microstructure of different material. The phenomena of the semiconductor are discussed below.

2.3.1.2 Semiconductors

Materials have discrete energy bands in which electrons can occur. When electrons are not excited, they will be in their lowest possible energy band. However, due to the Pauli Exclusion Principle, each energy band can only house a finite number of electrons [113]. For this reason, it is the outermost two energy bands, the valence band and the conduction band, which have the maximum effect on the material’s electrical properties (Figure 9) [113].

Metals have a full valence band, and a number of electrons in the conduction band that are free to move, enabling them to conduct charge [114]. The energy difference between these two states is referred to as the band gap energy (E_g) [115]. For an electron to change energy states, it must receive an amount of energy at least equal to the band gap energy. An insulating material has an empty conduction band while in its ground state and thus large band gap energy, making it hard to excite an electron out of the valence band. When in its lowest energy and/or ground state semiconductors have a full valence band and empty conduction band. And behave electrically, exactly like an insulator [116]. The difference is that semiconductor materials have much smaller band gap energies on the order of 1 eV as shown in Figure 9. The band gap energy is small enough that it is possible for photons to excite electrons from the valence band into the conduction band [117]. For a photon to excite an electron, it must have the least energy, $h\nu$, equal to the band gap energy of the semiconductor in which case the photon is absorbed. A photon with energy less than the band gap cannot be absorbed by the semiconductor. Photodiode detectors are based upon this principle. When photons clout the semiconductor, electrons are excited into the conduction band where they are free to move. An induced potential is applied causing the electrons to flow in a photocurrent, which is then detected [118].

A schematic representation of the energy band gap, a semiconductor absorbing a photon, and a semiconductor emitting a photon is shown in Figure 9. When an electron is excited into the conduction band, it leaves behind a hole, which can be treated as a positive particle [118]. It is possible for a photon to have more energy than the band gap energy and still be absorbed, in which case the electron is excited from lower in the valence band to higher in the conduction band. This excess energy is lost, however, through inelastic collisions as the electron settles to the bottom of the conduction band and the hole rises to the top of the valence band [115].

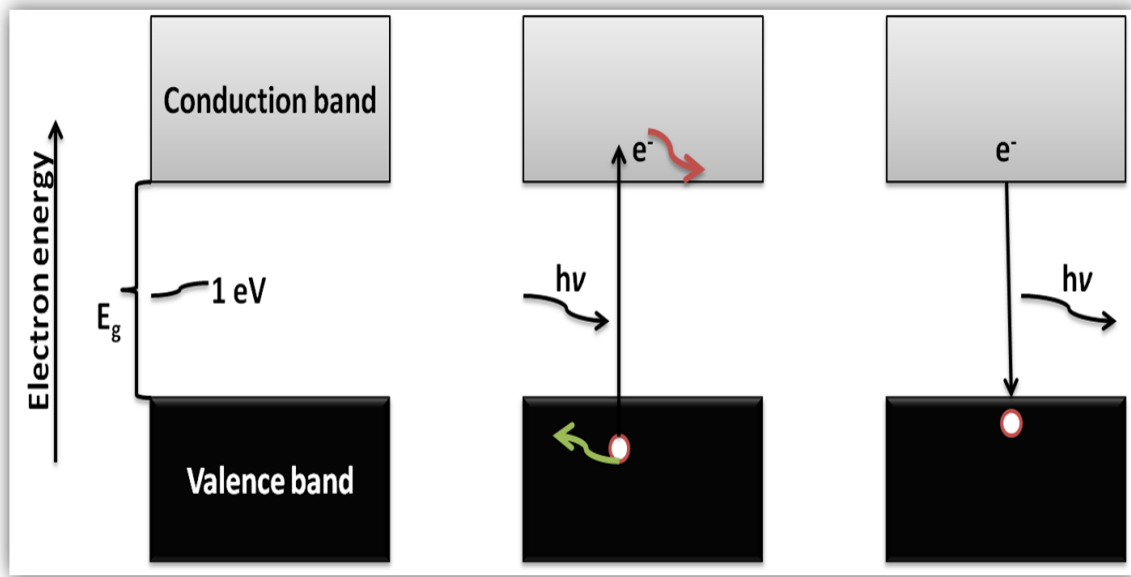


Figure 9. Semiconductor energy system.

Since materials will always return to their ground state if possible, the hole and the electron will then recombine emitting a photon with energy equal to the band gap energy. Quantum dots (also known as zero dimensional semiconductors and artificial atoms) are very, very tiny particles on the order of a nanometers in size (1-20 nm; the size, shape and number of electrons can be precisely controlled) [119], compared to that of atom and bulk materials (1.2 Å and >20 nm) [120], Figure. 10 A. The nanomaterials exhibit unique optical properties due to a combination of their material band gap energy and quantum well phenomena [121]. They are composed of a hundred to a thousand atoms [121; 122]. The electrons are behaving like “particles-in-a-box” and their resulting new energy levels are determined by quantum “confinement” effects. As a result [123], discrete energy levels are needed to describe the electron excitation and transport in quantum dots [124]. The corresponding wave functions are spatially localized within the quantum dot, but extend over many periods of the crystal lattice [125]. Being zero-dimensional, quantum dots have a sharper density of states than higher-dimensional structures i.e. bulk (3D), quantum wells (2D) and quantum wires (1D) [126], Figure 10 B and C.

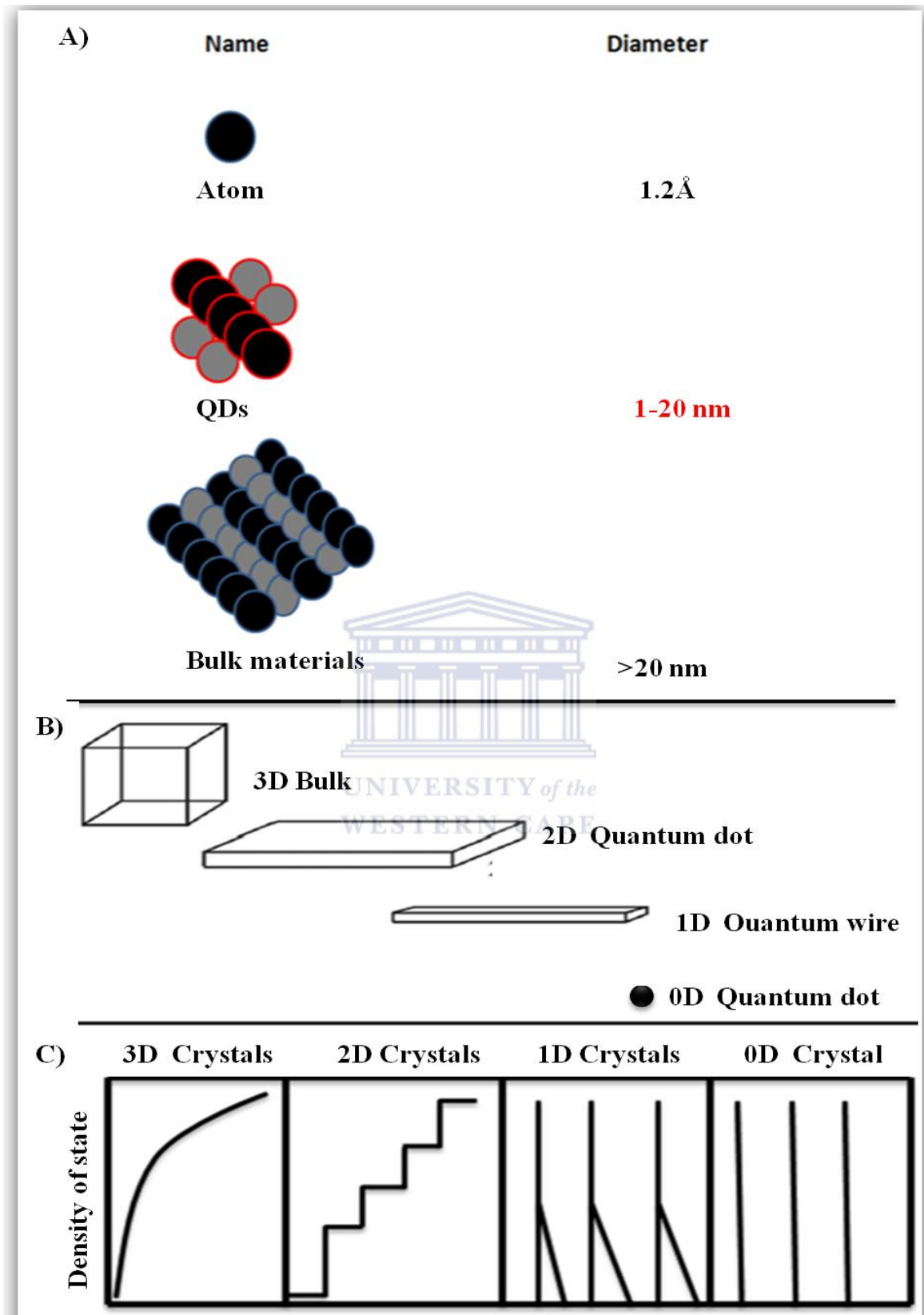


Figure 10. Schematic representation quantum dots, Atoms and bulk materials.

As a result, they have superior transport and optical properties, and are being researched for use in diode lasers, amplifiers, and biological sensors. Quantum dots are of much interest for the other unusual properties that they possess. These other properties include electrical and nonlinear optical properties [127; 128]. The unique properties of nano sized particles are partly the result of the unusually high surface to volume ratios for the particles, as many as one-third of the atoms are on the surface of the particle [129]. Compared to bulk materials and quantum wells (continuous density of state), quantum dots are also known as semiconductor nanostructure that confines the motion of conduction band electrons [130], valence band holes, or excitons (bound pairs of conduction band electrons and valence band holes) in all three spatial directions [131], Figure 11B. As a result electrons and "holes" (holes result when an electron moves away from a bond, leaving a positively charged particle) are confined in a limited space inside the cluster [130]. Quantum confinement enables QDs to emit light at different wavelengths dependent upon their core diameter [132; 133], larger QDs having smaller band gaps, resulting in emission of red light, whilst smaller QDs emit blue light of higher energy [133] (Figure 11A). Furthermore, due to their small size the entire crystal acts as a single molecule with all constituent atoms being excited and emitting light together [133], with high resultant signal intensity (narrow emission spectra). Their small size means that electrons do not have to travel as far as with larger particles, thus electronic devices can operate faster [134]. Moreover, the ability to create dots that emit a rainbow of colours (Figure 11A) and that acts as semiconductor, suggests that they could be used in multiple fields (e.g. biosensors, biomedical etc.) [134; 135].

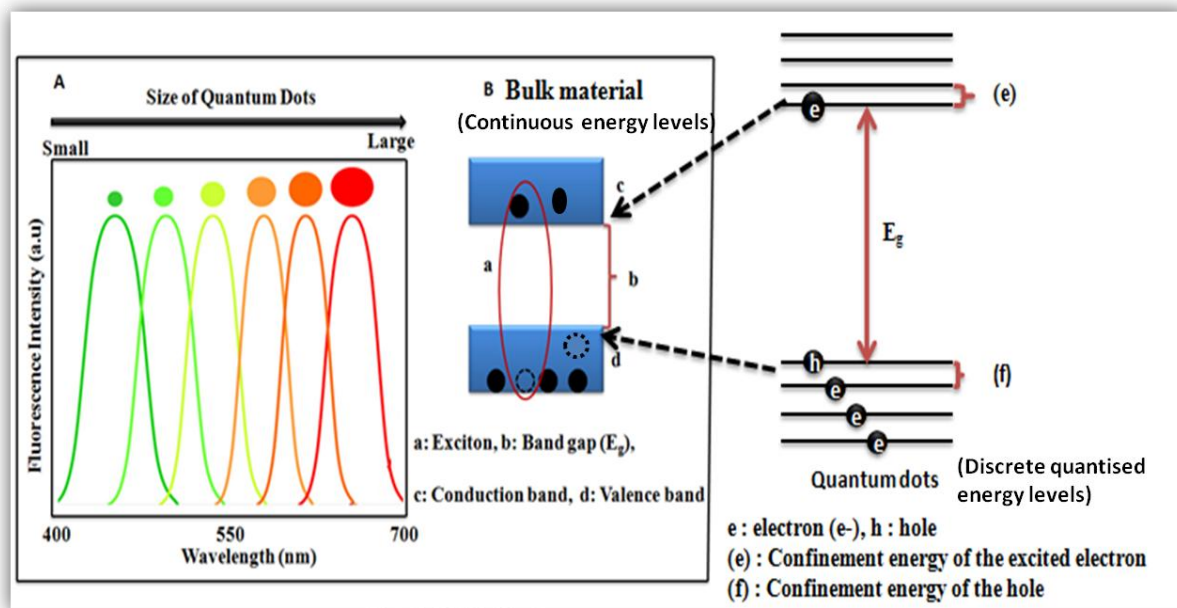


Figure 11. Schematic representation of quantum dots and bulk materials.

2.3.1.3 Advantages of quantum dots over conventional methods

Organic dyes have been widely used as fluorophores in biomedical imaging and detection. However, organic dyes are generally vulnerable to the physiological environment and are quickly photo-bleached under normal imaging conditions [136]. They are also not good for multicolour imaging because of two inherent properties: (a) organic dyes have relatively broad emission spectra and hence result in the signal overlap from different dyes; and (b) one organic dye can only be suitably excited by the lights within a certain narrow wavelength range and it thus needs nearly the same numbers of excitation light sources as the dyes used [136; 137; 138]. On the other hand, inorganic quantum dots are usually bright (20–80% quantum efficiency) and stable under relative harsh environments [132]; the absorption spectra of quantum dots are continuous, and the emission spectra are narrow (typically 20–30 nm) [132; 139]. Excitation–emission matrix (EEM) reveals that quantum dots always emit the same lights no matter what excitation wavelength used.

Therefore, the entire different emission colours from quantum dots can be seen at the same time by only one laser excitation source, Figure 11A. The emission intensity of quantum dots could also be used as a variant for imaging because of their excellent photostability [126]. Theoretically, six colours with 10 intensity levels could determine (10^6-1) nucleic acid or protein sequences [140]. The long-term multiplexed biomedical imaging has recently become one of the hottest research topics [29; 141].

2.3.1.4 Challenges/disadvantages facing quantum dots on their applications

2.3.1.4.1 The toxicity of quantum dots

The cytotoxicity of the quantum dots is probably the most cited limitation for in vivo applications. Although not many toxicity studies have been done, great concern has been raised over use of quantum dots in live cells and animals. Toxicity of quantum dots arises mainly from their composition [142; 143]. The reason for this is that quantum dots mostly contain heavy metal atoms such as cadmium, mercury, lead and arsenic which are toxic [143]. The metal in the core shell of some quantum dots is therefore believed to be responsible for extra cellular cytotoxicity. Particularly, cadmium based quantum dots have been reported to show some cytotoxicity, emanating from release of cadmium ions (Cd^{2+}) upon exposure to air or UV radiation [144]. Cd^{2+} ions are able to bind to thiol groups on critical molecules in the mitochondria leading to enough stress and damage to cause significant cell death [137]. Small sized quantum dots, with green emission have more harmful effects than large red emitting quantum dots [145], implying that the size of the quantum dots affects their toxicity too. The surface capping and functionalizing materials as well as their concentrations could also affect the extent of the cytotoxicity of quantum dots. Hoshino *et al.*, [146] investigated the cytotoxicity of differently capped quantum dots using a

number of techniques which included comet assay and flow cytometry. Studies by these authors suggested that the ligand used to cover the quantum dots was responsible for the cytotoxicity effect and not the nanoparticle itself. The lowest cytotoxicity was observed by these authors with thioglycerol-coated quantum dots compared to carboxylic acid and amine-coated quantum dots. Besides extra cellular cytotoxicity, reports by Chang *et al.*, established that quantum dots could also cause endo-cellular cytotoxicity, especially when they enter the cells by endocytosis [147]. The authors further suggested that, irrespective of the surface coating of quantum dots, cell death is highly related to the amount of quantum dots' uptake into the cells. Once in the cell, quantum dot metabolism and degradation is largely unknown and accumulation of quantum dots in the kidney, spleen and the liver has been reported in several studies [130]. Also it is unknown whether the quantum dots can be cleared from the body [130]. Researchers in the recent past have proposed silicon based quantum dots as alternative to potentially toxic quantum dots [148; 149]. These quantum dots, like many others can allow for surface modification. An even friendlier alternative to heavy metals for synthesis of quantum dots is zinc. Zinc is one of the most important minerals that are found naturally in our bodies and assists body functions in a number of ways. At cellular level, zinc helps in cell division and assists in liver functioning as well as expediting healing of wounds. It assists in other important functions such as carbohydrate metabolism, prevention of infections, synthesis of DNA and in male reproductive health. Zinc is mostly found in the muscle tissue and in the bone. The recommended intake of zinc per day is 7 mg for females and 9.5 mg for males. On average however, an adult ingests about 10-15 mg of zinc daily as a nutrient [149]. Of this, about 5 mg is absorbed into the body and this is considered a trace amount which is unhazardous to human body. Furthermore, zinc based quantum dots such as ZnSe when doped with manganese or copper can cover an emission range similar to that of CdSe quantum dots [150]. They are also less sensitive to environmental changes such as

chemical, thermal and photochemical disturbances. Zinc based quantum dots can therefore suitably replace the toxic and heavy metal based quantum dots since they pose no toxic risks to those involved in synthesis as well as those applying them.

2.3.1.4.2 Insolubility of quantum dots

Quantum dots are insoluble in polar solvents because the surface of their core shell is hydrophobic and in most cases, the surface coatings are also hydrophobic [151]. They are therefore only soluble in organic solvents. This restricts the extent to which they can be applied in biological uses and calls for modification of the surface chemistry of these nanocrystals. Without further modification, quantum dots would not be endocytosed, therefore limiting their use in biological experiments to studies using electroporation. If water soluble quantum dots are desired, the method chosen for the core shell synthesis has to allow for post synthesis modification of the surface to hydrophilise the quantum dots without significant loss of other properties of the nanocrystals.

2.3.1.4.3 Intermittent blinking

Quantum dots are known to switch between fluorescent and non fluorescent states with continuous illumination [137; 139], a property commonly referred to as intermittent blinking. This arises from surface defects on the quantum dots, which acts as temporary “traps”, affecting electron-hole recombination [137]. Blinking of quantum dots is also associated with reduced quantum yield [137]. Whereas intermittent blinking of quantum dots may be interpreted as a limitation to application of quantum dots in some areas, especially those that require continuous illumination, it is seen as an added advantage in single molecule studies since the quantum dots can become periodically available for detection.

The factors that are interpreted as limitations to particular applications of quantum dots are therefore put into consideration when designing a method for synthesis.

2.3.1.4.4 Photo bleaching

This refers to the permanent destruction of fluorescence by light- induced conversion of a fluorophore to a chemically non fluorescent compound. Quantum dots show some degree of photo oxidation, although they are much photo stable than organic dyes.

2.3.1.4.5 Non specific binding

Depending on the surface functionality, quantum dots have been reported to non specifically bind to biomolecules such as tissues and cells. This nonspecific binding problem causes a high level of background fluorescence that degrades the signal-to-noise ratio and limits tagging specificity and detection sensitivity. Coating of quantum dots with ligands containing methoxy groups, e.g. polyethylene glycol (PEG 5000) where 5000 represents the molecular weight (g) have been reported to reduce non specific binding.

2.3.1.4.6 Agglomeration of quantum dots

One of the typical features of quantum dots is their spontaneous self aggregation to form functional structures driven by the energetic of the system. Self aggregation occurs through non covalent interactions such as electrostatic forces, host-guest interaction, hydrogen bonding interaction, charge transfer interaction, acid/base proton transfer, van der Waals forces as well as π - π interaction [152]. Aggregation of quantum dots is also reported when they are in biological environments, for instance inside the cells [153], during in situ hybridisation [154; 155] or when used as markers for molecular recognition cell surfaces [155]. This limits the biological applications of quantum dots to in vitro studies.

2.4 Properties of quantum dots

2.4.1 Quantum confinement

Quantum confinement is the phenomenon which is the widening of the bandgap energy of the semiconductor material when its size has been shrunken to nano scale. The band gap of a material is the energy required to create an electron and a hole with zero kinetic energy at a distance far enough apart, that their coulombic attraction could be ignored [156]. A bound electron-hole pair called exciton (whose energy is a few meV lower than the band-gap), could be generated if one carrier approaches the other [156; 157]. This electron-hole (exciton) behaves like a hydrogen atom, except that a hole, which is not a proton, forms the nucleus. Since the mass of a hole is small than that of a photon, this affects the solutions to the Schrödinger wave equation [158].

The distance between the electron and hole is defined as an exciton Bohr radius (r_B). If m_e and m_h are the effective masses of electrons and holes, respectively, the exciton Bohr radius can be expressed by the following equation:

$$r_B = \hbar \varepsilon e^2 \left(\frac{1}{m_e} + \frac{1}{m_h} \right) \quad (1)$$

where ε , \hbar and e are the dielectric constant, reduced *Planck constant* and the charge of an electron respectively [159; 160]. If the radius (R) of a quantum dot is reduced to r_B , especially when $R < r_B$, the motion of the electrons and holes are strongly confined spatially to the dimension of the quantum dot. Consequently, an increase in the excitonic transition energy, luminescence and the resulting blue shift in the quantum dot will be observed.

2.4.2 Radiative Relaxation

Radiative Relaxation is the spontaneous luminescence from quantum dots. It consists of several types of mechanisms: band edge or near band edge transition, defect or activator quantum states transition [160].

2.4.3 Band edge emission

The most general Radiative relaxation processes in intrinsic semiconductors and insulators are band edge and near band edge (exciton) emission [161]. The recombination of an excited electron in the conduction band with a hole in the valence band is called band edge emission. An electron and hole pair may be bound by a few meV to form an exciton. The radiative recombination of an exciton leads to near band edge emission at energies slightly lower than the band gap.

Radiative emission may also be characterized as either fluorescence or phosphorescence, depending on the path required to relax. Fluorescence exhibits short radiative relaxation lifetimes (10^{-9} - 10^{-5} s) [130; 162]. Radiative relaxation processes with lifetimes longer than 10^{-5} s are called phosphorescence. In a typical photoluminescence (PL) process, an electron in a quantum dot is excited by absorption of an electromagnetic wave, $h\nu$, from its ground state to an excited state. Through a fast vibrational (nonradiative) process, the excited electron relaxes to its lowest energy excited vibrational state. For electronic relaxation in molecules, nanoparticles or bulk solids, the emitted photon is red shifted relative to the excitation photon energy/wavelength (i.e. Stokes shift) because of the presence of vibrational level in the excited state as well as the lower energy (e.g. ground) states [162]. Both organic and inorganic luminescent quantum dots exhibit Stokes shift. In organic quantum dots, this relaxation process may be complicated by crossing from singlet to triplet excited states [130].

When intersystem crossing happens, the lifetime is long (10^{-5} ~ 10 s) and the emission is classified as phosphorescence.

2.4.4 Defect emission

Radiative emission from quantum dots also comes from localized impurity and/or activator quantum states in the band gap. Defect states are called dark states when they lie inside the bands themselves. Depending on the type of defect or impurity, the state can act as a donor (has excess electrons) or an acceptor (has a deficit of electrons). Electrons or holes are attracted to these sites of deficient or excess local charge due to coulombic attraction [163].

2.4.5 Activator emission

Luminescence generated by intentionally incorporated impurities is called extrinsic luminescence.

The band structure could be perturbed by the impurities, the so-called activators, in the way of creating local quantum states that lies within the band gap. The predominant radiative mechanism in extrinsic luminescence is electron-hole recombination, which can occur via transition from conduction band to acceptor state, donor state to valance band or donor state to acceptor state [164; 165; 166].

2.4.6 Non-radiative relaxation

In the case of the transition from excited state to the ground state, quantum dot might not emit the photons. Therefore, deep level traps have a tendency to undergo nonradiative recombination by emitting phonons. This non-radiative relaxation process consists of three types: internal conversion, external conversion or Auger recombination. Internal conversion

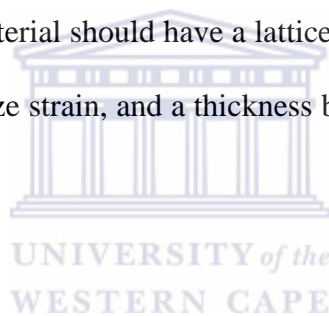
is the nonradiative recombination through crystalline and/or molecular vibrations, and is also one of the reasons for Stokes shift. External conversion is the process where non-radiative relaxation occurred at surface states, defects due to unsaturated dangling bonds etc. Auger non-radiative relaxation refers to strong carrier-to-carrier interaction, which is the process where the excess energy is transferred to another electron that is called an Auger electron instead of releasing the energy as photon or phonon [167; 168; 169].

2.4.7 Surface Passivation

As described from previous section, we already know that in order to reduce the non-radiative relaxation, one of the effective ways is to reduce the surface defects, getting rid of temporary “traps” for the electrons, holes or excitons, resulting better quantum yield for quantum dots. Therefore, in order to achieve photostable quantum dots product, capping or passivation of the surface is critical. Generally, there are two ways to accomplish this goal. One is to cap the quantum dots by organic molecules. The other is of course to cap the quantum dots by inorganic layers. In general, phosphenes, (e.g. tri-n-octylphosphene oxide, namely TOPO [25]) or mercaptans (-SH [170]) are the most widely used capping ligands. Organic molecules however are distorted in shape and, as a result, coverage of surface atoms with the organic capping molecules may be sterically hindered. Besides, the organic capped quantum dots are photounstable [171; 172].

The bonding at the interface between the capping molecules and surface atoms is generally weak, leading to the failure of passivation and creation of new surface states, especially under UV irradiation. The surface states of nanocrystals are known by sites of preferential photodegradation and luminescence quenching [172]. Compared with organic passivated quantum dots, inorganic layer passivated quantum dots have some merits. Uniform coating could be coated on the surface of the quantum dots in order to accomplish high quantum

yield. The maximum of core/shell quantum dots is also dependent upon the thickness of the shell layer. Thicker capping layers lead to formation of misfit dislocations, which are also non-radiative recombination sites which decrease the luminescence intensity [173]. Generally, materials with wider band gap normally play the coating role, while the materials with narrower band gap are made to be the quantum dots core. In this way, exciton could be confined into the core region by the band offset potentials. Another factor to consider when selecting the quantum dots inorganic shell material includes whether it is hydrophobic or hydrophilic. Most inorganic core/shell quantum dots are not compatible with dispersion in water due to the hydrophobic surface property of the shell. In order to be biologically friendly, an appropriate water-compatible coating such as amorphous silica layers is crucial. For best passivation, the shell material should have a lattice parameter within 12% of the core to encourage epitaxy and minimize strain, and a thickness below the critical value that results in misfit dislocations [174].



2.5 Quantum dots synthesis processes

Fabrication of QDs became possible because of the development of epitaxial growth techniques for semiconductor heterostructures in the early 1970s [175; 176]. Quantum dots are compounds with specific characteristics and multiple uses. Their high fluorescence and narrow spectrum shape makes them a unique tagging alternative compared to conventional fluorescent dyes. For the past decades, extensive research has been performed on the properties and uses of quantum dots. There are several viable methods to make quantum dots, but some are limited in producing nanodots that can be used for environmental and biological testing. Properties and uses of quantum dots are determined in part by the materials that compose the nanomaterials as well as how the dots are made. All quantum dots (QDs) have a

core made up of group (II-VI) elements. Common group (II) elements are cadmium and zinc [175; 177]. Common group (VI) elements are selenium, tellurium, and sulphur. The most studied combination is CdSe and CdTe. ZnS is also prevalent in research (Figure 12A). The II-VI core has very high fluorescence, but also a tendency to flash like a firefly (Chan and Nie)[139; 156] . To make the fluorescence constant, QDs are often coated with an outer layer of either a different II-VI compound, or a buffer, also known as a stabilizer or capper [171; 178].

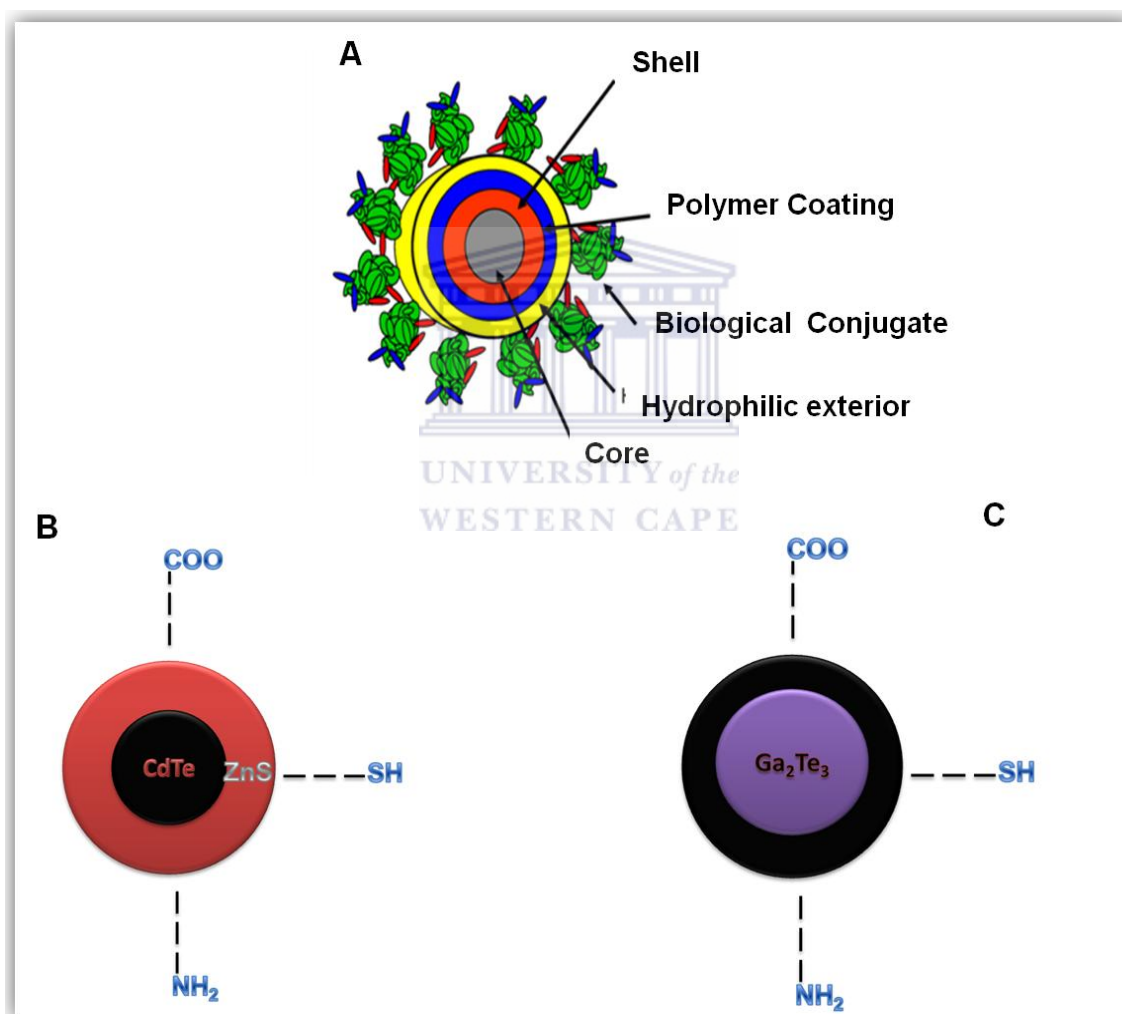
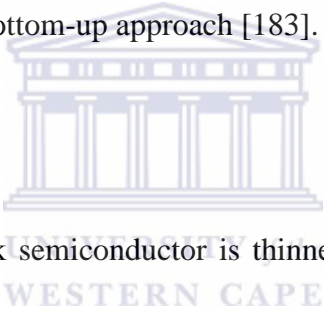


Figure 12. (A) Defines shells and core shells of different quantum dots, (B) Quantum dot (TGA-CdTe/ZnS) with two II-VI layers (Core and shell) capped with TGA and (C) Quantum dots (3MSA-Ga₂Te₃) with only the core capped with MSA and MPA.

Common stabilizers include thioglycolic acid (TGA, also called mercaptoacetic acid, mercaptosuccinic/mercaptopropionic acid (MSA/MPA), and trioctylphospine (TOP) and trioctylphosphine oxide (TOPO). This second layer keeps the dots from flashing or blinking (Chan and Nie), and can adjust the properties of the dots, such as increasing fluorescence or making them water soluble [156; 179] (Figure 12). Depending on how the nanodots are formed, they may or may not be suitable for biological tests. For example, dots grown in organic solvents cannot be used in biological tests [180], while dots grown aqueously can be (Figure 12 B and C) [181]. This is because aqueous dots are water soluble, which is necessary for biological uses of quantum dots [182; 183]. Currently, several routes have been used to synthesis quantum dots. Generally, there are two popular techniques used to synthesise quantum dots i.e. top-down and bottom-up approach [183].

2.5.1 Top-down synthesis



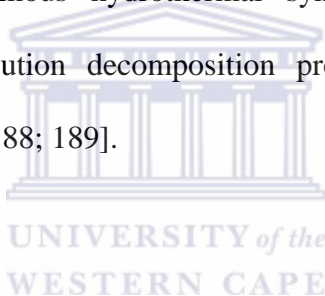
In the top-down approaches, bulk semiconductor is thinned to form quantum dots. Several other facilities have been involved in research work like this for decades, e.g. electron beam lithography (EML), reactive-ion etching, focused ion beams and dip pen lithography [184]. The major shortcomings with these approaches include incorporation of impurities into the quantum dots materials and structural imperfections by patterning. In this research work, we are not going to use this method to synthesize our quantum dots [185].

2.5.2 Bottom-up approach

Bottom-up approach means to synthesize the nano scale material by taking advantage of the chemistry and physics to artificially combine the atoms and molecules in a nanoparticles cluster [186]. In this method a number of different self-assembly techniques such as wet-chemical and vapour-phase methods have been used [187].

2.5.3 Chemical methods

By careful controlling of the parameters for a single solution or mixture of solution to precipitate, nucleuses are generated and further nanoparticles growth may be achieved [127; 156]. Nucleation may be categorized as homogeneous, heterogeneous or secondary nucleation. Homogeneous nucleation occurs when solute atoms or molecules combine and reach a critical size without the assistance of a pre-existing solid interface. By varying factors such as temperature, electrostatic double layer thickness, stabilizers or micelle formation, concentrations of precursors, ratios of anionic to cationic species and solvent, quantum dot of the desired size, shape and composition have been produced [156; 188]. Some of the common synthesis processes are the famous hydrothermal synthesis process, sol-gel process, microemulsion process, hot solution decomposition process, and microwave synthesis process to name just a few [156; 188; 189].



2.5.4 Physical methods

Physical methods for synthesizing quantum dots begin with steps in which layers are grown in an atom-by-atom process [156]. For example, molecular beam epitaxy (MBE) has been used to deposit the overlayers and grow elemental, compound or alloy semiconductor nanostructured materials on a heated substrate under ultra-high vacuum ($\sim 10^{-10}$ Torr) conditions [190]. Physical vapour deposition (PVD) grows layer by condensing of solid from vapours produced by thermal evaporation or sputtering. Quantum dots can be self assembled on a thin film by chemical vapour deposition (CVD) [191; 192].

2.6 Surface modification and functionalisation of Quantum dots with biomolecules

Surface capping and functionalisation of quantum dots involve introduction of additional layer(s) or coating(s) on the core shell structure (Figure 12). The process is intended to make the nanomaterials stable, reduce or eliminate toxicity, avoid agglomeration as well as to improve their luminescence properties. In the process of functionalisation, particular groups are introduced on the surface of the quantum dot material to suit particular applications (e.g. DNA attachment). For example, a carboxylic acid group can be introduced on the surface of a quantum dot to confer solubility properties. There is a huge diversity of different surface modifications and these give rise to quantum dots of very different optical and chemical properties. This diversity of surface modifications allows for multiple applications of the nanodots. However, the surface coatings of quantum dots affect two key aspects of the properties of quantum dots. These are photophysical and physicochemical aspects. The particular photophysical characteristics affected are emission, wavelength, quantum yield and photostability whereas the physicochemical characteristics are size, charge as well as the aggregation stability of the particle suspension in biological systems. The most commonly used surface functionalizing/stabilizing compounds for quantum dots are organic polymeric materials and small inorganic ligands as mentioned earlier. Whether organic polymeric materials or small inorganic ligands, two approaches are mostly used to modify quantum dots in various ways. These approaches are ligand exchange reactions of hydrophobic surfactant molecules for hydrophilic bifunctional ones [29] or phase transfer methods using amphiphilic molecules. In both surface exchange reactions and phase transfer mechanisms, two main approaches are employed to functionalize quantum dots. In one of these methods, a previously synthesised functionalizing polymeric ligand with the desired groups is grafted onto the surface of the quantum dots.

The second method involves initiating growth of the desired functionalizing polymeric ligand on the surface of the quantum dot when the nanocrystals are nucleating. This approach will call for balancing between nanocrystal growth conditions and polymerization conditions. Many polymerization conditions are incompatible with nanocrystals. For example, during polymerization, radicals that initiate the polymerization process may damage the nanocrystals. Therefore, controlled radical polymerization mechanisms have to be designed so that nanocrystal growth and polymerization can take place simultaneously in the same solution. This approach is therefore cumbersome and not commonly applied in quantum dot synthesis, capping and functionalisation procedures. On the other hand, the first approach is a convenient route for introducing macromolecules onto the quantum dot surface and directs them out towards the environment for solubilisation or bioconjugation. Using this approach, quantum dot functionalisation can be done during or after synthesis, thus making it a convenient method for functionalizing commercially available quantum dots.

2.7 Applications of quantum dots

Quantum dots have so many applications in solar cells, light emitting devices, photo bio-labeling technologies (figure 5) because of the following reasons:

- Absorbance and emissions can be tuned with size
- Higher quantum yields
- Broad excitation window but narrow emission peaks
- Less photobleaching
- Higher extinction coefficients
- Minimal interference with each other could be avoided when used in the same assay
- Functionality possible with different bio-active agents in order to suit specific outcomes.

- More photostable when exposed to ultraviolet excitation than organic dyes. [193]

The diagram below shows different fields in which the nanocrystals can be used (Figure 13).

As mentioned earlier that there are several application of the quantum dots and our interest is in **bio-imaging**.

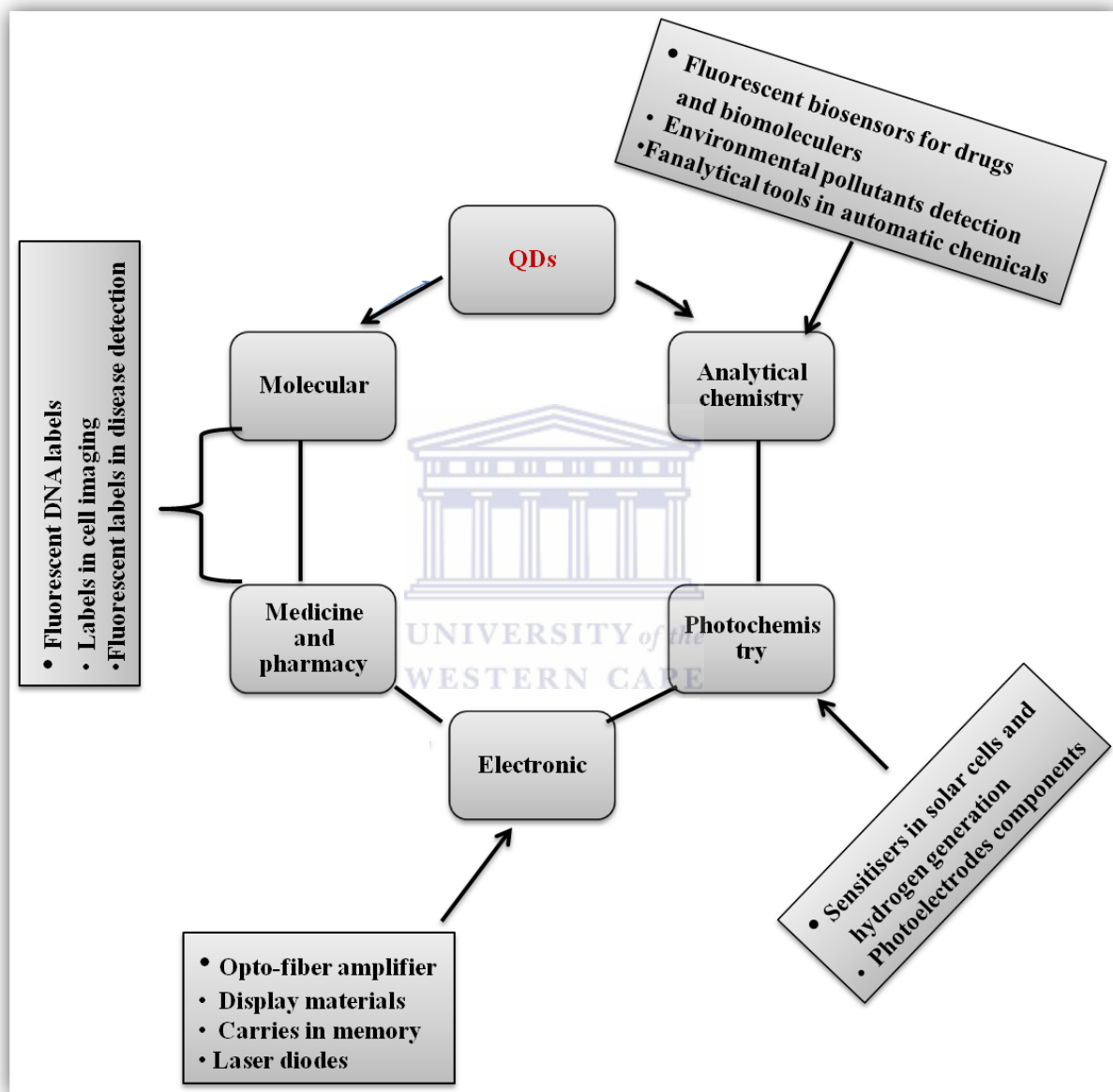


Figure 13. The versatility of quantum dots application in different branches of science.

2.7.1 Bio-imaging application of quantum dots

Currently employed, Magnetic resonance imaging (MRI), optical imaging and nuclear imaging are emerging as key techniques in biological systems. These techniques differ in selectivity, sensitivity, acquisition time, complexity and operational cost. However these techniques have issues that affect their performance. Currently, a significant amount of research is aimed at using unique optical properties of QDs in the present application. Much of optical bio-imaging was based on traditional dyes, but as mentioned earlier that there are several draw-backs associated with the use of this conventional method. Quantum dots on the other hand are of much interest in biology for several reasons, which were also mentioned earlier. Among nanostructure materials, quantum dots based sized-tuned emission colour offers the potential to develop a multicolour optical coding technique, e.g. by functionalising different sized nanocrystal (Ga_2Te_3) with different molecules. The artificial atoms (QDs) are small, compared with biological tissues, they are robust and very stable light emitters and they can be broadly tuned simply through size variation, making them become competitive candidates for biological applications. In the past two years, there has been development of a wide range of methods for bio-conjugating colloidal quantum dots [194; 195] for cell labelling, cell tracking, *in vivo* imaging and DNA detection [195]. General scheme demonstrating cancer cell bio-imaging is shown in Figure 14.

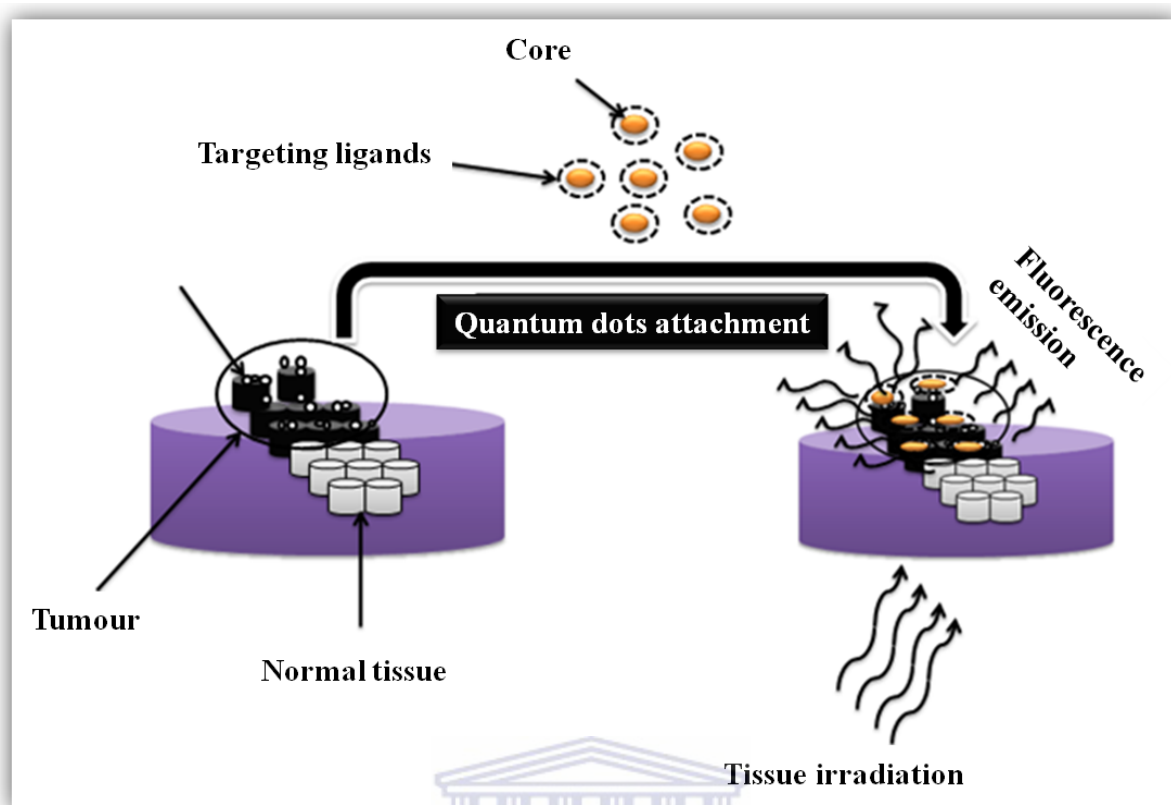


Figure 14. Application of quantum dots in tumour cells.

Applications of nanocrystals as fluorescent labels for cancer cells have been reported. Maestro *et al.*, [193; 196] studied the potential use of CdSe quantum dots for two-photon fluorescence thermal imaging. Two-photon excitation provided the improvement of image resolution and the temperature-dependent contrast. The proposed system seems to be especially useful for cell imaging based on non-homogenous distribution of nanocrystals in cancer cells [196]. QDs might be also ideal probes for real-time fluorescence detection in living cells and live animals. Larson *et al.*, [197] have used two-photon excitation confocal microscopy to image blood vessels in live mice after intravenous CdSe/ZnS QD injection. The studies demonstrated higher contrast and imaging depth at a lower excitation power than with organic dyes. Luo *et al.*, [198] observed the changes of CdTe QD fluorescence intensity during the growth of E-coli allowing dynamic monitoring of total bacterial concentration. Moreover, this group showed better co-operative antimicrobial activity of CdTe QD-rocephin

complex against E-coli in comparison to biocidal efficiency of QDs and antibiotic separately. Recently, a multimodal tumour imaging system based on magnetic resonance imaging (MRI) and the fluorescence imaging was proposed by Tan *et al.*, [199]. This system was prepared by co-encapsulation of QDs and super-paramagnetic iron-oxide in the nanoparticles of poly(lactic acid)-D-alpha-tocopheryl polyethylene glycol succinate [199]. After absorption of polymeric nanoparticles loaded with QDs and iron oxide by the tumour tissue the intensive fluorescent and magnetic signal were observed. Liu *et al.*, [200] have developed other. The authors fabricated gadolinium-doped zinc oxide QDs with enhanced fluorescence and used them to label HeLa cells. These QDs were also characterized by strong positive MRI contrast [200]. A number of useful applications are available on the basis of near-infrared-emitting QDs to medicine and pharmacy [201]. Near-infrared light exhibits numerous benefits including minimal overlapping with water and hemoglobin absorption peaks, deeper tissue penetration than visible light and minimal interference from tissue auto fluorescence. Lately, the group of Pang presented the work describing synthesis of water-dispersible AgSe quantum dots with near-infrared photoluminescence emission at 820 nm and their application for the living nude mouse imaging [202]. Meanwhile, other group prepared CdS-PbS near-infrared fluorescent nanocrystals and demonstrated their muscle tissue imaging capabilities [201]. Wang *et al.*, synthesised near-infrared emitting PbS quantum dots and demonstrated their successful application for in vivo sentinel lymph node mapping of mice [203].

2.8 Electrochemical sensors based on quantum dots and their functions

Generally, a sensor comprises of an active sensing element and a signal transducer, and produces an electrical, optical, thermal or magnetic output signal. While the sensing element is responsible for the selective detection of the analyte, the transducer converts a chemical event into an appropriate signal that can be used with or without amplification to determine

the analyte concentration, acidity levels (pH) etc, in a given test sample as shown by Figure 15. In general, these devices are composed of a bioactive substance as well as a physical transducer. There are different types of sensors namely calorimetric, Potentiometric, amperometric, optical and acoustic biosensors [204; 205]. Below are the components of a genosensor (DNA biosensor) that can detect the individual nucleotides that comprise a genome (DNA) molecule. Automated genosensors enable rapid, nondestructive sequencing of DNA molecules. biosensor as shown in Figure 15.

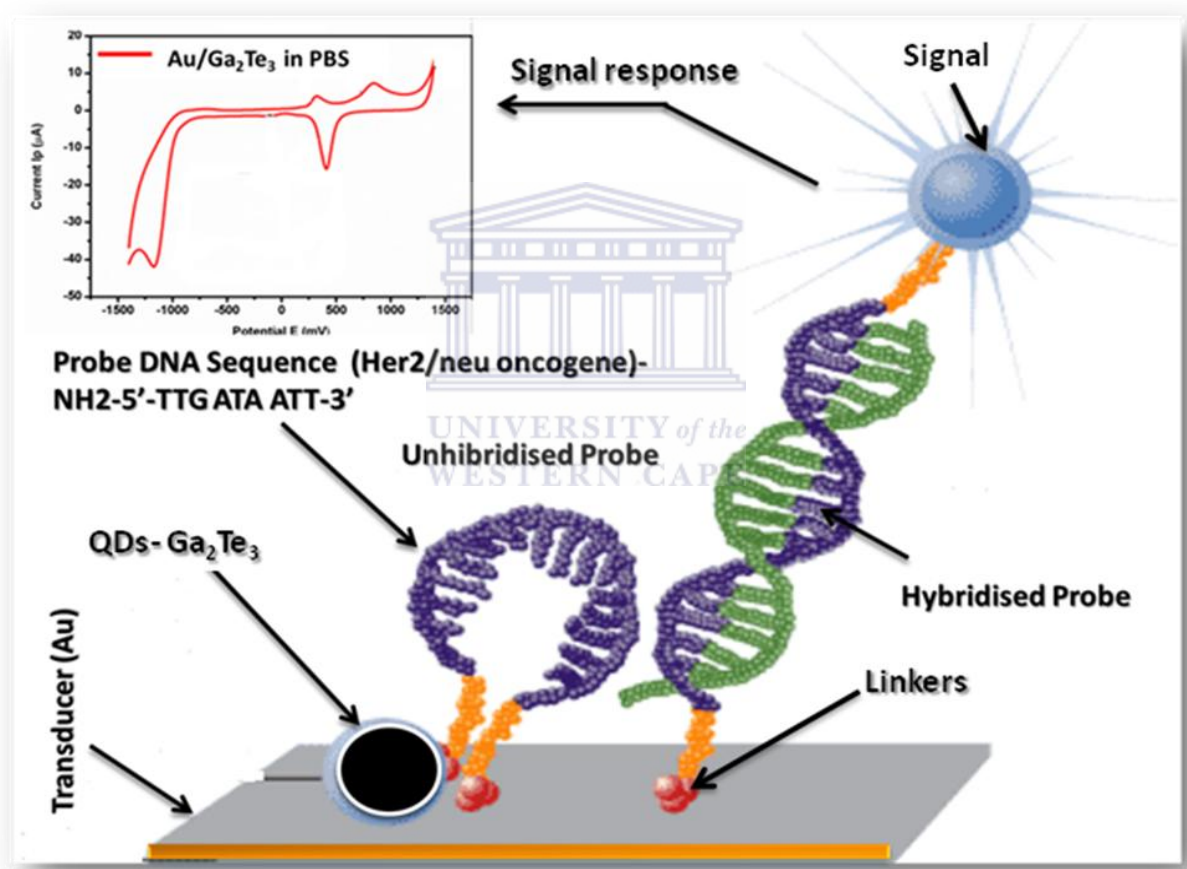


Figure 15. Schematics of genosensing process.

Since the new concept of ‘the electrochemical DNA hybridization biosensor’ was first introduced by Millan and Mikkelsen back in 1993 [1], this exciting research area has received intense attention from several groups around the world.

DNA biosensors convert the Watson–Crick base pair recognition event into a readable analytical signal. A basic DNA biosensor is designed by the immobilization of a single-stranded (ss) oligonucleotide (probe) on a transducer surface to recognize its complementary (target) DNA sequence via hybridization. The DNA duplex formed on the electrode surface is known as a hybrid. This event is then converted into an analytical signal by the transducer, which can be an electrochemical, optical, gravimetric, surface plasmon resonance-based or electrical device [206]. Electrochemistry has superior properties over the other existing measurement systems, because electrochemical biosensors enable fast, highly sensitive inexpensive, easy-to-use, low-cost detection, portable and compatible with micro fabrication technologies. Moreover, in contrast with optical detection schemes, the electrical responses are independent of sample turbidity. In order to make DNA testing more convenient, more economically feasible and ultimately more widely used, the appealing promise of electrochemical detection technologies is thus driving an intense research effort by hundreds of laboratories world-wide. A genosensor is a biosensor which employs an immobilised oligonucleotide as the biorecognition element or electronic sensors that are able to detect and measure the presence of biomolecules such as sugars or DNA segments. Specifically, electrochemical genosensors rely upon the conversion of the base-pair recognition event into a useful electrical signal. Typically, the design of an electrochemical genosensor involves immobilisation of the DNA probe, hybridisation with the target sequence, labelling and electrochemical investigation of the surface. Recent progresses in the development of electrochemical genosensors have been summarised in some excellent reviews [195]. Hence, this chapter will focus on electrochemical DNA biosensors and sensors developed using carbon and gold electrodes as the transducer. Each step in the assays procedure will be discussed in detail, highlighting advantages and disadvantages of different methods.

2.8.1 Biosensing applications based on quantum dots

QDs have been widely used in different fields, especially in biology (DNA and Proteins). Understanding the interactions between QDs with DNAs could benefit the application of QDs in genomic studies [207; 208]. Figure 16 distinguishes possible routes for QDs interactions with DNA/proteins. These interactions include covalent linkage, adsorption, electrostatic interactions, multiple hydrogen bonds, van der Waals force, hydrophobic interactions, p-p stacking, and mercapto (–SH) exchange [209; 210; 211; 212]. Covalent interactions of DNAs to QDs typically occur after QDs surface modification. The modification is done by introducing functional groups of interests such as of sulphide, amine, or carboxyl groups. This only means that the interactions between QDs with proteins mainly depend on the capping reagents [213]. For example, interaction of Ga₂Te₃ QDs modified with mercaptosuccinic and mercaptopropionic acid, L-cysteine, and GSH reveals that QDs/MPA < QDs/L-cysteine < QDs/GSH in the electrostatic interaction with BSA [214]. Due to their unique physical and optical properties, quantum dots have been used to develop advance methods of biosensing. In many case the nano-size QDs allow the nanocrystal to become the central structure component that can accommodate numerous copies of particular biomolecules (e.g. DNA or proteins) or several different biomolecules simultaneously, as a result these bioconjugates are referred to as nanosensors. Based on the latter there are several nanosensors or quantum based sensor which have been developed/fabricated. Recently, Jie *et al.*, prepared hybrid structures containing quantum dots for electrochemiluminescence detection of adenosine triphosphate (ATP) [215] and thrombin [216]. In the first case, magnetic nanoparticles modified with polyamidoamine (PAMAM) dendrimers were linked to CdSe/CdS quantum dots [215]. In the second case, the system was based on Fe₃O₄ coated with CdSe quantum dots [216].

Both structures were characterized by intense electrochemiluminescence, fluorescence and magnetic properties. Gui *et al.*, developed a biosensor based on l-cysteine capped CdTe quantum dots to monitor physiological pH changes in fixed and living cells by means of pH-dependent fluorescence emission color of quantum dots [217].

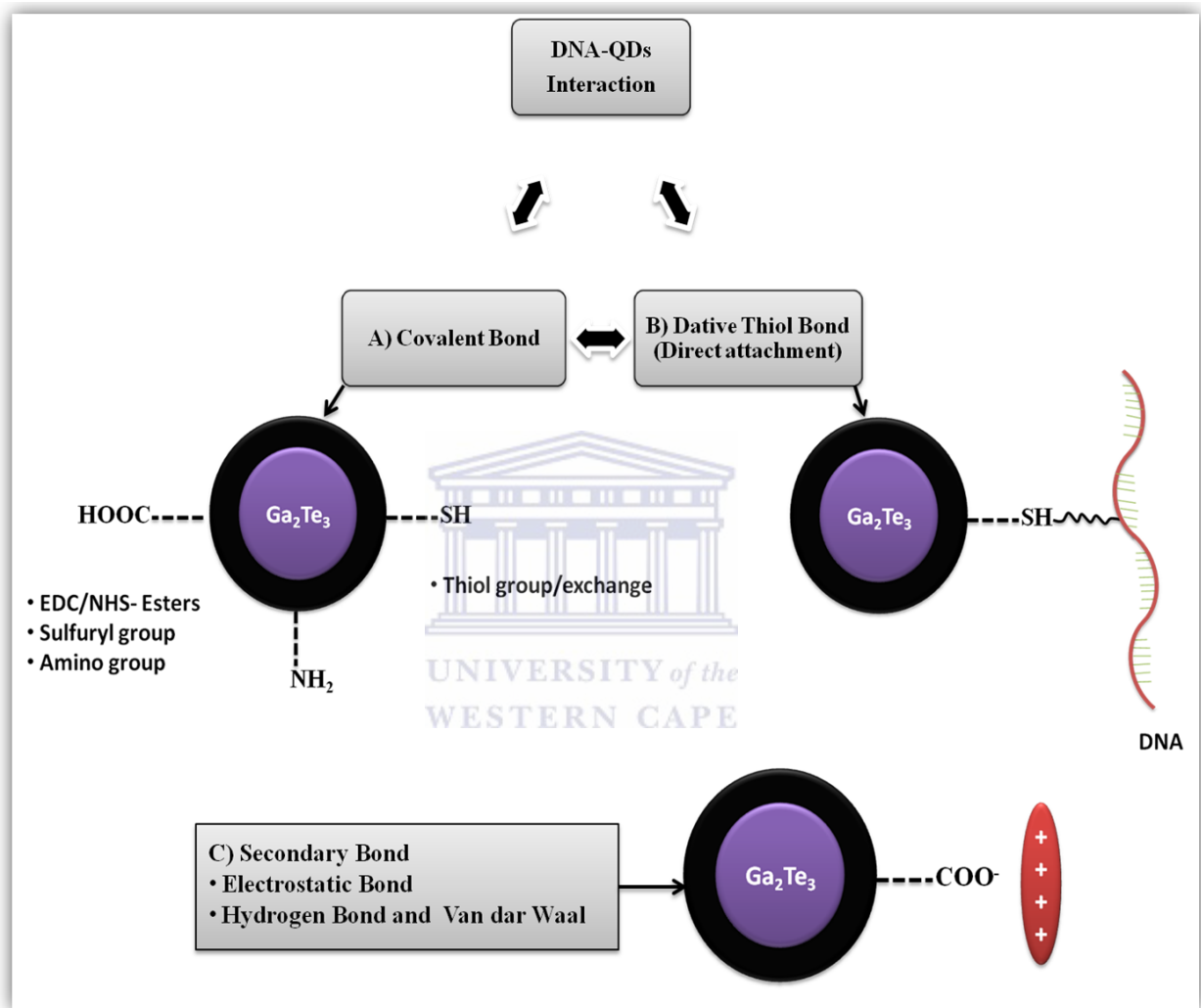
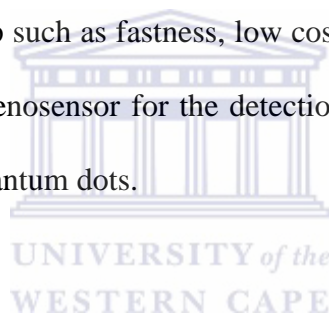
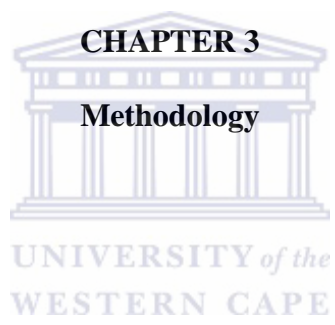


Figure 16. Schematic representation of QDs – DNA interactions.

CdSe/ZnS quantum dots coated with cyclodextrins for the determination of phenols in water was studied by Li and Han [218]. The authors demonstrated that α -cyclodextrin-modified QDs are sensitive toward *p*-nitrophenol while β -cyclodextrin-coated QDs exhibited fluorescence sensitivity toward 1-naphthol [218]. Moreover, Chen *et al.*, [219] reported on the synthesis of l-cysteine-capped CdTe QDs and their application as fluorescent probe for selective trinitrotoluene (TNT) detection. The detection consists on Meisenheimer complex formation between TNT and cysteine and subsequent quenching of nanocrystal fluorescence. Quantum dots are also commonly used as fluorescent sensors for drugs and drug metabolites. Algarra *et al.*, [220] prepared CdTe QDs coupled with 11-[(ethoxycarbonyl)mercapto]undecanoyl- β -cyclodextrin showing fluorescence enhancement after acetylsalicylic acid (ASA) addition. The authors explored the affinity of the cyclodextrin for ASA and its metabolites to form inclusion complexes. In other work thioglycolic acid-capped core/shell CdTe/CdSe QDs have been successfully used as pH-sensitive fluorescent probe for a simple and rapid determination of ascorbic acid in commercial tablets [221]. It was demonstrated that conjugation of QDs with appropriate immunomolecules can be used for recognition of specific antibodies or antigens by measuring the luminescence emission of QDs. An electrochemical immunosensor for the detection of prostate specific antigen (PSA) being the cancer biomarker was studied by Yang *et al.*, [222]. The antigen was detected in patient serum samples using CdS quantum dots functionalized graphene sheets as labels. The group of Yew *et al.*, [223] developed an immunosensor based on CdSe/ZnS quantum dots for detection of human serum albumin (HSA). The immunosensor was composed of anti-HSA immobilized on APTES-modified glass to which HSA captured specifically. After anti-HSA–QD complex conjugation with HSA molecules the fluorescence signal was converted into photocurrent corresponding to the amount of QDs specifically conjugated with HSA [223].

Tian *et al.*, also proposed other quantum dot-based nanosensor for simultaneous detection of two tumour markers [224]. CdTe quantum dots were used for detection of human serum alpha fetoprotein and carcinoembryonic antigen by use of fluorescence polarization immunoassay [224]. The proposed strategy was characterized by wide linear range (from 0.5 to 500 ng mol⁻¹), low detection limit (0.36 ng mol⁻¹ and 0.28 ng mol⁻¹ for carcinoembryonic antigen and alpha fetoprotein, respectively), high sensitivity, good specificity, ease of use and short analysis time. Other group [225] developed immunochromatography test strip based on quantum dots for detection of already mentioned alpha fetoprotein being a valuable marker for diagnosis of primary hepatic carcinoma. The proposed system combines strong luminescence and high photostability of CdSe quantum dots with the advantages of immunochromatography test strip such as fastness, low cost and the ease of use [225]. In our study we will be developing a genosensor for the detection of Her2/neu oncogene in breast cancer by using novel Ga₂Te₃ quantum dots.





This chapter describes the various analytical techniques employed, detailed research methodology and general experimental procedures for the chemical synthesis of quantum dots and nanocrystals as well as electrochemical, microscopic and spectroscopic characterisation of the synthesised quantum dots. Also described in this chapter are procedures for the fabrication, characterisation and application of voltammetric and impedimetric sensors and genosensors for detection of selected analytes; mainly oligonucleotide sequence related to 5-human epidermal receptor growth factor-2-3-phosphate kinase, a common vector gene in breast cancer.

Experimental procedures

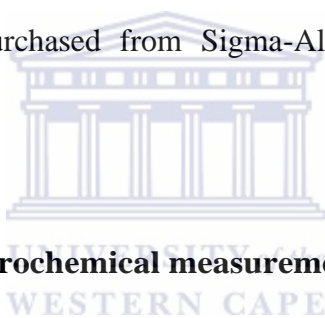
3.1 Reagents and materials

Gallium metal (Ga, 99.99%), tellurium powder (Te, 99.99%), tri-sodium citrate dehydrate ($C_6H_5Na_3O_7 \cdot 2H_2O$, 99.3%), sodium tellurite (Na_2TeO_3 , 99%), sodium borohydride ($NaBH_4$, 99.99%), mercaptopropionic acid (MPA, 99.0%), mercaptosuccinic acid (MSA, 99.0%), acetone (99.8%), 1-ethyl-3-(3-dimethylaminopropyl) carbodiimide hydrochloride (EDC), N-hydroxysuccinimide (NHS, 98%) and tris-ethylenediamine tetraacetic acid buffer (TE buffer) which comprised of 10 mM Tris-HCl and 1.00 mM EDTA, pH 8.00 ± 0.1 , perchloric acid ($HClO_4$) and hydrazine mono-hydrate were all purchased from Sigma-Aldrich. 18-20 base oligonucleotide DNA sequences were purchased from Inqaba Biotechnical Industries (Pty) Ltd., Hatfield, South Africa and Hatfield, South Africa and Eurogentec s.a, Rue du Bois Saint Jean, 5, 4102 Seraing, Dublin. Their base sequences were as shown below:

- An amine terminated DNA with the sequence NH_2 -5'- AAT TCC AGT GGC CAT CAA-3', was used as the probe DNA

- Target DNA (complementary): 5'-GAA CAT GAA GGA CCG GTG GGC-3', which is a section of ERF gene of HER-2/neu.
- Non complementary: 5'-CAT AGT TGC AGC TGC CAC TG-3'
- 3-base mismatch: 5'-GAT CAT GAA GCA CCG GAG GG-3'.

The oligonucleotide DNA stock solutions were prepared with TE and PBs buffer and stored in a freezer at -20 °C when not in use. Phosphate buffer solution (PBS), 0.1 M, pH 7.0 was prepared from anhydrous disodium hydrogen phosphate (Na₂HPO₄) and sodium dihydrogen phosphate (NaH₂PO₄). Deionised water (18.2 MΩ) purified by a milli-QTM system (Millipore) was used for aqueous solution preparations. Analytical grade argon (Afrox, South Africa) was used to degas the system. Sodium hydroxide (99.9%) and hydrochloric acid (HCl, 75%) used were also purchased from Sigma-Aldrich. These chemicals were of analytical grade.



3.2 Instrumentation and electrochemical measurements

3.2.1 Instrumentation

Electrochemical experiments were performed using BAS100W Bioanalytical System (Model No: 100B) and CH instruments Bioanalytical System 600 (Model No: 100B), The three-electrode electrochemical cell comprised a platinum wire counter electrode, a Ag/AgCl (3 M) electrode, glassy carbon (GCE) and gold (Au) electrode were used as reference (0.0707 cm² in thickness and 0.02 cm² in diameter). Fourier Transform Infrared Spectroscopy (FTIR) experiments were performed on a Perkin Elmer spectrometer (Spectrum Model No 100), contact angle measurements were performed on drop sensor analyser (DSA100, made in Germany), Fluorescence experiments were performed on (Type FL3- 2IHR, made in France).

Uv-vis spectroscopy were performed on (Nicolet Evolution Model No 100, thermo Electron, made in UK), X-ray diffraction spectroscopy were performed on (XRD, Model No D/MAX-PC 2500 X-ray, made in UK), X-ray photoelectron spectroscopy (XPS,). Electrochemical measurements were also performed on electrochemical quartz crystal microbalance (EQCM, AUTOLAB AUT84864, made in Netherlands) and electrochemical impedance spectroscopy (EIS, Model No PGZ2402 674R052 N006, Radiometer analytical S.A, made in France). Microscopic analyses were performed by using high resolution transmission electron microscopy (HR-TEM, Tecnai Model No G2 F20X-Twin MAT 200 kV, made in Netherlands), scanning electron microscopy (SEM,), atomic force microscopy (AFM, Nanosurf easyScan2 Model No, made in Japan). Raman spectra were obtained on (Horiba scientific, Olympus Model No BX41TF MAT 200 kV, made in Japan).

3.2.2 Synthesis of quantum dots using mercaptopropanoic acid (3-MPA) and 3-mercaptopropanoic acid (3-MSA) as a capping agent (stability)

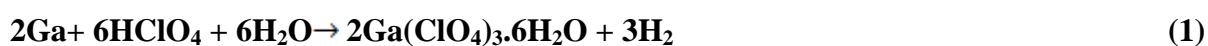
3.2.2.1 Two-pot synthesis of Ga₂Te₃ capped with 3-mercaptopropanoic acid



Scheme 1. MPA interaction with Ga₂Te₃ quantum dots.

3.87 g of Ga metal was weighed into a round bottomed flask and 2 mL of concentrated HClO₄ was added. The mixture was refluxed under constant stirring for 8 h at 120 °C, after which, a white precipitate of Ga(ClO₄)₃·6H₂O was formed. 0.38 g of the gallium salt was dissolved in 20 mL of distilled water and 138.9 μL (4.06 μM) of concentrated MPA was

added. The pH of the solution was adjusted to 12 and 7.4 using 1 M NaOH and saturated with N₂ for 1 h. Te²⁻ was prepared by mixing 0.032 g, of Te powder with 0.016 g NaBH₄ and dissolved in 20 mL distilled water; this was done in an inert atmosphere since Tellurium is susceptible to oxygen. The resulting concentrations were 0.02 M and 0.04 M, respectively. The mixture was then stirred continuously at room temperature under nitrogen saturation for 8 h after which a dark purple solution was formed. Freshly prepared Te²⁻ was added dropwise into the nitrogen saturated Ga(ClO₄)₃/3MPA solution followed by reflux for 4 h resulting in a yellow solution (Ga₂Te₃ quantum dots in solution).



After preparation/formation of the gallium telluride (3MPA-Ga₂Te₃, see scheme 1: overall reaction) quantum dots, a precipitation (powder form) of the nanomaterials was required for further analysis of X-ray diffractive (XRD), X-ray photoelectron spectroscopy (XPS) and Atomic force microscopy (AFM). These analyses of quantum dots were carried out to determine their crystallinity, the oxidation/reduction states and their structural morphology. For the analyses, the solution was cooled in an ice bath, following a 4 h reflux (100 °C) and precipitated by adding acetone (35 mL), drop-wise to the reaction mixture under continuous stirring. The precipitate was collected via centrifugation (10 min, 14,000 rpm) and the materials washed with water several times in order to remove free ions, using a combination of sonication and centrifugation. 70% yield of the powdered quantum dots (3MPA-Ga₂Te₃) was realised and re-dispersion was possible in 0.2 M phosphate buffer (pH 7.4) when required.

The quantum dots were redispersed in 0.2 M phosphate buffer (PBS) pH 7.4. Figure 17 show the preparation method of the synthesised quantum dots.

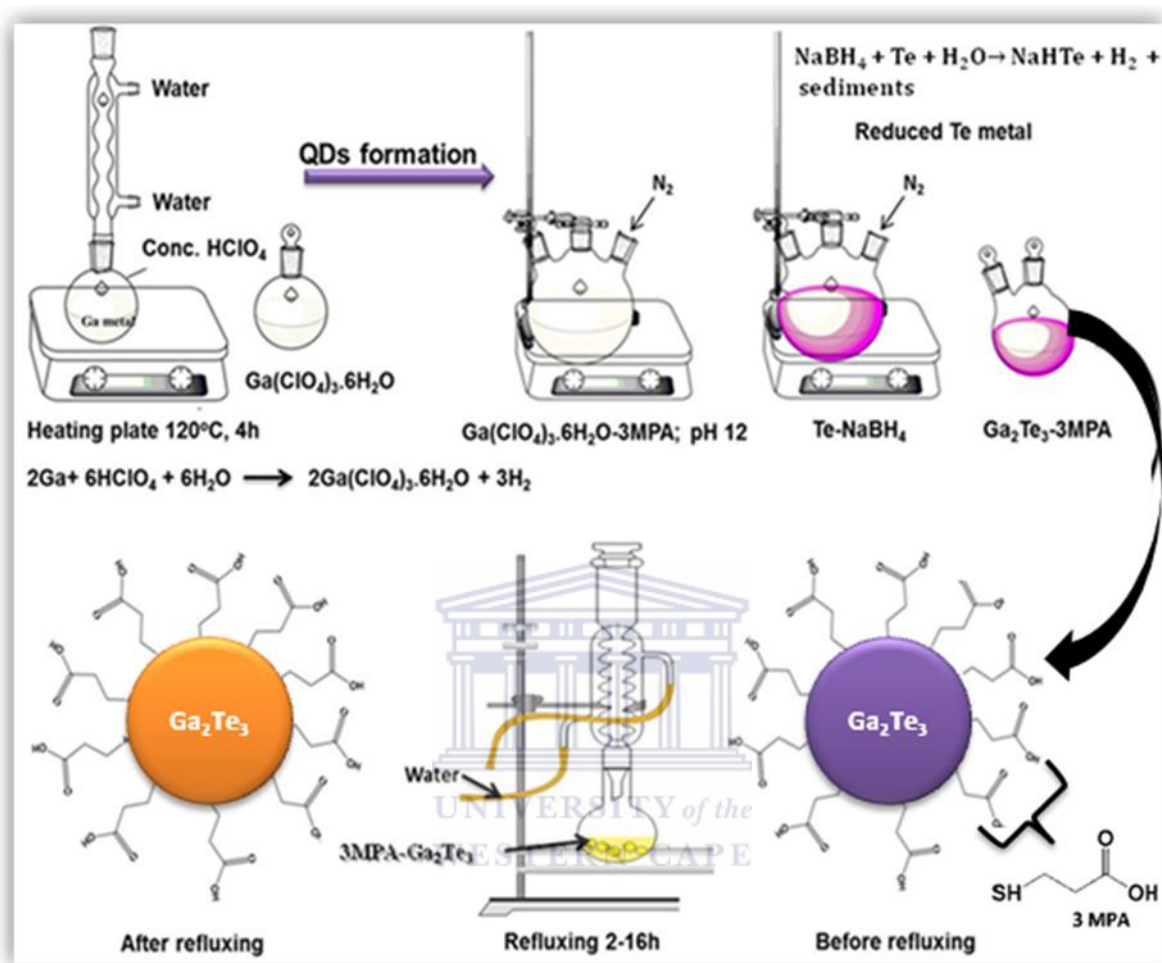
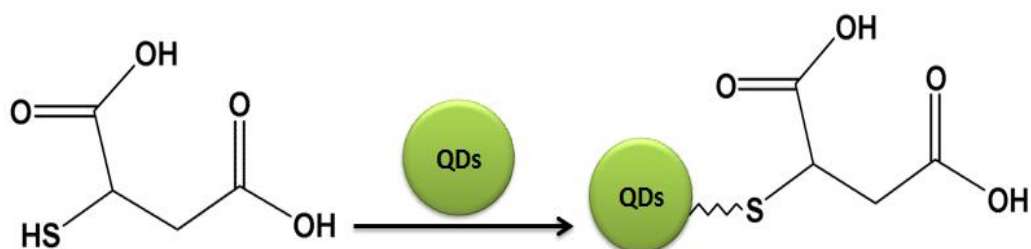


Figure 17. Two-pot synthesis of Ga₂Te₃ capped with 3-mercaptopropionic acid.

3.2.2.2 One-pot synthesis of Ga₂Te₃ capped with 3-mercaptopropionic acid



Scheme 2. MSA interaction with Ga₂Te₃ quantum dots.

MSA-capped Ga_2Te_3 QDs (scheme 2) were synthesised via two modified procedures according to the previous report [226; 227]. Typically, gallium perchlorate solution ($\text{Ga}(\text{ClO}_4)_3 \cdot 6\text{H}_2\text{O}$, 0.04 M, 4 mL) was diluted to 50 mL in a one neck flask, with and without tri-sodium citrate dihydrate (400 mg), Na_2TeO_3 (0.01M, 4 mL), mercaptosuccinic acid (MSA, 100 mg) and sodium borohydride (NaBH_4 , 50 mg) were added under vigorous stirring. When the solution became green, the flask was attached to a condenser and refluxed at 100°C for the desired period of time (2 h) under N_2 flow. An equal volume of acetone was added to the QDs aqueous solution and the precipitated QDs were collected via centrifugation (145 rpm, 20 min). After decanting the supernatant, the QDs were redispersed in PBS, and reprecipitated by ethanol.

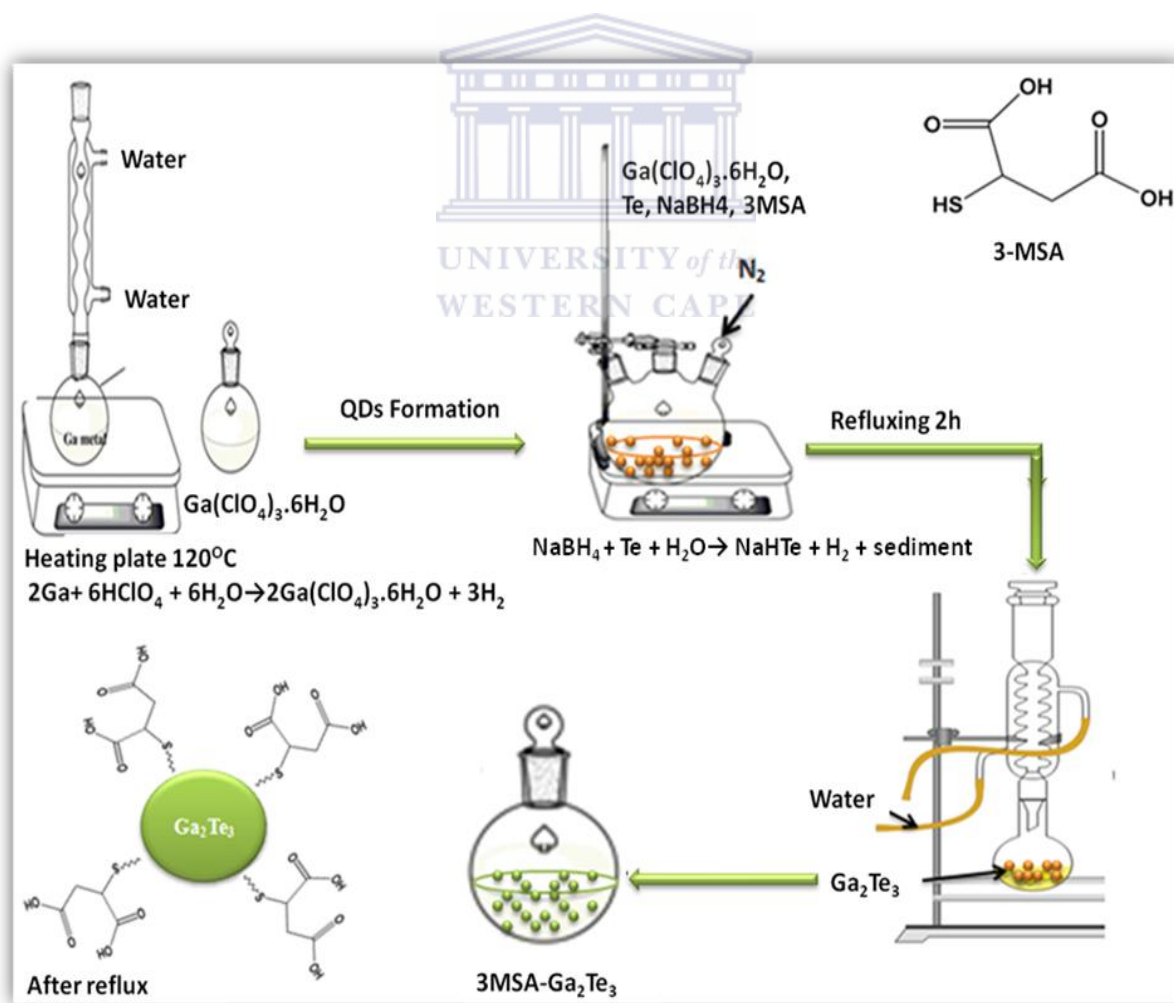


Figure 18. One-pot synthesis of Ga_2Te_3 capped with 3-mercaptopropionic acid.

The same procedure was repeated 3 times to wash away the free ions thoroughly. The QDs were finally dispersed in Milli-Q water for further characterization. The nanomaterials were synthesised at pHs 7.4. Figure 18 above shows quantum dots preparation method.

3.3 Preparation of Ga₂Te₃-MPA/Au and Ga₂Te₃-MPA/GCE electrodes.

Gold (Au) and glassy carbon (GCE) electrodes were thoroughly cleaned by polishing them on a soft polishing pad using 1.0, 0.3 and 0.05 μM slurries of alumina, respectively, while rinsing with de-ionised water after each polish. This was followed by ultrasonication in de-ionised water for 5 min. The electrodes were drop-coated with Ga₂Te₃-3MPA solution for 12 h and left to dry in air/oven to form Au/Ga₂Te₃-3MPA. The modified electrodes were then removed from the Ga₂Te₃-3MPA solution and gently rinsed with de-ionized water to remove any physically or weakly adsorbed nanocrystals. The electrode was then immersed in a mixture of phosphate buffer (pH 7.40) solution of 0.2 M for electrochemical analyses. Different scan rates of 5, 10, 15, 20, 25, 30 mV s^{-1} were carried out on the modified electrodes. Gold and carbon screen printed electrode (SPE) were also used in our study for comparison.

3.4 DNA genosensor fabrication (dsDNA/Ga₂Te₃-MPA/Au)

Hybridization, or pairing, of complementary biomolecules is a basic principle of molecular biology used in methods such as Southern and Northern blotting and in nucleic acid amplifications such as the polymerase chain reaction (PCR) [228]. Is the process in which two DNA or RNA single chains from different biological sources, make the double catenary configuration, based on contingent sequence homology of the two sources, resulting DNA-DNA, RNA-RNA or DNA-RNA hybrids [228].

The main reason is to identify or localize certain nucleic acid sequences (genes) in the genome of some species. The target molecule representing the DNA, RNA and/or protein sequence that should be identified or located by the probe DNA molecule (that identifies the target molecule by hybridisation). Hybridisation on a solid carrier is: Southern blotting, Northern blotting, and Western blotting. Hybridisation stages is: probe synthesis, probe marking (radioactively or non-radioactively), target DNA processing, target DNA denaturation, target DNA transfer to solid carrier, molecular hybridisation [229]. Figure 19 describe this phenomenon.

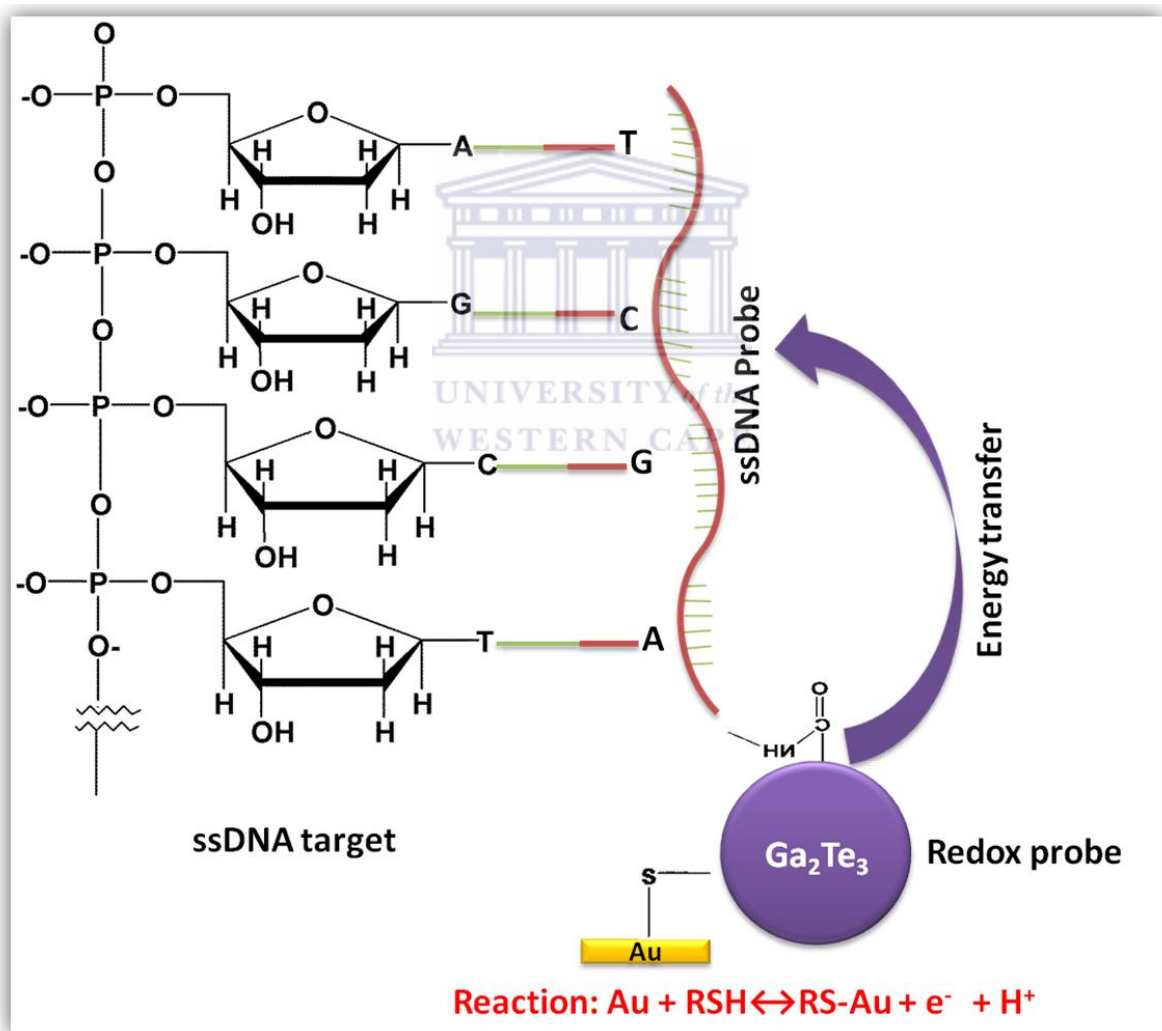


Figure 19. Schematic representation of quantum dots-DNA with common DNA (hybridisation).

The QDs modified gold electrode ($\text{Ga}_2\text{Te}_3\text{-MPA/Au}$) was activated via EDC-NHS steps (Schematic 3) prior to ssDNA attachment. The hybridisation step was performed by immersing the probe-modified gold electrode in different concentrations (0.1, 0.2, 0.3, 0.4, 0.5, 1, 2, 3, 4, 5, 6, 7 and 8 nM) of the target DNA (complimentary) for 5 min. The as-prepared electrode is labelled as dsDNA/3MPA- $\text{Ga}_2\text{Te}_3\text{-MPA/Au}$. A CV of the hybridised electrode was recorded following the incubation step. The same protocol was applied for hybridisation reactions of the probe-modified electrode with, 1-base mismatch sequence, 3-base mismatch and non-complimentary DNA.

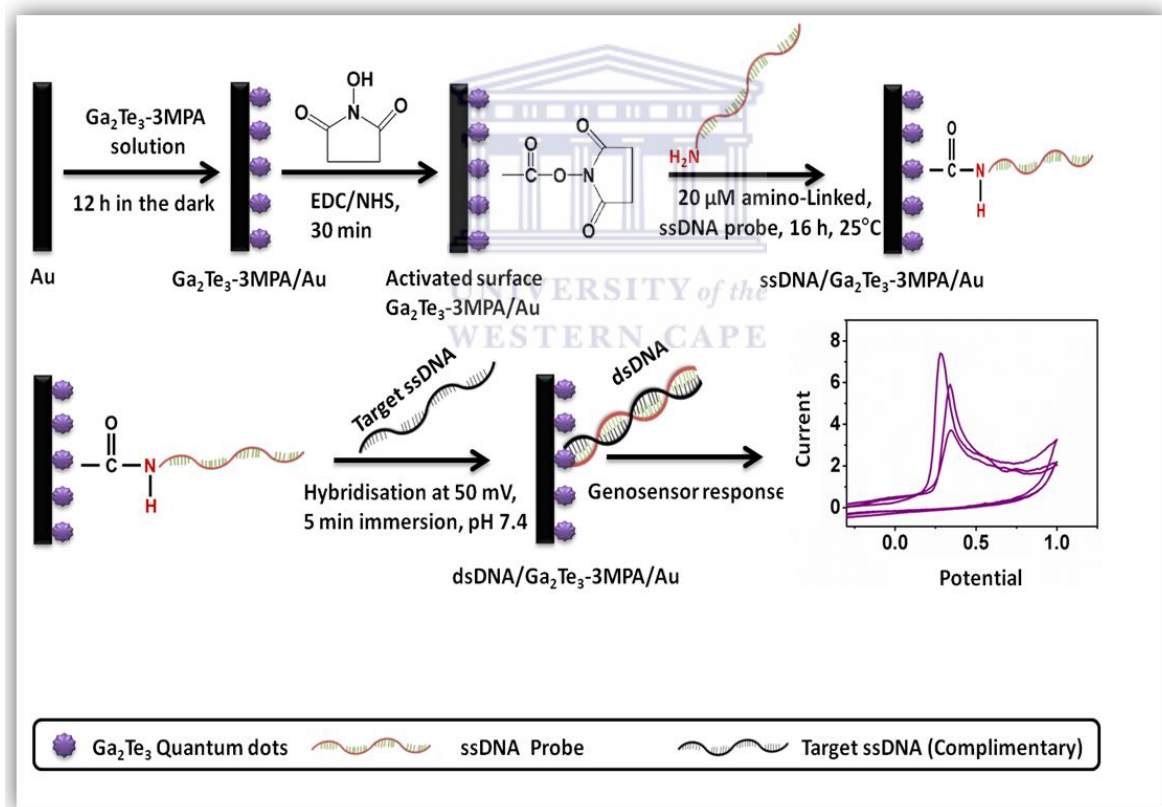
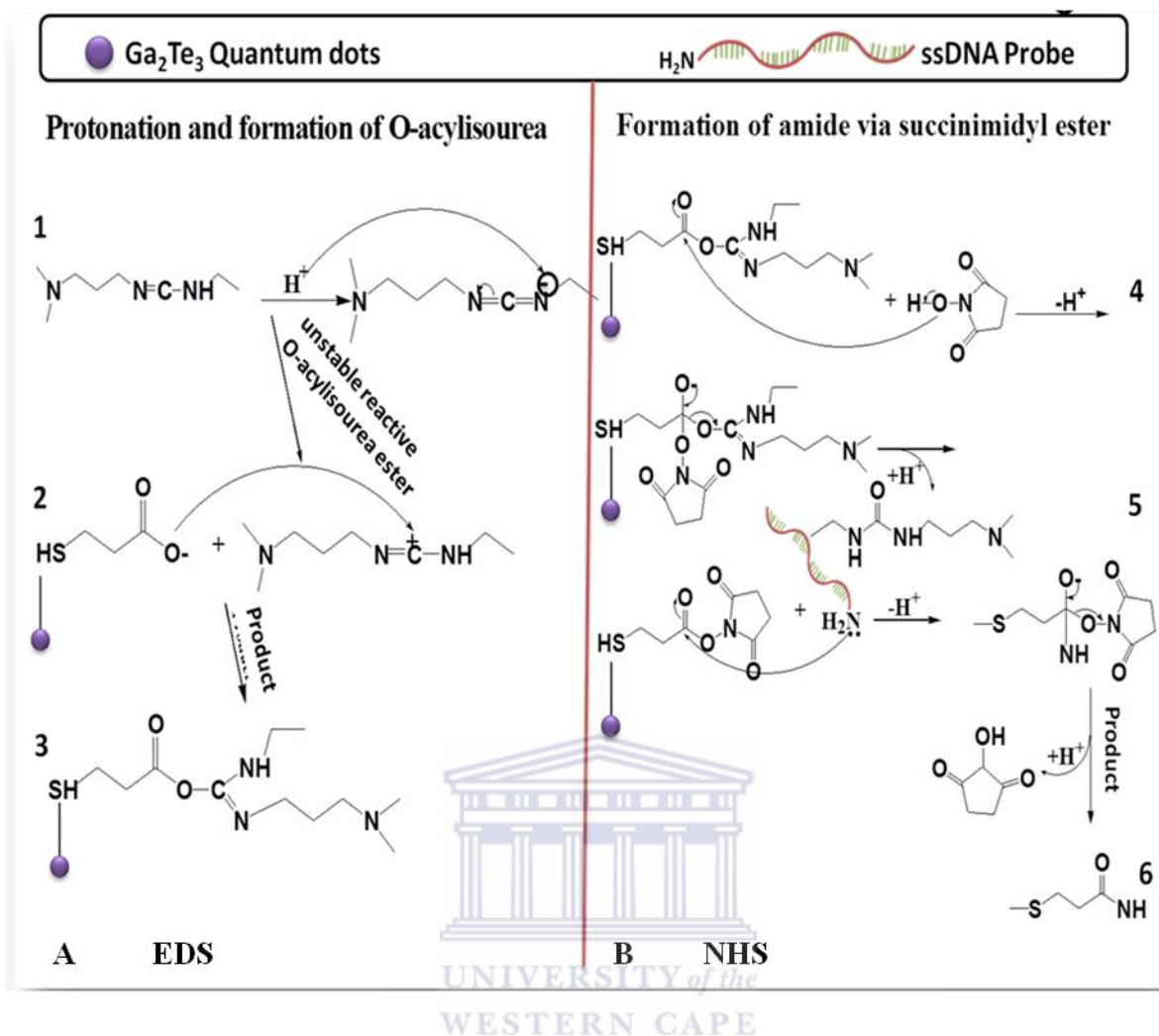


Figure 20. Schematic representation of genosensor fabrication.

3.5 Reaction mechanism electrostatic and covalent bonding between EDC/NHS and Mercapto Acids (3MPA and 3MSA)

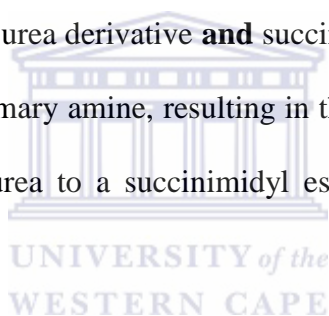
The reaction mechanism for the above schematic (Figure 20) diagram is shown in scheme 3. In the last decades there has been a much interest in the use of both (EDC) and (NHS). Much interest is in the modification of the solid surface/substrate and the possibility to cross-link and couple molecules e.g. acid (3MPA or 3MSA etc.). With its allene functional group, carbodiimide has shown great potential to attain this, and is a known tool in the field of bioconjugation [230], peptide synthesis [230] and modifications of polysaccharides [231]. The advantage of the carbodiimide reaction is the use of non-hazardous reagents and the reaction being done in aqueous medium. In addition, the carbodiimide-mediated amidation is done at room temperature, which most likely preserves the molecular distribution of native RCOO^- , in our case 3MPA [232; 233; 234]. Carbodiimide reaction is known to have low toxicity since its been transformed into a non-toxic urea derivative in the coupling reaction [235]. There are a couple of other carbodiimides, such as dicyclohexylcarbodiimide (DCC) and *N,N'*-diisopropylcarbodiimide (DIC), but they are allergens and since they are water-insoluble they require organic solvents, in which molecules such as 3MPA are not soluble. The carbodiimide reacts with carboxylic groups of e.g. Acid (3MPA), which is shown briefly in scheme 1; the reaction between a carboxyl group and carbodiimide results in a urea, which a nucleophile – a primary amine– can attack, resulting in an amide bond. The coupling is a zero-length crosslinker, meaning no additional residues besides the amide bond and amine have been added to 3MPA.



Scheme 3. Reaction mechanisms for the formation of amide bonds with (a) EDC and (b) NHS.

A thorough research has been made by Nakajima and Ikada [232] to unravel the mechanism of EDC with other molecules such as 3MPA. This mechanism has been accepted as true since is often referenced to in literature. The mechanism is shown in scheme 3A. The first step is the protonation of the carbodiimide, EDC, giving a carbocation **1**, which is hydrolysed into a urea derivate **1** in the absence of a dissociated carboxylic acid. In the presence of carboxylate, carbocation **2** is attacked giving *O*-acylisourea **3**. Up until this step the stoichiometric of H^+ shows that one proton is consumed for each *O*-acylisourea **3** formed. From here on different

scenarios are possible depending on the reaction conditions. Since the EDC forms an unstable amide bond formation due to the regeneration of the carboxylic group and hydrolysis will occur (more water formation) rather than the formation of primary amine, thus a product called *N*-acylurea is formed. For the reasons mentioned above *N*-hydroxysuccinimide (NHS) is employed since it is more advantageous than the later (EDC). NHS is a less hydrolysis-sensitive compound, and is more reactive towards primary amines. When NHS reacts with *O*-acylisourea, a succinimidyl ester is formed, which is more stable towards hydrolysis ($t_{1/2}$ of 40 min at pH 6.0 [236]), Scheme 3B. In addition, the formation of *N*-acylurea is hindered since the succinimidyl ester can not undergo N→O displacement as is the case for EDC. The mechanism is as follows; the dissociated hydroxyl group of NHS **4** makes a nucleophilic attack on *O*-acylisourea **3**, giving urea derivative **and** succinimidyl ester **5**, which can then be attacked by a non-dissociated primary amine, resulting in the amide **6** and regenerating NHS **5**. The conversion of *O*-acylisourea to a succinimidyl ester has enabled the formation of amide [233; 234; 236; 237; 238].



3.6 Methodology for genosensor-cation interaction (Mechanism)

0.1 M of both CsCl and LiCl were prepared for further analysis of genosensor response. The two solutions were used as the electrolyte in place of the normal phosphate buffer. The idea was to study the effect of these cations with the genosensor after hybridisation. Briefly, the bulk glassy carbon electrode was cleaned as mentioned previously and the cleaned electrode was immobilised with both 3MPA-Ga₂Te₃ and ssDNA. After adsorption for 16 h, the GC/3MPA-Ga₂Te₃/ssDNA was immersed in the electrochemical cell comprising of 3mL of 0.1 M CsCl/LiCl as an electrolyte before hybridisation. After electrochemical measurements the genosensor was then removed from the cell and was washed with deionised water (d.w), after which it was immersed in 0.1 nM common ssDNA (analyte) for

5minutes, then into the electrolyte for genosensor detection. After acquiring the voltammograms the GC/3MPA-Ga₂Te₃/dsDNA was remove from the cell and washed again with d.w then into the second concentration of the common ssDNA for further hybridisation (0.1-8 nM).

3.7 Sample preparation for cytotoxicity studies of 3MSA/Ga₂Te₃ on lung cancer cells

3.7.1 Experimental

3.7.1.1 Apparatus

All electrochemical measurements employed a CH Instruments Inc CH1630C potentiostat with single use carbon-Ag/AgCl screen printed electrodes (4 mm²) or prototype TOXOR electronic sensing devices (3.8 mm²). Spectroscopic assays were made on transparent flat bottom 96 well plates (FL medical) using a Biotek synergy H1 Hybrid Reader.

3.7.1.2 Reagents and materials

Sodium acetate (99%), 2-naphthol (99%), 2-naphthyl phosphate (98%), pentachlorophenol (98%), dimethyl sulfoxide (99.6%), cadmium chloride (99.99%), (98%), phosphate buffered saline tablets, RPMI media containing 25 mM HEPES, trypsin 0.5%-EDTA 0.2%, fetal bovine serum, penicillin 10,000 units per ml/streptomycin 10 mg per mL, L-glutamine 200 mM, polystyrene (35,000 Daltons) were all obtained from Sigma Aldrich. Silver/Silver chloride and carbon ink were supplied by Gwent, polyester 339 white 250 µm and polyester O 100 µm were melinex brand. Polyester A grade 500 µm was mylar brand. Other chemicals and suppliers used included acetic acid (99% Riedel de Haen), tetrahydrofuran (99.9% Lab scan analytical sciences), scotch crystal 19 x 66 mm tape and 0.22 µm hydrophilic filters (Whatman) and 3 M adhesive A4 sheets.

3.7.1.3 Sample preparation for electrochemical cytotoxicity assay

3MSA-CdTe and 3MSA-Ga₂Te₃ were selected as model toxins for this electronic cytotoxicity assay. Briefly, a 96 well plate was seeded with 4×10^4 cells per microwell and incubated for 24 h under previously described conditions. Following incubation the medium was removed and each microwell washed three times with PBS. Fresh medium (100 μ L) was added to each microwell plus 100 μ L of 3MSA-Ga₂Te₃ (0 - 500 μ g mL⁻¹), 3MSA-Ga₂Te₃ (0 - 1000 μ g mL⁻¹) prepared in either deionised water or PBS. All toxins were pre-sterilised using a 0.22 μ m hydrophilic filter [9]. The controls were prepared such that no greater than 0.1% v/v DMSO was present in each sample. Cells were exposed to toxins for 24 h after which time the toxins were removed and 2-naphthol generation measured by chronocoulometry following the previously described method. All cytotoxicity experiments (including controls) were carried out in triplicate.



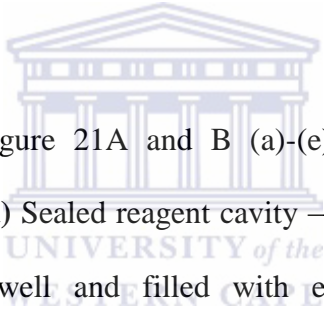
3.7.1.4 MTT cell viability assay

The cytotoxic effect of toxins was also assessed using the colorimetric MTT assay kit (Cayman chemical). Cells were seeded on a 96 well plate and exposed to toxins as described previously. After 24 h of incubation, 10 μ l of 5 μ g mL⁻¹ MTT reagents were added to each sample. The plate was placed on an orbital shaker for 1 min and then incubated for 4 h in a tissue culture incubator. After this time the toxin and medium was removed from the microwells and 100 μ L of crystal dissolving solution was added to each well. The plate was then placed on an orbital shaker for 5 min and then back in the tissue culture incubator for 10 min to ensure dissolution of formazan crystals. Formazan generation was measured at 570 nm using a microplate reader.

3.7.1.5 Design and fabrication of a TOXOR prototype for cellular enzyme measurement

3.7.1.5.1 Design and fabrication of prototype TOXOR device and GenoDot microanalyzer (GDMA)

The GDMA and TOXOR integrated mesofluidic/electronic detection devices were designed using CorelDraw Graphics Suite X5 software and constructed using a thin film lamination approach (5 layers of polyester materials) bonded via chemical adhesion (Figure 21). Each layer was machined individually using an Epilog Zing CO₂ laser cutter. The TOXOR and GDMA prototype were designed in such a way so as to allow a simplified version of the electrochemical AP cytotoxicity assay and genosensor to be carried out using a single shot device. Since the same procedure of preparing the prototype devices was used, only TOXOR will be discussed.



The on-card subcomponents (Figure 21A and B (a)-(e)) include combined fluidic and detection elements comprising: **(a)** Sealed reagent cavity – pear-shaped (capacity 175 μ L) in fluidic contact with the microwell and filled with enzyme substrate. This patented “membrane touch” activated component functions by the application of a manual (fingertip) force to a membrane above the cavity [26]. Fluid inside the cavity is then focussed towards a breakable valve and expelled into the microwell via a mesofluidic channel (0.2×7.96 mm). **(b)** Microwell – polystyrene coated polyester (capacity 40 μ l, area 44.4 mm²) which allows for cell immobilisation and growth. During a cytotoxicity assay, the cells immobilised in the microwell were exposed to a toxin for a defined exposure time, following which it was then flooded with substrate (2-NP 10 mM) contained in the reagent cavity. **(c)** Two “sinks” (volume 3.8 μ L, area 11 mm²), enable drainage sites for cell media, toxin and excess substrate following flooding of the microwell and are connected via a channel (3.5×2.0 mm). **(d)** Electrochemical detector (volume 2.44 μ L) consisting of stencil printed carbon

working electrode (3.8 mm^2) and Ag/AgCl reference electrode (2.8 mm^2) (Gwent Ag/AgCl paste). The detector is also connected to the microwell through a channel ($0.2 \times 1.94 \text{ mm}$) facilitating electrochemical analysis as the final stage in the assay. (e) Suction pump consisting of a sealed air filled cavity (volume $25 \text{ }\mu\text{L}$) activated by application of external pressure to a membrane above the cavity expelling air into the microwell. When force is no longer applied to the membrane, liquid from the microwell is drawn into the electrochemical cell (d) for measurement.

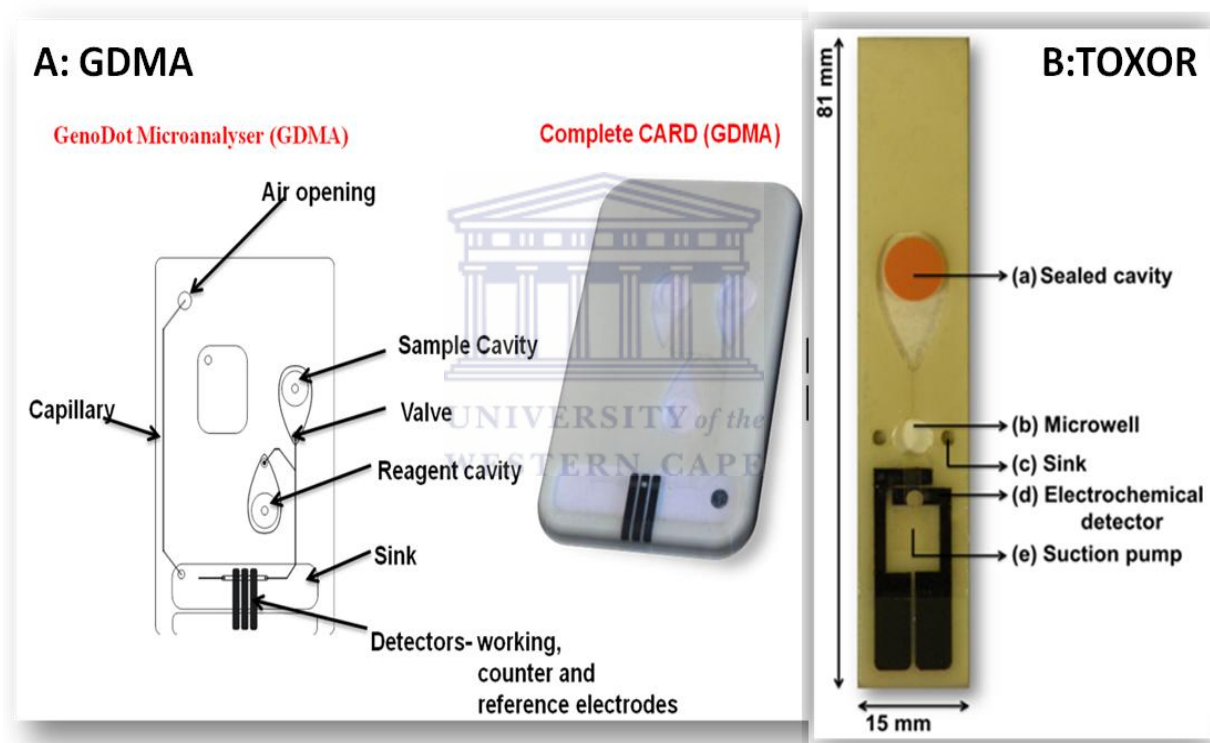


Figure 21. Fully assembled A) GDMA and B) TOXOR sensing devices. Displayed is the reagent cavity, microwell with immobilised cells, sink-overflow device and printed sensor for enzyme activity and ssDNA/3MPA-Ga₂Te₃ measurements.

3.7.1.6 Sample preparation for TEM analysis

Samples for transmission electron microscopy (TEM) were first fixed in 2.5% glutaraldehyde in 0.1 M phosphate buffer for a minimum of 1 h at room temperature and post fixed in 1% osmium tetroxide in Sørensen's phosphate buffer for 1 h at room temperature. Subsequently, the specimens were dehydrated in a graded ethanol series (30%, 50%, 70%, 90%, 100%). When dehydration was complete samples were transferred from 100% ethanol to a mixture of 1 part of ethanol and 1 part of epoxy resin for 1 h. To complete the resin infiltration the samples were placed in 100% resin at + 37 °C for 2 h. Finally samples were embedded in resin, placed at + 60 °C for 24 h until polymerisation was complete.

For orientation purposes sections from each sample were cut at 500 nm, stained with toluidine blue, and examined by light microscopy. From these survey sections areas of interest were identified and ultrathin (80 nm) sections were obtained using a Leica EM UC6 ultramicrotome (Leica Microsystems, Wetzlar, Germany). These sections were collected on 200 mesh thin bar copper grids, stained with uranyl acetate (20 min) and lead citrate (5 min) and examined by transmission electron microscopy (Tecnai G2 12 BioTWIN using an accelerating voltage of 120 kV).

3.8 Spectroscopic characterisation of the quantum dots

3.8.1 Ultraviolet–visible spectroscopy

Note: all measurements were carried in solution and in the region of 200-600 nM.

Freshly prepared samples of DNAs and 3MPA-Ga₂Te₃ quantum dots were used for UV-vis analysis. UV–visible (UV-vis) absorption measurements of samples were obtained in quartz cuvettes using a Nicolet Evolution 100 UV–visible spectrometer (Thermo Electron, UK). Absorbance spectra of quantum dots at different refluxing times (0 - 2, 4 and 16 h) were

carried out. UV-vis spectra of both quantum dots and probe DNA were acquired, respectively. Additionally, an absorbance spectrum of ssDNA + 3MPA-Ga₂Te₃ was acquired before and after different addition of the target DNA (Her2/neu oncogene).

3.8.2 Fluorescence spectroscopy

Fluorescence spectra of quantum dots at different refluxing times (0 - 2, 4 and 16 h) were carried out. Liquid samples were recorded using Horiba NanoLog™ 3-22- TRIAX (USA), with double grating excitation and emission monochromators at a slit width of 5 nm.

3.8.3 Fourier transforms infra red spectroscopy (FTIR).

Before analysis, liquid samples of quantum dots from the mother solution were pre-concentrated by centrifuging at 14000 rpm for 30 min. The pre-concentrated sample of each quantum dot was mounted on a CaF₂ disk/window for FTIR analysis. The FTIR spectra were recorded spectrum 100 FT-IR spectrometer (PerkinElmer, USA) in the region 400-4000 cm⁻¹.

3.8.4 X-ray diffraction spectroscopy (XRD) and X-ray photoelectron spectroscopy (XPS).

Before analysis, liquid samples of quantum dots from the mother solution were pre-concentrated by centrifuging three times at 14000 rpm, each for 30 min. The pre-concentrated quantum dot samples were then precipitated in absolute ethanol followed by a further 30 min centrifuging at 14000 rpm. Nitrogen gas was gently bubbled through the precipitate until all solvent was driven out. The XRD of the powdered samples was recorded in the range 20 – 70 degrees using a Rigaku D/MAX-PC 2500 X-ray diffractometer with a CuK_α ($\lambda = 1.54^\circ\text{A}$) radiation source operating at

40 kV and 200 mA. And the XPS of the powdered quantum dots samples were also recorded using the same protocol.

3.8.5 Raman spectroscopy

The powdered quantum dots were analysed using Raman spectroscopy to observe their stretching vibration. A naked tape was analysed before mounting the powdered MSA, Liquid MPA and the powdered quantum dots for further analysis. Raman analysis of the mounted quantum dots was done using a XploRA Horiba scientific, Olympus BX41TF MAT 200kV made in Japan.

3.9 Microscopic characterization of the quantum dots and nanocrystals

3.9 .1 High resolution transmission electron microscopy (HRTEM)

Before analysis, liquid samples of quantum dots or from the stock solution were pre-concentrated by centrifuging at 14000 rpm for 30 min. The pre-concentrated samples were dispersed in water and ultrasonicated for 5 min. A small drop of a dilute solution of the quantum dots in water was placed on a copper coated HRTEM grid and the solvent was left to dry. HRTEM analysis of the mounted quantum dots was done using a Tecnai G2 F20X-Twin MAT 200 kV field emission transmission electron microscope from FEI (Eindhoven, Netherlands).

3.9 .2 Atomic Force microscopy (AFM).

The preparation of samples for AFM analysis was as follows: 10 μ L of liquid quantum dots sample was dropped on silicon wafer substrate and left to dry in air. The samples were scanned with a silicon tip at a spring constant of 1-5 N/m and resonance frequency of 60 - 100 kHz. The experiment was carried out in air using a non-contact mode cantilever. The scanned AFM images were taken using (Nanosurf easyScan 2, made in USA). Contact angle

measurements were performed by placing 0.5 g of 3 MPA-Ga₂Te₃ and Ga₂Te₃ on solid surface of the drop-sensor analyser on which 10 µL of deionised water was dropped before taking video measurements.

3.10 Parameters used for our techniques

Table 1. Parameters used for CV at different scan rates and EQCM at different additions of analytes

EQCM microscopy		Cyclic Voltammetry Parameters	
Sensitivity	100 nA	Sensitivity	100.00 nA
Scan rate	25 mV s ⁻¹	Scan rate	5, 10, 15, 20, 25, 30 mV s ⁻¹
Driving force	0.88	Amplitude	50
Initial step	1000 mV	Initial step	1000 mV
Final step	-1000 mV	Final step	-1000 mV

Table 2. Parameters used for CV and SWV for different additions of Analytes

Cyclic Voltammetry Parameters		Square Wave Voltammetry Parameters	
Sensitivity	100 nA	Sensitivity	1.00 nA
Scan rate	25 mV s ⁻¹	Scan rate	25 mV s ⁻¹
Amplitude	50	Stepping potential	1
Initial step	1000 mV	Amplitude	50
Final step	-1000 mV	Frequency	5 Hz

Table 3. Parameters used UV/vis and EIS Spectroscopy for characterisation and different additions of Analytes

UV/vis spectroscopy		Electrochemical Impedances spectroscopy	
Wavelength	350 -700 nm	Potentials	400 mV
Bandwidth	2	Stepping potential	50
Cycles	1	Frequency	1 kHz- 25 MHz
Number of runs	14	Time	60 s
		Cycles	bare and modified, 1

Table 4. Parameters used chronocoulometry and time based-amperometry for different additions of analytes

Chronocoulometry		Time based Amperometry	
Sensitivity	100 nA	Sensitivity	1 nA
Scan rate	25 mV s ⁻¹	Scan rate	25 mV s ⁻¹
Amplitude	50	Stepping potential	1
Initial step	1000 mV	Amplitude	50
Final step	-1000 mV	Frequency	5 Hz

Electrochemical spectroscopy and microscopy techniques used



3.11 Electrochemical techniques

3.11.1 Electroanalytical techniques.

Electrochemistry affords some of the most sensitive and informative analytical techniques in the chemists arsenal. Electroanalytical methods such as cyclic voltammetry, stripping voltammetry, differential pulse polarography, square wave and chronoamperometry complements other analytical techniques such as chromatography and spectroscopy and are not only capable of assaying trace concentrations of an electroactive analyte, but also supply useful information concerning its physical and chemical properties. Electrochemical methods of analysis include all methods of analysis that measure current, potential and resistance and relate them to analyte concentration. Quantities such as oxidation potentials, diffusion coefficients, electron transfer rates, and electron transfer numbers are readily obtained using electroanalytical methods which are difficult to obtain using other techniques. Arguably, the most popular electroanalytical techniques are cyclic voltammetry and square wave voltammetry. This section describes the basic components of the modern electroanalytical system, the principles of cyclic voltammetry and square wave voltammetry.

3.11.2 Basic components of an electroanalytical system

The basic components of a modern electroanalytical system for voltammetric measurements are a potentiostat, an electrochemical cell and a computer. The role of the potentiostat is to apply accurate and controlled potential and monitor the current produced. The electrochemical cell, where the electrochemical measurements are carried out, consists of a working (indicator) electrode, reference electrode, and counter (auxiliary) electrode. The working electrode is where the reaction or electron (e^-) transfers of interest take place hence usually referred to as the indicator electrode.

In this three electrode system, voltage is carefully regulated between the working and the reference electrodes, while the current passes between the working and the counter electrode. It is noteworthy that at no time does current pass through the reference electrode; this is ensured by the use of a potentiostat. Figure 22 show a three electrode arrangement.

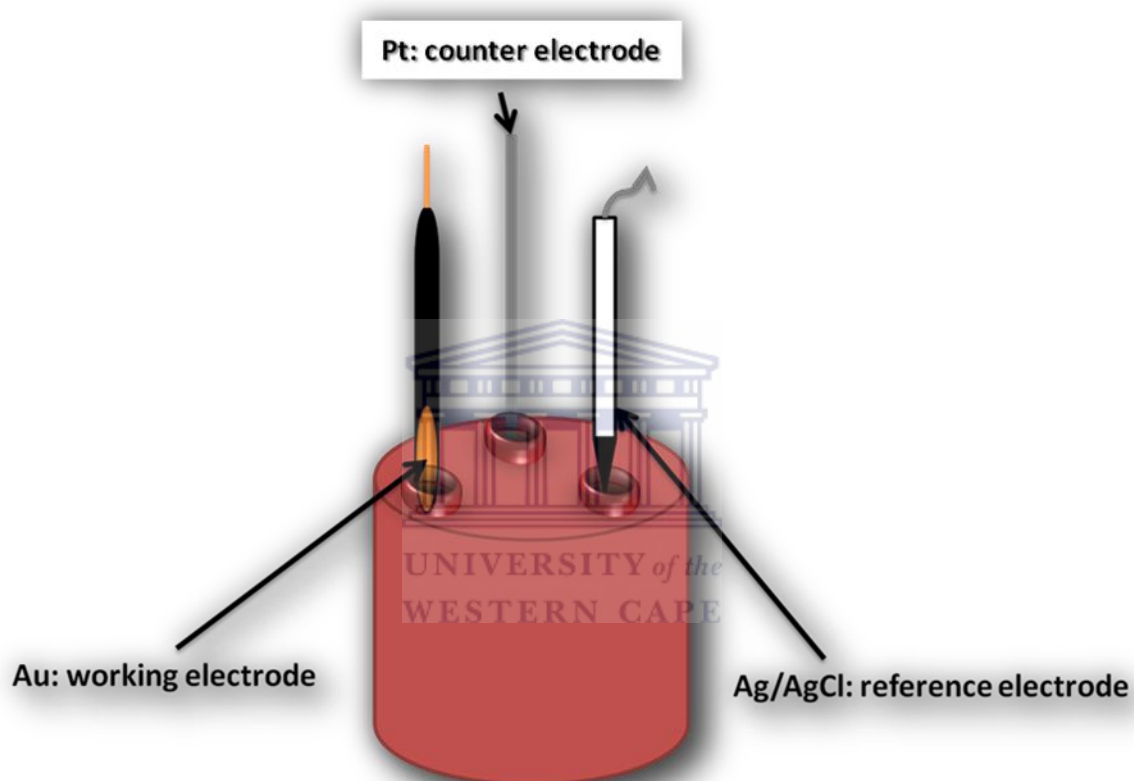


Figure 22. Representation of an electrochemical cell consisting of three electrodes.

Electrodes used were gold (Au) and glassy carbon (GCE) working electrode, Ag/AgCl reference electrode and Pt wire as the counter electrode.

Working electrode (indicator electrode)

This is the electrode at which the electrochemical phenomena investigated takes place. The commonly used materials for working electrodes include platinum, gold or glassy carbon in my case we used boron doped diamond.

Reference electrode

This is the electrode with a constant and a known potential. Its potential is taken as the reference, against which the potentials of the other electrodes are measured. The commonly used reference electrodes for aqueous solutions are the saturated calomel electrode (SCE) and silver/silver chloride (3 M Ag/AgCl).

Counter electrode (auxiliary electrode)

It acts as a sink for electrons so that current can be passed from the external circuit through the cell. Reactions occurring at the counter electrode surface are unimportant as long as it conducts current well. In most cases the counter electrode consists of a metallic foil of thin platinum wire, although gold and sometimes graphite may be used.

3.11.2.1 Cyclic voltammetry (CV)

It is a technique which is widely used in the study of oxidation/reduction reactions and the detection of reaction intermediates. It is a type of potentiodynamic electrochemical measurement. The aim of cyclic voltammetry is to provide qualitative information about electrochemical processes under various conditions. In a cyclic voltammetry experiment the working electrode potential is ramped linearly versus time like linear sweep voltammetry. Cyclic voltammetry takes the experiment a step further than linear sweep voltammetry which ends when it reaches a set potential.

When cyclic voltammetry reaches a set potential, the working electrode's potential ramp is inverted. This inversion can happen multiple times during a single experiment. The current at the working electrode is plotted versus the applied voltage to give the cyclic voltammogram trace. Cyclic voltammetry is generally used to study the electrochemical properties of an analyte in solution; it is widely applicable in the study of oxidation/reduction reactions. The utility of cyclic voltammetry is highly dependent on the analyte being studied. The analyte has to be redox active within the experimental potential window. It is also highly desirable for the analyte to display a reversible wave [239]. A reversible wave is when an analyte is reduced or oxidized on a forward scan and is then reoxidized or rereduced in a predictable way on the return scan as shown by Figure 23.

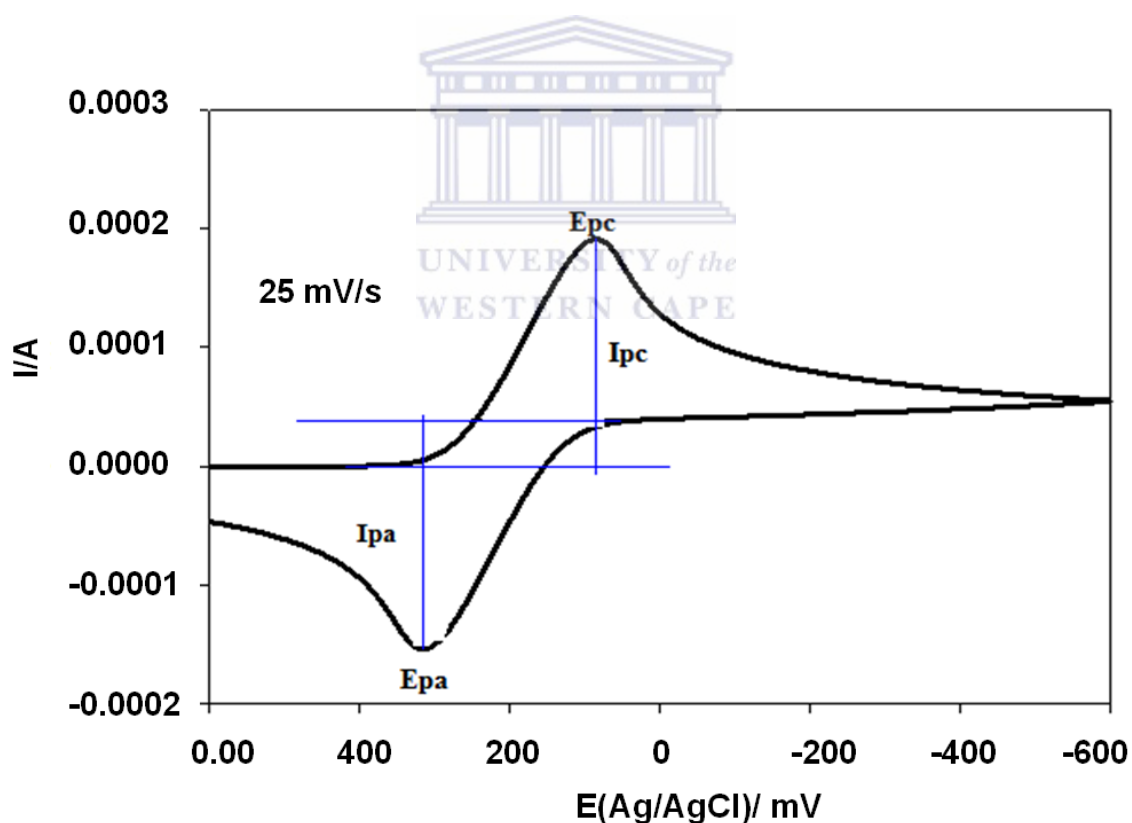


Figure 23. A cyclic voltammogram of 5 mM ferricyanide using boron-doped diamond (BDD) electrode at a scan rate of 25 mV s^{-1} .

Important parameters are usually obtained from cyclic voltammogram for analysis of redox properties of an electroactive sample. These parameters include peak potentials (E_{pc} , E_{pa}) and peak currents ($I_{p,c}$, $I_{p,a}$) for the cathodic and anodic peaks, respectively. Consequently, important information about the sample under investigation can be obtained from the above peak parameters. This includes whether the electrochemical process displayed by the sample is reversible, irreversible or quasi-reversible. It also gives an insight into how fast the electron process is, relative to other processes such as diffusion. For instance, if the electron transfer is fast relative to the diffusion of electroactive species from the bulk solution at the surface of the electrode, the reaction is said to be electrochemically reversible and the peak separation (ΔE_p) is given below;

For reversible reaction, the concentration is related to peak current by the Randles-Sevcik equation (at 25 °C)



$$I_p = 2.69 \times 10^5 n^{3/2} A D^{1/2} \nu^{1/2} C \quad (2)$$

For an irreversible reaction:

$$I_p = (2.99 \times 10^5) n (\alpha n_a)^{1/2} A D^{1/2} \nu^{1/2} C \quad (3)$$

where, I_p is the peak current in amperes, ν is the rate at which the potential is swept in $V s^{-1}$, A is the electrode area (cm^2), n is the number of electrons transferred, D is the diffusion coefficient ($cm^2 s^{-1}$) α is the transfer coefficient, n_a is the number of electrons involved in a charge-transfer step and C is the concentration in $mol cm^{-3}$. Several voltammograms performed at different scan rates can lead to linear plots whose slopes could give further information about the redox properties of the sample in question.

For, instance, when the peak current is plotted against the square root of the scan rate, the slope of the linear plot can be used to estimate the diffusion coefficient according to the Randles-Sevcik, equation shown above. When plotted, the log of peak current versus the log of scan rate gives a linear plot whose slope distinguishes between diffusion controlled peaks, adsorption peaks or even a mixture of the two. At plot of the log I_p versus log ν there's linearity, in which a slope of 0.5 for diffusion peak and a slope of 1 for an adsorption peak is obtained. Intermediate values of the slope are sometimes observed, suggesting a “mixed” diffusion-adsorption peak in some cases, the sample to be characterized may be deposited on the surface of the electrode (chemically modified electrodes). In such cases, one can estimate the surface concentration of the adsorbed material by the use of the Brown-Anson equation:

$$\frac{I_p}{\nu} = \frac{n^2 F^2 A \Gamma}{4RT} \quad (4)$$

where, Γ represents the surface coverage concentration (mol cm^{-2}) R is the gas constant and F is Faraday's constant (96485 C mol^{-1}). [204; 240; 241]

3.11.2.2 Square wave voltammetry (SWV)

It is a large amplitude differential technique in which waveform composed of a symmetrical square wave: (a) is superimposed on a base staircase potential and (b) it is applied to the working electrode (Figure 24) below,

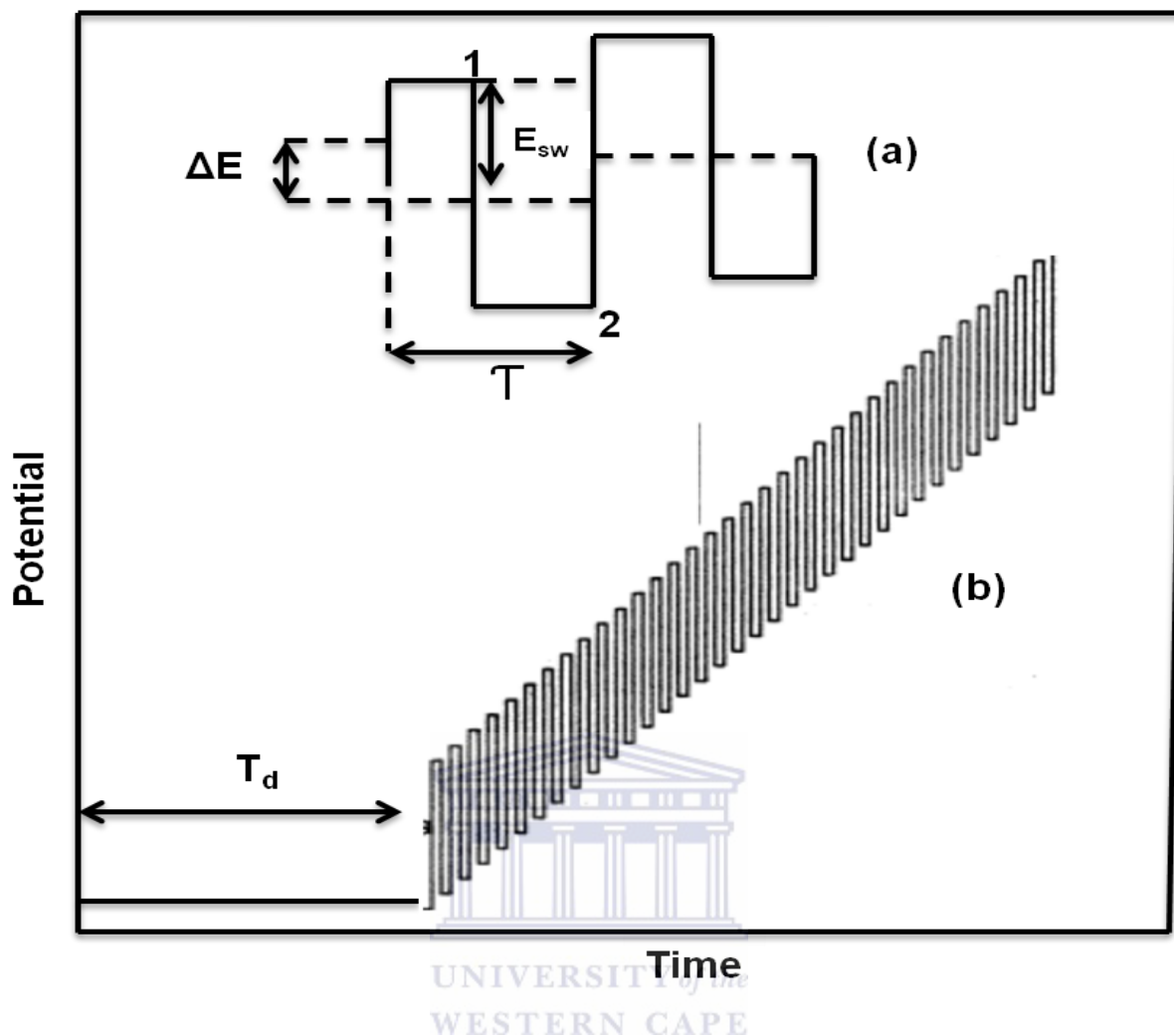


Figure 24. Square-wave waveform showing the amplitude, E_{sw} ; step height, E ; square-wave period, delay time, T_d ; and current measurement times, 1 (forward pulse) and 2 (reverse pulse).

The current is sampled twice during the end of the forward pulse and once at the end of the reverse pulse. The difference between the two measurements is plotted versus the base staircase potential. A dimensionless plot of the theoretical forward, reverse and difference in currents for a rapid reversible redox system is shown below (Figure 25)

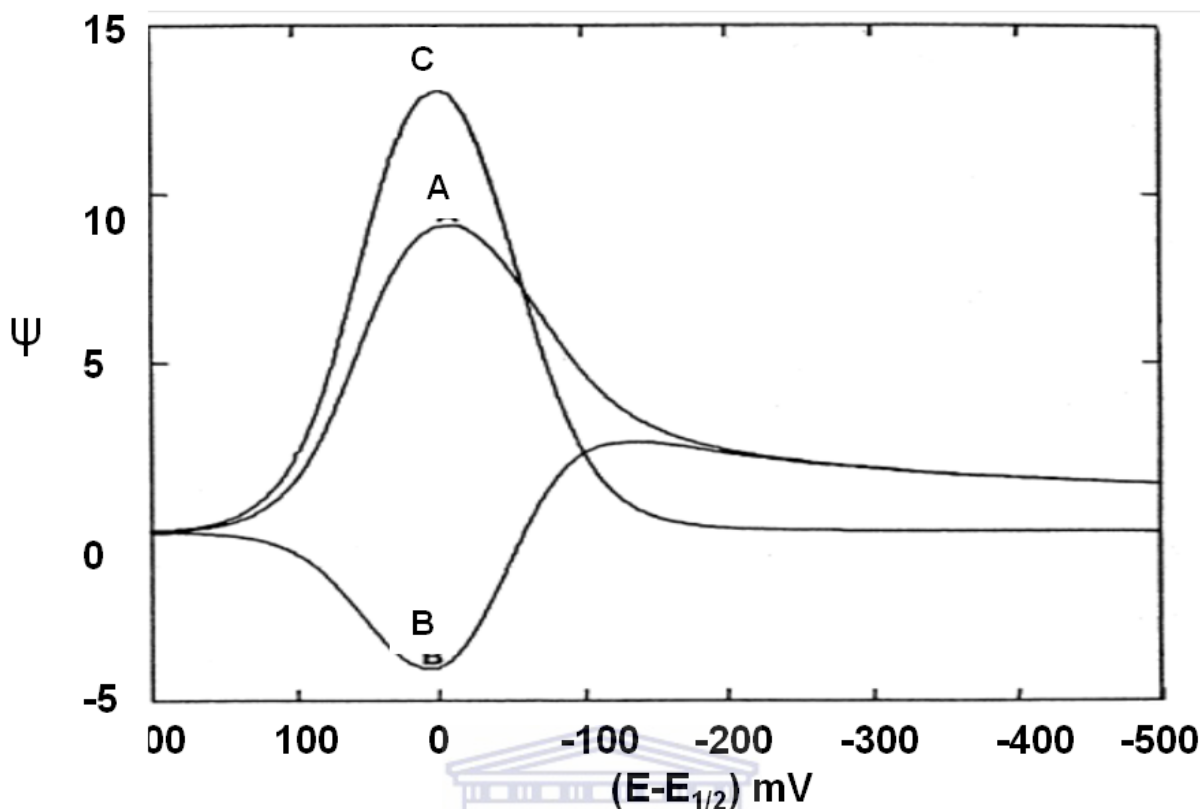


Figure 25. Square-wave voltammograms for reversible electron transfer. Curve A; forward current. Curve B: reverse current. Curve C: net current.

The resulting peak-shaped voltammogram is symmetrical about the half-wave potential, the peak potential is proportional to the concentration. Its excellent sensitivity occurs from the fact that the net current is larger than either the forward or the reverse components (since it is the difference between them). The sensitivity is higher than differential pulse polarography (in which the reverse current is not used). Very low detection limits near 1×10^{-8} can be attained for reverse and irreversible cases. For reversible and irreversible cases the square-wave currents are 4-3.3 times higher than DPV or CV. The peak potential and peak current are described by the following equations:

$$E_{1/2} = E^0 + \left(\frac{RT}{nF} \right) \ln \left(\frac{D_R}{D_O} \right)^{1/2} \Delta\psi_p \quad (5)$$

$$\Delta I_p = \frac{\pi^{1/2} t_p^{1/2} D^{1/2}}{nFAC_O \Delta\psi_p} \quad (6)$$

where, D_O is the diffusion coefficient of species O ($\text{cm}^2 \text{s}^{-1}$), C_O is the concentration of species O (mol cm^{-3}), t_p is the experimental time scale (1/2 Square period - Sample window), $E_{1/2}$ is the half-wave potential and $\Delta\psi_p$ is a dimensionless peak current parameter depends on, number of moles.

Advantages of Square wave voltammetry is its speed, the effective scan rate is given by frequency (f) and ΔE_s (E_s static potential). Frequency of 1-100 cycles per second permit the use of extremely fast potential scan rates (e.g. $f = 50 \text{ Hz}$, $\Delta E_s = 10 \text{ mV}$, then the effective scan rate is 0.5 V s^{-1}) as a results the analysis time is drastically reduced, a complete voltammogram can be recorded within few seconds and kinetic studies can also benefit from the rapid scanning capability and the reversal nature of square-wave voltammetry [241; 242; 243].

3.11.2.3 Chronocoulometry

Chronocoulometry (CC) is a measure of the time dependence of the quantity of electricity (integrated current: which is the amount of charge passed) as a function of time under chrono-amperometric conditions. The usual observables in controlled-potential experiments are currents as functions of time or potential. In some experiments, it is useful to record the integral of the current versus time (chronocoulometry). In this work chronocoulometry was used for the response of the quantum based genosensor (Figure 26).

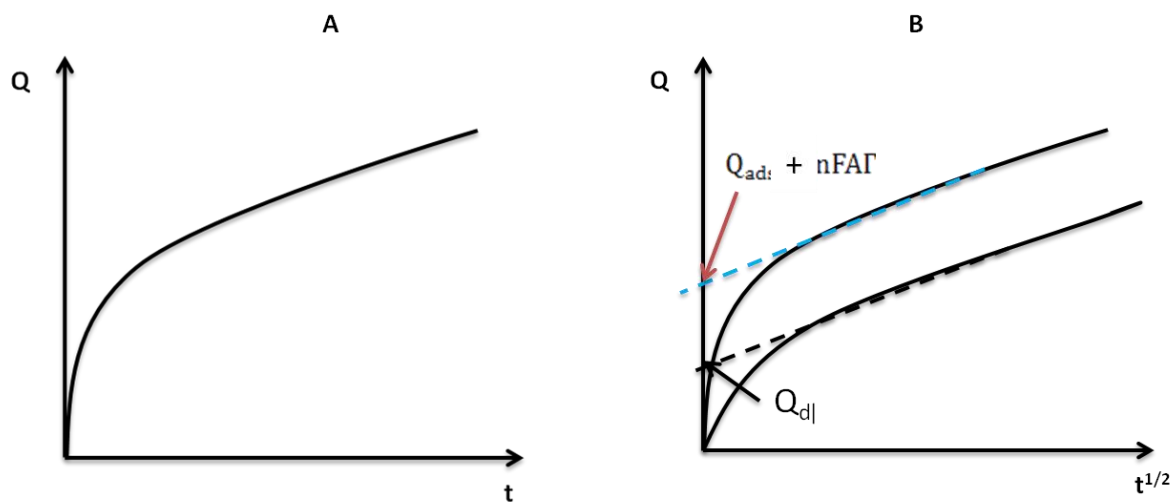


Figure 26. Typical chronocoulometry of 3MPA-Ga₂Te₃.

The coulometry mode was popularized by Anson and co-workers. It is widely employed instead of chronoamperometry because it offers crucial experimental advantages: (a) The measured signal often grows with time; hence the later parts of the transient, which are most accessible experimentally and are least distorted by non ideal potential rise, offer better signal-to-noise ratios than the early time results, (b) The act of integration smooths random noise on the current transients; hence the chronocoulometric records are inherently cleaner and (c) Contributions to $Q(t)$ from double layer charging and from electrode reactions of adsorbed species can be distinguished from those due to diffusing electro reactants. An analogous separation of the components of a current transient is not generally feasible. This latter advantage of chronocoulometry is especially valuable for the study of surface processes. Chronocoulometry is useful to study adsorption on an electrode surface. When adsorbed species exist on an electrode surface, it is electrolyzed immediately, whereas solution species must diffuse the electrode in order to react. The total charge Q is measured in a potential step experiment.

As mentioned earlier that chronocoulometry was taken by one treatment of chronoamperometry in which the current response was integrated to give a response to the charge. The charge-time curve of the forward step for chronocoulometry is the integral of eq. 7: this is called the Anson equation (eq. 8).

$$I = \frac{nFACD^{1/2}}{\pi^{1/2}t^{1/2}} = kt^{-1/2} \quad (7)$$

$$Q = \frac{nFACD^{1/2}t^{1/2}}{\pi^{1/2}} = 2kt^{1/2} \quad (8)$$

As shown in Figure 26A, Q rises with time, and a plot of its value vs. $t^{1/2}$ is linear. The slope of this plot is useful for evaluating any one of the variables n , A , Do , k or C , given knowledge of the others. Equation 9 shows that the diffusional component to the charge is zero at $t = 0$, yet a plot of the total charge Q vs. $t^{1/2}$ generally does not pass through the origin, because additional components of Q arise from double-layer charging and from the electro-reduction of any molecules that might be adsorbed at E_{-v} (Figure 26B). The charges devoted to these processes are passed very quickly compared to the slow accumulation of the diffusional component; hence they may be included by adding two time-independent terms (eq. 9-10):

$$Q = \frac{nFACD^{1/2}t^{1/2}}{\pi^{1/2}} + Q_{ads} + Q_{dl} \quad (9)$$

$$Q_{ads} = nFAT\Gamma \quad (10)$$

where, Q_{dl} is the capacitive charge, Q_{ads} is the adsorbed specie charge and $nFAT$ quantifies the faradaic component given to the reduction of the surface excess, Γ (mol cm^{-2}) is the amount of adsorbed species. The intercept of Q vs. $t^{1/2}$ is therefore $Q_{dl} + nFAT$ (equation 10). Q_{total} is obtained by summing Q , Q_{ads} and Q_{dl} . As the expression of Q in eq. 9, a plot of Q vs. $t^{1/2}$ is a straight line. The Anson plot should be linear with intercept that is equal to the second and third terms in eq. 9. If Q_{dl} is known, then the value Q_{ads} can be calculated for an electrode of the known electrode area. When double step chronocoulometry is used, the difference in the intercepts of forward and reverse steps is Q_{ads} . [204; 244]

3.11.2.4 Electrochemical quartz micro-balance (EQCM)

An electrochemical quartz crystal microbalance (EQCM) is an electroanalytical method, which is capable of measuring minute mass changes on its surface while providing conventional electrochemical data in the same time. A quartz crystal microbalance (QCM) can also be defined as a mass-sensing device, capable of measuring mass changes equivalent to the formation of a monolayer. The QCM is based on the converse piezoelectric effect, discovered by Curie brothers, where a mechanical stress in a quartz crystal was induced upon the application of an electrical potential. The QCM is composed of a thin quartz wafer sandwiched between two metal disks, attached to an oscillator circuit. AT-cut quartz crystals are commonly used because of their frequency stability as a function of temperature. When an alternating potential is applied perpendicular to the crystal surface, a shear stress is induced in the crystal, and the atomic displacement of quartz occurs in the direction parallel to its surface. The shear vibration results in acoustic waves travelling perpendicular to the

surface. When extra mass is uniformly added on top of the quartz crystal, the thickness of the quartz crystal changes and a change in the resonance frequency is observed. If the added mass is less than 2% of the mass of the quartz crystal, the relationship between Δf and mass change is linear, and described by the Sauerbrey equation;

$$\Delta f = -C_f \cdot \Delta m \quad (11)$$

where, Δf is the observed frequency change, in Hz, Δm is the change in mass per unit area, in g cm^{-2} , and C_f is the sensitivity factor for the crystal used (i.e. $56.6 \text{ Hz } \mu\text{g cm}^{-2}$ for a 5MHz AT-cut quartz crystal at room temperature. The negative sign in the Sauerbrey equation indicates that Δf decreases when mass is added to a QCM electrode and vice versa. Sauerbrey¹ was the first to recognize the potential usefulness of the Quartz Crystal Microbalance (QCM) technology and demonstrate the extremely sensitive nature of these piezoelectric devices towards mass changes at the surface of QCM electrodes. The results of his work are embodied in the Sauerbrey equation, which relates the mass change per unit area at the QCM electrode surface to the observed change in oscillation frequency of the crystal, (eq. 1). The Sauerbrey equation relies on a linear sensitivity factor, C_f , which is a fundamental property of the QCM crystal. Thus, in theory, the QCM mass sensor does not require calibration. However, it must be kept in mind, that the Sauerbrey equation is only strictly applicable to uniform, rigid, thin-film deposits. Vacuum and gas phase thin-film depositions which fail to fulfill any of these conditions actually exhibit more complicated frequency-mass correlations and often require some calibration to yield accurate results.

For many years, QCMs were just regarded as gas-phase mass detectors; however, more recently their application has been extended since scientists realized that they can be operated in contact with liquids and viscoelastic deposits. In this case, both frequency and series resonance resistance of the quartz oscillator are important to completely characterize the material in contact with the crystal electrode. Due to its high sensitivity the development of QCM Systems for use in fluids opened a new world of applications, including electrochemistry and microrheology. More recent developments have focused on tailoring electrode surface chemistry (i.e. specialized polymer coatings) so that these devices can be applied as discriminating mass detectors for (1) specific gas detection, (2) environmental monitoring, (3) DNA-biosensing and (3) basic surface-molecule interaction studies. [245; 246; 247; 248]

3.12 Spectroscopic Methods

3.12.1 UV/vis spectroscopy



UV-vis is a reliable and accurate analytical laboratory assessment procedure for analysis of a substance. Specifically, ultraviolet and visible spectroscopy measures the absorption, emission, or scattering of electromagnetic radiation by atoms or molecules. It comprises only a small portion of the wide range electromagnetic radiation spectrum. Although lower in frequency and therefore lower in energy than cosmic, gamma or X-rays, ultraviolet and visible light are of a higher frequency and, therefore of higher energy, than infrared, microwave and radio waves.

The technique is also used to study the electronic transition of materials with transition energy in the approximate range between 10^2 and 10^3 kJ mol⁻¹, which span the near IR through the visible to the UV region of electromagnetic spectrum.

For most semiconductors, the energy required for promotion of an electron from valence band to conduction band is in the same energy region, and thus UV-vis spectroscopy is a powerful technique to study the interband electronic transition in semiconductors. The study of optical absorption is therefore important to understand the behaviour of semiconductor nanocrystals. A fundamental property of semiconductors is the band gap-the energy separation between the filled valence band and the empty conduction band. The band gap energy is calculated using the following equation.

$$E_g = \frac{hc}{\lambda} \quad (12)$$

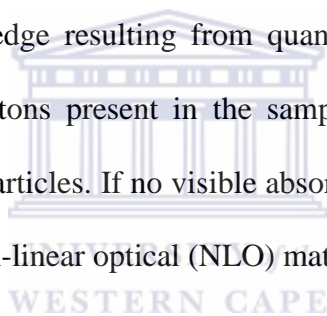
where, E_g is the band gap energy, h is the Plancks constant = 6.626×10^{-34} J.s (4.136×10^{-15} eV.s), C is the speed of light = 3.0×10^8 cm s⁻¹, λ is the wavelength. Optical excitation of electrons across the band gap is strongly allowed, producing an abrupt increase in absorption at the wavelength corresponding to the band gap energy. The absorption of light at a particular wavelength is determined by the ratio of transmitted light and incident light (I/I_o). Therefore absorbance can be expressed as:

$$A = -\log\left(\frac{I}{I_o}\right) \quad (13)$$

Each molecule in a solution absorbs a certain amount of light. Beer's Law quantifies the absorbance of each molecule at a wavelength to its concentration and the length of the light path.

$$A = \epsilon bc \quad (14)$$

where, ϵ is the molar extinction coefficient at wavelength λ , c is the concentration and l is the length of light path. Typically the light path is a constant equal to the quartz cell length of 1cm, while the concentration may vary. Based on experimentally measured absorbance, it is possible to determine ϵ or c if one of the values is known. UV-vis absorption spectroscopy is also an effective technique used to study particle growth of nanocrystals [223]. According to the effective mass model, the radius of the particle is related to the absorption band [224]. UV-vis characterisation gives an idea about the size of the particles under investigation since the band edge depends on the particle size. Absorption peak occurring at lower wavelengths imply a blueshifted absorption edge resulting from quantum confinement of the excitons present in the sample. The excitons present in the sample cause a more discrete energy spectrum of the individual nanoparticles. If no visible absorption is seen in the visible region, the system can be said to be a non-linear optical (NLO) material.[241; 249]



3.12.2 Fluorescence spectroscopy

Fluorescence is one of the different luminescence techniques or processes in which molecules emit light. Fluorescence is the emission of light by a molecule (fluorophore) that occurs within microseconds after the absorption of light (excitation) of shorter wavelength. The best representation of fluorescence is the energy diagram.

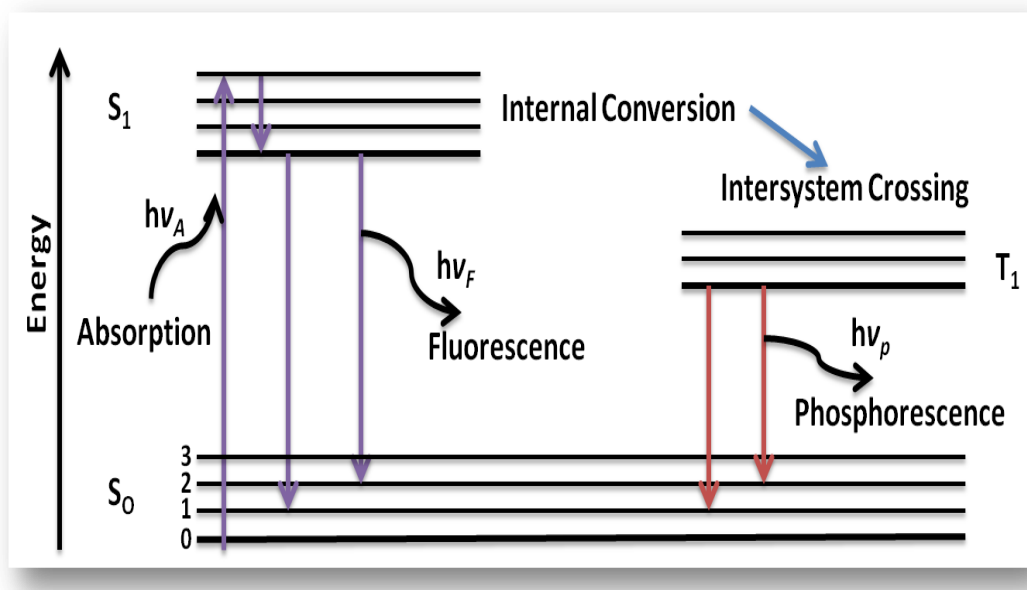


Figure 27. A Jablonski diagram representing the energy levels for a fluorescent molecule and several important transitions.

The characteristic molecular states and relaxation process involved in fluorescence emission are as illustrated in Figure 27. The diagram is known or referred to as the Jablonski diagram. S_0 and S_1 are the single electronic states, and T_1 is the lowest energy triplet state for the molecule. Triplet and singlet states are distinguished by the orientation of the electron spins. The closely spaced levels within each electronic state represent the vibrational levels of the molecule. The vibrational levels are sometimes very similar for different electronic states. Due to the quantum mechanical nature of the underlying processes, energy is absorbed or emitted in discrete units (photons). A single photon has energy $h\nu$, as defined in the figure caption.

3.12.2.1 Absorption and Fluorescence relaxation pathways

At room temperature a fluorescence molecule will normally occupy the ground state (S_0) of electronic and vibrational energy levels. Before fluorescence emission can occur, an energy source i.e. an absorbed photon of energy $h\nu_A$, is required to excite the molecule. The energy of the absorbed photon will lift the molecule to higher level electronic and vibronic energy states, a simple absorption transition, Figure 27. Subsequent photon absorption, an excited molecule will rapidly relax to the ground vibrational level of S_1 . This fast vibrational process is called internal conversion and it occurs on the picoseconds (10^{-12} s). One drawback of rapid internal conversion is that all subsequent relaxation pathways proceed from the lowest vibrational level (S_1). Once reached the ground state of the excited state, there are three main pathways by which the molecule may depopulate the S_1 state: (1) fluorescence emission, (2) nonradiative relaxation and (3) intersystem crossing to the triplet state (Figure 27).

3.12.2.2. Fluorescence emission

Fluorescence is generated when a molecule occupying the singlet electronic excited state relaxes to the ground state through spontaneous photo emission, an incoherent radiative process. There are several parameters used in characterising fluorescence emission, only Stokes' shift and nonradiative relaxation will be discussed.

3.12.2.3 Stokes's shift

From the information gathered thus far one can conclude that the energy of any photon emitted via fluorescence is less than that of the originally absorbed photon due to the energy lost to internal conversion.

Fluorescence emission will thus have a redder colour (i.e. longer wavelength and lower energy photons) than the original excitation source. This shift in wavelength or the red shift is called the Stokes' shift. The actual extent of the red shift depends on the particular molecule and solvent. An example of the Stokes' shift is shown in Figure 28.

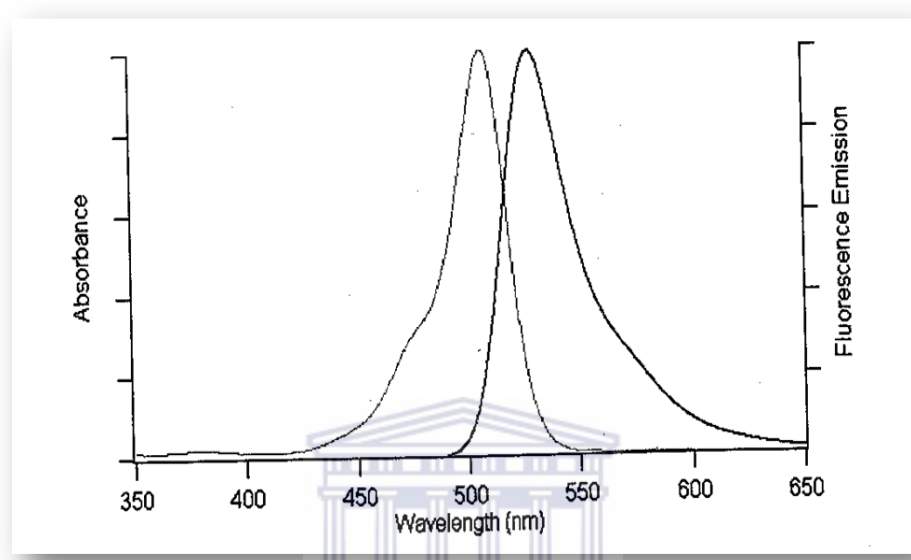


Figure 28. Overlaying of absorbance and fluorescence spectra showing the Stokes' shift.

It is worth noting that the Stokes' shift is very important for the extremely high sensitivity of fluorescence imaging measurements. The red shift allows the use of optical filters, which can block the excitation source from reaching the detector so that fluorescence detection (unlike absorption) is measured against a very low background.

3.12.2.4 Nonradiative relaxation

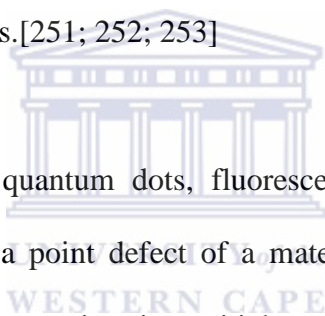
This is a mechanism which allows an excited molecule to relax back to the ground state without any associated fluorescence emission. The reason for this behaviour may be due to intramolecular or intermolecular relaxation pathways and are said to quench the fluorescence.

Quenching pathways compete with the fluorescence relaxation pathways and will thus reduce fluorescence emission. Examples of nonradiative relaxation mechanisms include **resonance energy transfer** a process in which an excited state molecule (the donor) transfers its energy to a nearby molecule (the acceptor) through near-field electromagnetic interaction, excited chemical reaction, **static quenching** occurs when a fluorophore forms a non-fluorescent complex with another molecule and **collisional quenching refers to the loss of the fluorophore's excited state energy upon colliding with a quenching agent**. Example of fluorescence quenchers includes e.g. oxygen and metals

3.12.2.5 Intersystem crossing and phosphorescence and/or the radiative transition of an excited molecule.

Intersystem crossing occurs when an excited molecule relaxes to the triplet excited state. The triplet state is distinguished from singlet states by the opposite orientation of an electron spin (Fig3). From a triplet excited state, a molecule may undergo a radiative transition to the ground state. This is accompanied by a spontaneous emission of (photon) light and the process is called phosphorescence. A radiative electron-hole recombination may also occur, causing a direct transition from a singlet excited state to the ground state. This produces a photon emission spectrum and the process is called fluorescence. The photon energies produced in both fluorescence and phosphorescence reflect the various energy states that are present in the quantum dot. These different energy states are produced by different defects as well as the many different ways though which impurities are incorporated into the lattice. Typically, fluorescence results from a transition between the lowest energy level of the first excited singlet state and some vibrational level of the ground state. The delay between absorption and emission in fluorescence is of the order of 10^{-8} seconds or less whereas it is much longer in phosphorescence.

The emission delay in phosphorescence is believed to result from the presence of vacant lattice sites (trap states), impurities, lattice defects, and/or irregularities in the host lattice that detain or trap the charge carriers (electrons/holes) before their radiative recombination with the luminescent centres. Fluorescence therefore exhibits shorter life time than phosphorescence, a property that allows for fast analysis. The use of fluorescence as an analytical probe tool was inspired by J.B Birk's work., [250] who used fundamental fluorescence to study the photophysical properties of simple aromatic molecules in solution. Since then, fluorescence spectroscopic studies have been extended to more complex systems. Today, fluorescence spectroscopy has been established as a sensitive, selective, non-destructive, and versatile tool for probing various systems such as solutions, colloids, organic and inorganic solids, and polymers.[251; 252; 253]



In characterisation of colloidal quantum dots, fluorescence emission spectrum provides information about the nature of a point defect of a material by determining not only the presence, but also the type of vacancies, interstitials, and impurities in the lattice. It is however important to mention that, single-wavelength emission spectrum can be limited for the analysis of complicated multicomponent samples, or even a simple mixture which contains grossly overlapping emission and/or excitation spectra. This is because conventional fluorescence spectra reveals the fluorescence of a sample within one spectral region, and may not provide enough data to distinguish between two or more closely related emitting molecules. Advanced fluorescence measurements known as three-dimensional excitation–emission matrix (EEM) fluorescence spectroscopic analyses are therefore necessary for analysis of quantum dot point defects, trap states, types of vacancies, interstitials and impurities in the lattice.

EEM produces fluorescence spectra at many excitation wavelengths providing an overall view of all features existing within the selected spectral range. It has been proven to be a useful technique to differentiate the changes and transformations of organic matters in natural environments [250; 254]. The prominent advantage of the EEM fluorescence spectroscopy is that the information regarding the fluorescence characteristics can be completely obtained by changing the excitation wavelength and emission wavelength simultaneously. By analyzing different spectral regions, EEM could be also used to distinguish the fluorophores present in colloidal quantum dot samples. [255]

3.12.2.6 Quantum yield

The quantum yield of a fluorescence is a measure of its fluorescence efficiency, defined as the fraction of all excited molecules that relax by fluorescence emission, as the probability that a given excited molecule will produce a fluorescence photo or simply as a measure of how bright the sample/fluorophore is (in our case the Ga₂Te₃ quantum dots). The quantum yield is also defined in terms of the rate constants as:

$$Q = \frac{\Gamma}{\Gamma + K_{nf}} \quad (15)$$

where, K is the adsorption rate constant. From the equation it is apparent that the quantum yield would reach its maximum value of unity only when fluorescence is of single allowed relaxation process. Fluorescent molecules commonly used as probes in microscopy have quantum yields ranging from very low (< 0.05) to near unity. High quantum yield is desirable in most imaging applications. In this study the quantum yield of the quantum dots which is used as an imaging probe is compared with that of rhodiamined 6G and was calculated to be higher than that of the later as expected.

Quantum Yield was calculated using the following equation (eq. 16):

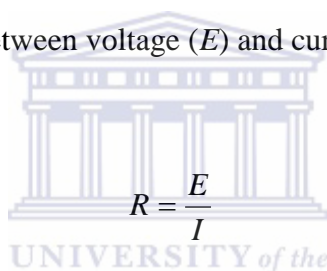
$$Y_s = Y_r \cdot \frac{F_s}{F_r} \cdot \frac{A_r}{A_s} \cdot \frac{G_s^2}{G_r^2} \quad (16)$$

where, Y_s = Yield of the sample, Y_r = Yield of the reference, which was known as 0.95 (or 95%) (Qu and Peng), F_s = Peak fluorescence intensity of the sample, F_r = Peak fluorescence intensity of the reference, measured as 234.4169, A_r = Absorption of the reference at the excitation wavelength (must be <0.1), measured as 0.089358, A_s = Absorption of the sample at the excitation wavelength (must be <0.1), G_s = Index of the reference material of the sample; water was used, and the index is 1.3329, G_r = Index of the reference material of the reference; ethanol was used, and the index is 1.3611.[256; 257]

3.12.3 Electrochemical Impedance Spectroscopy (EIS)

EIS is an electrochemical technique with applications in corrosion, biosensors, battery development, fuel cell development, paint characterization, sensor development, and physical electrochemistry. EIS can even be used to test the quality of food, Robinson *et al.*, [200]. The reason for this popularity is the high information content. EIS provides a more thorough understanding of an electrochemical system than any other electrochemical technique. Its principle aim is to measure the impedance between the current and the potential at a fixed DC potential during frequency scan with a fixed superimpose AC signal of small amplitude. The physical values are the phase (ϕ) shift and modulus (Z).

In cyclic voltammetry and other dynamic electroanalysis, an applied potential is either constant (potentiostatic) or changing (potentiodynamic) when ramped at a constant rate of $v = dE/dt$. However, in impedance, a small perturbing potential is applied across a cell or sample and changes in a cyclic sinusoidal manner and generates a current resulting from the over potential (η) caused by the small displacements of the potential from the equilibrium value. Because the potential is only perturbing, it has the advantage of minimizing the concentration change after the experiment. The induced current alternates because the voltage changes in a cyclic manner, and hence the term alternating current (AC). The term impedance is therefore a measure of the ability of a circuit to resist the flow of an alternating current (AC). It is synonymous to resistance (R) used in direct current (DC), which is defined by Ohm's law (eq. 17) as the ratio between voltage (E) and current (I)



$R = \frac{E}{I}$

(17)

EIS is an excellent, non-destructive, accurate and rapid insitu technique for examining processes occurring at the electrode surface. During a controlled-potential EIS experiment, the electrochemical cell is held at equilibrium at a fixed DC potential, and a small amplitude (5–10 mV) AC wave form is superimposed on the DC potential to generate a response from the equilibrium position. The response to the applied perturbation, which is generally sinusoidal, can differ in phase and amplitude from the Z'' (usually, the positive y-axis correspond to $-Z'' = Z_{\text{real}}$), over a wide frequency range normally ranging from 100 kHz to 0.1 Hz. The Nyquist plot of impedance spectra includes a semicircle portion and a linear portion (but these is not always the case), with the former at higher frequencies corresponding to the electron transfer process and the latter at lower frequencies corresponding to the diffusion process (Figure 29). The electron transfer resistance (R_{ct}) at the electrode surface is equal to

the semicircle diameter, which can be used to describe the interface properties of the electrode (Figure 30)

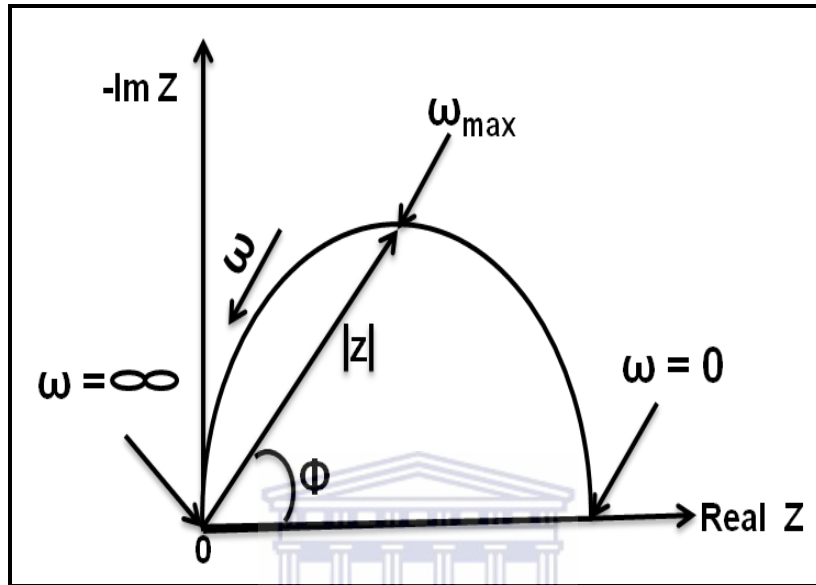


Figure 29. Nyquist plot.

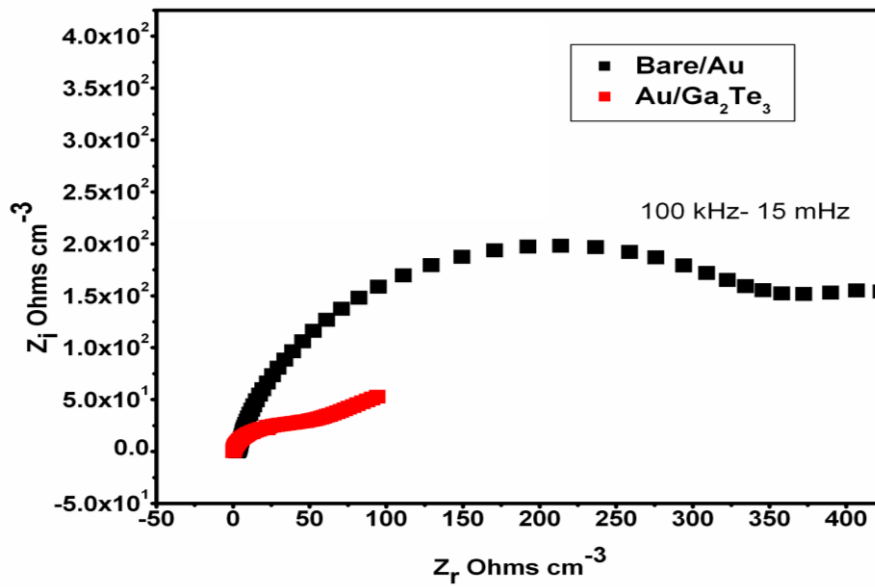


Figure 30. A typical Nyquist plot.

Another way of presenting impedance data is a Bode plot in which the logarithm of the absolute value of Z' (Z_{real}) and the phase angle (ϕ) are plotted against the logarithm of the frequency (f) (Figure 31). This can be plotted together or separately. Nyquist plots are more commonly displayed for historical reasons, the data is however often poorly resolved (particularly at high frequencies), and the explicit frequency dependence is not displayed in the plot. In contrast, bode plots directly displays the frequency dependence; in addition, the data is well resolved at all frequencies, since a logarithmic frequency scale is used. When the frequency of the AC waveform is varied over a wide range of frequency (ca about 10^{-4} and $> 10^6$ Hz), the impedance obtained for the system is a function of the operating frequency. Spectra of the resulting impedance at different frequencies do reveal the different electrochemical kinetics involved in the system. While dipolar properties are manifest at the high frequency regions, bulk and surface properties will be evident at intermediate and low frequencies respectively. The total impedance of a system is determined by the impedances of the various components of the electrochemical cell; for example, electron transfer kinetics, diffusion and passivating layers. The relative contribution of the various components typically varies with frequency; for example, electron transfer. Measuring impedance over a wide frequency range allows processes with different time scales such as electron transfer, mass transport and chemical reaction to be detected within the same experiment. Impedance data is commonly analyzed by fitting it to an equivalent circuit model. The frequently used circuit, called the Randles equivalent circuit (Figure 32) is composed of different elements such as resistors, capacitors, and inductors joined in series or in parallel. Figure 31 below shows the impedance diagram for the real impedance (x-axis) and imaginary impedance- (y-axis) with low frequency data being on the right side of the plot and higher frequencies are on the left.

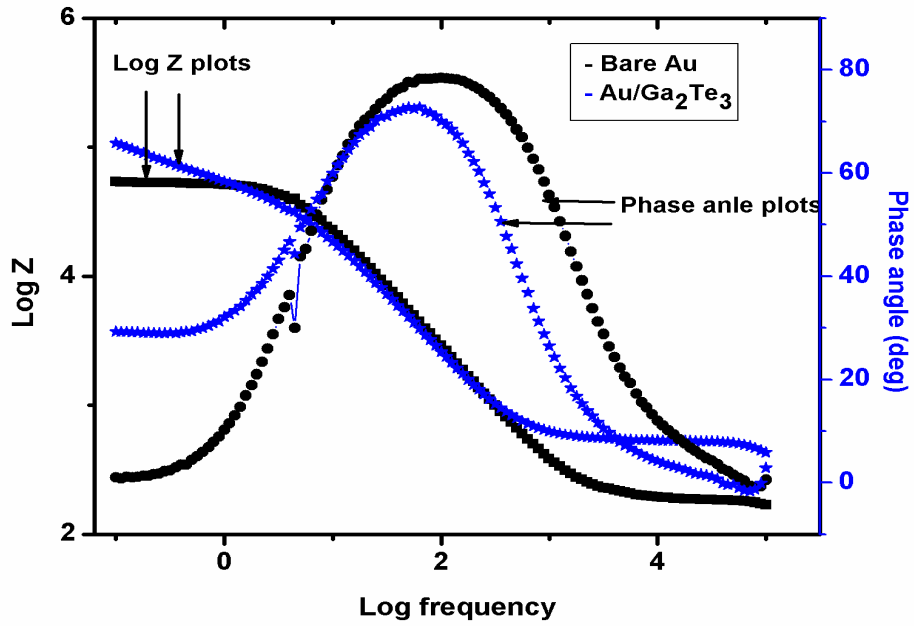


Figure 31. Typical Bode plot of bare Au and Au/3MPA- Ga₂Te₃ in PBS showing variation of impedance and phase angle with changes in frequency.

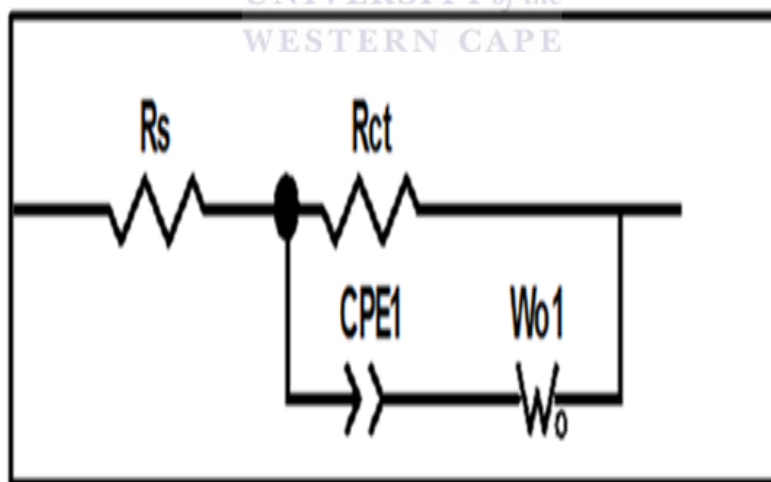


Figure 32. Equivalent circuit of a capacitor and a resistor in parallel at one time constant.

3.12.3.1 Electrical circuit elements

Electrochemical Impedance plots often contain several time constants, but often only a portion of one or more of their semicircles is seen. The shape varies depending on the equivalent electrical circuits for the system. Figure 32 is a typical equivalent circuit of a capacitor and a resistor in parallel.

Any electrochemical cell can be represented in terms of an equivalent electrical circuit that comprises a combination of resistances and capacitances. There could also be contribution of inductances at very high frequencies. Contributions to the resistance of a cell are the solution resistance (R_s), the charge transfer resistance (R_{ct}), Warburg impedance (Z_w) while contribution to the capacitance could be as a capacitor (C) and constant phase element (CPE). These elements are described briefly underneath.

Solution resistance (R_s): The solution resistance is the resistance between the working electrode and the reference electrode. This is indicated as a small offset on the real impedance axis. It is measured at high frequency intercept near the origin of the Nyquist plot. The resistance of an ionic solution depends on the ionic concentration and type of ions the electrolyte is made up, temperature and the geometry of the area in which current is carried. In a bounded area with area A and length l carrying a uniform current the resistance is defined as:

$$R = \rho \frac{l}{A} \quad (18)$$

The conductivity of the solution, ρ , is more commonly used in solution resistance calculations. Its relationship with solution resistance is:

Charge transfer resistance (R_{ct}): This is the resistance associated with the charge transfer mechanisms for electrode reactions.

It is the resistance to electron transfer at the electrode interface. It is deduced from the kinetically controlled electrochemical reaction at low over-potentials. The equation for Charge transfer resistance below is deduced from Bard and Faulkner.

$$R_{ct} = \frac{RT}{nFI_o} \quad (19)$$

From this equation the exchange current density (I_o) can be calculated when R_{ct} is known. The charge transfer resistance is estimated from the diameter of the semicircular region on the real impedance axis of the Nyquist plot. When the chemical system is kinetically sluggish, the R_{ct} will be very large and may display a limited frequency region where mass transfer is a significant factor. However, if the system is kinetically facile, then the mass transfer always plays a role and the semicircular region and R_{ct} is not well formed.

Warburg Impedance (ZW): This is the resistance associated with the diffusion of ions across the electrode/electrolyte interface. This impedance is associated with the difficulty of mass transport of electroactive species. Layers of ions at the electrode interface behave like an RC element (i.e. a resistor and a capacitor in parallel) and this produces infinite sum of RC elements called the Warburg impedance. It is characterised as a linear portion at an angle of 45° and slope of unity on the Nyquist plot and a slope of -0.5 on the Bode plot.

Capacitor (C): The capacitance (C) is the ability of an electrochemical system to store or retain charge. An electrical double layer exists on the interface between an electrode and its surrounding electrolyte. This double layer is formed as ions from the solution "stick on" the electrode surface. The potential at the terminals of this double layer (capacitor) is proportional to its charge. The impedance of a capacitor is given by the equation

$$Z_{(o)} = Z'' = \frac{1}{j\omega C} \quad (20)$$

Therefore; Z is the imaginary value, Z'' is Z real impedance, C is the capacitance and ω is the frequency

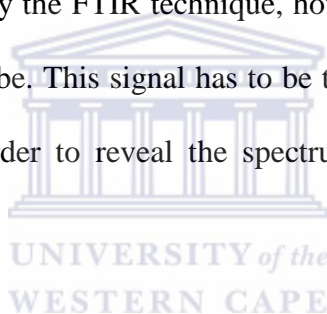
Constant phase element (CPE): A constant phase element is a non-intuitive circuit element that was invented while looking at the response of real-world systems. Often, a *CPE* is used in a model in place of a capacitor due to deviation of capacitance parameters from expected values. In some systems the Nyquist plot was expected to be a semicircle with the center on the x-axis. However, the observed plot may be an arc of a circle with the center being some distance below the x-axis. These depressed semicircles have been linked to a number of phenomena, depending on the nature of the system being investigated. This behaviour was traced to the non-homogeneity of the system or that there is some distribution (dispersion) of the value of some physical property of the system. The impedance of a *CPE* is represented by equation

$$CPE = Z = A(j\omega)^{-\alpha} = \frac{1}{(Cj\omega)^{-\alpha}} \quad (21)$$

This is similar to that of a capacitor except that the constant $A = 1/C$ (the inverse of the capacitance) and the exponent $\alpha = 1$ for a true capacitor. For a constant phase element, the exponent α is less than one. When $\alpha = 0.5$, a 45° line is produced on the complex plane graph and could be used for an infinite length of warburg element. During circuit fitting, the *CPE* is defined by two values, i.e., the capacitance, C , and the *CPE* exponent, α , which has a value between 0.5 and 1 for a non-ideal capacitor. If n equals 1, the equation is identical to that of a capacitor and smaller values can be related to surface roughness and in-homogeneities, which lead to frequency dispersion [240; 258].

3.12.4 Fourier Transform Infrared Spectroscopy (FTIR).

Infrared spectroscopy reveals information about the vibrational states of a molecule. Intensity and spectral position of IR absorptions allow the identification of structural elements of molecule. Among them are typical functional groups, hydrogen bonding, but also determination of conformations or even investigation of chemical reactions. Typical vibrations of functional groups make infrared spectroscopy also an important analytical tool. In the gas phase a rotational fine structure can often be observed from which the moment of inertia of the molecule can be determined. When a spectrum is recorded using a conventional, dispersive IR spectrometer, each data point reveals the transmitted light at the respective frequency. The signal provided by the FTIR technique, however, contains information about the complete spectrum of the probe. This signal has to be transformed from the time-domain into the frequency-domain in order to reveal the spectrum. This transformation is called Fourier transformation [239].



3.12.5 Raman spectroscopy

Raman spectroscopy is a spectroscopic technique based on inelastic scattering of monochromatic light, usually from a laser source. Inelastic scattering means that the frequency of photons in monochromatic light changes upon interaction with a sample. Photons of the laser light are absorbed by the sample and then reemitted. Frequency of the reemitted photons is shifted up or down in comparison with original monochromatic frequency, which is called the Raman effect. This shift provides information about vibrational, rotational and other low frequency transitions in molecules. Raman spectroscopy can be used to study solid, liquid and gaseous samples. The Raman effect is based on molecular deformations in electric field E determined by molecular polarisability α . The laser

beam can be considered as an oscillating electromagnetic wave with electrical vector E . Upon interaction with the sample it induces electric dipole moment $P = \alpha E$ which deforms molecules. Because of periodical deformation, molecules start vibrating with characteristic frequency ν_m .

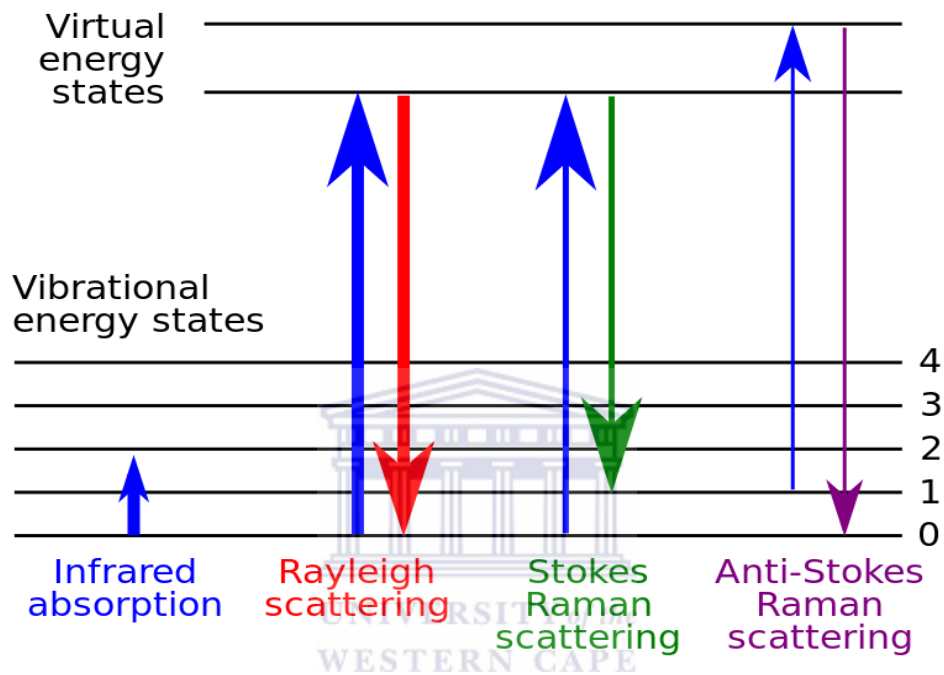
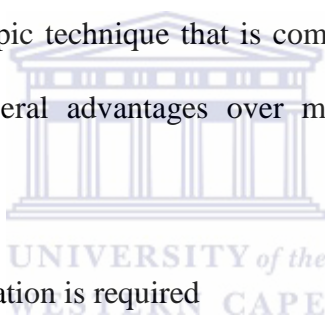


Figure 33. Energy-level diagram showing the states involved in Raman signal. The line thickness is roughly proportional to the signal strength from the different transitions.

Amplitude of vibration is called a nuclear displacement. In other words, monochromatic laser light with frequency ν_0 excites molecules and transforms them into oscillating dipoles. Such oscillating dipoles emit light of three different frequencies (Figure 33) when: **1)** A molecule with no Raman-active modes absorbs a photon with the frequency ν_0 . The excited molecule returns back to the same basic vibrational state and emits light with the same frequency ν_0 as an excitation source.

This type of interaction is called an elastic **Rayleigh scattering**. **2)** A photon with frequency ν_0 is absorbed by a Raman-active molecule which at the time of interaction is in the basic vibrational state. Part of the photon's energy is transferred to the Raman-active mode with frequency ν_m and the resulting frequency of scattered light is reduced to $\nu_0 - \nu_m$. This Raman frequency is called **Stokes frequency**, or just "Stokes". **3)** A photon with frequency ν_0 is absorbed by a Raman-active molecule, which, at the time of interaction, is already in the excited vibrational state. Excessive energy of excited Raman active mode is released, molecule returns to the basic vibrational state and the resulting frequency of scattered light goes up to $\nu_0 + \nu_m$. This Raman frequency is called **Anti-Stokes frequency**, or just "Anti-Stokes"

Raman scattering is a spectroscopic technique that is complementary to infrared absorption spectroscopy. Raman offers several advantages over mid-IR and near-IR spectroscopy, including:

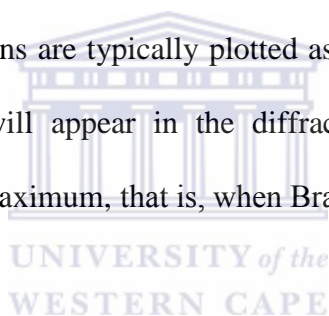


- Little or no sample preparation is required
- Water is a weak scatterer - no special accessories are needed for measuring aqueous solutions
- Water and CO₂ vapours are very weak scatterers - purging is unnecessary
- Inexpensive glass sample holders are ideal in most cases
- Fiber optics (up to 100's of meters in length) can be used for remote analyses
- Since fundamental modes are measured, Raman bands can be easily related to chemical structure
- Raman spectra are "cleaner" than mid-IR spectra - Raman bands are narrower, and overtone and combination bands are generally weak

- The standard spectral range reaches well below 400 cm^{-1} , making the technique ideal for both organic and inorganic species
- Raman spectroscopy can be used to measure bands of symmetric linkages which are weak in an infrared spectrum (e.g. -S-S-, -C-S-, -C=C-). [259; 260; 261]

3.12.6 X-ray diffraction spectroscopy (XRD)

English physicists Sir W.H. Bragg and his son Sir W.L. Bragg developed a relationship in 1913 to explain why the cleavage faces of crystals appear to reflect X-ray beams at certain angles of incidence (theta, θ). The variable d is the distance between atomic layers in a crystal, and the variable λ is the wavelength of the incident X-ray beam; n is an integer, Powder diffraction patterns are typically plotted as the intensity of the diffracted X-rays vs. the angle 2θ . Peaks will appear in the diffraction pattern at 2θ values when constructive interference is at a maximum, that is, when Bragg's Law (eq. 22) is satisfied.



$$n\lambda = 2d \sin \theta \quad (22)$$

This observation is an example of X-ray wave interference Roentgenstrahlinterferenzen, commonly known as X-ray diffraction (XRD), and was direct evidence for the periodic atomic structure of crystals postulated for several centuries (Figure 34).

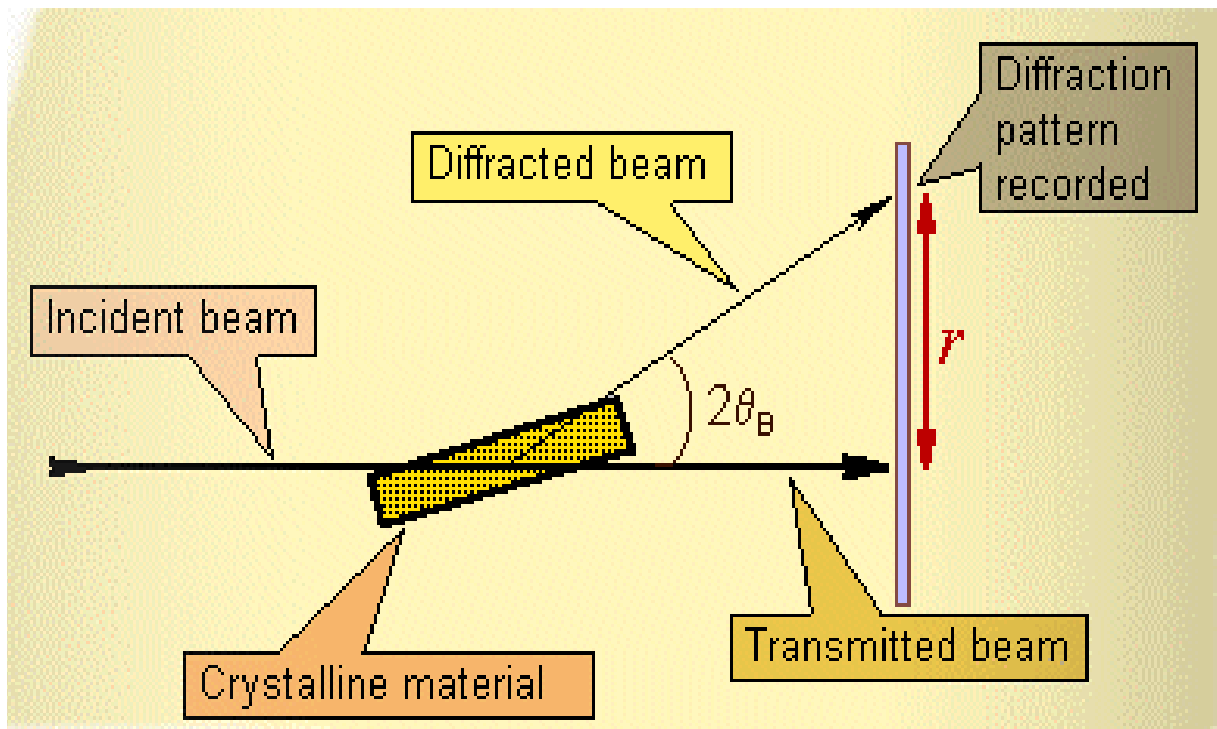
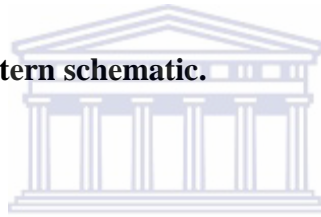


Figure 34. X-ray diffraction pattern schematic.



X-ray diffraction spectroscopy is a versatile non destructive technique that reveals detailed information about the chemical composition and crystallographic structure of natural and synthetic compounds. A crystalline lattice is a regular three dimensional distribution (cubic, rhombic) of atoms in space. The atoms are arranged in such a manner that they form a series of parallel planes separated from one another by a distance (d), which varies according to the nature of the material. When a monochromatic x-ray beam with a wavelength lambda (λ) is projected onto a crystalline material at an angle theta (θ), diffraction occurs only when the distance travelled by the rays reflected from successive planes differs by a complete number of wavelengths. To calculate the size of the crystallite the Bragg's equation (eq. 23) is used;

$$d = \frac{0.94\lambda}{\beta \cos \theta} \quad (23)$$

The parameters are as mentioned in the paragraph above. From the given or acquired spectra of the crystallite, each crystalline substance has a unique X-ray diffraction pattern (Figure 3). The number of observed peaks is related to the symmetry of the unit cell (higher symmetry generally means fewer peaks). The d -spacings of the observed peaks are related to the repeating distances between planes of atoms in the structure. And finally, the intensities of the peaks are related to what kinds of atoms are in the repeating planes. The scattering intensities for X-rays are directly related to the number of electrons in the atom. Hence, light atoms scatter X-rays weakly, while heavy atoms scatter X-rays more effectively. These three features of a diffraction pattern: the number of peaks, the positions of the peaks, and the intensities of the peaks, define a unique, fingerprint X-ray powder pattern for every crystalline material. For example, the X-ray diffraction patterns of the as prepared 3MPA- Ga_2Te_3 are as shown in Figure 35.

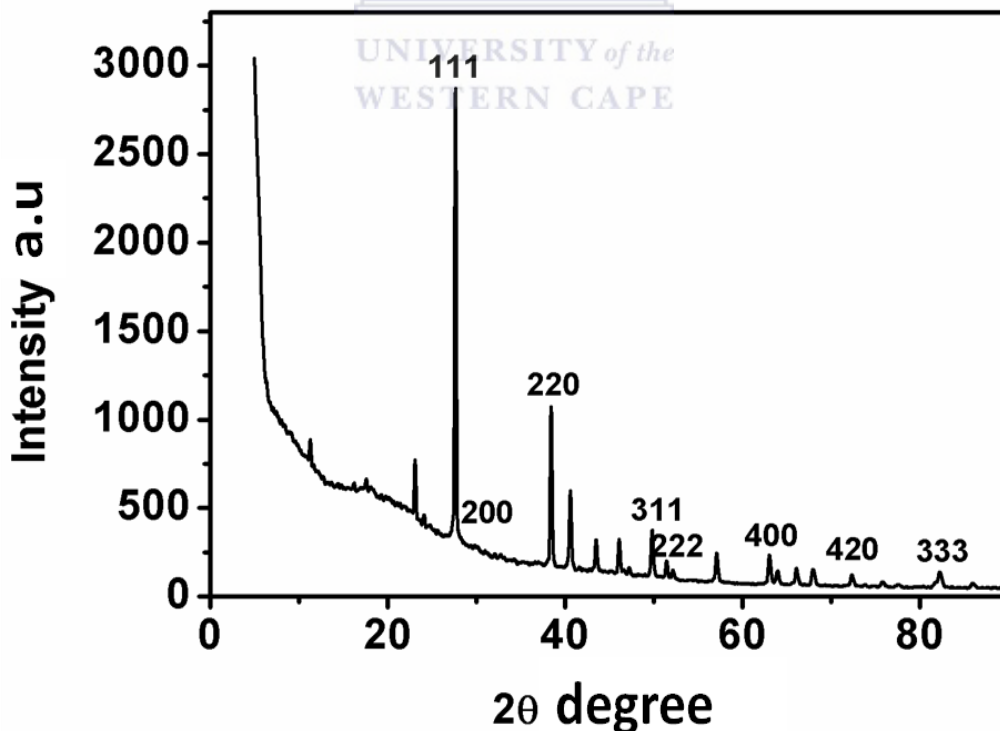


Figure 35. XRD spectra of 3MPA- Ga_2Te_3 showing lattice patterns and phase angles.

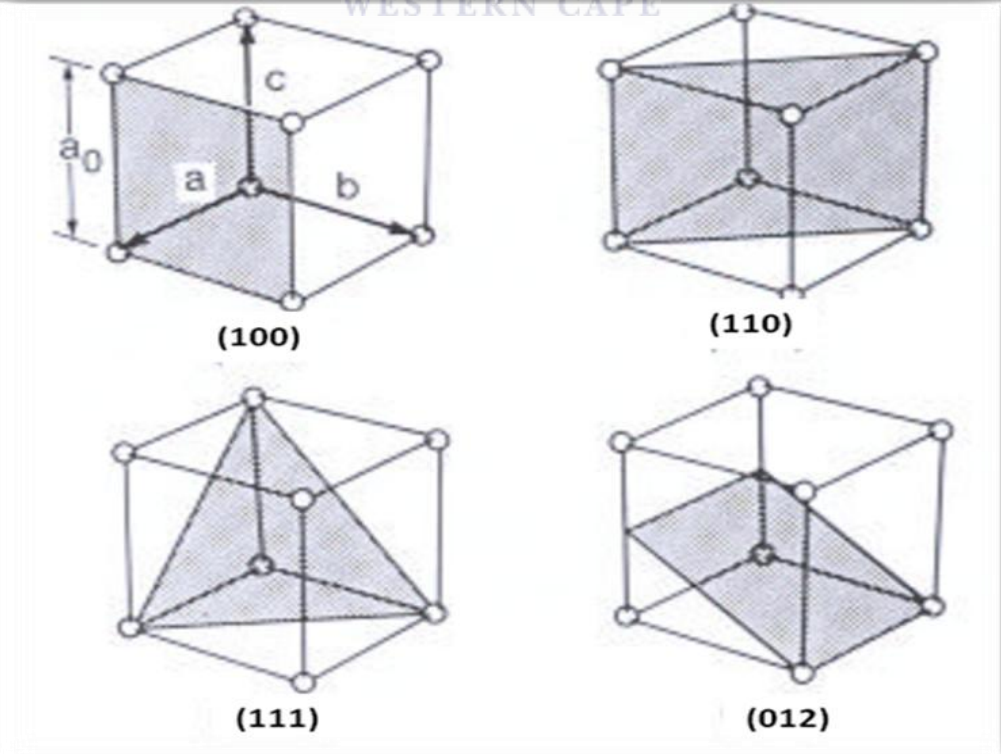
From the spectra it can be noted that the relative peak intensities of the nanodots differ magnificently this can be due to several reason and large cell unit can be one of them. X-ray powder diffraction is a powerful tool for characterizing the products of a solid state synthesis reaction. At the simplest level, diffraction patterns can be analyzed for phase identification (determining what crystalline substances are present in a given sample). More quantitatively, the peak positions can be used to refine the *lattice parameters* for a given unit cell. Unit cells in three-dimensional repeating structures have different shapes based upon the symmetry of the structure. In all cases, the unit cells are parallelepipeds, but the different shapes arise depending on restrictions placed on the lengths of the three edges (a , b , and c) and the values of the three angles (θ , λ , and β). The seven different unit cell shapes or seven crystal systems that result from these restrictions are listed below in Table 5.

3.12.6.1 Applications of XRD

- XRD is a non-destructive technique
- To identify crystalline phases and orientation
- To determine structural properties:
 - Lattice parameters (10^{-4} Å), strain, grain size,
 - expitaxy, phase composition, preferred orientation
 - (Laue) order-disorder transformation, thermal expansion
- To measure thickness of thin films and multi-layers*
- To determine atomic arrangement
- Detection limits: ~3% in a two phase mixture; can be ~0.1% with synchrotron radiation.[262; 263; 264; 265]

Table 5. The seven crystal systems and the restrictions placed on the lattice parameters of the unit cell.

Crystal system	Lattice parameter restrictions
Cubic	$a = b = c$ $\alpha = \beta = \gamma = 90^\circ$
Tetragonal	$a = b \neq c$ $\alpha = \beta = \gamma = 90^\circ$
Orthorhombic	$a \neq b \neq c$ $\alpha = \beta = \gamma = 90^\circ$
Monoclinic	$a \neq b \neq c$ $\alpha = \beta = \gamma \neq 90^\circ$
Triclinic	$a \neq b \neq c$ $\alpha \neq \beta \neq \gamma \neq 90^\circ$
Hexagonal	$a = b \neq c$ $\alpha = \beta = 90^\circ; \gamma = 120^\circ$
Trigonal	$a = b \neq c$ $\alpha = \beta = 90^\circ; \gamma = 120^\circ$



3.12.7 X-Ray Photoelectron Spectroscopy (XPS)

X-ray photoelectron spectroscopy (XPS) also known as electron spectroscopy for chemical analysis (ESCA) is a technique for analyzing the surface chemistry of a material. The technique is used to measure the elemental composition, empirical formula, chemical state and electronic state of the elements within a material. XPS spectra are acquired by irradiating a solid surface with a beam of X-rays and in parallel measuring the kinetic energy and electrons that are emitted from the top 1 - 10 nm of the material being analysed. A photoelectron spectrum is acquired by counting ejected electrons over a wide range of electron kinetic energies, Figure 36. Peaks are observed in the spectrum from atoms emitting electrons of a particular characteristic energy.

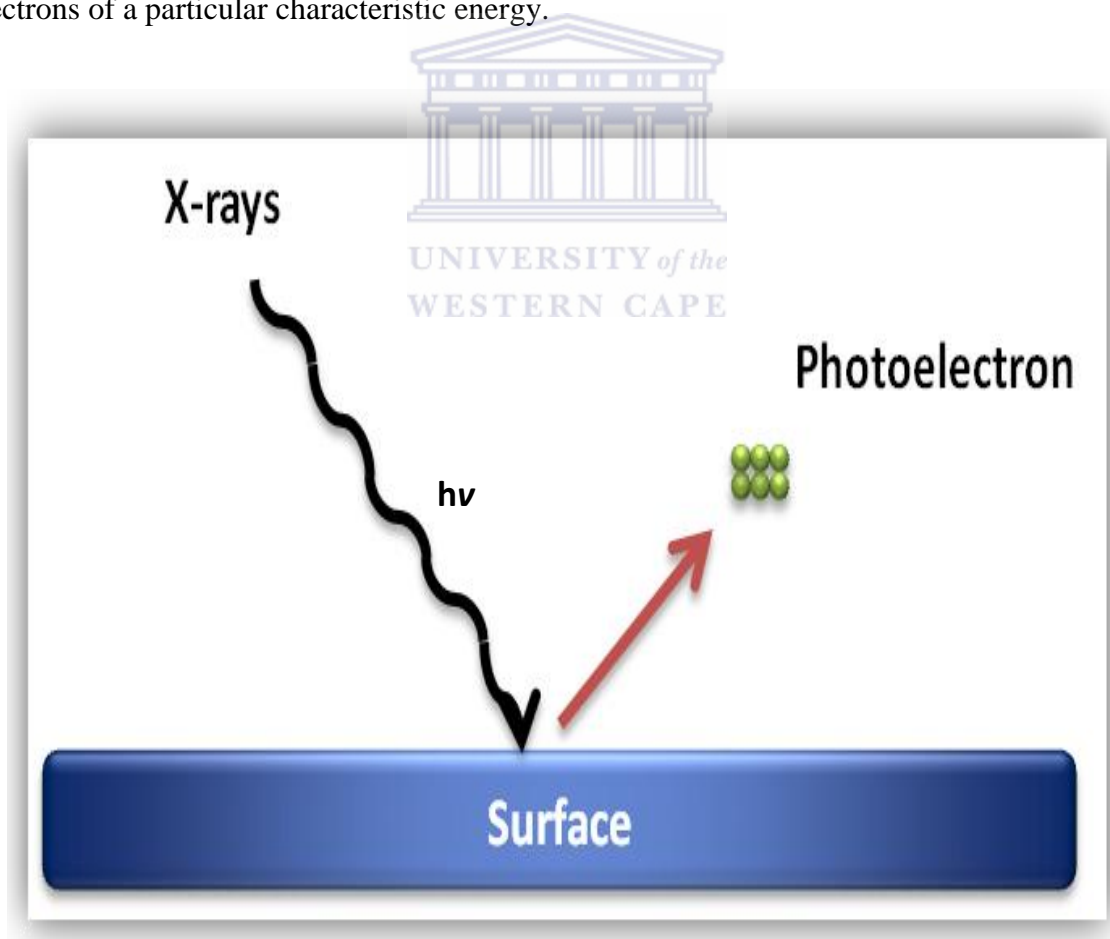


Figure 36. Ejection of photoelectrons.

The energies and intensities of the photoelectron peaks enable identification and quantification of all surface elements (except hydrogen). There is a high increase for material performance as is the importance for surface engineering. Problems associated with modern materials can be solved by understanding the chemical and physical interactions that occur at the surface or at the interfaces of a material's layers. Surface chemistry will influence such factors as corrosion rates, catalytic activity, adhesive properties, wettability, contact potential and failure mechanisms.

The material's surface is the point of interaction with the external environment and other materials. Therefore, surface modification can be used in a wide variety of applications to alter or improve the performance and behaviour of a material. XPS can be used to analyze the surface chemistry of a material after an applied treatment such as fracturing, cutting or scraping. From non-stick cookware coatings to thin-film electronics and bio-active surfaces, XPS is the standard tool for surface material characterization.

3.12.7.1 The Photoemission Process

When an atom or molecule absorbs an X-ray photon, an electron can be ejected. The kinetic energy (KE) of the electron depends upon the photon energy ($h\nu$) and the binding energy (BE) of the electron (i.e., the energy required to remove the electron from the surface), Figure 37.

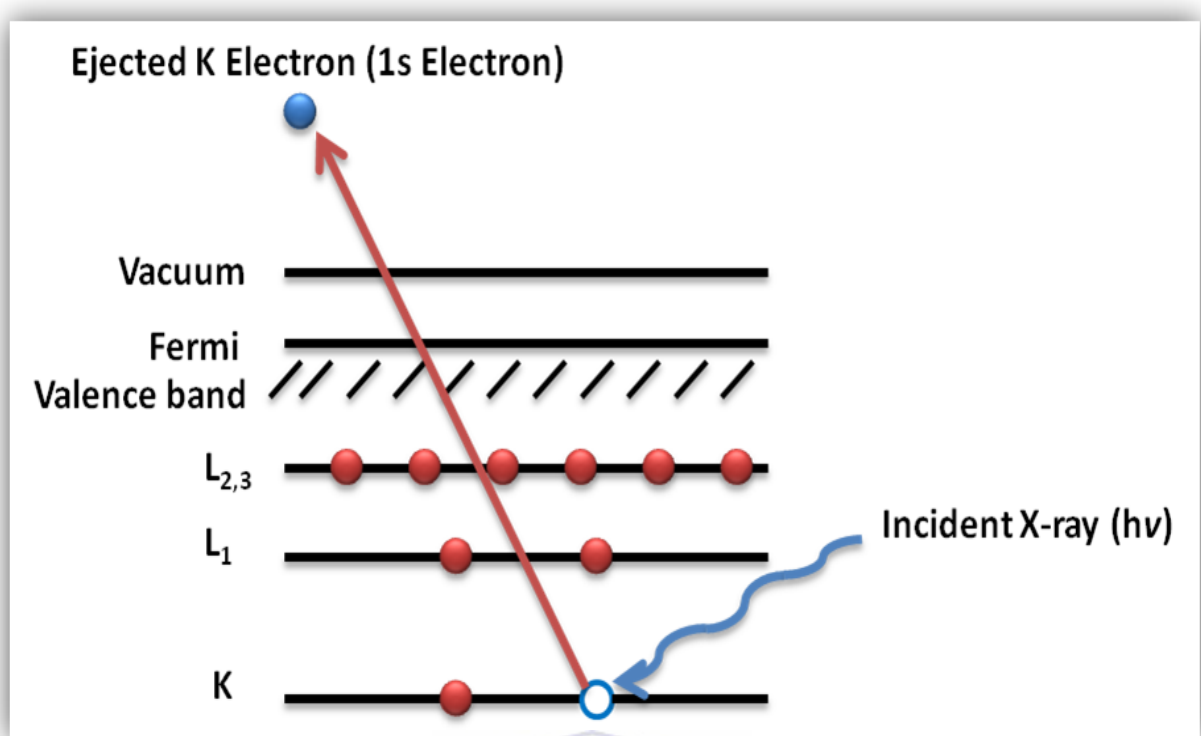


Figure 37. The photoemission process involved for XPS surface analysis.

The round circles represent electrons and the bars represent energy levels within the material being analyzed. The equation governing the process is: P E

$$KE = h\nu - BE \quad (24)$$

By measuring the kinetic energy of the emitted electrons, it is possible to determine which elements are near a material's surface, their chemical states and the binding energy of the electron. The binding energy depends on several factors, such as the following:

- The element from which the electron is emitted.
- The orbital from which the electron is ejected
- The chemical environment of the atom from which the electron was emitted.

XPS is a quantitative technique because the cross-section for the emission of a photoelectron is not dependent upon the chemical environment of the atom.

3.12.7.2 Spectroscopy

To demonstrate an XPS spectrum, a survey spectrum of 3 MPA-Ga₂Te₃ quantum dots was produced using a wide energy range (Figure 38). The spectrum shows elemental Ga, Te, S, C as well as the O peaks, which are the main components of the nanodots.

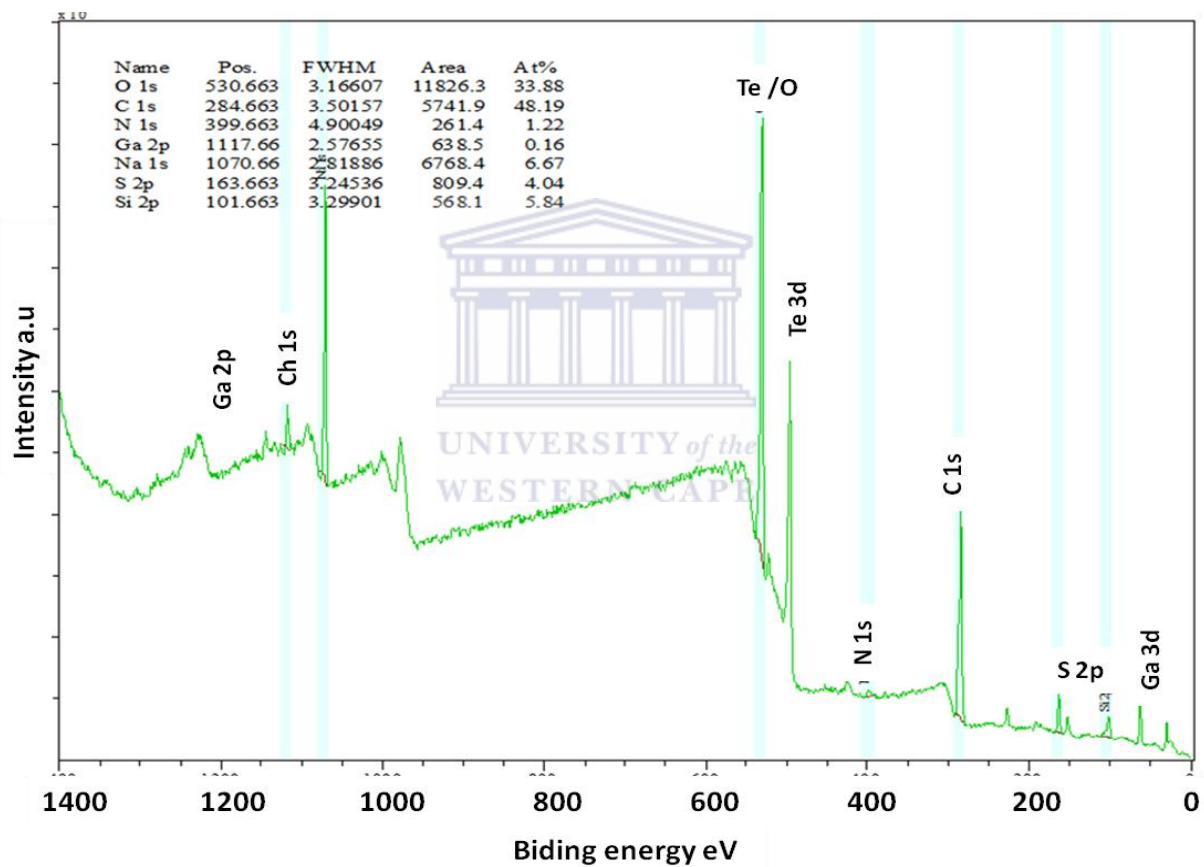


Figure 38. Spectrum from 3 MPA-Ga₂Te₃ showing various sulphur, gallium, oxygen and carbon peaks.

There is a significant background beneath the peaks in the spectrum, which is caused by electrons that are inelastically scattered before leaving the sample surface. Such scattering reduces the kinetic energy of the electrons and reduces intensity from the peaks. The background must be removed from the spectrum before quantifying the spectrum see Figure 39 below.

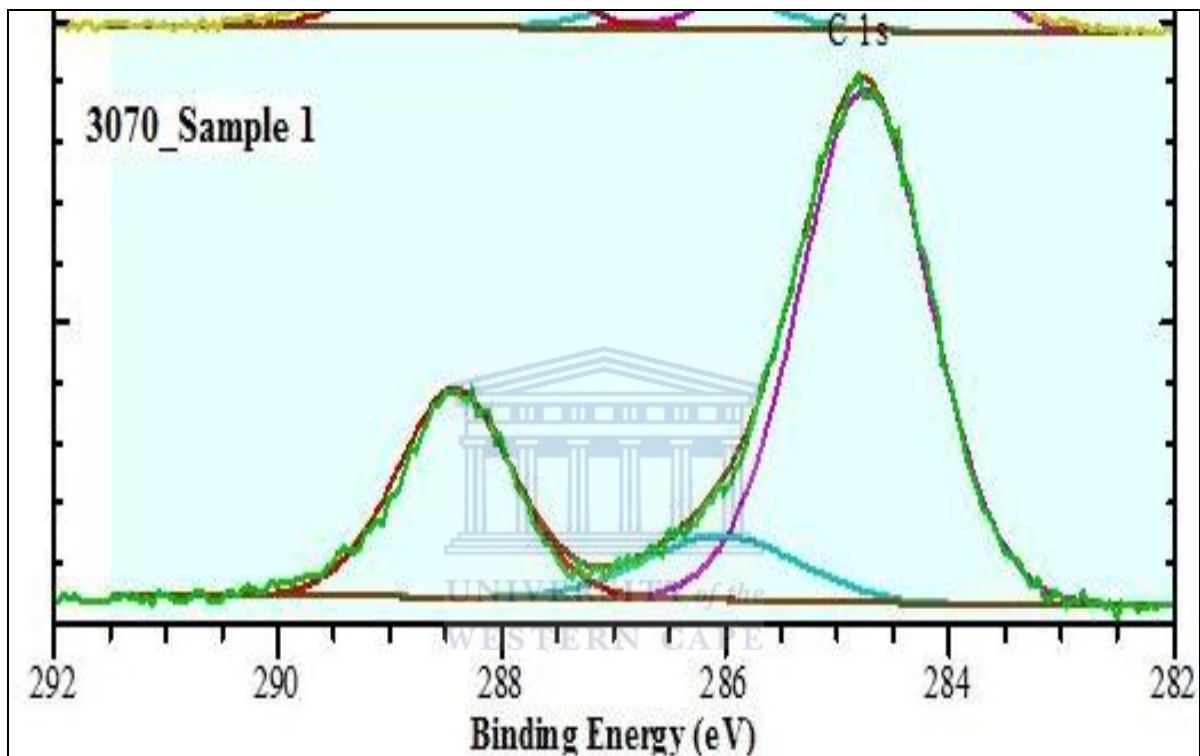


Figure 39. The C 1s region of the XPS spectrum from spin-cast and sheet 3 MPA- Ga_2Te_3 . Carbon is present in three distinct chemical states.

It is also possible to determine chemical states from an XPS spectrum. The C 1s region of the XPS spectrum from Ga_2Te_3 is shown in Figure 39. The method of preparation was a spin cast the carbon atoms are present in three chemical states, which are reflected in the three peaks of the XPS spectrum above.[266; 267; 268]

3.13 Microscopic techniques

3.13.1 High resolution transmission electron microscopy

Nanotechnology materials enable scientists to improve bulk physical properties for different applications and, with the resulting products, open new markets for the nanotechnology industry. The physical properties of nanotechnology materials are strongly correlated with their crystalline structure. It is, however, the real structure complete with interfaces and defects that is of importance and not just the ideal crystalline structure. Hence a thorough understanding of interfaces and defects is required to be able to correlate microscopic structures with macroscopic physical properties. High resolution transmission microscopy which is an imaging mode of the transmission electron microscope that allows the imaging of the crystallographic structure of a sample at an atomic scale becomes a valuable tool to study nanoscale properties of crystalline material such as semiconductors and metals. HRTEM allows the direct imaging of nanoparticles and provides more information on the quality of individual particles. Useful information about the morphology of a material include its size, shape and the arrangement of the particles which make up the specimen as well as their relationship to each other on the scale of atomic diameters. The crystallographic information includes the arrangement of atoms in the specimen and the degree of order and detection of atomic scale defects in areas a few nanometers in diameter. This technique can therefore be used to determine whether particles that make up the specimen are either dispersed or agglomerated. Coupled with energy dispersive spectrometric technique, HRTEM can further give the elemental composition of a sample and their respective ratios. A typical example is the quantum dots used in our system which were characterised using the technique.[269; 270; 271; 272]

3.13.2 Scanning Electron Microscopy (SEM)

A scanning electron microscope (SEM) uses an electron microscope to image samples by scanning it with a high-energy beam of electrons in a raster scan pattern. The electrons interact with the atoms that make up the sample producing signals that contain information about the sample's surface topography, composition, and other properties such as electrical conductivity. In a typical SEM, an electron beam is thermionically emitted from an electron gun fitted with a tungsten filament cathode. Tungsten is normally used in thermionic electron guns because it has the highest melting point and lowest vapour pressure of all metals, thereby allowing it to be heated for electron emission, and because of its low cost. When the primary electron beam interacts with the sample, the electrons lose energy by repeated random scattering and absorption within a teardrop-shaped volume of the specimen known as the interaction volume, which extends from less than 100 nm to around 5 μm into the surface. The size of the interaction volume depends on the electron's landing energy, the atomic number of the specimen and the specimen's density. The energy exchange between the electron beam and the sample, results in the reflection of high-energy electrons by elastic scattering. All samples must also be of an appropriate size to fit in the specimen chamber and are generally mounted rigidly on a specimen holder called a specimen stub. Several models of SEM can examine any part of a 6-inch (15 cm) semiconductor wafer, and some can tilt an object of that size to 45°. For SEM, a specimen is normally required to be completely dry, since the specimen chamber is at high vacuum. Hard, dry materials such as wood, bone, feathers, dried insects or shells can be examined with little further treatment, but living cells and tissues and whole, soft-bodied organisms usually require chemical fixation to preserve and stabilize their structure [273; 274]. The data was analyzed using associated EDAX Genesis 2000 software.

3.13.3 Atomic force microscopy (AFM)

The atomic force microscope is an instrument that can analyze and characterize surfaces of samples at a microscope level (from 100 μm to $< 1 \mu\text{m}$). The instrument was invented by Gerd Binnig in 1986 (Figure 40) to overcome the main limitation of scanning tunnelling microscope that it could only image materials that conduct tunnelling current.

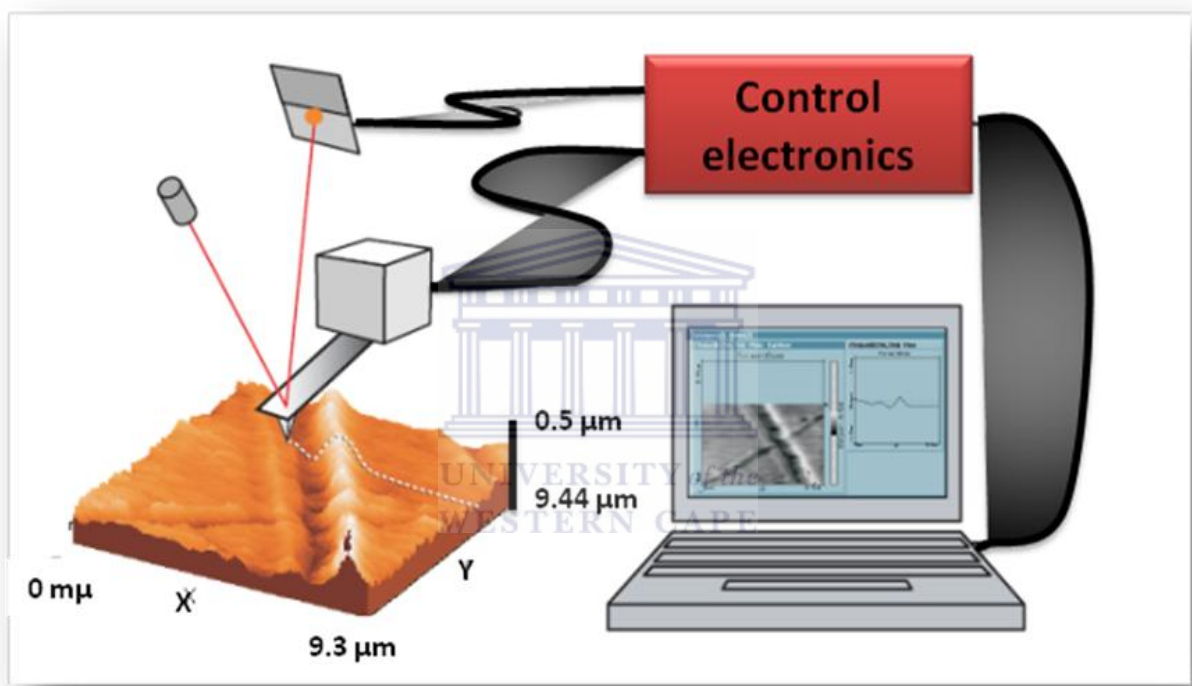


Figure 40. AFM schematic system with sample topography.

In AFM imaging, a sharp tip, usually a few microns long and less than 100 \AA is brought into contact or in a very close proximity with the sample being imaged. The tip, normally located at the end of a 100 to 200 μm long cantilever scans the sample beneath it. During scanning, some forces either attract or repel the tip, causing deflections that are recorded and processed using imaging software. The resulting image is a topographical representation of the sample being imaged. The main advantage of AFM is that it can measure a number of characteristic properties of a sample that other forms of microscopy cannot give.

For instance, AFM provides extraordinary topographic contrast height measurements with unobstructed surface feature as opposed to scanning electron microscope. Whereas HRTEM gives 2 dimensional profiled images viewed from cross-sectioned samples, AFM yields 3 dimensional images with in-depth information without expensive sample preparation. Unlike scanning tunnelling microscopy, SEM and HRTEM, AFM does not require the sample to be conductive. AFM can also be used to study a wide variety of samples i.e. plastics, metals, glasses, semiconductors, biological samples such as cell walls and bacteria.[275; 276; 277]

3.14 Drop shape analyser

Contact angle is one of the common ways to measure the wettability of a surface or material, Figure 41. Wetting refers to the study of how a liquid deposited on a solid (or liquid) substrate spreads out or the ability of liquids to form boundary surfaces with solid states. The wetting, as mentioned before is determined by measuring the contact angle, which the liquid forms in contact with the solids or liquids. The wetting tendency is larger, the smaller the contact angle or the surface tension is. A wetting liquid; is a liquid that forms a contact angle with the solid which is smaller than 90° . A non-wetting liquid creates a contact angle between 90° and 180° with the solid.

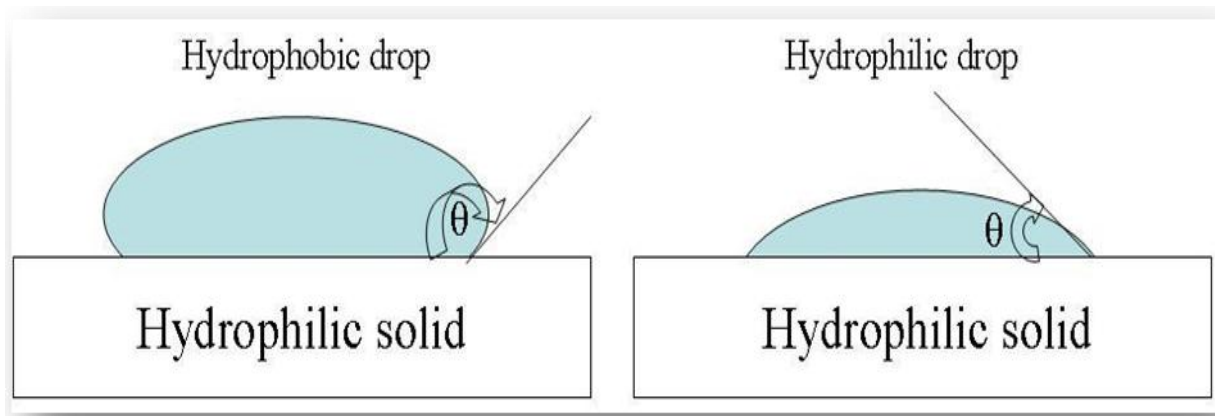


Figure 41. Hydrophobic surface (left) and hydrophilic surface (right) [279].

- The smaller the contact angle - cohesive forces are weaker than adhesive forces and molecules of the liquid tend to interact more with solid molecules than liquid molecules.
- The larger the contact angle - cohesive forces are stronger than adhesive forces and the molecules of the liquid tend to interact more with each other than with the solid molecules.

3.14.1 Thermodynamics

Thomas Young (13 June 1773 – 10 May 1829) proposed treating the contact angle of a liquid with a surface as the mechanical equilibrium of a drop resting on a plane solid surface under the restraints of three surface tensions: γ_{lv} (at the interface of the liquid and vapour phases), γ_{sl} (at the interface of the solid and liquid phases) and γ_{sv} (at the interface of the solid and vapour phase), Figure 42. This led to *Young's equation*:



$$\gamma_{sv} - \gamma_{sl} = \gamma_{lv} \cos \theta \quad (25)$$

This equation is deceptively simple, but there are a few difficulties with it because of the definitions of the surface tension of the solid-vapour and solid liquid phases.

Another approach avoids specifying the field of intermolecular forces between solid and liquid and instead offers a thermodynamic solution. This led to Young and Dupre's equation which introduces the reversible work of adhesion of liquid and solid and its relation to the surface tension between liquid and vapour phases and the contact angle:

$$W_A = \gamma_{lv} (1 - \cos \theta) \quad (26)$$

where, W_A is the reversible work of adhesion of the liquid to the solid when coated with an adsorbed film of the saturated vapour.

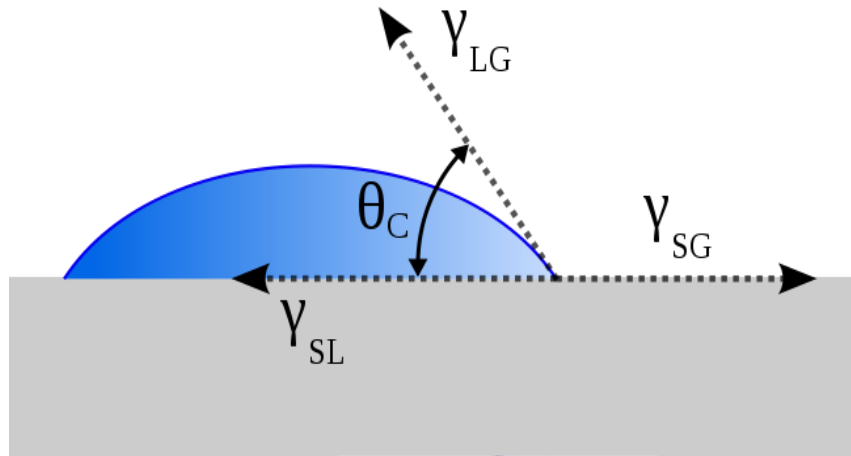


Figure 42. Demonstration of the $\theta/2$ method (Young's modulus) [278; 279].

3.14.2 Applications

The interest in contact angles is because it plays a significant role in a number of technological, environmental and biological phenomena. Water imbibition into porous media theory has been shown to have a multidisciplinary validity in food, soil physics, geology, printings and more. Imbibition of a liquid by a porous solid is a phenomenon highly dependent on wetting. Capillary imbibition is a mechanism that plays a significant role during rehydration of dry food particles that are considered as porous media. Imbibition is highly dependent on the wettability of the porous media, which is usually determined by measuring contact angles which liquids form with the solid [278; 279].



CHAPTER 4

Results and discussion 1

Characterisation of 3MPA-Ga₂Te₃ quantum dots

UNIVERSITY *of the*
WESTERN CAPE

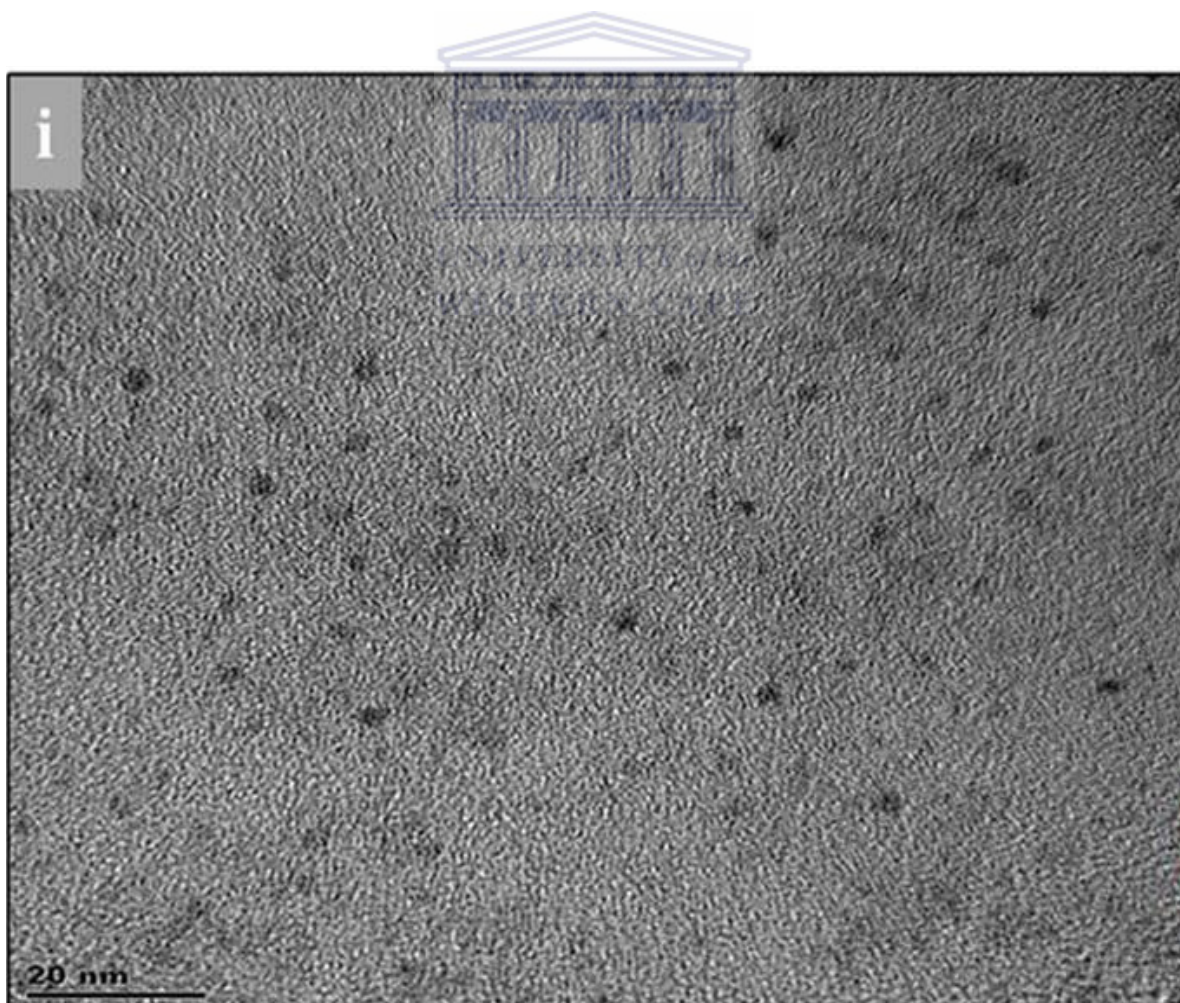
4.1 Introduction

Investigation of materials at nanoscale has become one of the major priorities in the research world. These nanomaterials have unique magnetic and electronic properties which can be manipulated easily. Their unique properties give researchers a great platform to explore and investigate their versatile applications in different fields (e.g. electronic, molecular, analytical chemistry etc.). Zero dimensional semiconductors (Quantum dots) were found to possess these properties hence they were investigated in this project. Chalcogenide quantum dots, depending on the composition of the transition metal may exhibit structural vacancies that give rise to numerous electronic, structural and optical properties. For instance, semiconductors consisting of group II and VI elements are typically characterised by sp^3 hybridised bonding, accommodating all eight electrons in each cation-anion pair. These semiconductors therefore exhibit valence match and crystallize to form either zinc blende or wurzite structures. For semiconductors consisting of group III and VI however, the sp^3 hybridised bonding is difficult to form and their crystalline structure stabilises by forming structural vacancies. The aim in this chapter is to discuss the morphological structure, crystallinity, conductivity, composition and photoluminescence of the Ga_2Te_3 quantum dots by characterising them using several microscopic and spectroscopic techniques.

4.2 Atomic force and electron microscopy (AFM, HR-TEM, TEM, STEM and SEM)

4.2.1 Characterisation of 3MPA-Ga₂Te₃ quantum dots

The structural morphology and particle size of the synthesised Ga₂Te₃ quantum dots were characterised using TEM, HR-TEM, SEM, STEM and AFM. HR-TEM was also used in determine the crystal structure of the quantum dots. Both the copper grid and the silicon grid were used as sample holders for the immobilisation of Ga₂Te₃ quantum dots. Images of the synthesised Ga₂Te₃ quantum dots were as observed in Figure 43, 44, 45, 46 and 47. The nanodots were well distributed on the surface of the copper grid, confirming the nature of the zero dimensional structures.



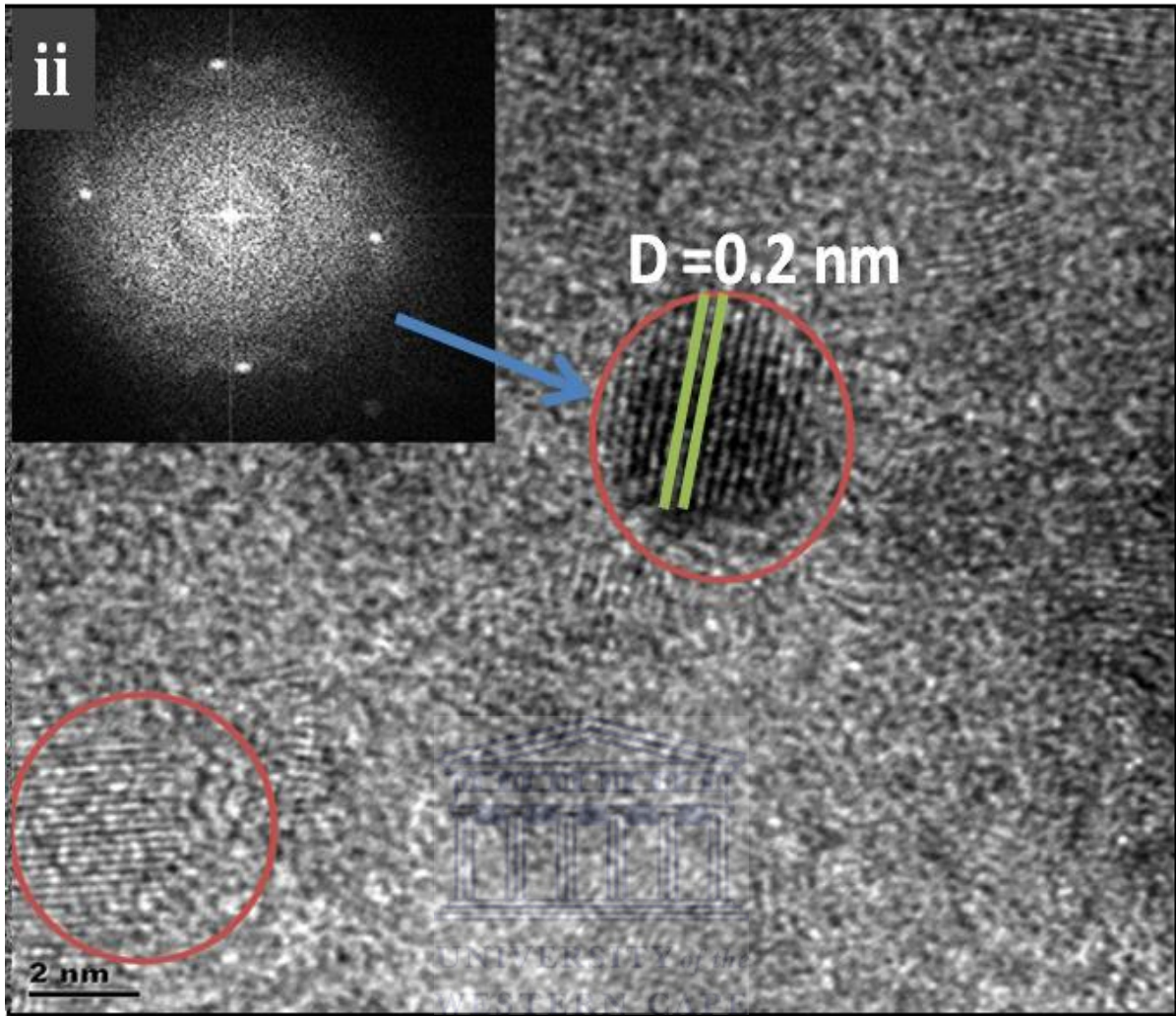
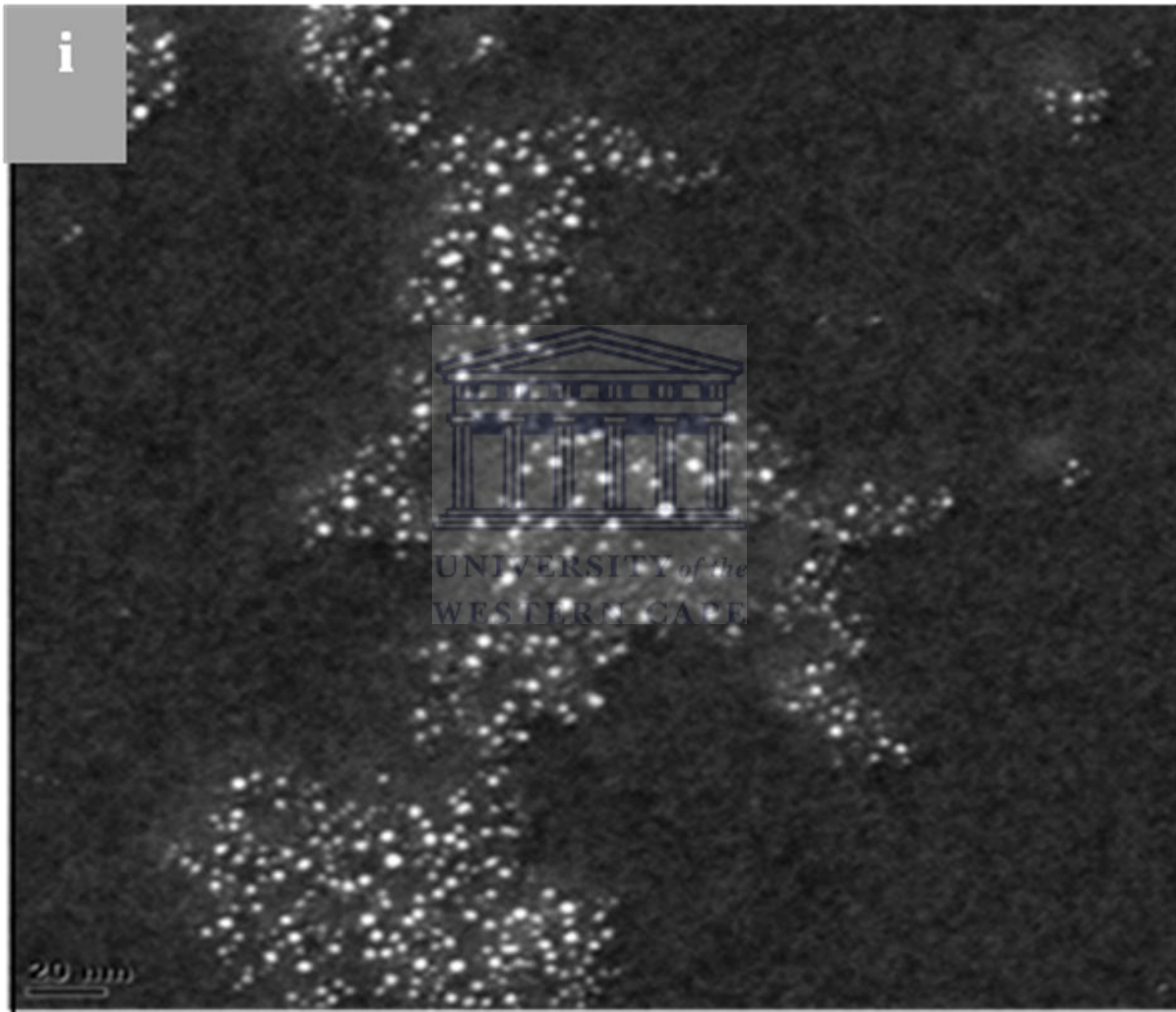


Figure 43. TEM (i), HRTEM (ii) and FFT (insert) images of 3MPA- Ga_2Te_3 .

Typical TEM and HRTEM images of the synthesised Ga_2Te_3 quantum dots with size distribution are as observed in Figure 43 (i and ii), From the TEM and HRTEM studies, the average diameter ($n = 10$) of the QDs was estimated to be 5 ± 0.5 nm. HRTEM images showed the uni-directional lattice fringes (d spacing 0.2 nm), confirming the mono-crystallinity of the material [280; 281]. FFT images are shown in Figure 43 (ii: insert), this images were obtained from the same areas as in TEM images (Figure 43 ii). The observed results from the FFT were in good agreement with that obtained from HRTEM, evident by mono-crystallinity of the nanodots.

Images and data obtained from the STEM (Figure 44 i) were in tally with the results acquired from HRTEM. SEM images also confirm the oval structure of the quantum dots and their particle size (Figure 44 ii). However, only bigger particles were observed (200 nm) in SEM due to lower sensitivity of the technique.



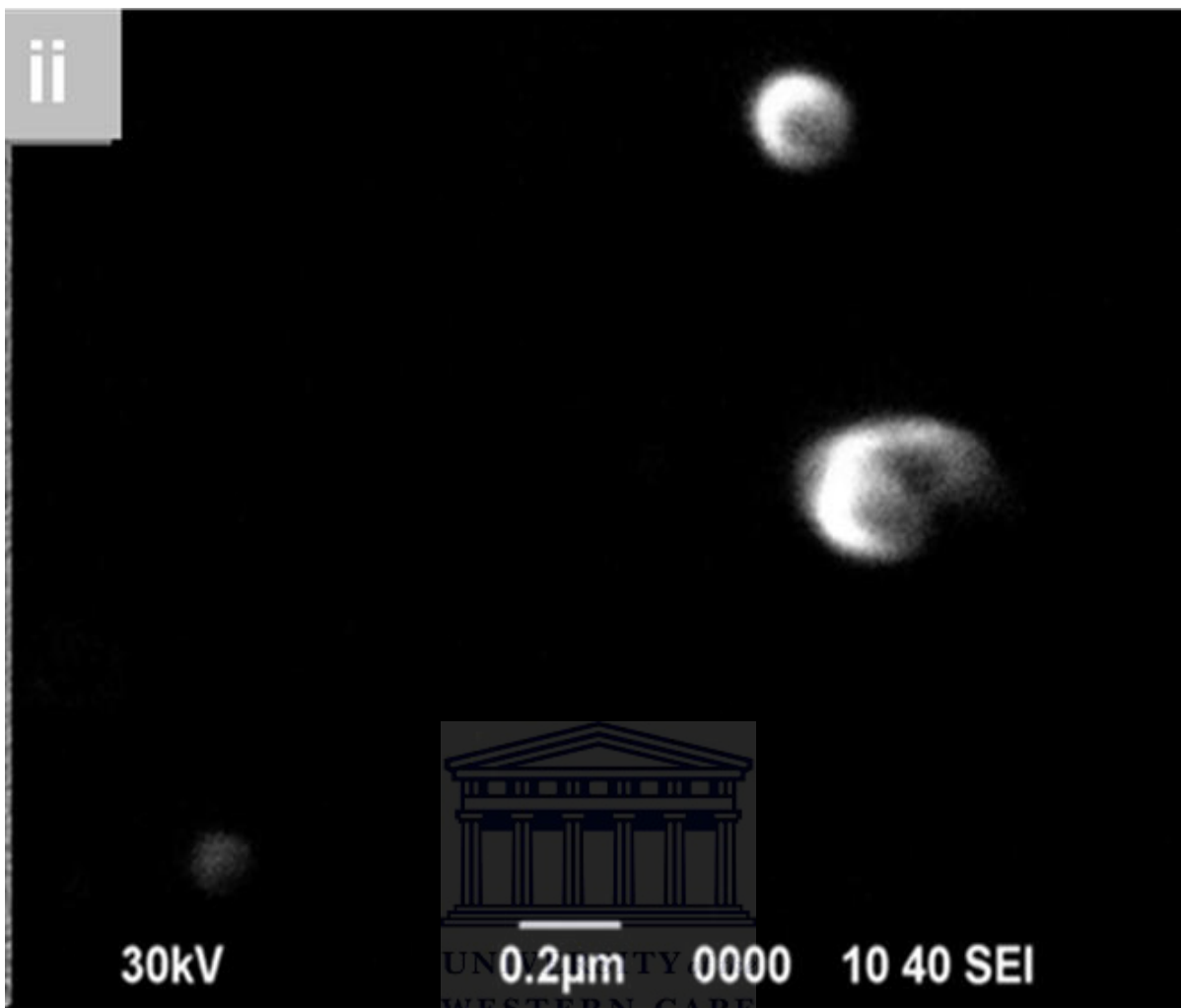
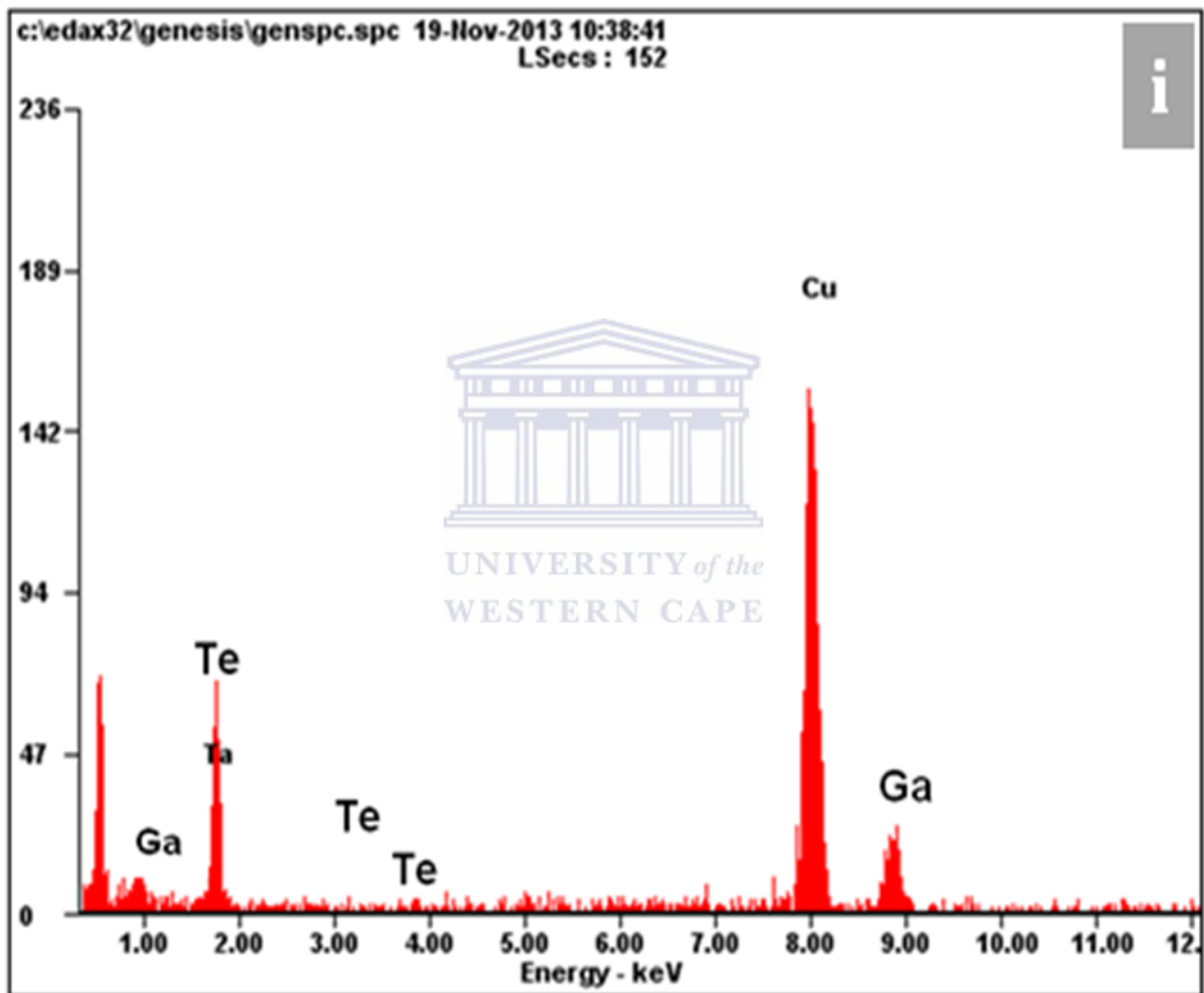


Figure 44. STEM (i) and SEM (ii) image of 3MPA- Ga₂Te₃ quantum dots.

The EDS and mapping analyses (Figure 45 i-ii) were used to quantify the nanomaterials. The energy-dispersive X-ray spectroscopy (EDS, Figure 45 i) analysis further confirm the presence of Ga and Te in Ga₂Te₃ quantum dots sample which are the main components of the material. Other metal (copper, Cu) was observed in the spectrum as a result of the sample preparation (sample stub) used in TEM/EDS analysis.

Mapping also confirmed the presence of the two elements in the as-synthesised Ga₂Te₃ quantum dots (Figure 45 ii-iv). From both the EDS and mapping the image intensity/density is almost proportional to the square of the Z number of elements (Ga: 69.72 g mol⁻¹ and Te: 127.60 g mol⁻¹) which also confirms the ratio of the metals been 2:1.



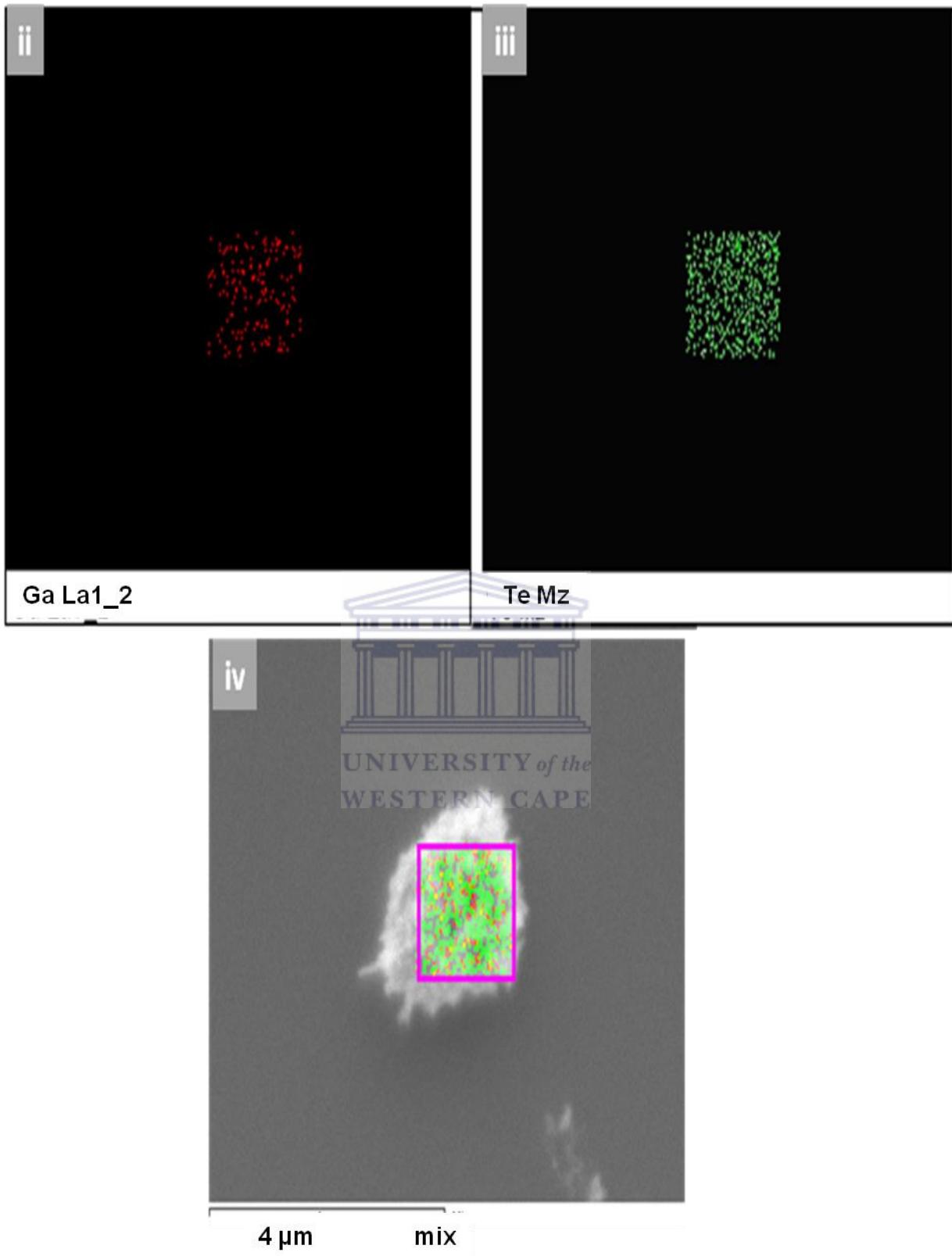
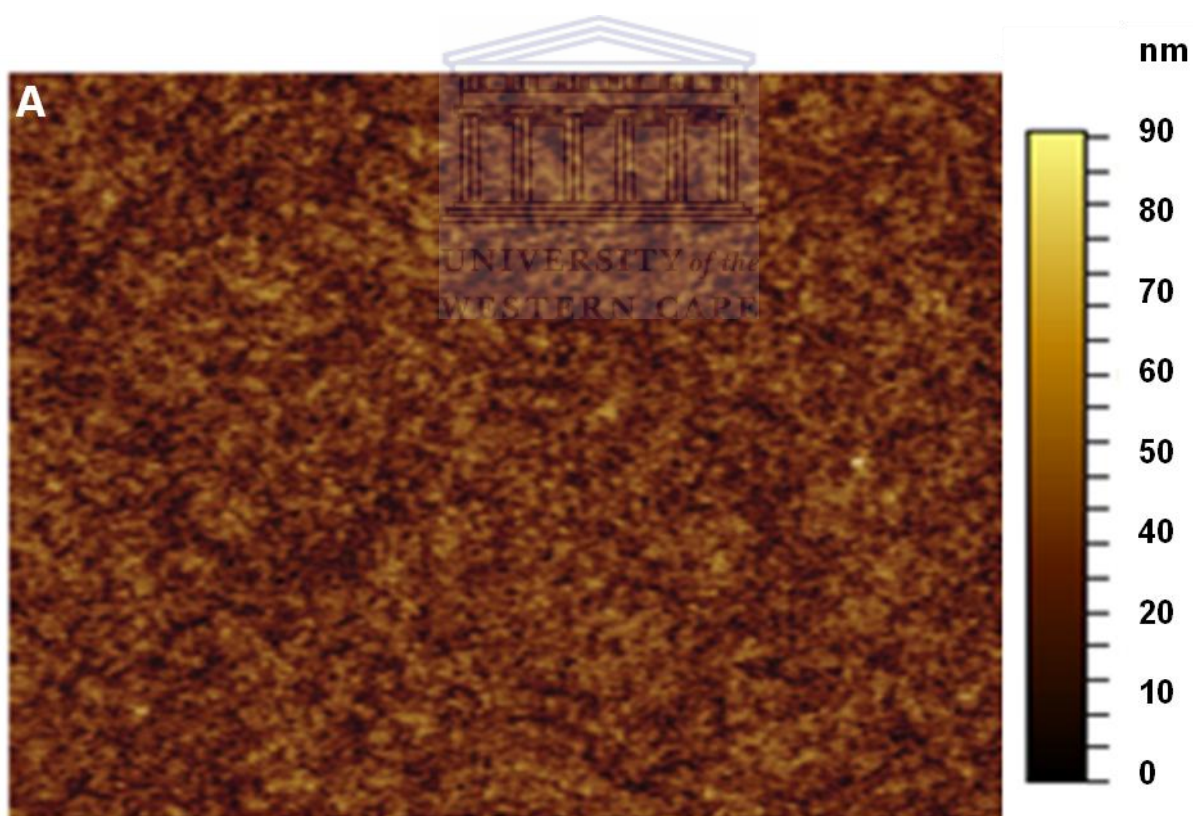


Figure 45. EDS (i) and mapping (ii-iv) images of 3MPA-Ga₂Te₃ quantum dots.

4.3 Atomic force microscopy (AFM)

4.3.1 Characterisation of 3MPA-Ga₂Te₃ using AFM

The particle size, roughness, particle distribution, topography and 3D images of the synthesised Ga₂Te₃ QDs were characterised by using AFM. The aim here was to compare the results obtained from SEM, TEM, STEM and HR-TEM and also confirming the surface modification of the nanodots onto the silicon wafer substrates. This was done by comparing the topography of the bare and modified silicon substrate, in which the roughness of each substrate was calculated or estimated. The results acquired from the AFM are as shown in Figure 46, 47 and 48.



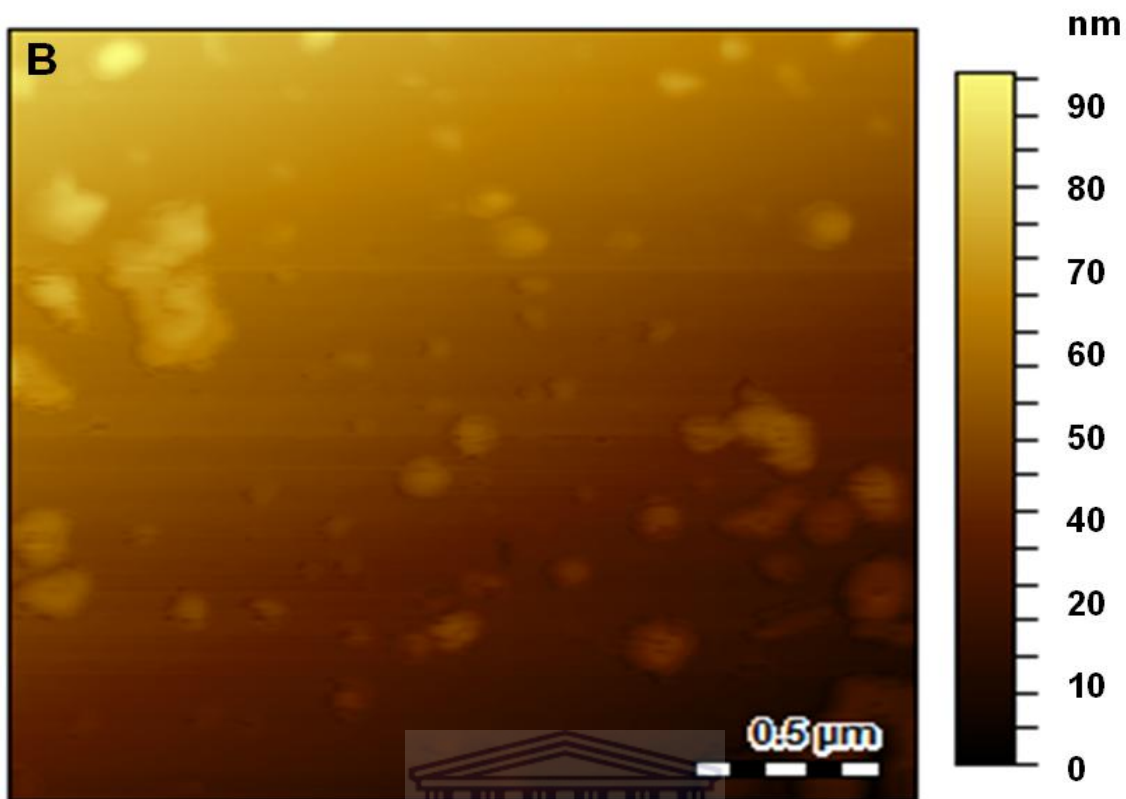


Figure 46. AFM images of 3MPA-Ga₂Te₃ quantum dots.

AFM analyses were carried out using silicon wafer as a substrate for the characterisation of the nanodots. AFM images of bare silicon wafer, silicon-wafer/3MPA-Ga₂Te₃ and 3D of as-synthesised quantum dots were carried out using a non-contact mode cantilever (Figure 46 and 47). Compared to bare substrate, modified substrate showed clear images of the as-prepared 3MPA-Ga₂Te₃ quantum dots, evident by round structures like dots (Figure 46 A and B). The particle size/diameter of the nanodots ranged from 10-20 nm (Figure 46 B and 47). There were few small agglomerated nanodots on the substrate-surface, which were related to over-refluxing, less centrifugation and sonication of the 3MPA-Ga₂Te₃ QDs.

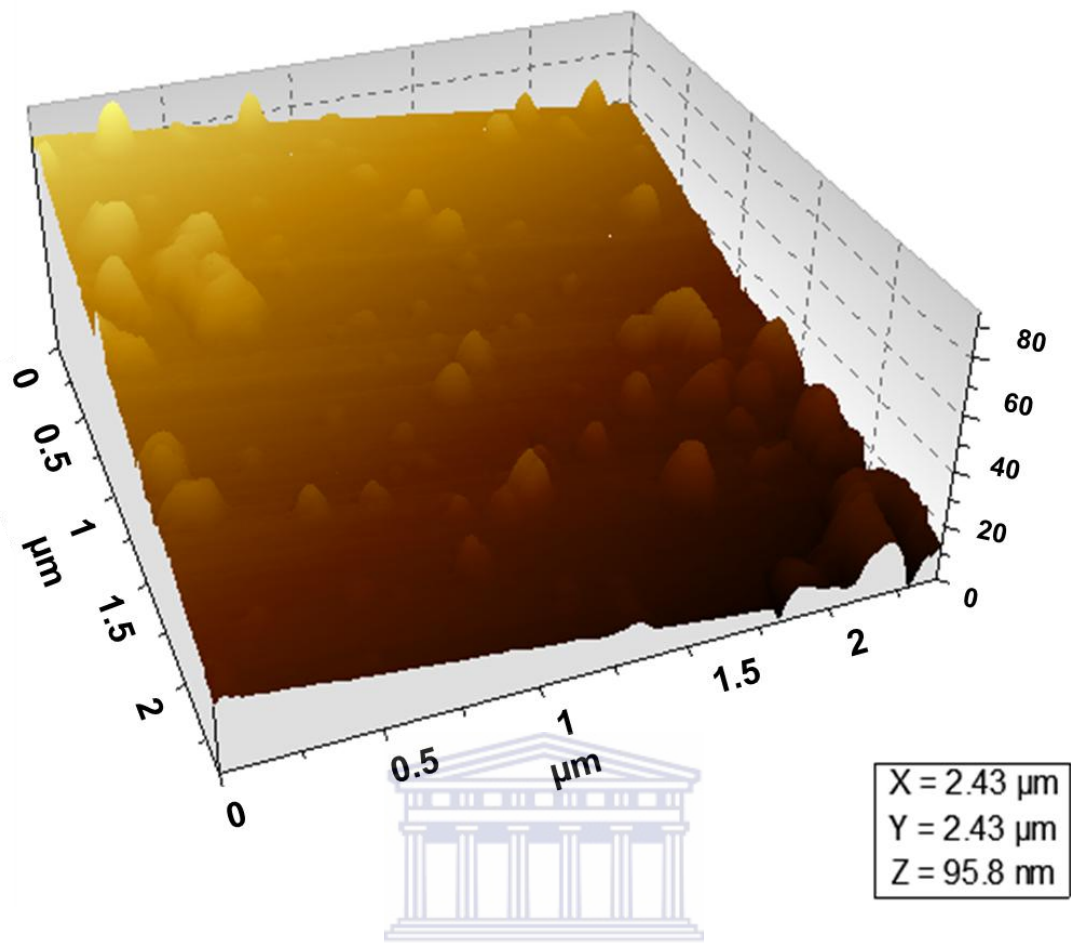


Figure 47. AFM images of 3MPA-Ga₂Te₃ quantum dots.

The roughness (Ra) of both bare and modified silicon wafer was calculated using AFM technique and was found to range from 0.03 - 26.60 nm, respectively (Figure 46 A and 47). From the obtained data and acquired images one can clearly distinguish between the modified and unmodified substrate, apparent by a change in substrate roughness. Figure 48, shows the particle distribution of the quantum dots on the silicon substrate. From the observed histogram the particle height was found to range between 19.2 - 86.2 nm and percentage was from 0 - 80%, which suggests that the nanomaterials were almost evenly-distributed on the silicon substrate surface and thus showed less agglomeration.

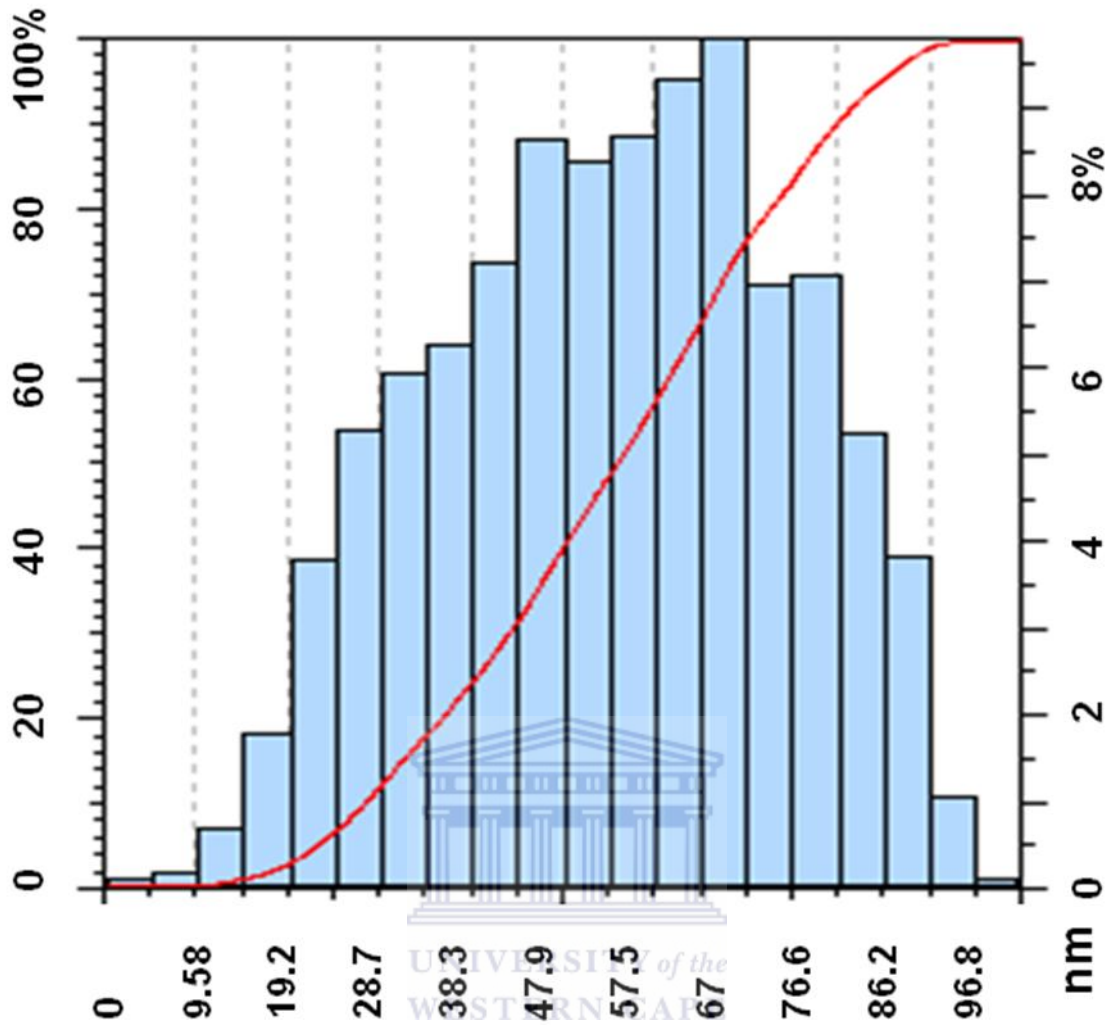


Figure 48. AFM images of 3MPA-Ga₂Te₃ quantum dots.

4.4 X-ray diffraction analysis of 3MPA-Ga₂Te₃ quantum dots

X-ray diffraction (XRD) is one of the crucial methods in characterising materials especially nanomaterial. It is used to measure the average spacing between layers or rows of atoms, determine the orientation of a single crystal or grain, find the crystal structure of an unknown material, measure the size, shape and internal stress of small crystalline regions. The as-prepared Ga₂Te₃ quantum dots were characterised using this technique. And diffraction patterns of as-prepared Ga₂Te₃ crystals, taken with graphite monochromated CuK α radiation are shown in Figure 49.

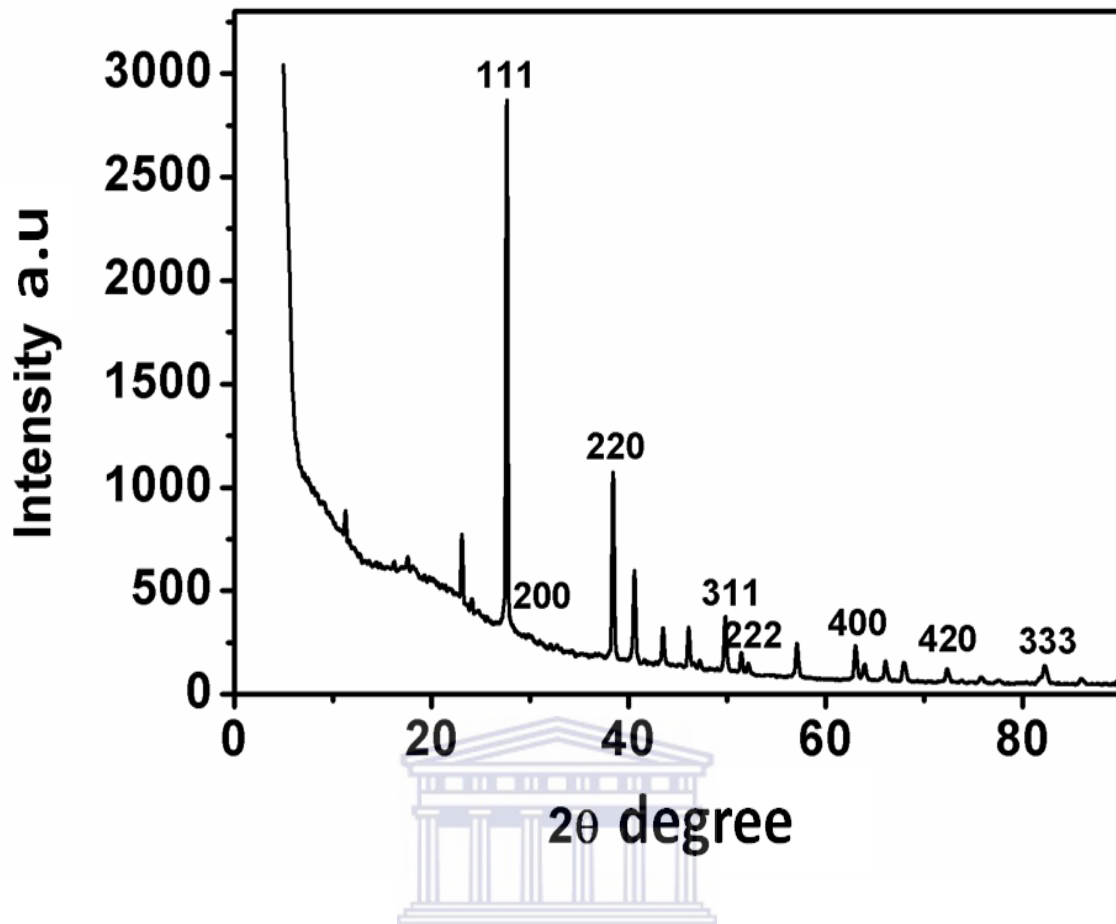


Figure 49. X-ray diffraction pattern of 3MPA-Ga₂Te₃ quantum dots.

XRD analysis was employed for the structure and size verification of the synthesised material. The diffraction peaks observed indicates the nanocrystalite nature. The peaks situated at angles (2θ) of 27.6°, 28.0°, 39.5°, 43.4°, 50.0°, 51.5°, 62.9°, 73.8°, 83.0° corresponds to the reflections from: (111), (200), (220), (311), (222), (400), (420) and (333) crystal planes, respectively. From the careful analysis of peak positions, lattice parameters and in accordance with the literature, [282; 283] XRD patterns of the nanodots were indexed/associated to the cubic phase (zinc blende) structure for Ga₂Te₃ with lattice constant, $a = 5.89 \text{ \AA}$ [284]. In the XRD patterns, the (111) plane was found to be very clear and abundant which indicates preferential growth of the crystallites in this particular direction.

Based on this observation the average crystal size was calculated based on the width of the peak by using the Scherrer's equation (eq. 23) [285]. The average particle size was calculated to be 6 nm, which confirms or is within the average values obtained from the HRTEM, TEM and STEM. The peak at 57.02 could be assigned to (321/2), corresponding to chalcopyrite structure, indicating the existence of chalcopyrite type orderings in as-grown Ga₂Te₃ crystals. Few additional peaks (Figure 49) were observed in the diffraction pattern which could be either due to different Te species or due to the existence of chalcopyrite type orderings, which requires further experimental investigations.

4.5 Fourier Transform Infra-Red spectroscopy (FTIR) analysis of 3MPA-Ga₂Te₃ quantum dots

Fourier transform infrared spectroscopy (FTIR) is a powerful technique that provides information about the chemical bonding or molecular structure of materials. FTIR works on the principle that bonds and groups of bonds vibrate at characteristic frequencies. Upon exposure of a molecule to infrared rays, the molecule absorbs infrared energy at frequencies that are characteristic to that molecule. During FTIR analysis, a spot on the specimen is subjected to a modulated IR beam. The specimen's transmittance and reflectance of the infrared rays at different frequencies is translated into an IR absorption plot consisting of reverse peaks. The resulting FTIR spectra is then analyzed and matched with known signatures of identified materials in the FTIR library.

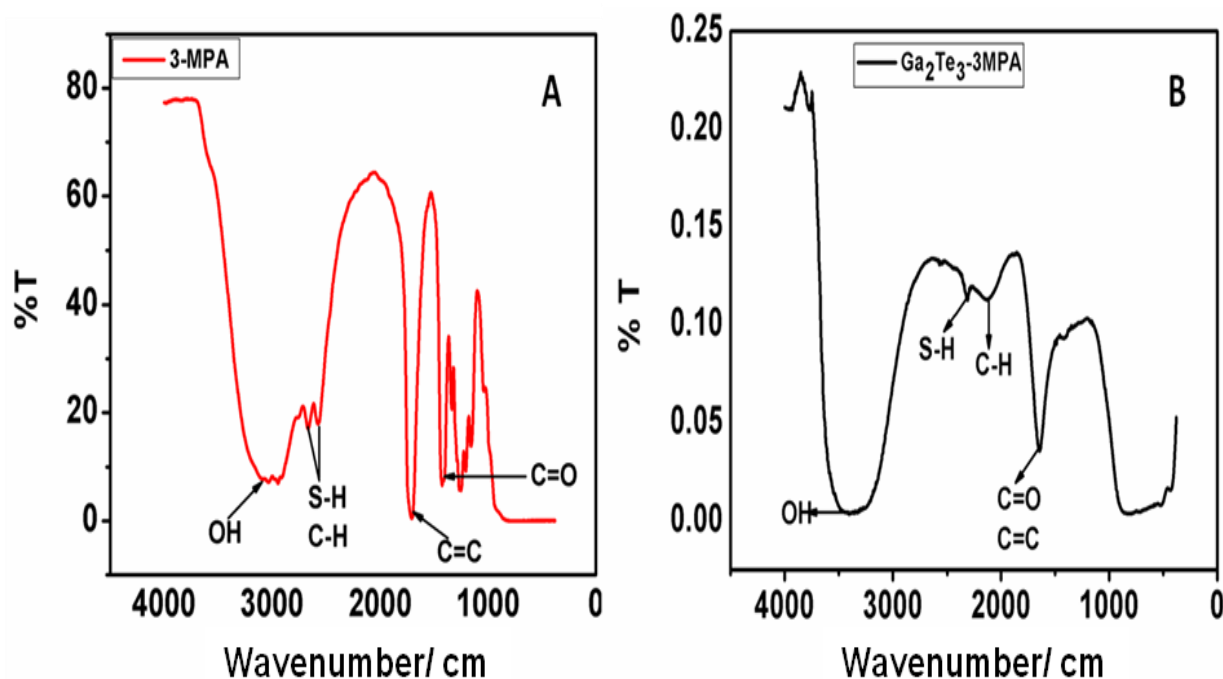


Figure 50. FTIR spectra of A) 3 MPA and B) 3MPA-Ga₂Te₃.

With the aim of determining the vibrational stretches and ensuring stable and well capped quantum dots FTIR analyses were employed. Surface capping and functionalisation of quantum dots involve introduction of additional layer(s) or coating(s) on the core shell structure. The process was intended to make the quantum dots stable, reduce or eliminate toxicity, avoid agglomeration as well as to improve their luminescence properties. In the process of functionalisation, particular groups are introduced on the surface of the quantum dots material to suit particular applications. For instance, a carboxylic acid group can be introduced on the surface of a quantum dot to confer solubility properties. In our synthesis of quantum dots, 3-mercaptopropionic acid was incorporated as an amphiphilic molecule. It was expected that the thiol group (HS-) of the 3-mercaptopropionic acid which is hydrophilic would covalently bind with the hydrophobic surface of the quantum dot while the carboxylic acid group (-COOH) extends to a water molecule to make the quantum dot soluble.

It was therefore necessary to analyze the quantum dots to check if the 3-mercaptopropionic acid was truly retained on the quantum dot surface. The FTIR was thus carried out to mainly check the presence of 3-mercaptopropionic acid in the synthesised quantum dots Figure 50 B.

Figure 50 A shows the spectrum of 3MPA alone, with the vibrational stretches at 3000 cm^{-1} , 2500 cm^{-1} , 2000 cm^{-1} and 1500 cm^{-1} which were due to OH, -SH, C=O and C-H respectively. Compared to the control (Figure 50 B and A; MPA alone and Figure 50 A and B-QDs), the intensity of -SH vibrational stretches in the quantum dots sample decreased with a slight shift in wavenumbers, indicating that the quantum dots were sufficiently capped with 3MPA.

4.6 Raman spectra of 3MPA-Ga₂Te₃ quantum dots, 3MPA and the naked substrate

In the present work, structural change of powder 3MPA-Ga₂Te₃ and 3MPA on a glass + tape substrate were investigated by Raman spectroscopy. The behavioural change of 3MPA-Ga₂Te₃ against 3MPA was scrutinised by observing changes in intensities and shifts in wavenumbers. Raman measurements were made at room temperature in backscattering configuration, using the 532 nm lines of an Ar⁺ ion laser. The spectra acquired from Raman spectroscopy was obtained with a power of the incident laser light, Figure 51.

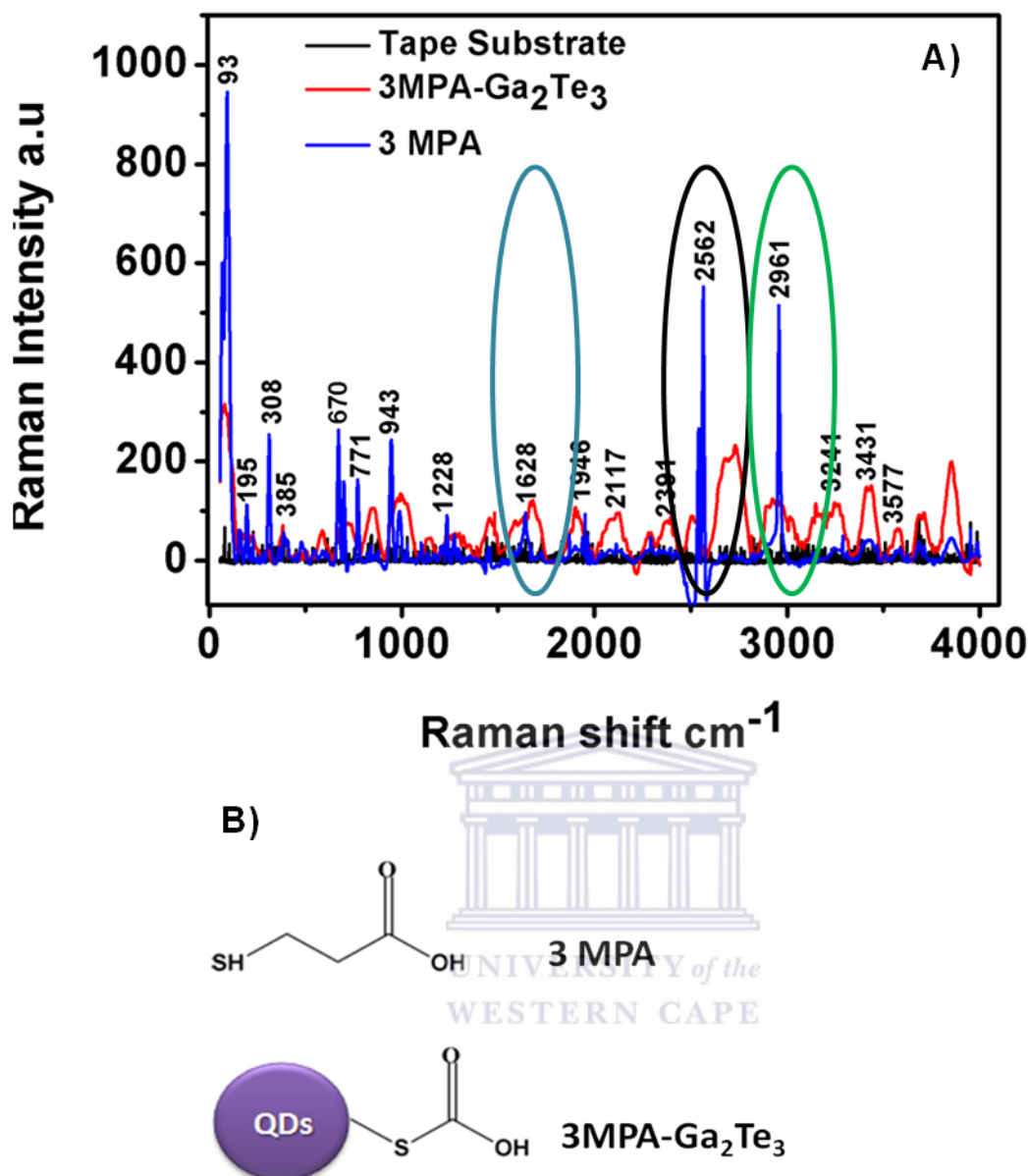


Figure 51. Raman spectra of A) 3 MPA, Ga_2Te_3 -3 MPA, tape and B) Chemical structure of 3MPA and 3 MPA- Ga_2Te_3 (Abbreviations: ν , stretching; δ , in-plane bending; ζ , out-of-plane bending; τ , rocking, wagging).

Raman spectra gave information about the structure and the composition of the samples. Figure 51A shows typical Raman spectra of substrate (tape), 3MPA and 3 MPA- Ga_2Te_3 in the range between 50 and 4000 cm^{-1} . As can be seen in Figure 51, there are no Raman bands observed on a naked substrate. However there are strong 3MPA Raman bands observed at

195 cm^{-1} (C-C), 385 cm^{-1} $\delta(\text{SCC})$, 1228 cm^{-1} $\text{tw}(\text{CH}_2)$, 1628 cm^{-1} $\nu(\text{C}=\text{O})$, 1946 cm^{-1} $\nu(\text{OCO})$. The most intense bands are observed at 308 cm^{-1} , 771 cm^{-1} , 943 cm^{-1} , 670 cm^{-1} , 2562 cm^{-1} and 2961 cm^{-1} these bands are characteristic of very weak $\delta(\text{SCC})$, strong $\nu(\text{SC})_{\text{T}}$, weak $\rho(\text{CH}_2)$, $\nu(\text{CS})_{\text{G}}$, very strong $\nu(\text{SH})$ and $\nu(\text{CH}_2)$, respectively. The observed bands and/or wavenumbers are in agreement with literature reports [286; 287] for 3MPA (Figure 51B). Furthermore these bands confirm the composition of the pure 3MPA structure. Raman spectra of 3MPA- Ga_2Te_3 with chemical structure observed in Figure 51B, was also studied (Figure 51A). Literature values for Ga_2Te_3 and Te crystal were found to occur at different wavenumbers. There are peaks at 140, 118, and 93 cm^{-1} which correspond to the phonon frequencies of Te and the formation of Ga_2Te_3 was assumed to be at 119 cm^{-1} due to the co-existence of Te at this location [288; 289]. These peaks were observed in our spectrum, Figure 51A. A strong peak at 93 cm^{-1} was observed and very weak peaks at 140, 118 cm^{-1} were acquired in our spectrum. Again our obtained data agrees with literature values. Compared to 3MPA, 3MPA- Ga_2Te_3 showed a vast decrease in the Raman intensities at 308 cm^{-1} , 771 cm^{-1} , 943 cm^{-1} , 670 cm^{-1} , 2562 cm^{-1} and 2961 cm^{-1} and red shift from; 670 - 714 cm^{-1} , 771 - 847 cm^{-1} , 943 - 993 cm^{-1} , 1228 - 1285 cm^{-1} and 2562-2732 cm^{-1} was also observed. Based on the data obtained it can be concluded that quantum dots were well capped with MPA (Figure 51B) and the results are comparable with that of FTIR and XPS.

4.7 X-ray photo-electron spectroscopy (XPS) analysis of 3MPA- Ga_2Te_3 quantum dots

As both FTIR and EDS, XPS is also used as one of the techniques for analysing the surface chemistry of a material. The technique is used to measure the elemental composition, empirical formula, chemical state and electronic state of the elements within a material. The components of the as-synthesised 3MPA- Ga_2Te_3 quantum dots are as shown in Figure 52.

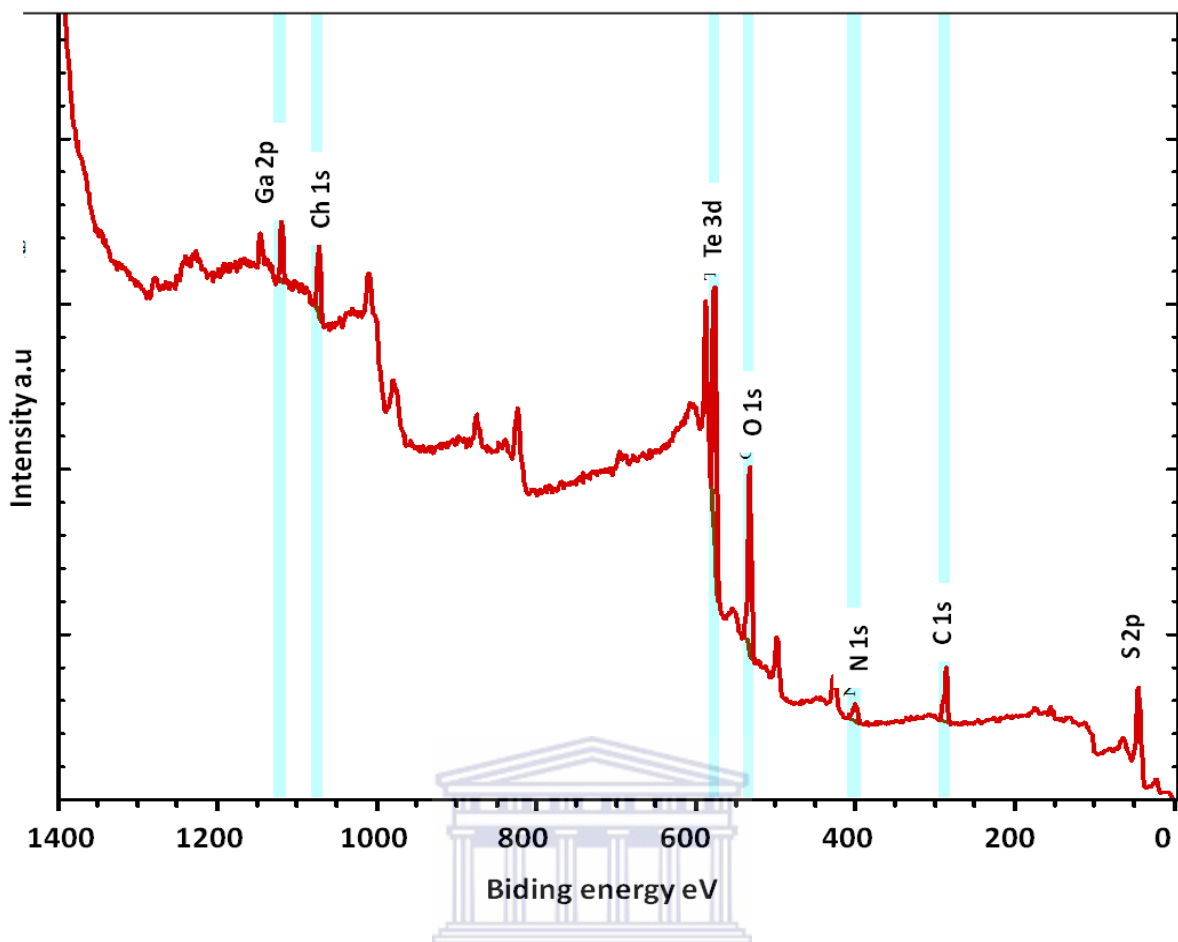


Figure 52. XPS spectra of 3MPA-Ga₂Te₃.

Chemical states of the elements C, O, Ga and Te can be identified from the high resolution spectra during XPS analysis, Figure 53 a and b. Ga:Te surface concentration was found to be 1:5.6 which is higher than the expected Ga:Te composition. This indicates that surface is Te enriched and possibly Ga and Te may present in more than one oxidation state. From careful analysis it is observed that Ga and Te are present in more than one oxidation state; Ga₂Te₃ (42.70%), Ga₂O₃ (15%), Ph₂Te₂/Te (35.4%) and TeO₃ (6.80%). The difference in observed composition may arise from the following factors; (i) surface composition vs. bulk composition, surface is Te enriched, (ii) overlapping of O and Ga/Te signal may give rise to variation in composition.

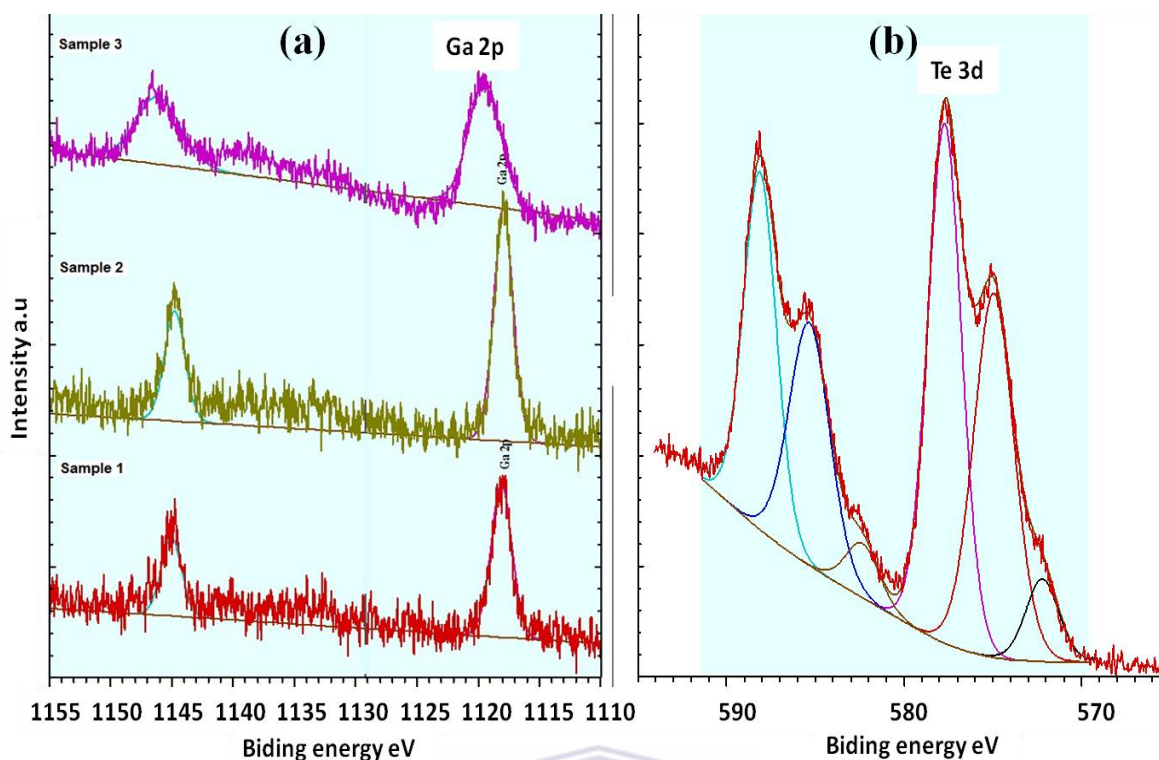
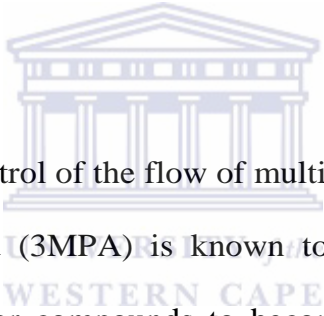


Figure 53. XPS spectra of 3MPA-Ga₂Te₃.

There was a substantial amount of oxygen, however, due to co-existing oxygen and oxygenated carbon species, it was difficult to distinguish the contribution from oxidised Ga/Te in the corresponding O 1s spectra. The higher surface composition of Te compared to nominal composition also confirm that Te is present in different oxidation state (elemental tellurium, TeO₃, Ga₂Te₃ etc). In addition, from the bimetallic compositions other than Ga₂Te₃ crystals it is possible that Te is segregated at Ga₂Te₃ surface based upon surface free energy arguments. However, in such cases the bimetallic compositions are notably affected by adsorbates from the surrounding gaseous environment and the metal having the highest affinity for these adsorbates will preferentially segregate to the surface. The C-1s spectra consists of peaks arising due to C-C, C-H, C-O, C-OH, C=O) functionalities arising due to the use of MPA as a capping agent during quantum dots synthesis and interaction with environmental oxygen.

In order to investigate the oxidation states and surface species together with surface composition of Ga and Te in the nanomaterial, X-ray photoelectron spectroscopy (XPS) analysis was performed. Figure 53a-b summarises the XPS results with Ga 2p, Te 3d, O 1s and C 1s core level regions examined. Doublet peaks for Ga and Te result from 2p and 3d photo- electron transitions due to spin-orbit coupling. The asymmetry in the peaks is indicative of the presence of more than one oxidation state for Ga and Te. The peaks are fitted with a doublet separation characteristic of Ga and Te and full width half maximum (FWHM) is constrained for different chemical states.

4.8 Hydrophilic and hydrophobic nature of the quantum dots (capped and uncapped Ga₂Te₃)



Contact angle is a principal control of the flow of multiple fluid phases through porous media. Mercaptopropionic acid (3MPA) is known to be an amphiphilic molecule, which assist other molecules or compounds to become more water-soluble. In this study contact angle measurements were carried out to investigate or confirm the effect of 3MPA on capped quantum dots (3 MPA-Ga₂Te₃). Additionally the hydrophilic and hydrophobic nature of the two samples (3 MPA-Ga₂Te₃ and Ga₂Te₃) was investigated by employing drop sensor analyser where by a contact angle measurement of each was determined. We have conducted several measurements, and we investigated two different powdered phase samples on a solid surface, water being the only aqueous phase: Figure 54 (A) Deionised water, (B) Ga₂Te₃ and (C) 3 MPA-Ga₂Te₃.

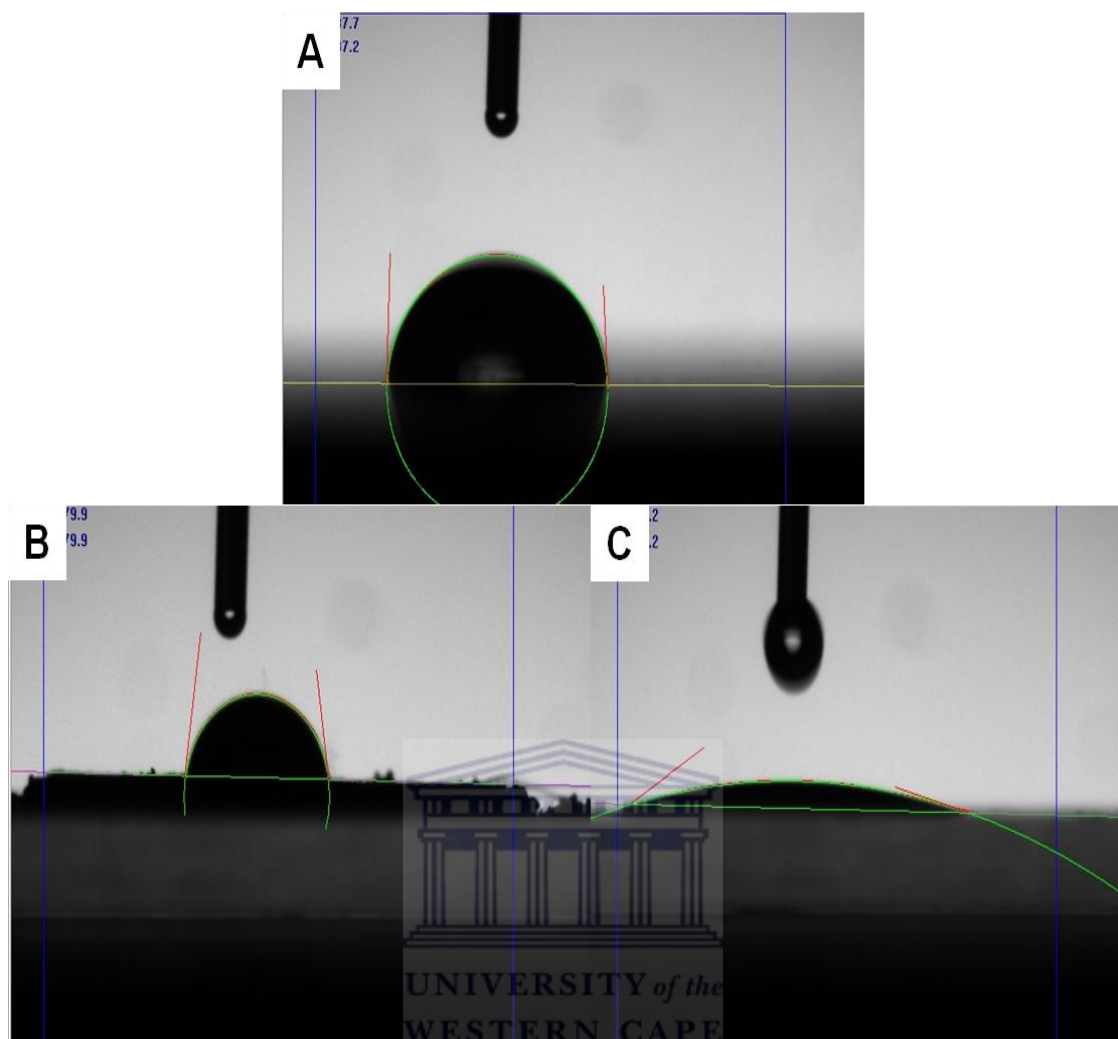


Figure 54. Hydrophobic surface and hydrophilic surface of A) Solid surface (blank), B) Ga_2Te_3 and C) 3 MPA- Ga_2Te_3 .

The hydrophilic nature of the capped quantum dots were confirmed by contact angle measurements, evident by contact angle of 12.2° which showed good wetting compared to that of uncapped quantum dots 79.9° . Compared to the naked quantum dots (Ga_2Te_3), it can be concluded that the capped quantum dots (3 MPA- Ga_2Te_3) are strongly water-wet and confirm that the 3MPA had an effect on the wettability or the partly solubility of the capped Ga_2Te_3 quantum dots. The obtained results put a clear picture in understanding the hydrophilic nature of the quantum dots and also giving us an opportunity to investigate other capping agent which can aid in the solubility of the QDs for biological applications.

4.9 UV/vis and Fluorescence Spectroscopy

UV/vis and Fluorescence analyses of 3MPA-Ga₂Te₃ and 3-MPA were carried out before and after refluxing (Figure 55 and 56). The analyses were carried out to investigate the absorption, emission and excitation wavelength of 3MPA-Ga₂Te₃ quantum dots. The absorption wavelength (λ_{\max}) of 3-MPA capped (3MPA-Ga₂Te₃) was observed at 238 nm and that of MPA alone was observed at 298 nm, (Figure 55). Behaviour suggests that the absorption of a photon at this λ_{\max} by QDs causes electronic transition from the valence band to the conduction band, thereby leaving an electron-hole pair known as an exciton.

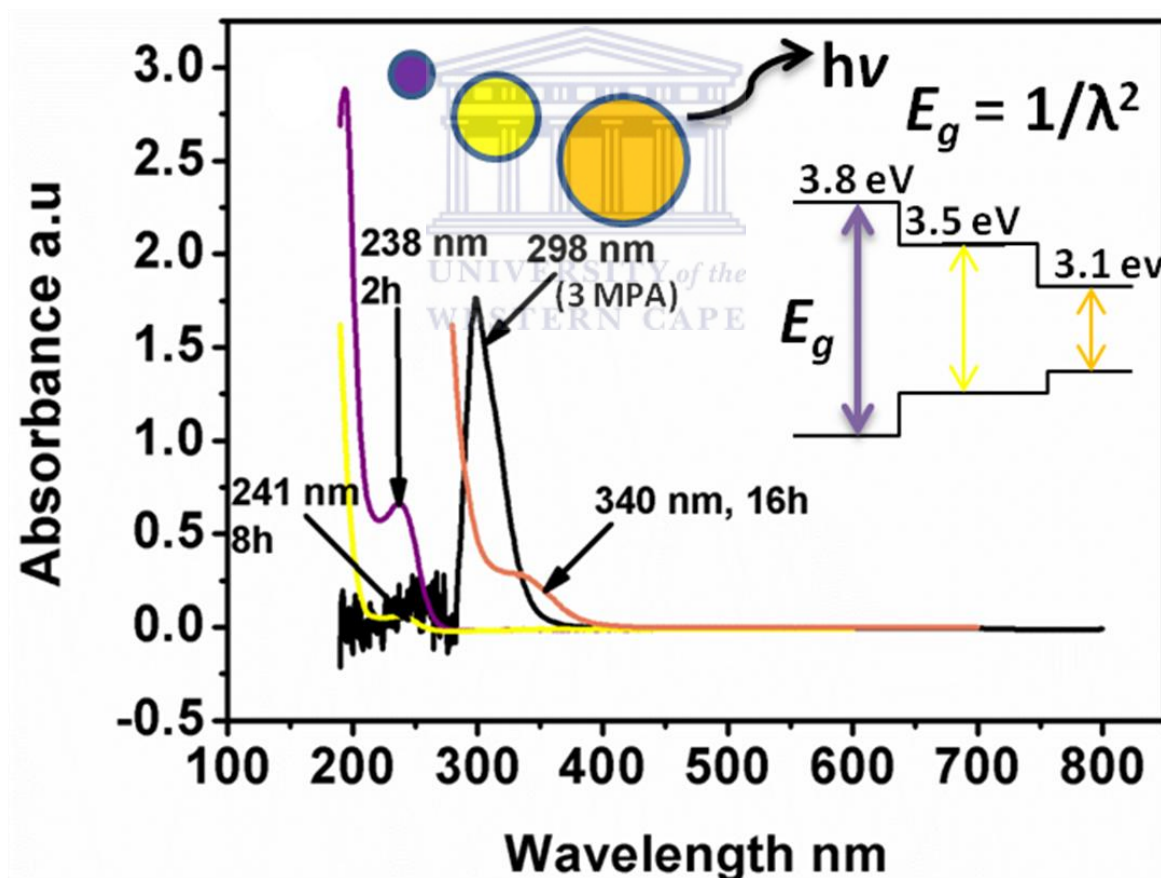
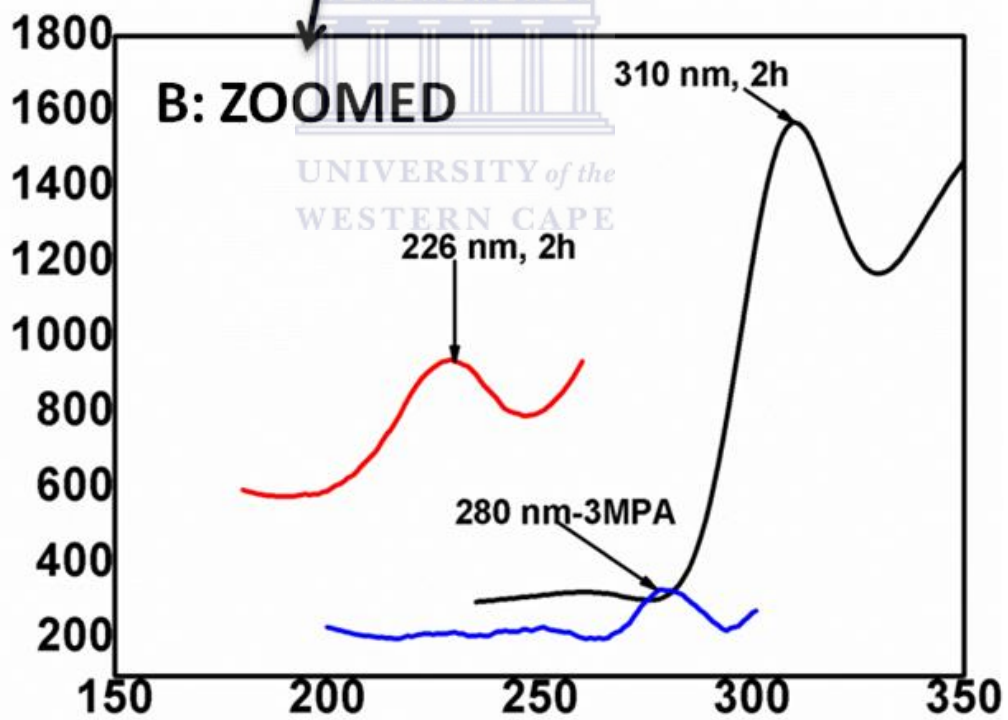
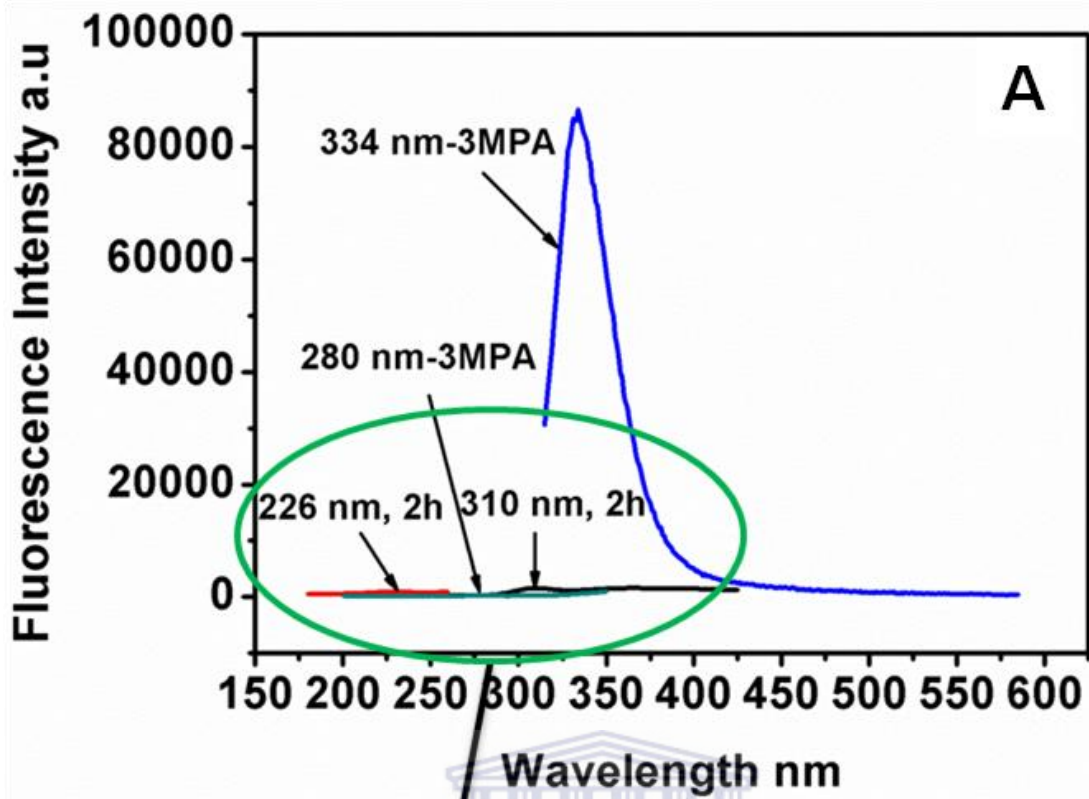


Figure 55. UV/vis of 3MPA-Ga₂Te₃ in solution (before and after refluxing).

Electrons in the valence band are tightly coupled with their respective nuclei, whereas electrons in the conduction band are somewhat separated from their nuclei therefore allowing for free motion within the solid. The effect of reflux (during QDs synthesis) over the different time period (for 2 - 16 h, at 100° C) was also monitored and the results are shown in Figure 55 A-C with absorption peaks evident at 238 nm (2 h), 241 nm (8 h) and 340 nm (16 h). This red shift over longer refluxing periods indicates size increment and decrease in band gap energies. This increment in size is due to quantum confinement effects, which may be observed when the size is sufficiently small, that the energy level spacing of the nanocrystal exceeds $K_B t$ (K_B is Boltzmann's constant and t is temperature), $1.3806488 \times 10^{-23} \text{ J K}^{-1}$ ($= \text{m}^2 \text{ kg s}^{-2} \text{ K}$). This effect allows the tuning of the energy-band gap with changes in quantum dots size, as it is observed in the absorption spectra, Figure 55. This also proves that the wavelength is inversely proportional to the band gap energy (E_g) of the material. Even though the nanodots increased in size they were still within limits (2 - 20 nm) of the semiconductors. In conclusion this behaviour confirms that the nano-materials are of conducting material (semiconductors). Fluorescence analysis for 3MPA-Ga₂Te₃ was carried out (Figure 56 A and B). The Ga₂Te₃ QDs was shown to emit at wavelength of 430 nm and excite at lower wavelengths of 380 nm and 228 nm. The Ga₂Te₃ QDs was found to be blue shifted (50 nm), the shift in wavelength was associated with Stokes shift. The energy of the emitted (430 nm) and excited (380 nm) molecule (Figure 55 and 56 A) and the band gap energy from fluorescence and UV-visible were calculated using eq.12. The energy of the emitted electron was calculated to be $4.62 \times 10^{-22} \text{ J}$ for excitation and $5.37 \times 10^{-22} \text{ J}$ for the absorption.



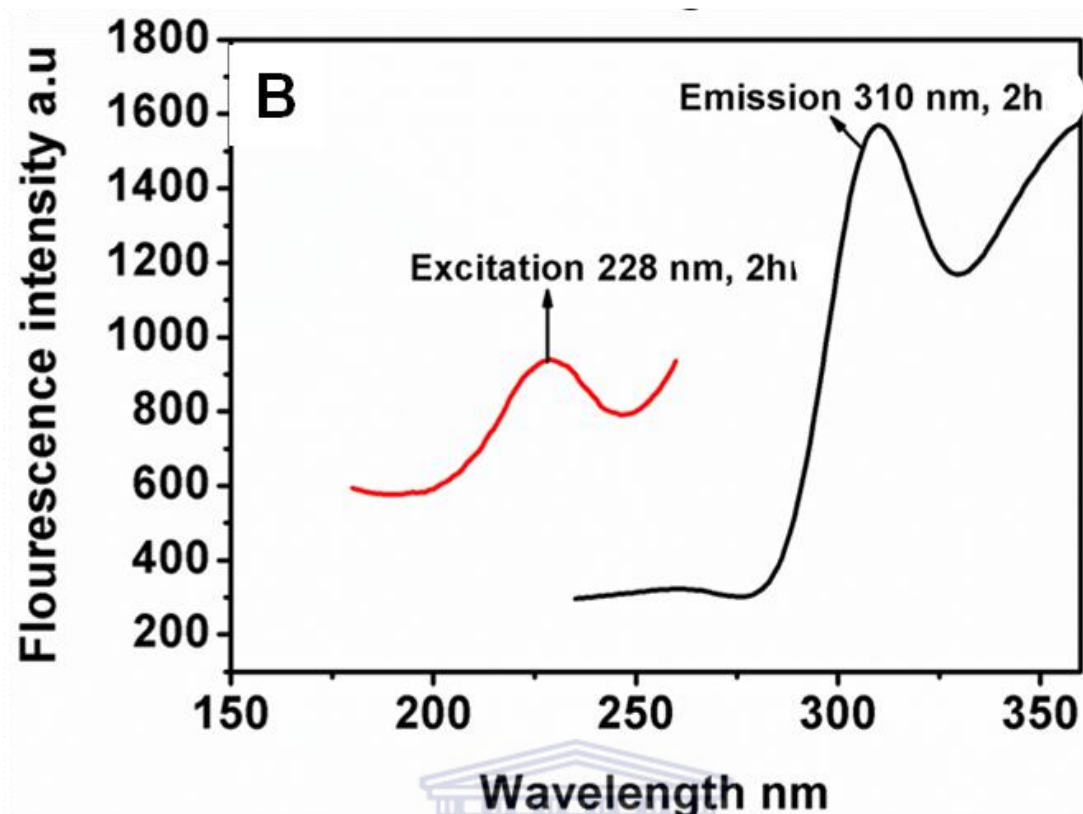


Figure 56. (A) Fluorescence spectra of 3MPA-Ga₂Te₃ showing and (B) Both emission and excitation in solution (before and after refluxing).

These energy values confirm that, larger energies are required to excite the molecule. The band gap of the material which is defined as the energy distance between the valence and conduction bands was calculated to be 3.30 eV for fluorescence and that of UV/visible was found to be 3.50 eV. These values were found to be reasonably smaller, within limits and comparable with literature values [10-17]. The values obtained from the two techniques are significantly comparable and suggest that the material is more electrically conductive (semiconductor). There is sufficient thermal energy to excite electrons from the valence band to the conduction band in this case.

Further analysis on the Ga₂Te₃ quantum dots were carried out using the three dimension fluorescence (Figure 57). The aim was to investigate the nature and the availability of the fluorophores in the bi-metallic (3MPA-Ga₂Te₃).

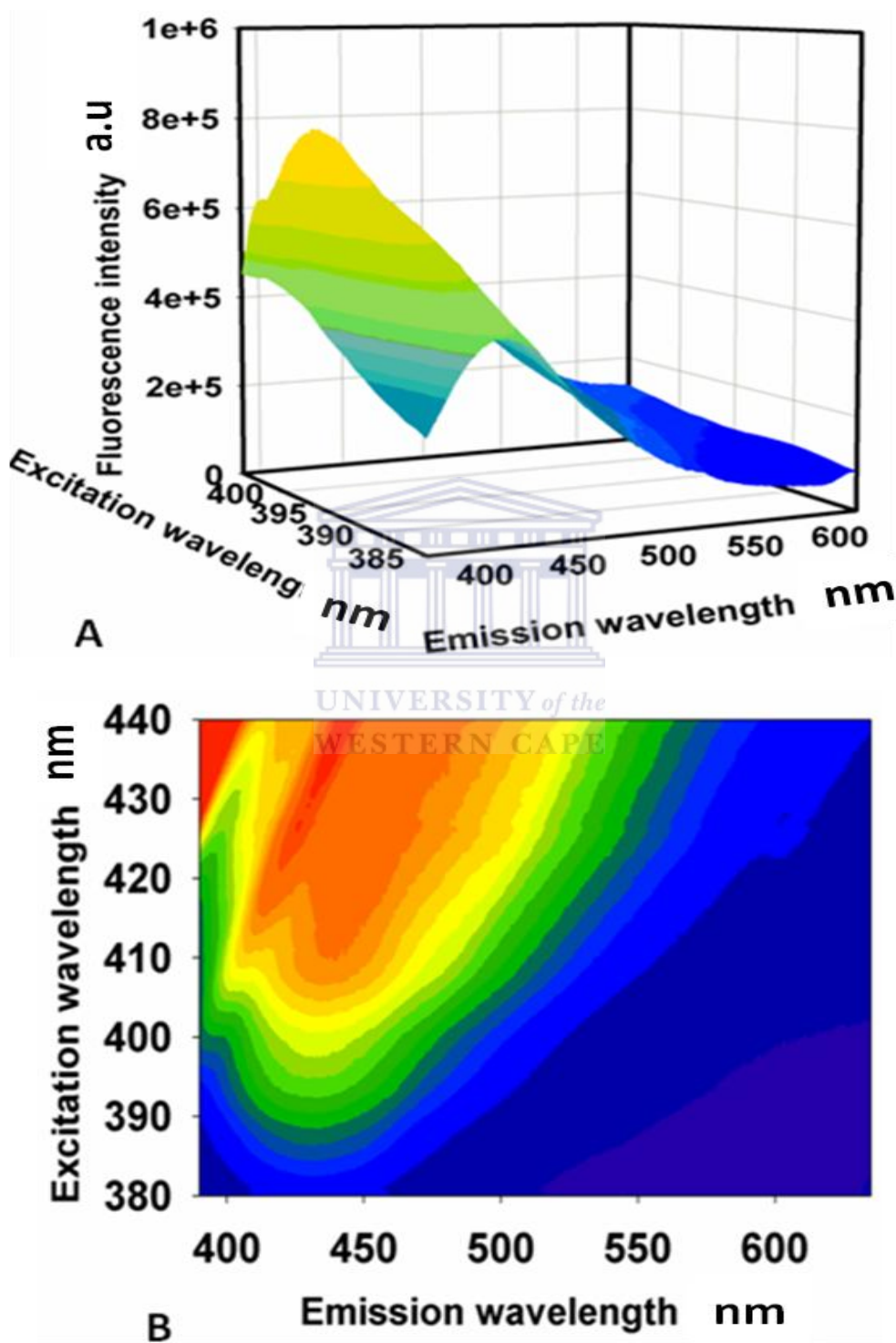


Figure 57. (A) 3D-Mesh and (B) Contour plots of 3MPA-Ga₂Te₃ in solution.

Figure 57 A, represents the 3D mesh and contour plots of the 3MPA-Ga₂Te₃ quantum dot. The 3D mesh plot agrees well with the intensities of both the emission and excitation plots. The contour plots (Figure 57 B) confirmed that there is only one molecule or fluorophore in our sample (3MPA-Ga₂Te₃), which was true in the emission and excitation plots, evident by a narrower emission peaks.

4.10 Quantum yield Comparison between 3MPA-Ga₂Te₃ quantum dots with Rhodamine 6G

Photophysical properties of rhodamine 6G (with quantum yield 0.95) and 3MPA-Ga₂Te₃ were analyzed using ultraviolet–visible (UV–vis) and photoluminescence (PL) spectrometer. The aim of the study was to compare the conventional methods with the modern methods. The absorbance and the fluorescent intensities of the as-synthesised nanodots and rhodamine 6G are as shown in Figure 58 A and B. Both rhodamine and 3MPA-Ga₂Te₃ exhibited weak UV–vis absorption peak at 257 nm and 527, respectively. The quantum yield of the conventional-dye and the nanodots was calculated (as previously reported from literature) [290] from both the UV–vis absorption peak and Fluorescent emission peak intensities. There are different equations that are been used in calculating the quantum yield i.e. a single or comparative ways. In this study comparative alternative was used. Fluorescent molecules commonly used as probes in microscopy have quantum yields ranging from very low (< 0.05) to near unity. High quantum yield is desirable in most imaging applications.

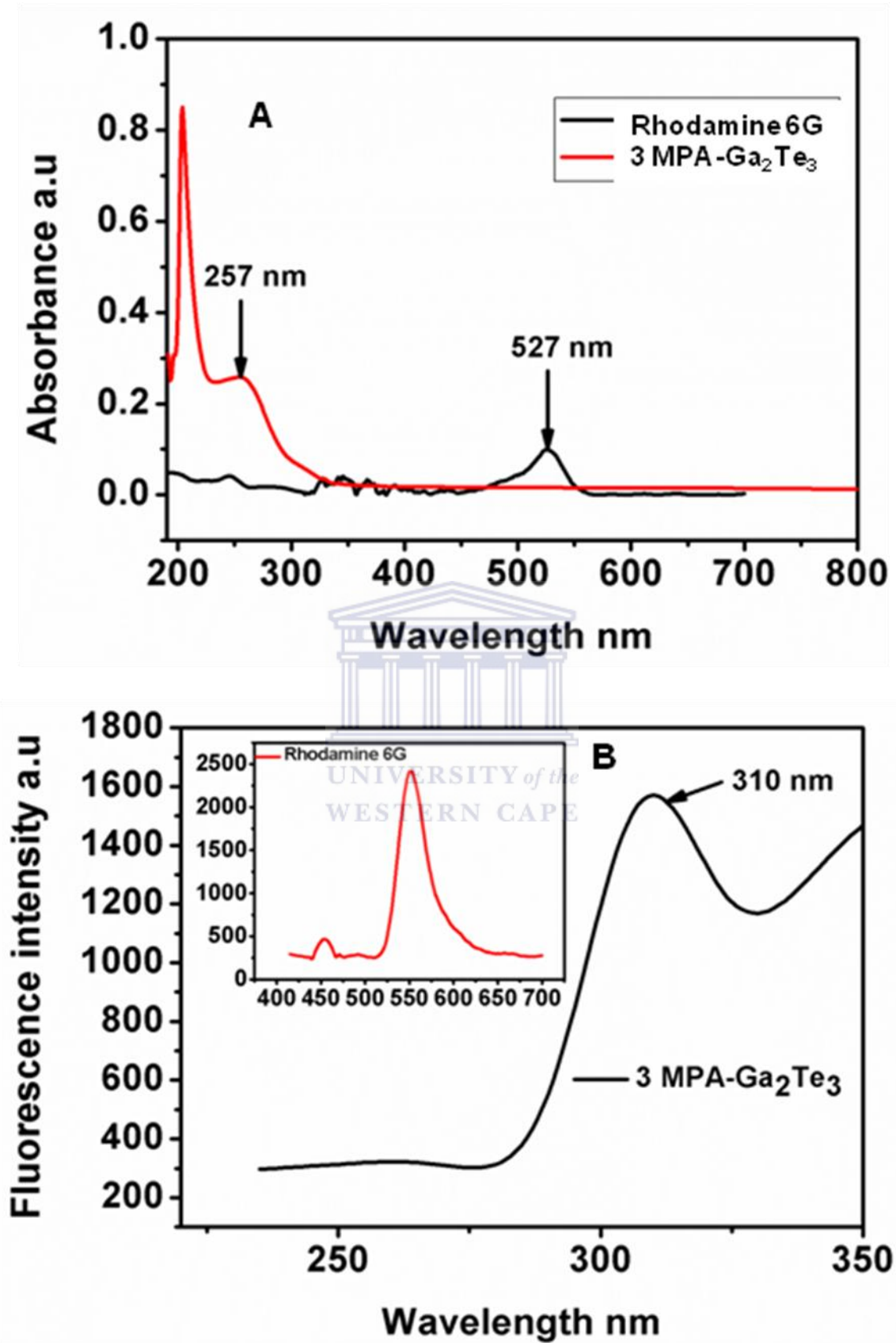


Figure 58. Comparison between rhodamine 6G and 3 MPA-Ga₂Te₃.

The quantum yield of the 3 MPA-Ga₂Te₃ quantum dots (**1.20**) which is used as an imaging probe was compared with that of rhodamine 6G (**0.90**) and was calculated to be higher than that of the later as expected. Quantum yields were calculated using (eq. 16) [290]. The results suggest that the nanodots have shown to be much more stable against photobleaching than fluorescent dyes as was observed in other results (Chan and Nie), in addition to being much brighter. It was estimated by Chan and Nie that ‘the fluorescence intensity of a single CdSe QD is equivalent to that of ~20 rhodamine molecules.’ This photostability means that quantum dots have been considered as an alternative to fluorescent dyes, notably in biological uses, since the 1980s.

4.11 Genosensor response using, electrochemical impedance spectroscopy (EIS)

Electrochemical impedance spectroscopy is a well known technique for interrogating interfacial electrical properties of surface modified electrodes. Figure 59 A below depicts the Nyquist plots for bare Au, Au/Ga₂Te₃-3MPA/ssDNA and Au/Ga₂Te₃-3MPA. Figure 59 C also shows the corresponding Randle’s equivalent circuit consisting of a solution resistance (R_s), charge transfer resistance (R_{ct}) and constant phase element (CPE). R_{ct} represents the resistance to the charge transfer between the electrolyte and the electrode and contains information on the electron transfer kinetics of the redox probe at the electrode interface. The Nyquist plots were accompanied with the bode plots to show the electrochemical properties of the materials Figure 59 B. A Bode Plot is actually a collection of 2 plots. The first shows the frequency content of a given signal. The x-axis of this plot is a frequency on a log scale and the y-axis is the weight of that frequency to the signal as a whole. Because the y-axis shows a weight in comparison to the signal as a whole, the units are in dB.

The frequency is shown in a log scale because there is so much frequency to cover in a single Bode plot. The second plot is generally positioned just below the first. This plot has the same x-axis: frequency on a log scale. The y-axis is in units of degrees or radians. This plot shows the phase offset at each frequency.

Figure 59 A depicts the Nyquist plots for bare Au, Au/Ga₂Te₃-3MPA and Au/Ga₂Te₃-3MPA/ssDNA electrodes. The aim of the experiment was to investigate the behaviour of the modified and unmodified electrodes at an applied potential of $E_p = 400$ mV (observed from CV measurements, Figure 60). The R_{ct} values of bare Au and Au/Ga₂Te₃-3MPA and Au/Ga₂Te₃-3MPA/ssDNA electrodes were 11.93, 9.02 and 10.32 Ω , respectively. The results obtained prove that the modified electrodes are more favourable than unmodified electrode, due to lower R_{ct} values. The behaviour in charge transfer resistance suggests a faster electron transfer, thus showing a more conducting system of Au/Ga₂Te₃-3MPA than both the bare Au and Au/Ga₂Te₃-3MPA/ssDNA. Furthermore, the ssDNA incorporated in the Au/Ga₂Te₃-3MPA modification behaves as an insulator thus masked or impeded the charge transfer of the modified gold electrode (Au/Ga₂Te₃-3MPA). Additionally the electron movement or the rate of electron transfer (k_{ct}) from the electrolyte solution and ssDNA become very sluggish to reach the semi-conductor (Ga₂Te₃-3MPA) at the electrode interface, hence the higher charge transfer (R_{ct}). This behaviour supports the theory/phenomena that states; the higher the charge transfer resistance the slower the electron movement at the electrode interface.

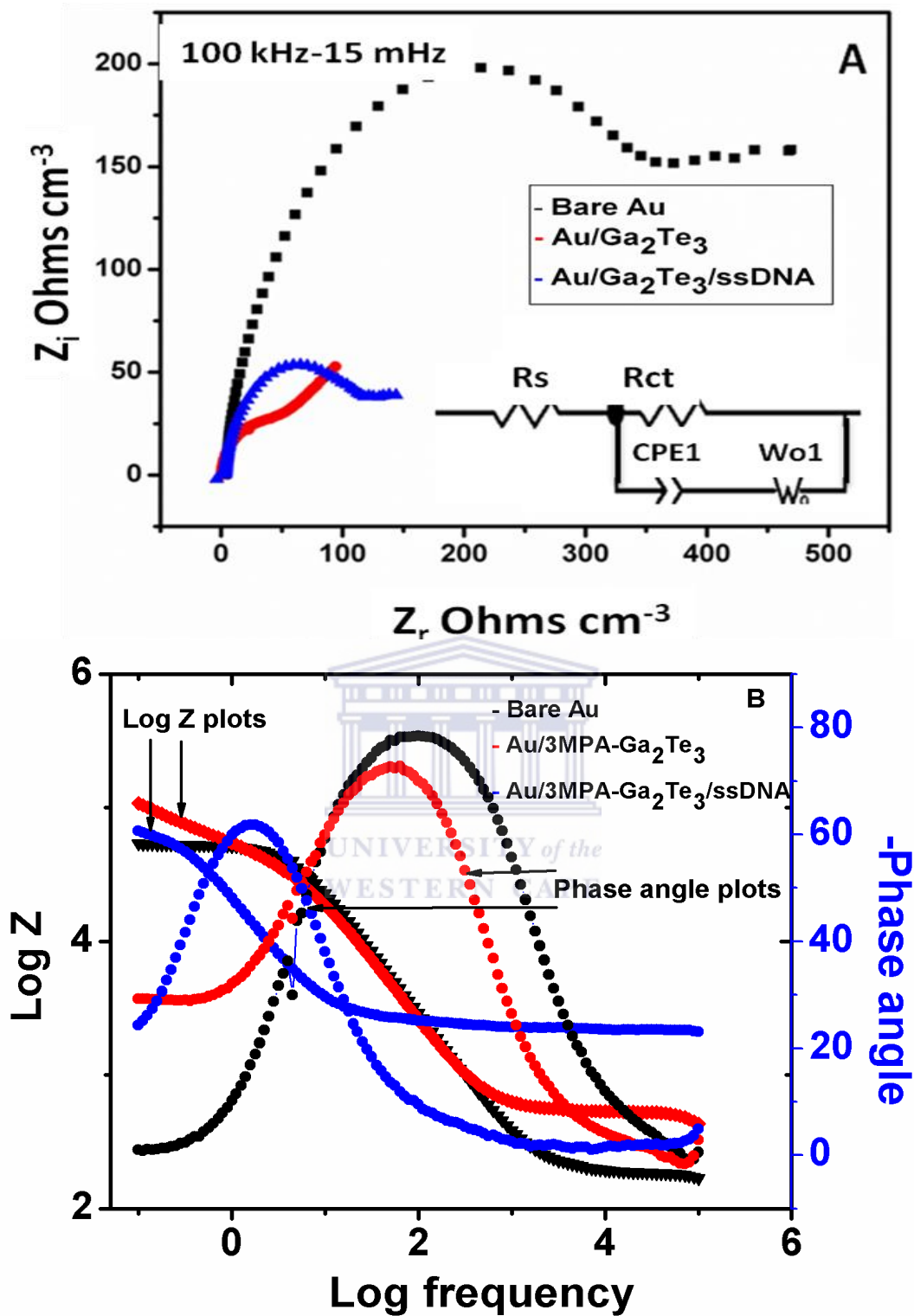


Figure 59. A) Nyquist plots of bare Au, Au/Ga₂Te₃-3MPA and Au/Ga₂Te₃-3MPA/ssDNA modified electrodes in 0.1 M PBS (pH = 7.4). (B) Bode plots and exploration of (A).

The surface coverage (θ) of the modified gold electrode was calculated using eq. 27.

$$\theta = 1 - \frac{R_{ct}(bare - Au)}{R_{ct}(Au / Ga_2Te_3 - 3MPA)} \quad (27)$$

The surface coverage (θ) of Au/Ga₂Te₃-3MPA was calculated to be 0.78 cm s⁻¹ and the electron transfer rate constant (k_{et}) for bare Au and Au/Ga₂Te₃-3MPA and Au/Ga₂Te₃-3MPA/ssDNA at 500 mV was calculated to be $1.79 \times 10^{-11} \text{ s}^{-1}$, $2.22 \times 10^{-10} \text{ s}^{-1}$ and $1.48 \times 10^{-10} \text{ s}^{-1}$, respectively. The behaviour of the modified electrodes suggest that the electron transport between the electrode interface and solution is faster as compared to bare electrode, evident by conductivity shown in bode plots (Figure 59 B). The bode plot (Figure 59B) confirms the electrical properties of the nano-material. The plot is in agreement with the nyquist plot, in which the modified electrode show more conductivity based on the phase angle of the material. As it is known that between 20 θ - 45 θ the material posses' semiconductor characteristic compare to 0 θ (insulator) and 90 θ which is of pure metal (more conducting). The Au/Ga₂Te₃-3MPA is more conducting due to the ($R_s + R_{ct} + CPE$) which are more predominant than in Au/Ga₂Te₃-3MPA/ssDNA which has a mixture of ($R_s + R_s + R_{ct}$) Figure 59 A. The total impedance, Z, data of Figure 59B confirmed the conductive nature of the Ga₂Te₃-MPA/Au. At log $F = 0$, the log Z(Ga₂Te₃-MPA/Au) = 4.3, whereas log Z(bare Au) = log Z(ssDNA/Ga₂Te₃-MPA/Au) = 4.7. This means that when the electrode systems were subjected to minimal frequency effects the QDs (which has additional metals in the system and without insulating oligonucleotide chains) is more conducting than the semiconducting gold electrode. There is a shift log 2 magnitude shift (increase) in frequency on changing from Au/Ga₂Te₃-3MPA electrode to Au/Ga₂Te₃-3MPA/ssDNA genosensor, due to the incorporation of the insulating probe-ssDNA in the sensor system. The values obtained

(decreased/shifted in frequency) from the graph are as follows: bare 1.99, Au/Ga₂Te₃-3MPA 1.74 and Au/Ga₂Te₃-3MPA/ssDNA 1.05; from these values it was clear that frequency is related to change in R_{ct} and thus conductivity due to a decrease in conductivity of the materials (Au/Ga₂Te₃-3MPA) (Figure 59 B) upon addition of ssDNA. In addition, the rate of electron transfer is also affected.

4.12 Sub-conclusion

As established, the morphology of the as-synthesised quantum dots was proven to be spherical with the lattice fringes of nanodots possessing single crystallinity and thus following the zinc-blende structure. The spherical Ga₂Te₃ quantum dots were proven to emit colours (green and brick red) at low to higher wavelengths and were found to be conductive, evident by the calculated band gap energies from both the UV-vis and Fluorescence spectroscopy. The conductivity of the quantum dots was confirmed by electrochemical impedance (EIS), apparent by higher phase angles and frequencies. From the obtained results it can be plainly stated that the 3MPA-Ga₂Te₃ quantum dots were synthesised successfully, apparent by the elemental composition and vibrational stretches observed from both the EDS, Raman, XPS and FTIR spectroscopy.



UNIVERSITY *of the*
WESTERN CAPE

CHAPTER 5

Results and discussion 2

Genosensor responses

5.1 Introduction

Quantum dots (QDs) have attracted vast interest owing to their many novel properties such as unique optical, electrochemical and electrochemical luminescence properties. One of the most dynamic trends is the application of QDs in electrochemical and biological sensing, due to their high surface-to-volume ratio, high reactivity and small size. Minor changes in the external environment will contribute to significant changes in particle valence and electron transfer. Furthermore, modifications can be made to the nanostructures to better suit their integration with biological systems, leading to such interesting properties as enhanced aqueous solubility, biocompatibility or bio-recognition. Based on these significant changes, QDs can be used to construct electrochemical biosensor with biological macromolecules, which is characterised by high sensitivity, rapid response and high selectivity. In this chapter, we review their applications in electrochemical luminescence sensors and DNA sensors.

5.2 Electrochemical responses of Her2/neu Oncogene genosensor

5.2.1 Detection mechanism

Cyclic voltammetry was employed to ascertain the successful attachment of DNA on the GCE/Ga₂Te₃-3MPA electrode and its ability to bind the target DNA (complimentary). Due to high sensitivity compared to cyclic voltammetry, square wave voltammetry was employed. The aim of the study was to compare the sensitivity, limit of detection as well as the linear dynamic range of the genosensor from the two systems (CV and SWV). The behaviour of the capture probe and different redox species at the electrode interface is shown by cyclic voltammograms, Figure 60A-B and 61A-B.

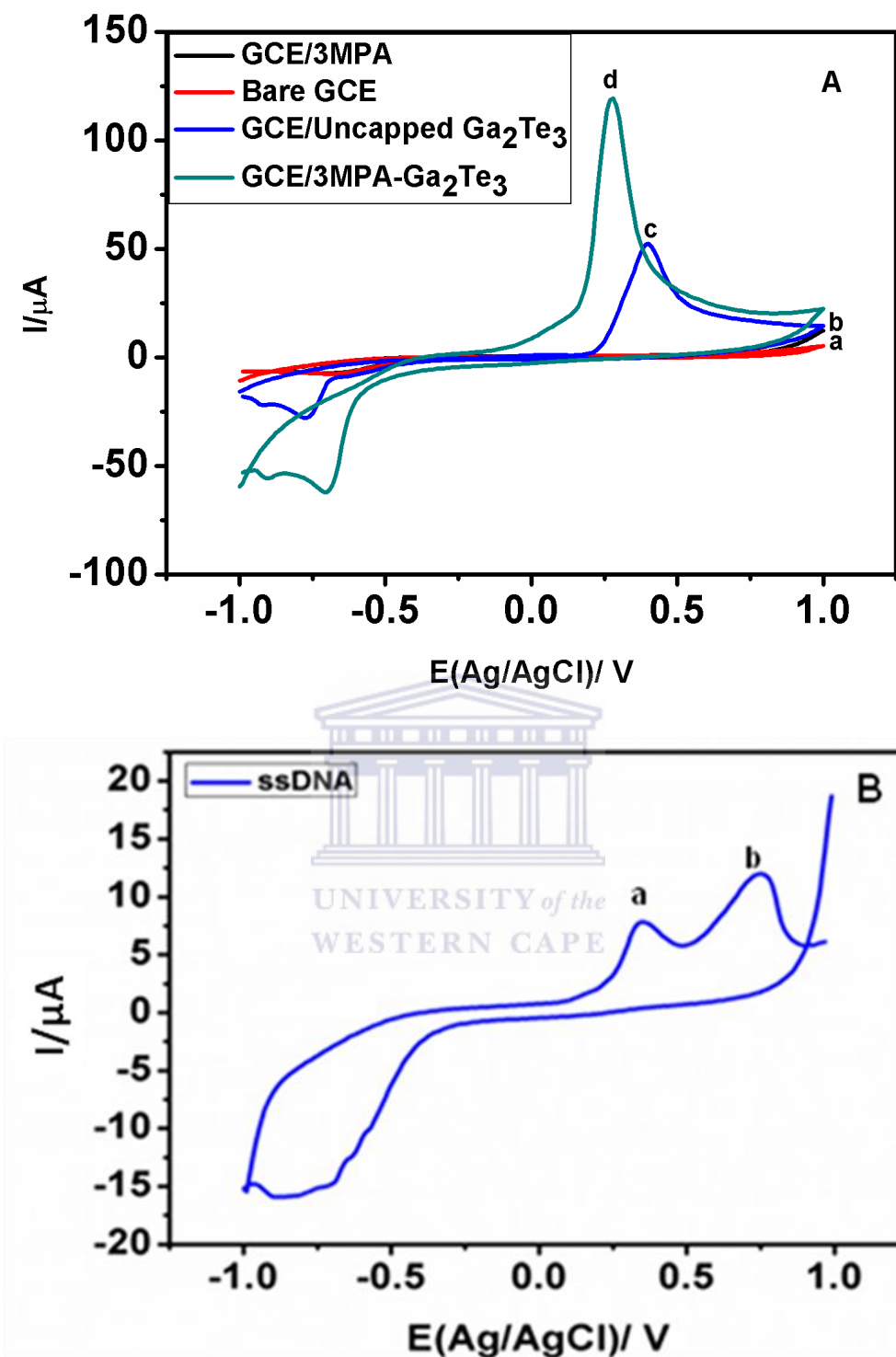


Figure 60. (A) Voltammetric plots of (a) bare GCE (b) GCE/3MPA (c) GCE/Ga₂Te₃ and (d) GCE/Ga₂Te₃-3MPA and (B) Cyclic voltammetry data of ssDNA on bare glassy carbon electrode (GCE/ssDNA), all the measurements were performed in PBS, pH 7.4 at a scan rate of 25 mV s⁻¹.

Redox properties of glassy carbon electrode immobilised 3MPA-Ga₂Te₃ quantum dots were investigated prior to DNA sensing. Figure 60 A shows the response for the bare, 3MPA, Ga₂Te₃ and 3MPA-Ga₂Te₃ modified glassy carbon electrodes. From the comparison of MPA capped (Figure 60 A, d) vs. uncapped quantum dots samples (Figure 60 A, c), a shift in peak potential from $E_p = 350$ mV to $E_p = 450$ mV (for Te oxidation process at $E_p = 270$ mV) as well as significant increment in anodic and cathodic current ($E_p = -700$ mV Ga³⁺ reduction wave) responses were observed, which may be attributed to the particle size effect. The capping agent may also have a co-catalytic effect, evident by an increase in peak current of the capped (GCE/Ga₂Te₃-3MPA) QDs compared to the uncapped (GCE/Ga₂Te₃). For comparison cyclic voltammetry response for ssDNA on bare glassy carbon electrode (GCE/ssDNA) in phosphate buffer solution was also recorded (Figure 60 B). The GC electrode was chosen specifically for this purpose due to additional gold oxidation and reduction peak currents which might interfere with the ssDNA peak currents (base pairs). As noted from Figure 60 B, there are prominent oxidation peaks at $E_p = 400$ mV (Figure 60 B, a) and $E_p = 800$ mV (Figure 60 B, b). These oxidation peaks are associated to the peak potentials of guanine as reviewed from literature. The redox properties of bulk materials, quantum dots and the genosensor response are as shown from Figure 61 A and B.

Figure 61A shows the cyclic voltammetry responses for (a) GCE/Te, (b) GCE/Ga₂Te₃-3MPA and (c) GCE/Ga₂Te₃-3MPA/ssDNA and (d) bare GCE in phosphate buffer solution. The GCE/Ga₂Te₃-3MPA electrode surface results in anodic peak current at 350 mV, which shifted to 500 mV, upon introducing the ssDNA. The ssDNA oxidation (Figure 60 B) was also observed at around this potential ($E_p = 400$ mV) as well as appeared at ($E_p = 850$ mV), and are associated with guanine. Since there's a shift and a catalytic effect observed at this peak potential ($E_p = 400$ mV), this peak was employed to monitor the interaction of the probe-modified electrode with the target DNA.

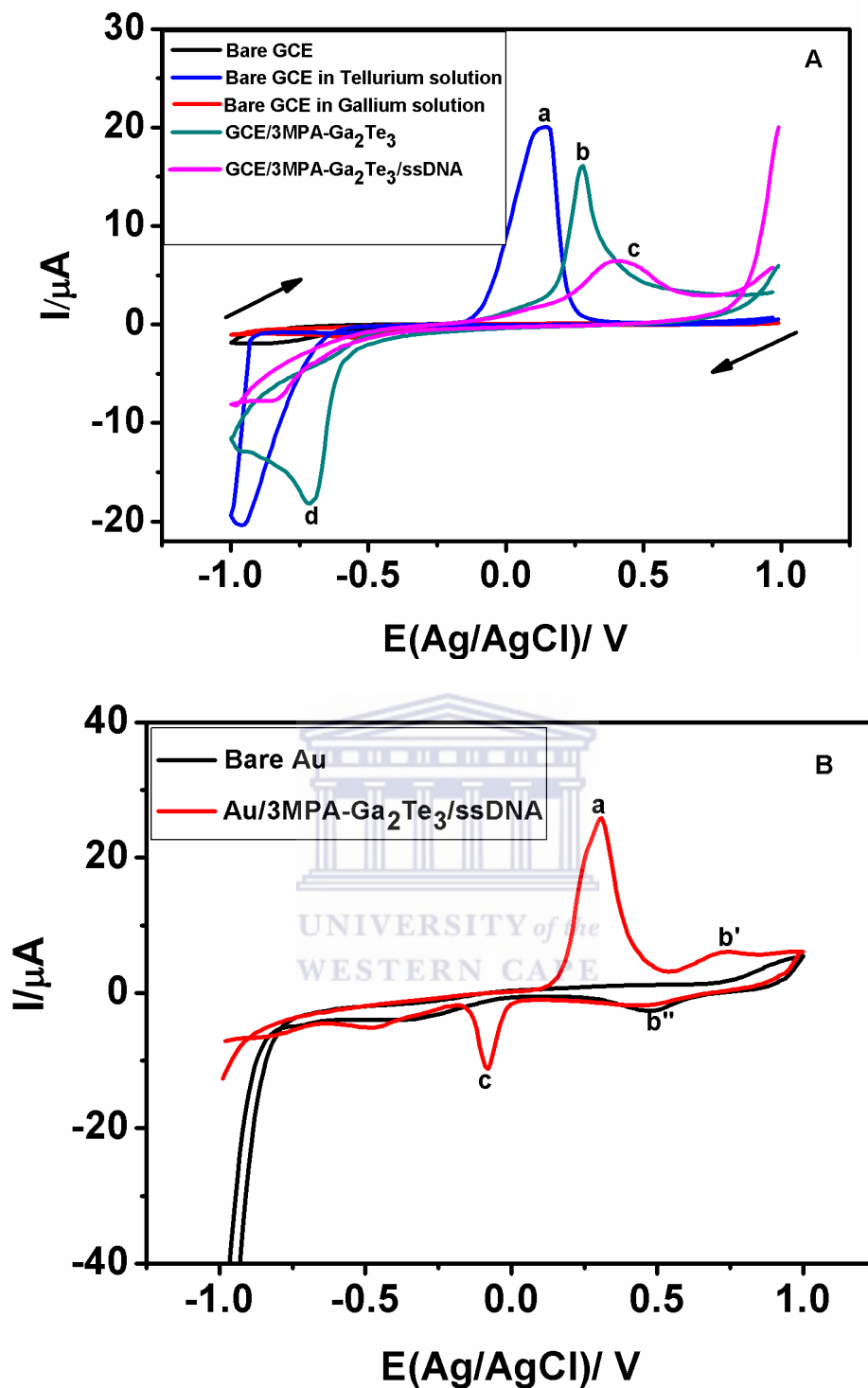
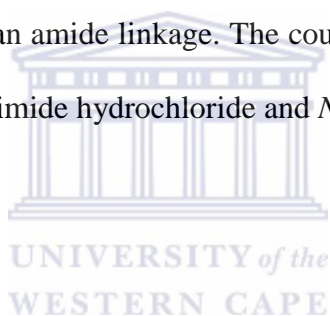
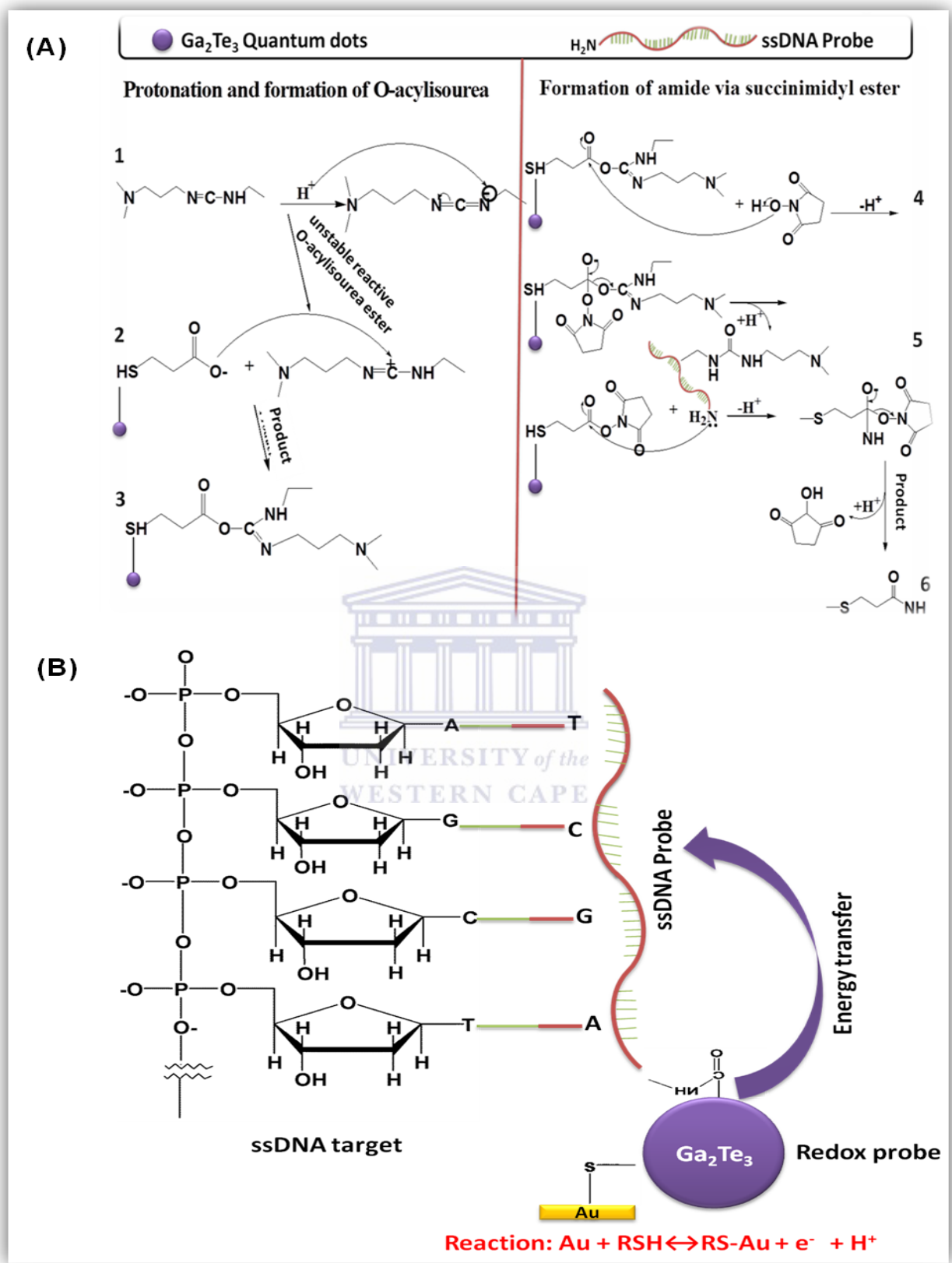


Figure 61. (A) Voltammetric plots of (a) GCE/Te, (b) GCE/ Ga_2Te_3 -3MPA and (c) GCE/ Ga_2Te_3 -3MPA /ssDNA and (d) bare GCE and. (B) Cyclic voltammetry response for Bare (Au) and Au/ Ga_2Te_3 -3MPA/ssDNA modified electrodes at a scan rate of 25 mVs^{-1} . All the measurements were performed in PBS, pH 7.4.

A comparison between GCE and Au electrodes was also carried out to see the associated electrochemistry, Figure 61 A and B. A clear reduction wave at -120 mV (peak labelled as c, Figure 61 B) on Au electrode was observed, which is associated with the oxidation products of the quantum dots. Whilst the redox reaction or the electrochemistry of gold electrode was also observed, Figure 61 B, b' and B, b''. Au electrode was used as the working electrode or transducer for further genosensor studies due to its capability with MPA interaction. Schematic 4 represent the reaction mechanism for Au electrode fabrication, which was selected due to its compatibility with the MPA capped quantum dots. We functionalised core Ga₂Te₃ quantum dots with short-chain 3-mercaptopropionic acid to render these nanodots semiconductor water-soluble. The surface provides coupling sites for amine modified DNA attachment, via the formation of an amide linkage. The coupling was promoted by 1-ethyl-3-(3-dimethylaminopropyl) carbodiimide hydrochloride and *N*-hydroxysuccinimide.





Schematic 4: Reaction mechanism of: (A) 3MPA-Ga₂Te₃ with linkers (EDC/NHS) and (B) Molecular structure of Au/3MPA-Ga₂Te₃/DNA–DNA assembly/interaction.

Figure 62 A and 62 B shows the response of the modified electrode at different scan rates. Gold metal solid electrodes (Au) are commonly considered to be inert [291; 292], and under certain electrochemical conditions these electrodes are highly active [292]. A general advantage of metal electrodes is their high conductivity. Gold electrodes offer a relatively large anodic potential ranges and very favourable electron transfer kinetics, but they have a limited cathodic potential range in aqueous solutions compared to glassy carbon [293; 294]. Because of the low hydrogen overvoltage at these noble metal electrode limits, cathodic ranges in aqueous solvents are limited (depending on the pH) [294]. In comparison to gold electrode, glassy carbon electrode is slow in electron transfer rates than gold electrodes [295]. Typical cyclic voltammograms of bare Au/GCE electrodes with preadsorbed fractions of Ga₂Te₃ different sizes in buffer solutions pH 7 are observed Figure 62 A and B. The oxidised peak current ($I_{p,c}$) associated with Ga₂Te₃ quantum dots at $E_p = 500$ mV increased as a function of increasing scan rate (Figure 62 A, d and 62 B, a). These results show that the semiconductors adsorbed on the surface of the electrode. Cyclic voltammetry with redox properties of gold electrode were observed with an oxidation peak potential ($I_{p,a}$) at $E_p = 1000$ mV and a reduction peak potential ($I_{p,c}$) at $E_p = 500$ mV, Figure 62 A, b' and b''. Shoulders or small reduction peaks were observed at oxidation peak potential ($I_{p,a}$) of $E_p = -100$ mV which can be due to the products of QDs, $E_p = -500$ mV which was associated with redox properties of Ga³⁺ (Figure 63 A, d and 63 B, a) and at $E_p = -850$ mV which was associated with redox properties of Te²⁻, Figure 63 A, e and 63 B, d. Nonetheless, an oxidation peak potential ($I_{p,a}$) at $E_p = 400$ mV was chosen as the peak of interest, due to an increasing in peak current when 3MPA-Ga₂Te₃ was introduced on the electrode surface (Figure 63A, a and 63 B, a). From both the voltammograms a significant increase in current as a function of scan rate was observed.

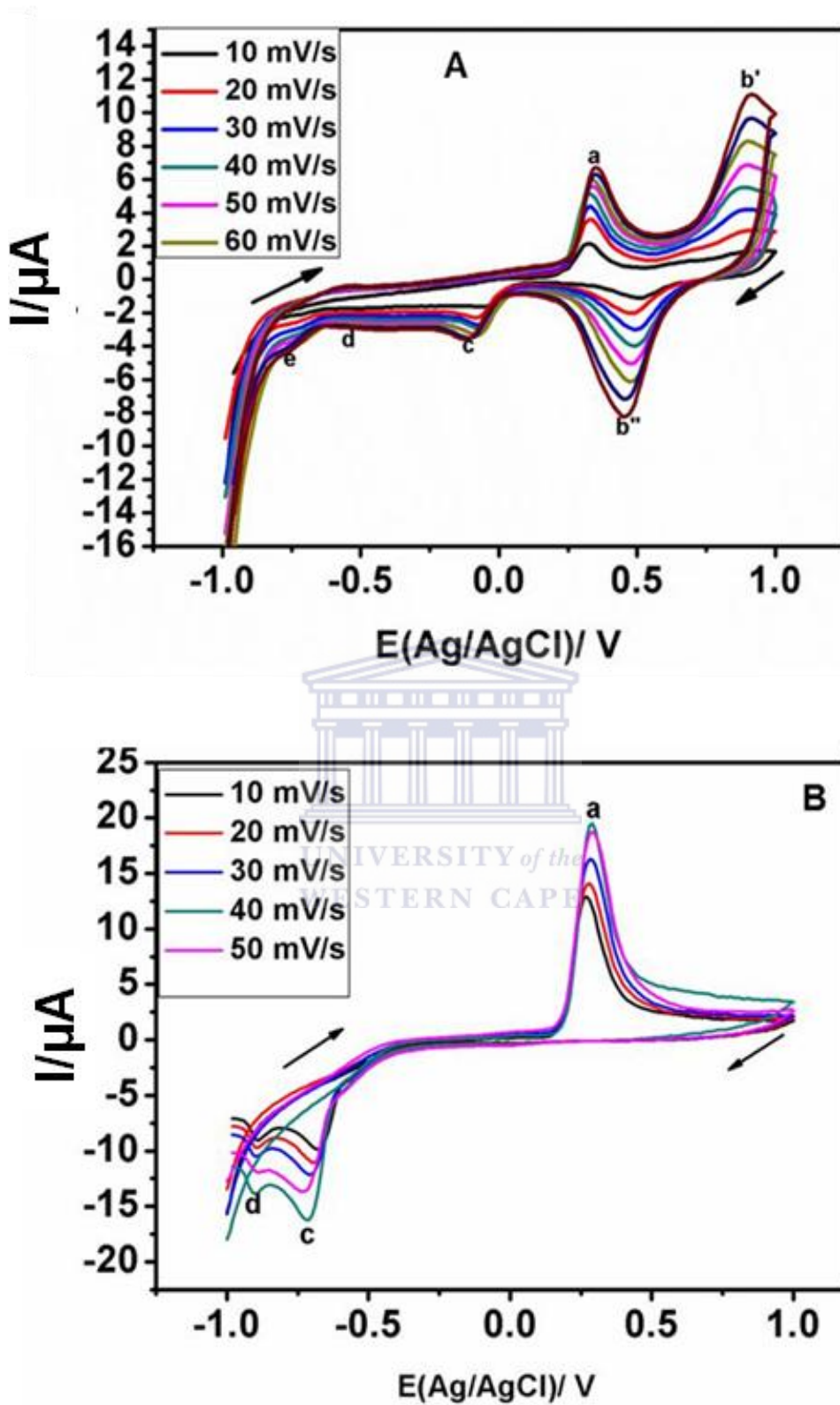
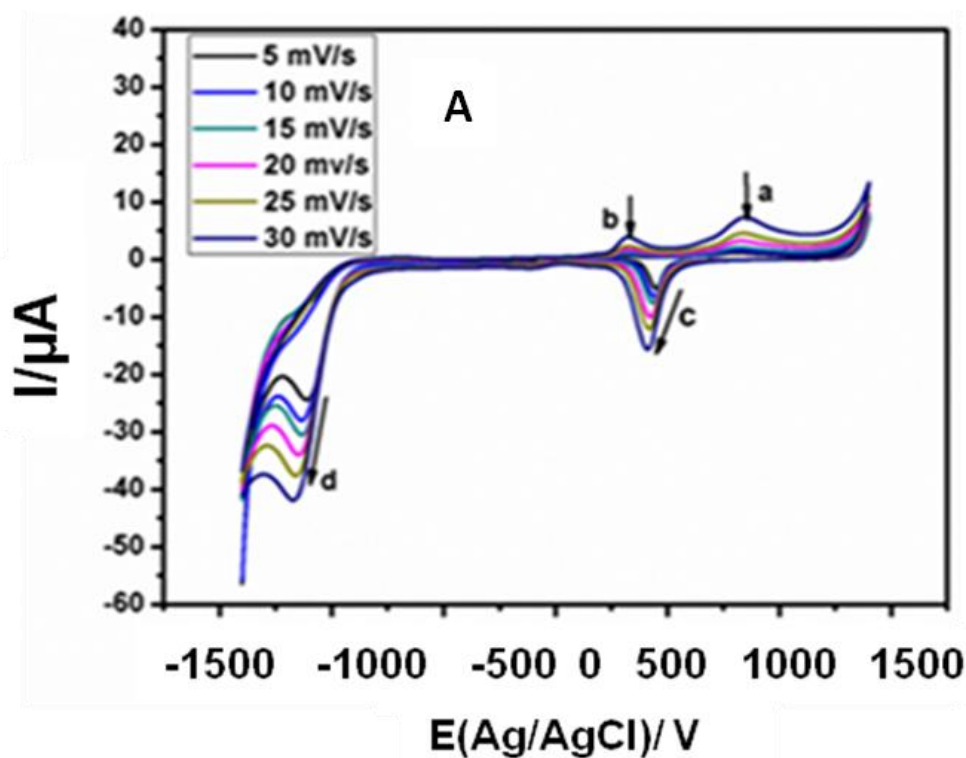


Figure 62. Voltammetric plots of (A) Au/Ga₂Te₃-3MPA and (B) GC/Ga₂Te₃-3MPA. All measurements were performed in PBs pH = 7.4 at a scan rate of 5-30 mV s⁻¹.

Genosensors (or DNA biosensors) are devices that combine a biological recognition agent (ssDNA, also called a probe) that confers selectivity, and a transducer that provides sensitivity and converts the recognition event into a measurable electronic signal. Electrochemical DNA devices have recently received considerable attention in the development of sequence specific DNA biosensors through combination of two complimentary single nucleic acids into a single molecule (hybridisation). Figure 63 A shows the response of the genosensor and the behaviour thereof. Cyclic voltammetry was carried out at different scan rates. The redox properties of gold electrode were observed with a oxidation peak potential ($I_{p,a}$) at $E_p = 1000$ mV and a reduction peak potential ($I_{p,c}$) at $E_p = 500$ mV, Figure 63 A, a and c. There is a clear reduction peak observed at $E_p = -800$ mV which was associated with redox properties of Ga^{3+} , Figure 63 A, d. However, an oxidation peak potential ($I_{p,a}$) at $E_p = 500$ mV was chosen as the peak of interest, due to an increasing in peak current when 3MPA- Ga_2Te_3 was introduced on the electrode surface (Figure 63A, b). An increase in current was observed as a function of increasing scan rate.



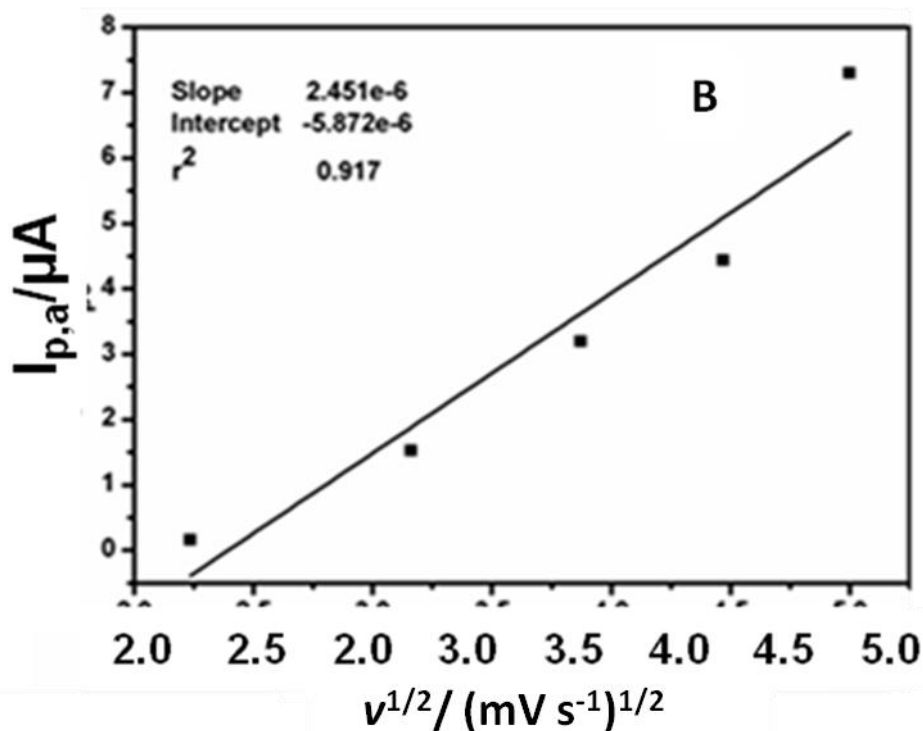
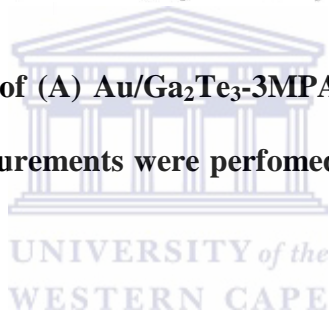


Figure 63. Voltammetric plots of (A) Au/Ga₂Te₃-3MPA/ssDNA and (B) Randel-Sevčik plot of data from ‘A’. All measurements were performed in PBs pH = 7.4 at a scan rate of 5-30 mV s⁻¹.



From the calibration plot of current vs. the root of scan rate (Figure 63 B), several parameters were calculated in order to show the behaviour of the genosensor. The system was found to be diffusionally controlled, evident by an increase in scan rate as a function of current. The calculated diffusion coefficient was found to be $3.42 \times 10^{-12} \text{ cm}^2 \text{ s}^{-1}$ with the correlation coefficient of (r^2) 0.92. The values were calculated using an irreversible equation (eq. 3). The Laviron equation (eq. 4) was used to demonstrate the relationship between the current and amount of adsorbed species at a solid surface. The peak current is directly proportional to the surface coverage, Γ and the potential scan rate, ν [296]. The scan rate dependence plot of the voltammetric peak currents of Ga₂Te₃ confirmed the behaviour of the system and its response are plotted in Figure 63 B.

The surface coverage of the genosensor was calculated using equation 2 above and was found to be $3.42 \times 10^{-8} \text{ cm s}^{-1}$. The sensitivity and the detection limit of the system were calculated to be $2.45 \times 10^{-6} \text{ nA M}^{-1}$ and 2.22 nM. These results suggest that our system can be able to detect samples or material from lower (nM) to higher (μM) concentrations. The electron transfer coefficient was calculated to be $2.45 \times 10^{-2} \text{ cm s}^{-1}$, using the following equation (eq. 28)

$$k_s(E_p) = 2.18 \left[\frac{D\alpha n F v}{RT} \right]^{1/2} \quad (28)$$

where, k_s is the electron transfer rate constant and other parameters are as discussed earlier.

5.2.2 Cyclic and square wave voltammetry responses

DNA biosensors, also known as genosensors, are analytical devices for the detection of specific DNA “target” sequences in solution, upon hybridization of the targets with complementary “probes” immobilized on a solid substrate [297; 298] or hybridization sensor that confirms the sequence specificity of the amplified product within about 45 min, even if the product is present in extremely small concentrations [299; 300]. A DNA sensor based on electrochemical cyclic voltammetry is a device that transduces changes in interfacial properties between the electrode and the electrolyte solution induced by DNA hybridization, conformational changes or DNA damage into an electrical signal. Different electrochemical systems/techniques were employed to ascertain the successful attachment of DNA on the Au/Ga₂Te₃-3MPA electrode and its ability to bind the target DNA (complimentary). Due to high sensitivity compared to cyclic voltammetry, square wave voltammetry was also employed. The behaviour of the genosensor with the target analyte at the electrode interface is as shown in Figure 64 A-B and 65 A-B.

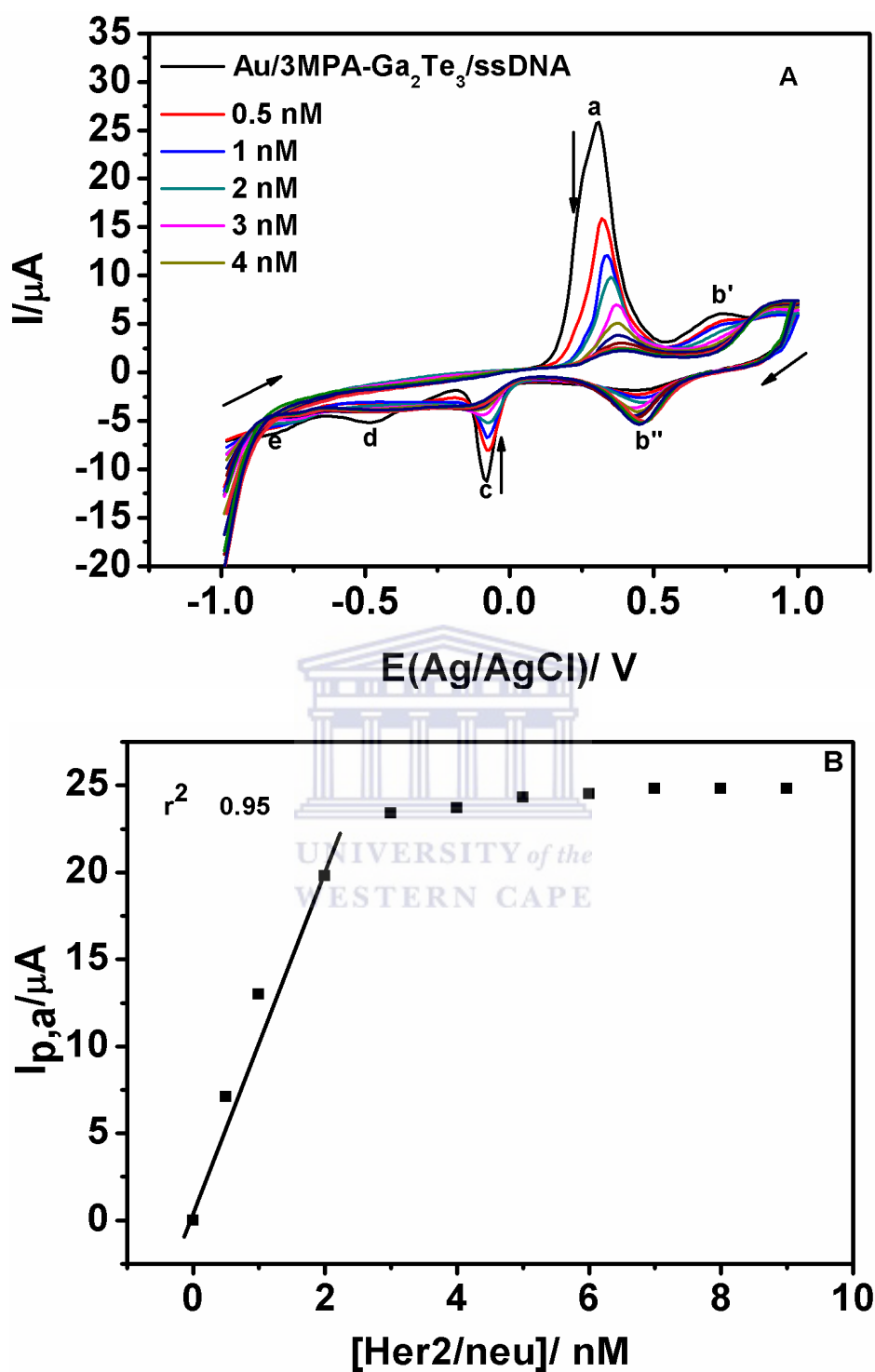


Figure 64. Voltammetric plots of Au/3MPA-Ga₂Te₃/ssDNA at different concentration of Her2/neu oncogene (0.1→1), (A) CV responses to Her2/oncogene and (B) Calibration curves of Her2/oncogene genosensor in 'A'.

Cyclic voltammetry was carried out to determine the binding event of the probe-DNA and the target DNA, which is our complementary DNA. The oxidation peak potential ($I_{p,a}$) at $E_p = 500$ mV (Figure 64 A, a) was used as the peak of interest. As we introduce different concentrations of the target molecule, the peak current decreases (Figure 64 A), suggesting interaction between the probe-DNA and the complementary DNA. This interaction was by stabilising the immobilized probe DNA on the surface of the transducer, by covalently attaching it through a linker bound to one of its ends. To achieve this, the probe DNA and the surface onto which the DNA is to be immobilised may be modified by introducing reactive functional groups that will allow for covalent coupling [301]. Several functionalities on either the electrode or the probe ssDNA have thus been reported for stable anchoring of the probe on the electrode surface. Commonly used reactive functional groups include thiols, carboxyls and amino groups among others [302]. Covalent coupling via functionalized probe or electrode surfaces are usually accompanied by chemical activation steps, which have also been developed according to the combination of the introduced functional groups [303; 304]. After the surface has been activated, functionalised and modified with the probe DNA, the target analyte was introduced to the system, in order to measure the behaviour of current with respect to concentration. The binding-event occurred after the introduction of 0.5 nM of the target molecule (Figure 64 A, a). The plot showed a decrease in current as the concentration increases, which confirm the binding of the analyte and the probe DNA at the electrode interface. A shift in peak potentials (50 mV) was also observed, which is a characteristic of electrode reactions having slow electron transfer kinetics. The binding behaviour of the two DNAs was also confirmed from the calibration curves of Her2/oncogene genosensor (Figure 64 B). It was clear from the plot that the sensor reached its point of saturation around 3 nM, suggesting that there is a little binding taking place between the two DNAs.

The sensitivity of the genosensor was found to be $7.59 \times 10^{-2} \mu\text{A ng}^{-1} \text{mL}^{-1}$ with regression coefficient of ($r^2 = 0.95$), linear range was found to be in the range of 0.5 - 3.0 nM and its detection limit was calculated to be 0.2 pg mL^{-1} , Figure 65. The results obtained were found to be significantly low than the physiological value of the Her2/neu in blood and comparatively low than literature values [11; 12].

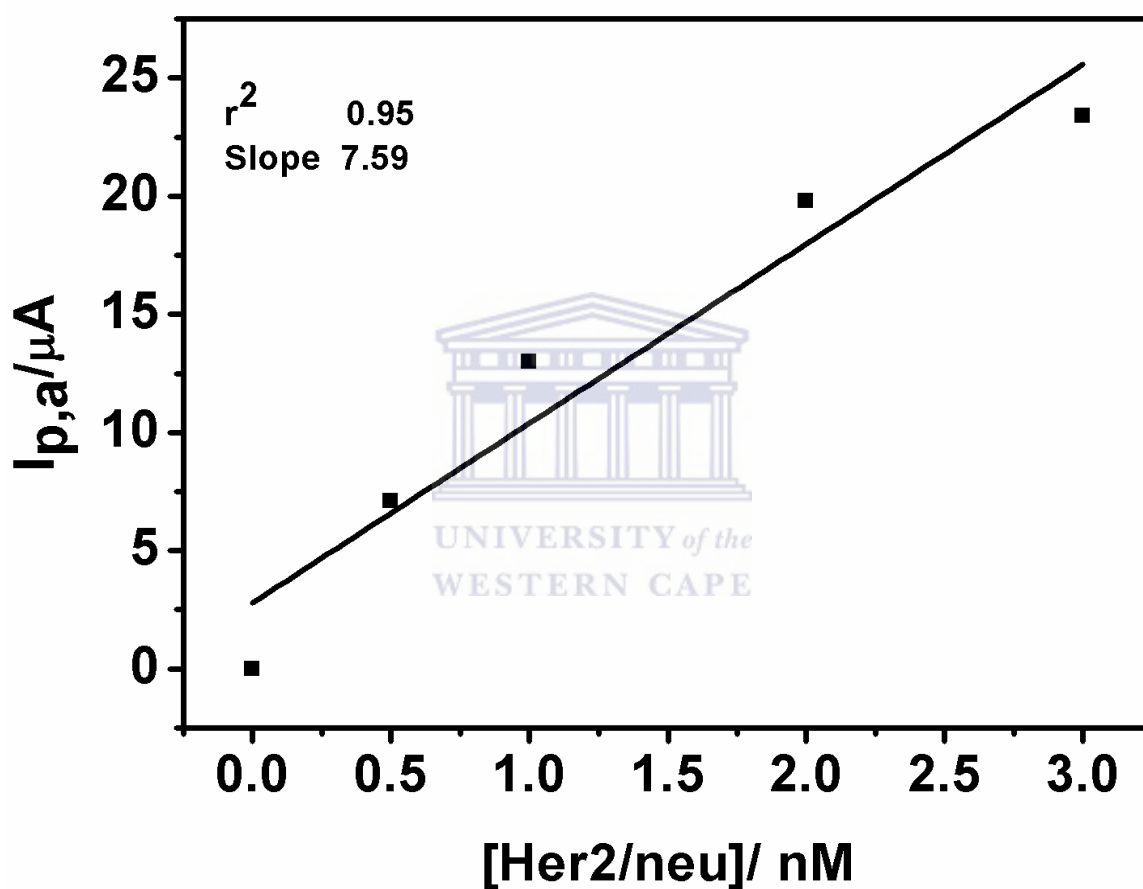
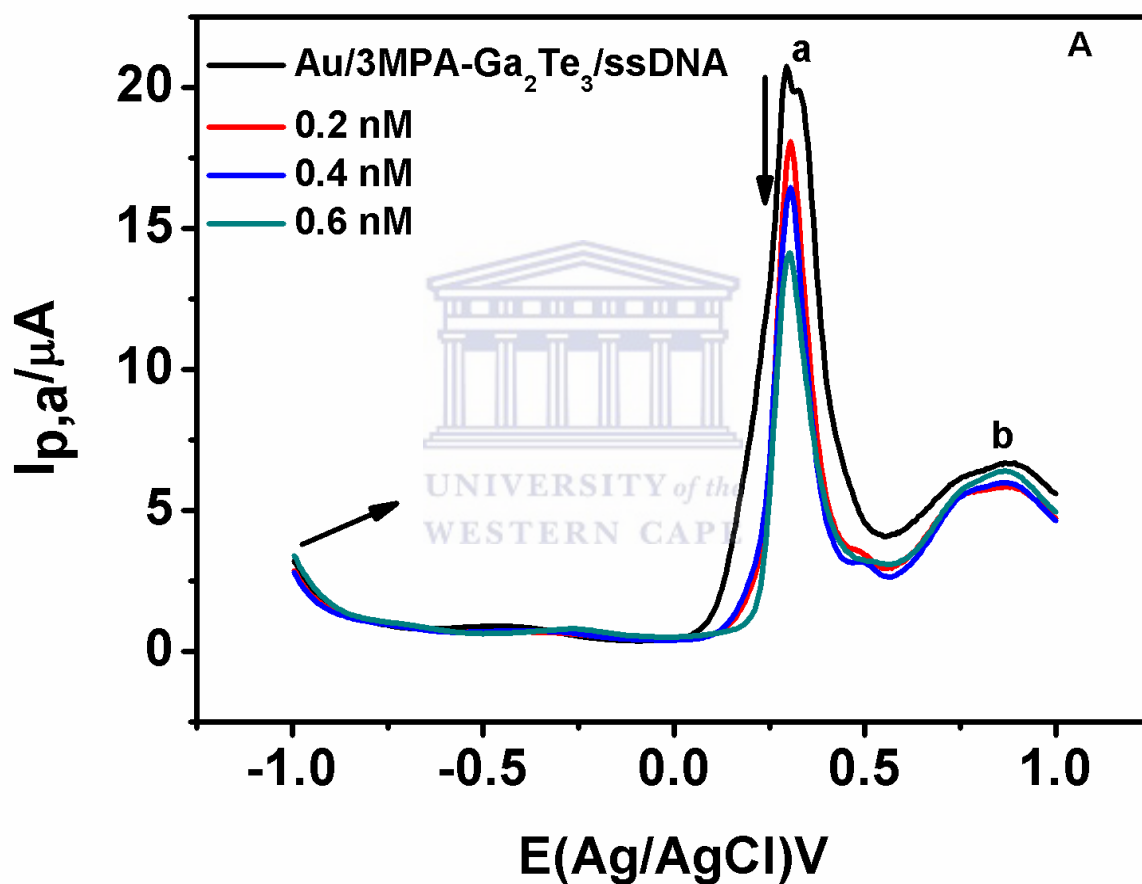


Figure 65. Calibration curve of Her2/oncogene with data from ‘64 B’.

Square wave voltammograms of Au/3MPA-Ga₂Te₃/ssDNA at different concentration of Her2/neu oncogene are shown in Figure 66 A. SWV showed two unresolved peaks, at oxidation peak potential ($I_{p,a}$) of $E_p = 400 \text{ mV}$ and $E_p = 900 \text{ mV}$ (Figure 66 A, a and b). These two peaks are denoted to the 3MPA-Ga₂Te₃/ssDNA and the unreacted tellurium (Te⁰), respectively.

The two peaks merged into single distinctive peak after the addition of target analyte. After each addition of the target analyte, the peak current at $E_p = 400$ mV decreased with increasing concentration (Figure 66 A, a). The saturation point of the genosensor was reached upon the addition of 2 nM of the target analyte, apparent by slight decrease in current after adding 3 nM of the target analyte, Figure 66 B.



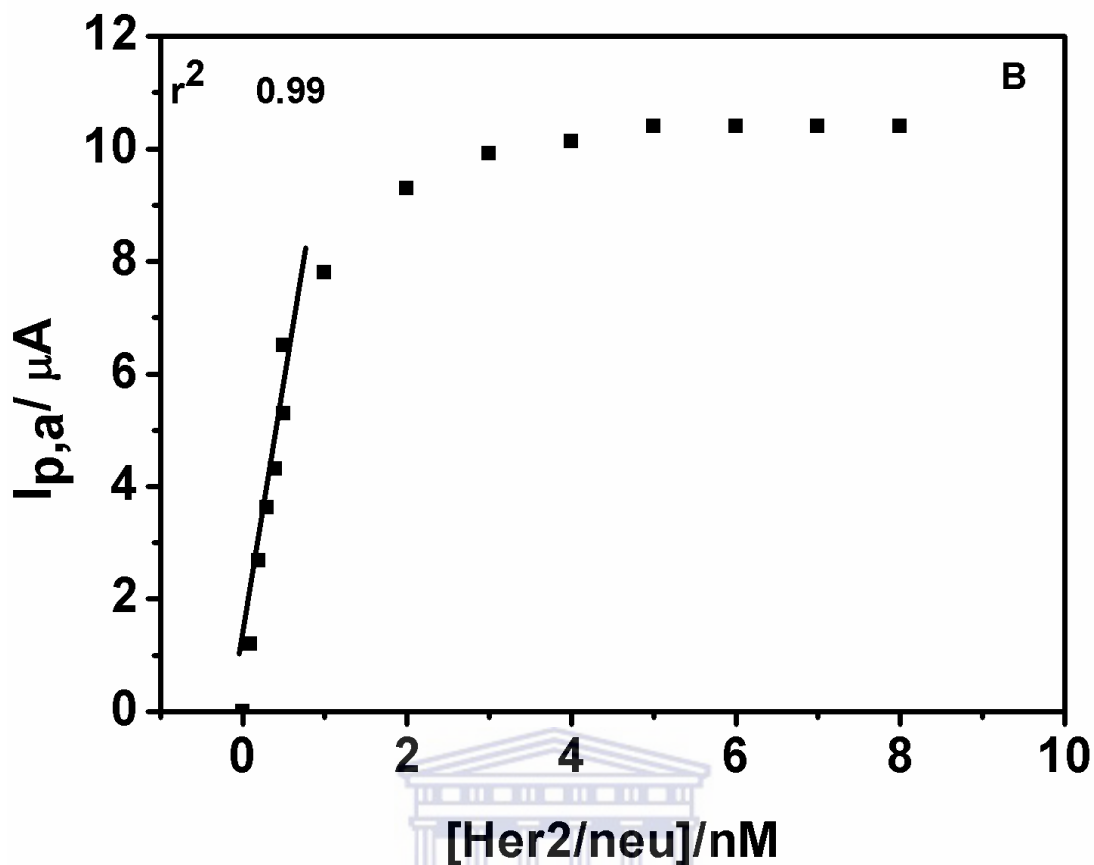


Figure 66. Voltammetric plots of Au/3MPA-Ga₂Te₃/ssDNA at different concentration of Her2/neu oncogene (0.1→1), (A) SWV responses to Her2/oncogene and (B) Calibration curves of Her2/oncogene genosensor in 'A'.

From the calibration curve (Figure 66 B and 67), the sensitivity and the linear range of the system were found to be 10.49 $\mu A \text{ ng}^{-1} \text{ mL}^{-1}$ and 0.1 - 1.0 nM respectively ($r^2 = 0.99$). The detection limit of the genosensor from the SWV was calculated to be 0.2 $\mu g \text{ mL}^{-1}$. These values were obtained by reploting the linear dynamic range values from Figure 66 B and the calibration curve obtained is shown in Figure 67. Table 1 shows the summary of the results obtained and compared with literature. The proposed genosensor proven to be better and well within limits for HER2/neu detection (2 - 15 ng mL^{-1}) and is comparable with literature values [11; 12].

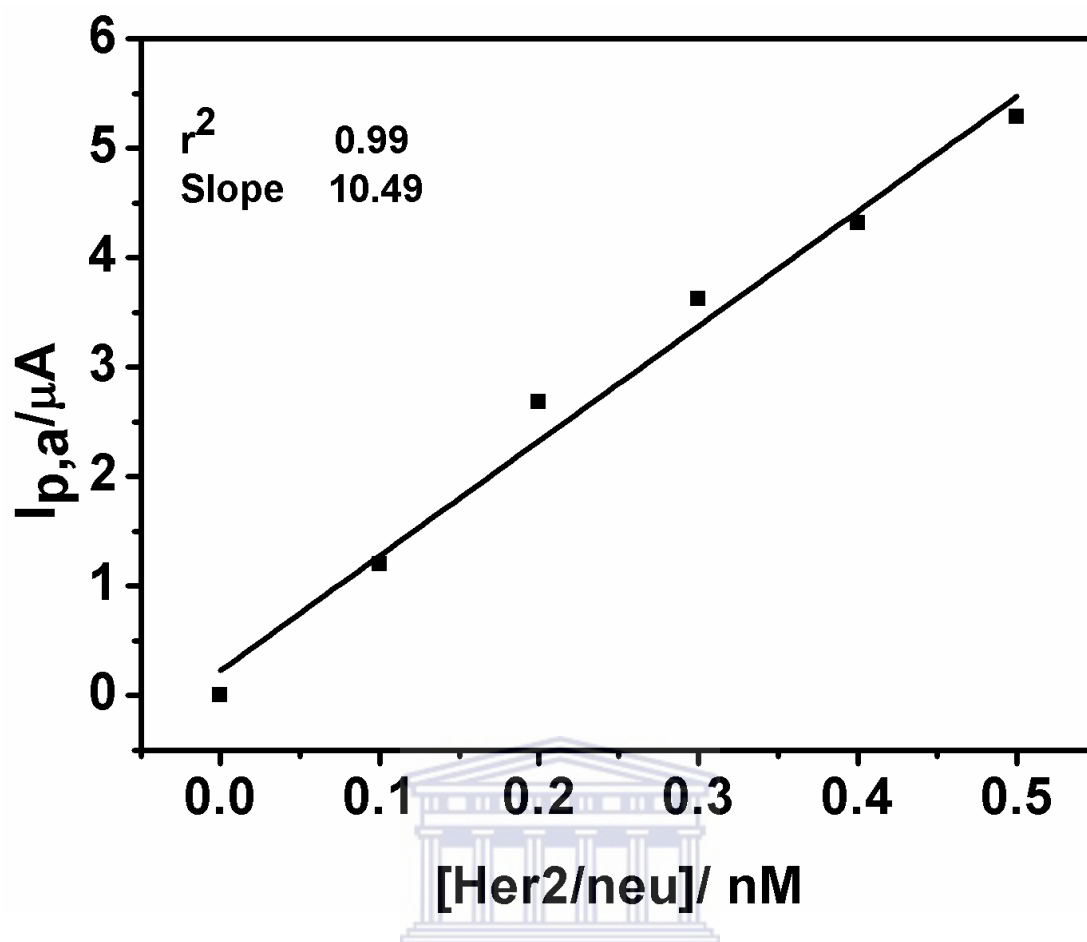
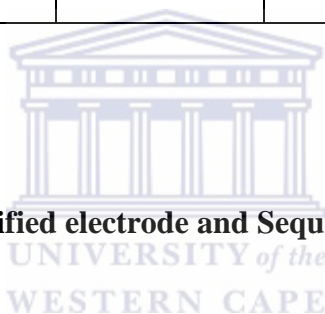


Figure 67. Calibration curves of Her2/oncogene with data from '66 B'.

The results demonstrated the potential of the proposed system as an effective genosensor in detecting the target analyte. Some of the systems which were used in detecting Her2/neu oncogene are listed in Table 6. The two systems showed very similar limit of detection but different dynamic range. It is well known that square wave voltammetry has a higher sensitivity than cyclic voltammetry hence a difference in the data obtained. The genosensor's *DLR* is comparable to those reported in the literature for other methods. More importantly, the *DLR* values of the genosensor are within the physiological Her2/neu oncogene concentrations in the blood of normal (2-15 ng mL⁻¹) and breast cancer (15 - 75 ng mL⁻¹) patients [11; 12].

Table 6. Comparison of different systems for detection of HER2/neu oncogene (The original values are all converted to ng mL⁻¹)

Sensors	<i>DLR</i> (ng mL ⁻¹)	Sensitivity (ng mL ⁻¹)	<i>LOD</i> (ng mL ⁻¹)
Genosensor (Ga ₂ Te ₃ -3MPA/ssDNA)	1.8-740	1.0 - 2.80×10 ⁻²	0.00007
PZT/glass PEMS [305]	-	13	111
PCR [306]	28	0.06	5.5
ELISA [307; 308; 309]	185 - 46250	100.00	0.1
Fluorescent silica nanosphere [310]	18 - 185	-	1.9
FISH and IHC [307]	-	-	>0.01



5.2.3 Stability of the probe-modified electrode and Sequence-specific hybridisation studies

Cross-reactivity (Selectivity and non-specific adsorption) experiments were performed to assess whether the Au/Ga₂Te₃-3MPA/ssDNA responded selectively to the complementary target (Figure 68). In this work, the complementary target DNA, the single-base mismatch target, the three-base mismatch target, and the non-complementary sequence DNA were used to study the sequence-specificity of the sensor. The CVs of the genosensor (Au/Ga₂Te₃-3MPA/ssDNA) responses for 5 nM of the different target DNA molecules are plotted in Figure 68.

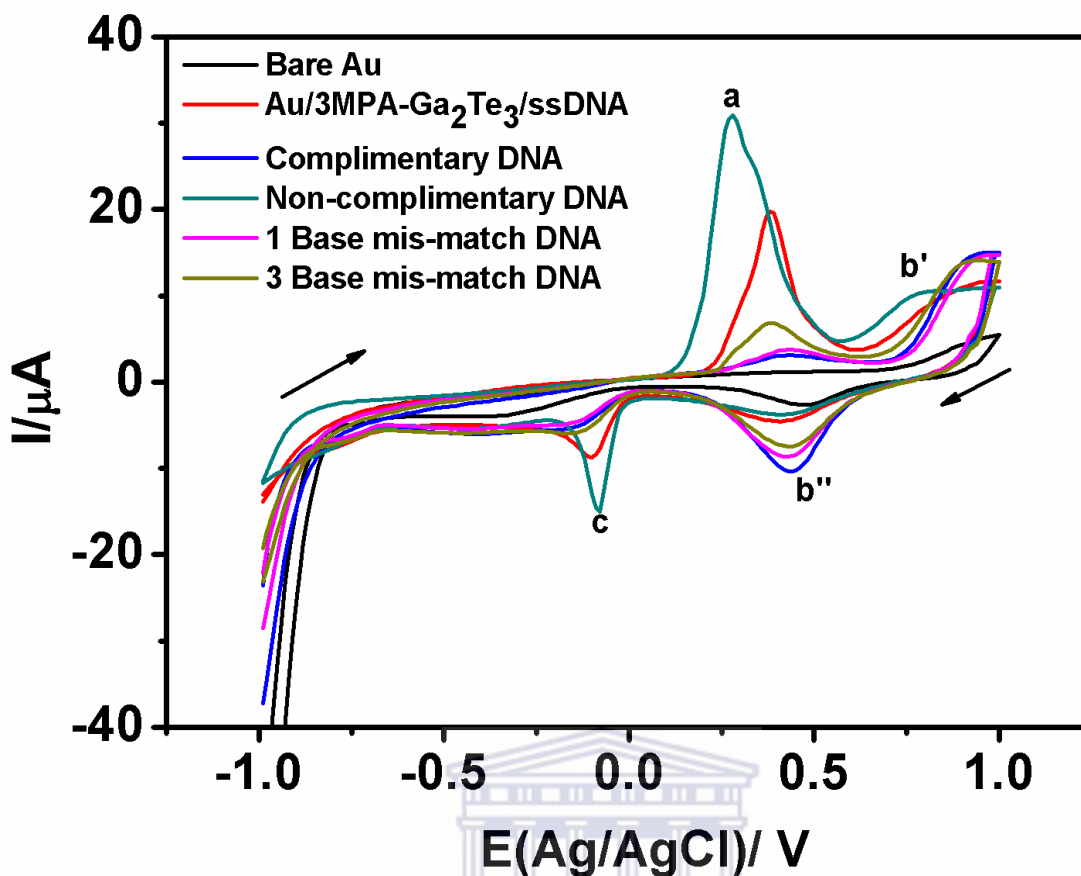


Figure 68. Voltammetric plots of Au/3MPA-Ga₂Te₃/ssDNA in 0.1M PBS pH = 7: at different analytes (0.5 nM) of Her2/oncogene, (Complimentary, 1-Base mis-match, non-complimentary and 3-Base mis-match) (A) Responses to Her2/oncogene.

The sensor exploits selective binding of certain biomolecules. The high specificity and affinity of these biochemical binding reactions lead to highly selective and sensitive sensing devices. Figure 68 shows the comparison of the peak currents between the blank and the four target DNA sequences with the same concentrations 5 nM. The oxidation signal responded differently with different analytes. These findings indicate that some of the analytes hybridization did not occur. A decrease in signal was observed when the probe electrode was hybridised with the 3-base mismatch and non-complimentary sequence, suggesting that hybridisation occurred at the electrode interface.

However, there was a high decrease in signal after the probe DNA was hybridised with both the complimentary and 1-base mismatch sequences. This could be due to the fact that the target analytes and the capture probe are fully bound. These results demonstrated that the complementary target sequence could form double-stranded DNA with the probe-DNA producing a significant decrease in signal. The stability and reproducibility of the genosensor (Au/3MPA-Ga₂Te₃/ssDNA) was carried out as shown in Figure 69.

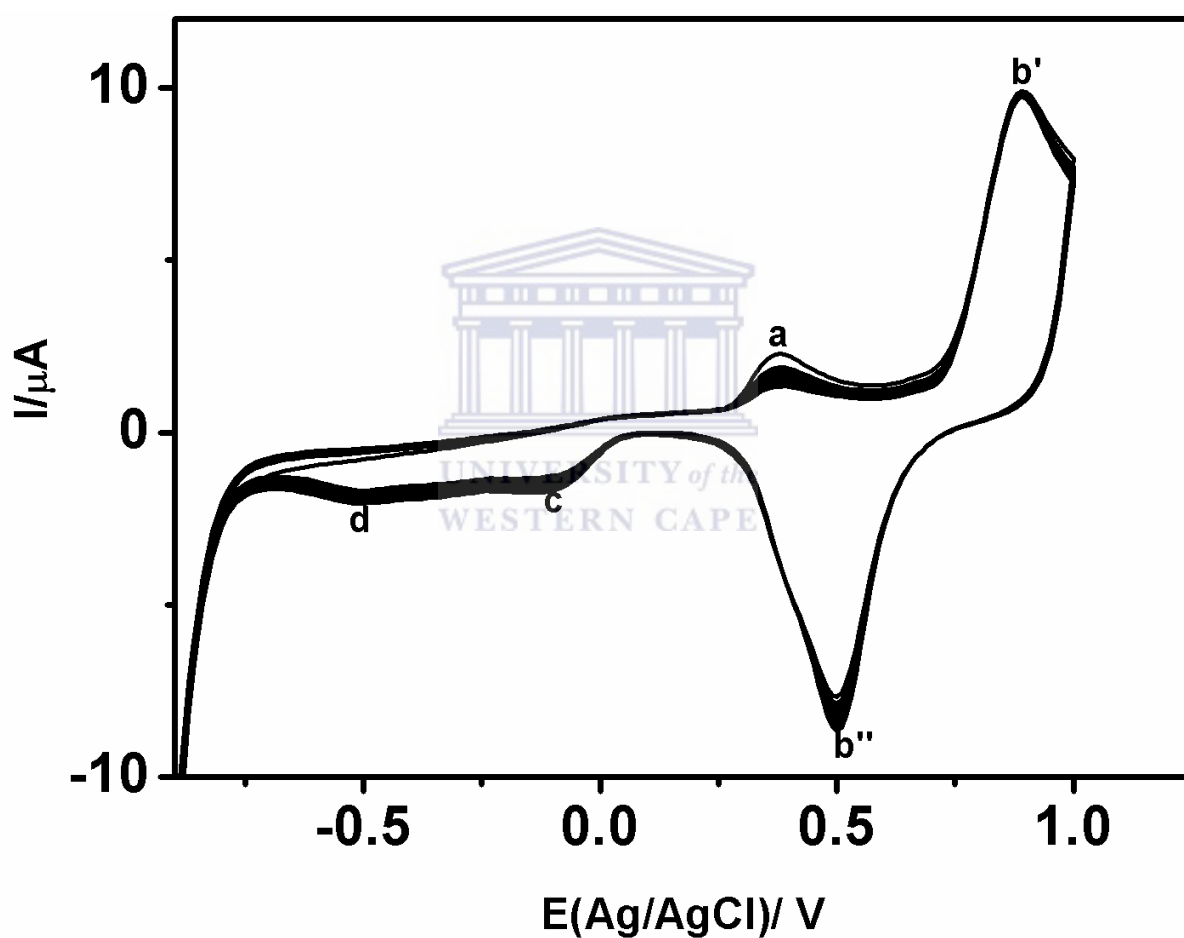


Figure 69. The stability of the genosensor (3MPA-Ga₂Te₃/ssDNA) in 0.1M PBS pH = 7: at a scan rate of 25 mV s⁻¹.

From Figure 69, Cyclic voltammograms of the redox properties of gold electrode were observed with an oxidation peak potential ($I_{p,a}$) at $E_p = 1000$ mV and a reduction peak potential ($I_{p,c}$) at $E_p = 500$ mV, Figure 69 b' and b''. And unresolved reduction peaks were observed at reduction peak potential ($I_{p,a}$) of $E_p = -100$ mV which can be due to the products of the QDs and $E_p = -500$ mV which was associated with redox properties of Ga^{3+} (Figure 69 d). However, the detection signal at ($I_{p,a}$) of $E_p = 400$ mV was chosen to study the stability or reproducibility of the sensor. The stability and reproducibility of the probe-modified electrode was done by leaving the electrode for 5 days in the freezer (20 °C) and cycling the modified electrode 20 times, Figure 69. After been used for CV analysis, the same electrode was used after several days and the reduction peak of the sensor was observed. The peak current of the electrode started decreasing but remained constant after the several cycles (Figure 69). Statistical analyses were performed based on the stability of the sensor. The average sum of $n = 9$ was calculated to be 16.98, whilst the calculated standard deviation (SD) and the mean values were calculated to be 0.23 and 1.69, respectively. The results suggest that the genosensor only degraded by 23%. Thus the modified electrode proved that our electrode can be used for several analysis without been depleted fully.

5.2.4 Impedimetric responses

In impedimetric genosensor, the presence of the target molecule causes electrical changes (e.g. capacitance or resistant changes) on the sensing surface. Figure 70 shows nyquist plots of modified Au electrode (Au/3MPA- Ga_2Te_3 /ssDNA) in the presence of target DNA. Compared with the bare Au electrode in PBs the modified Au electrode had a small charge resistance, as shown in our earlier results (Figure 59 A).

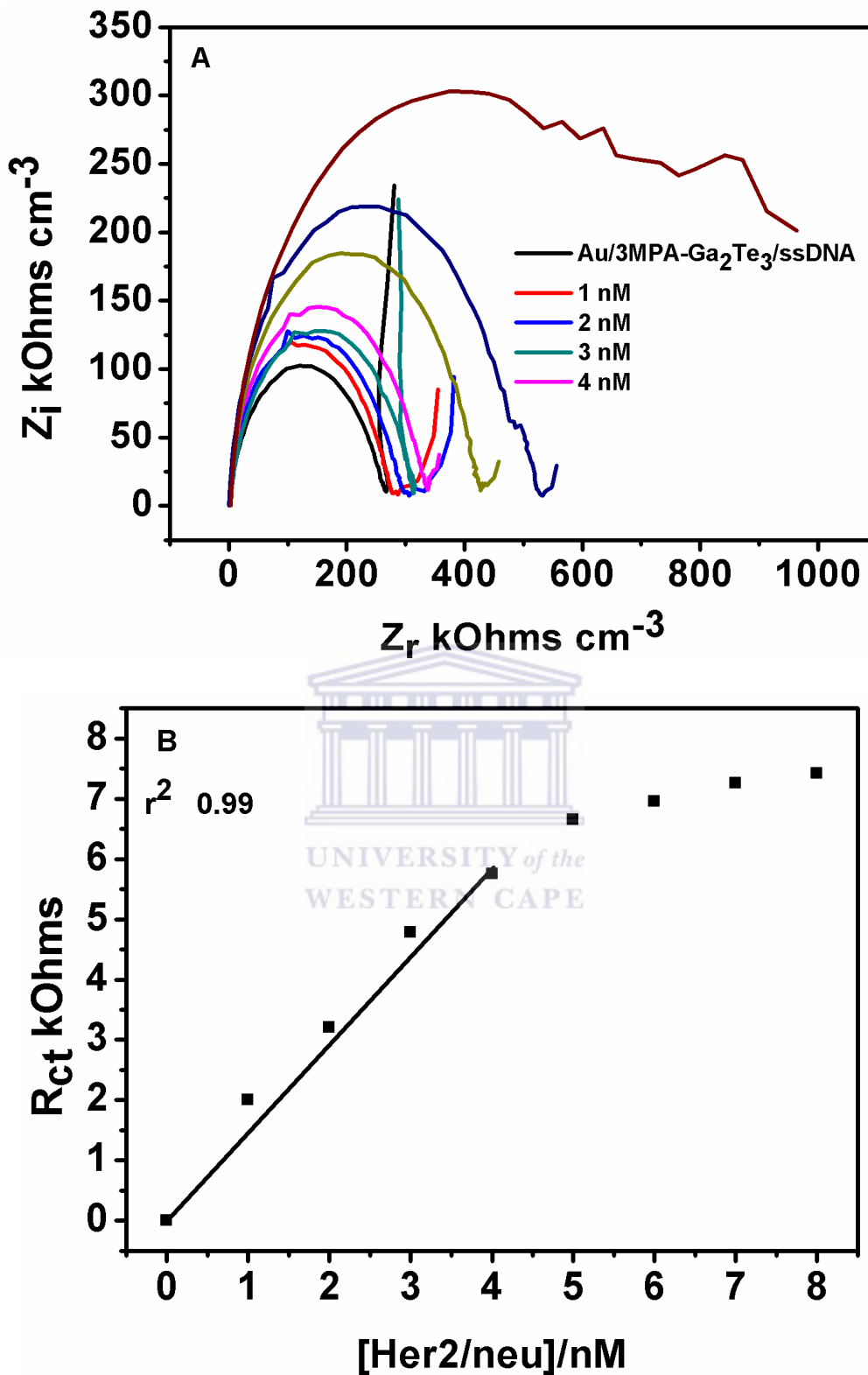


Figure 70. EIS/Nyquist plots of Au/3MPA-Ga₂Te₃/ssDNA in 0.1M PBS pH = 7: at different concentration of Her2/oncogene (A) Responses to Her2/oncogene and (B) Calibration curve of Her2/oncogene in 'A'.

When the probe DNA was introduced on the modified Au surface becoming Au/3MPA-Ga₂Te₃/ssDNA, the diameter of semicircle increased, suggesting that the probe DNA film acted as an insulating layer that made interfacial charge transfer inaccessible Figure 70 A. Then, different concentrations of the target DNA strand were introduced into the system and the diameters of semicircles become higher than that of Au/3MPA-Ga₂Te₃/ssDNA, showing that another insulating molecule was added into the system. The charge transfer resistance (R_{ct}) values increased with increasing concentration of the target DNA in the hybridisation reaction (Figure 70 B). The behaviour suggests a sluggish electron transfer. The sensitivity of the genosensor was found to be $1.43 \Omega n M^{-1}$ ($r^2 = 0.99$). Its linear range was found to be 0.5-4.0 nM which is in good agreement with the one obtained in cyclic voltammetry and its limit of detection was calculated to be 5.00×10^{-6} nM, Figure 71.

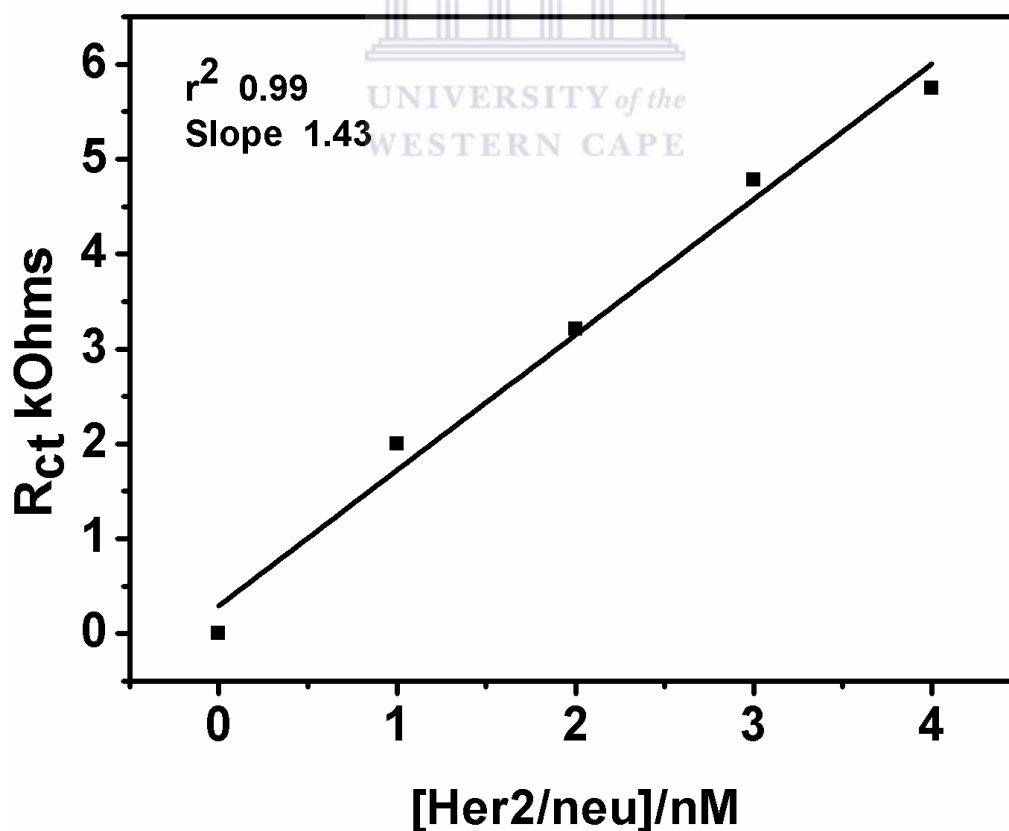
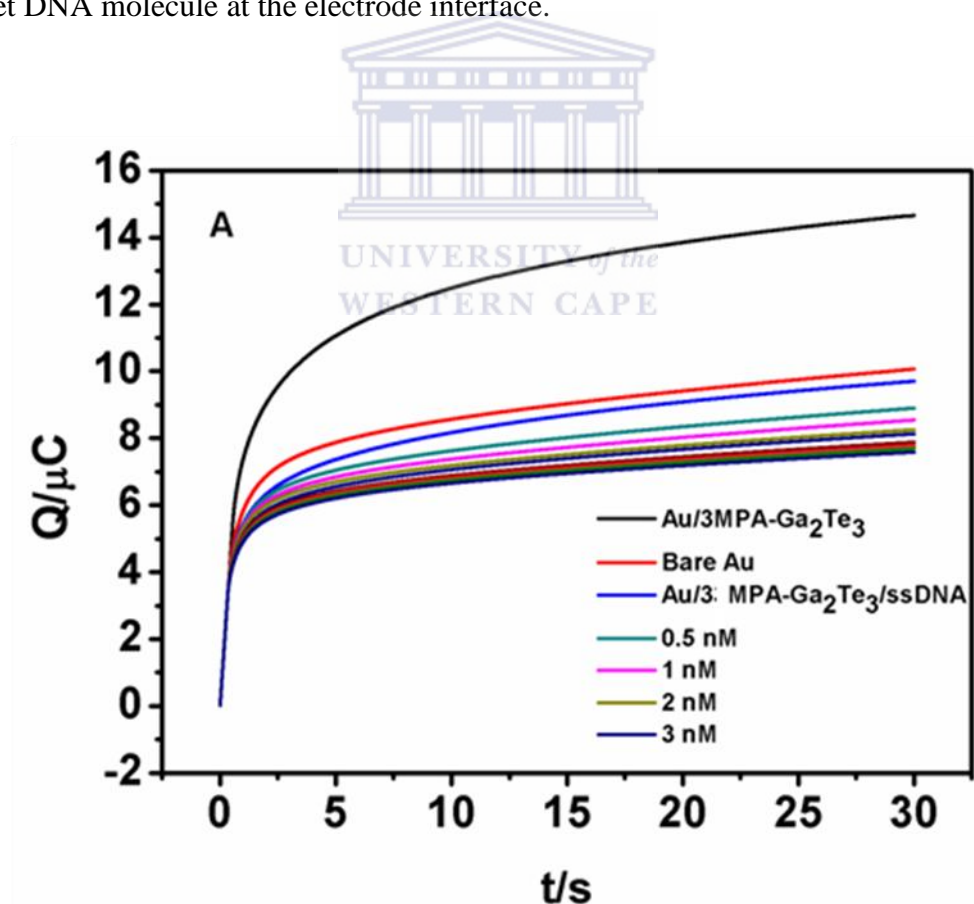


Figure 71. Calibration curve of Her2/oncogene with data from '70 B'.

5.2.5 Chronocoulometric responses

Chronocoulometry (CC) involves measurement of the charge vs. time response to an applied potential step waveform. The shape of the resulting chronocoulogram can be understood by considering the concentration gradients in the solution adjacent to the electrode surface. The technique was used to calculate the diffusion coefficients and rate constants for chemical reactions coupled to electron transfer reactions.

Chronocoulometric response of Au/3MPA-Ga₂Te₃ Au electrode modified to ssDNA was investigated in the unstirred of 0.20 M PBs pH 7.4. Figure 72A, represents the chronocoulograms of the genosensor response (Au/3MPA-Ga₂Te₃/ssDNA) in the presence of the target DNA molecule at the electrode interface.



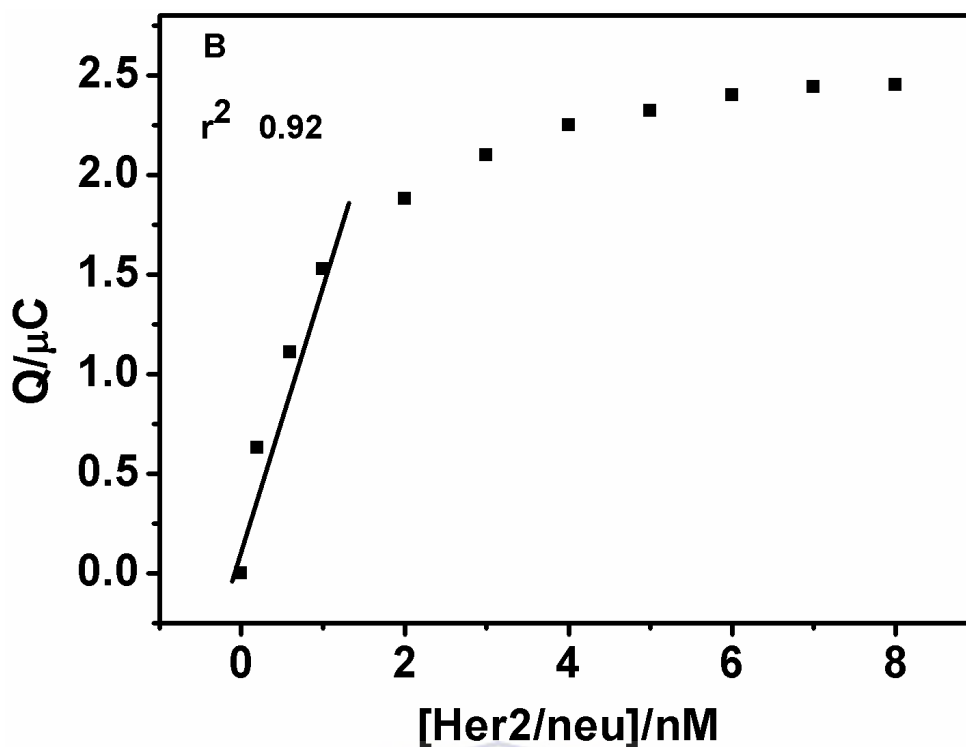


Figure 72. Chronocoulometric plots of Au/3MPA-Ga₂Te₃/ssDNA in 0.1 M PBs pH = 7.4: at different concentration of Her2/oncogene (A) Responses to Her2/oncogene and (B) Calibration curve of Her2/oncogene in 'A'.

As observed from the chronocoulogram the charge (C) of the genosensor decreases drastically as we introduce different concentration of the target DNA. This behaviour shows that the surface of the modified Au electrode has been insulated or hindered, thus a decrease in charge (Q). The diffusion coefficient of the system was calculated using the Cottrell equation (eq. 8). The calculated value for the diffusion coefficient with correlation coefficient (r^2) of 0.92 was found to be $1.58 \times 10^{-6} \text{ cm}^2 \text{ s}^{-1}$, the obtained values confirm that the system was diffusionally controlled and that the movement of electrons was fairly fast. And its surface coverage was calculated using the Cottrell's equation (eq. 10). The calculated values of the adsorbed species (analyte) at the electrode interface were found to range from 3.58 - 8.25 $\text{cm} \text{ s}^{-1}$, this shows that the surface of the (Au/3MPA-Ga₂Te₃/ssDNA) becomes depleted each time the target analyte accumulates at the electrode surface, suggesting that hybridization of the

two DNA molecules occurred. A plot of Q vs. $t^{1/2}$ was used to determine the slope of the system. The slope of the system was found to be 0.12 nC M^{-1} . Since the slope is directly proportional to the sensitivity, the smaller the slope the smaller the sensitivity of the system and thus the slower the rate of electrons (k_s). The gradient of the slope ($r^2: 0.99$) decrease with a decrease in charge, from each time we introduce the target analyte. The k_s was calculated from the following equation;

$$Q = (kC_o t)^{1/2} \quad (29)$$

where, Q is the charge of the electroactive species and C_o is the concentration of the active analyte (mol mL^{-1}).

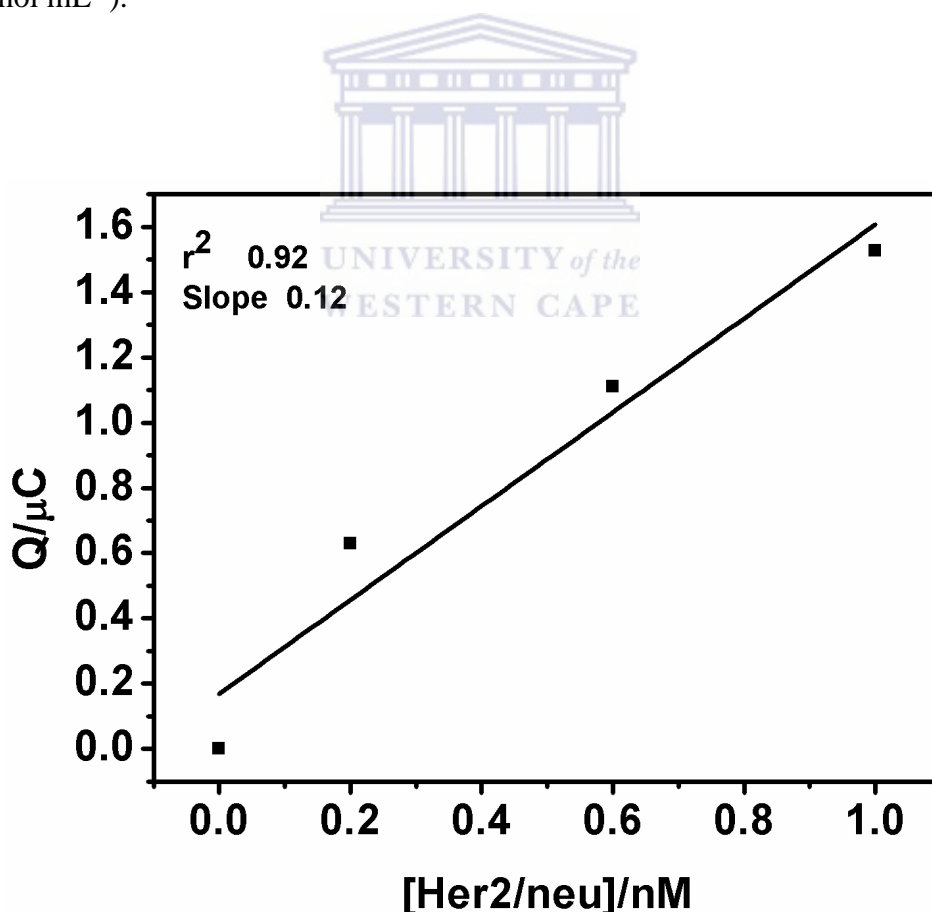


Figure 73. Calibration curve of Her2/oncogene with data from '72B'.

The calculated values for the rate constants were found to be in the range $0.34 - 0.05 \text{ cm s}^{-1}$. The rate at which the electroactive species were travelling towards the electrode interface become sluggish after addition of 1 nM of the target analyte into the system. This behaviour was monitored by calculating the electron transfer rate constant (k). The calculated values (k) for both EIS and CC were in good agreement. The limit of detection and the sensitivity of the two systems were found to be 0.34 nC M^{-1} , $0.005 \times 10^{-3} \text{ nM}$, $1.43 \text{ } \Omega\text{n M}^{-1}$ and $0.12 \text{ } \Omega\text{n M}^{-1}$, respectively (Figure 73). The linear dynamic range of the system was replotted as shown from Figure 73 in order to determine the *LOD* and the sensitivity. The two systems (EIS and CC) were found to be comparable with the linear ranges of $0.5 - 5 \text{ nM}$ and reached the saturation point after the sixth addition of the target DNA (Figure 71 B). The saturation point at the Au/modified electrode interface confirms a little or no interaction between the target analyte with probe DNA.

5.2.6 Time-based Amperometry responses

Compared with the cyclic voltammetry, constant-potential amperometry is more attractive for an evaluation of kinetics of continuous inhibition properties. Figure 74 A, shows typical current-time profile of the Au/GC/3MP-Ga₂Te₃/ssDNA electrode at a fixed applied potential of 0.4 V (vs. Ag/AgCl). After the current baseline had been established with buffer solution, 0.5 nM of target DNA was added into the measuring cell, with constant stirring. Then, aliquot of target DNA was added stepwise to electrolyte buffer ($0.5 - 8.0 \text{ nM}$). As expected, the current response for the electrode Au/GC/3MP-Ga₂Te₃A/ssDNA in 0.10 M PBs (pH7) was higher than for the Au/GC/3MP-Ga₂Te₃A/ssDNA in the presence of the target DNA, the cause for this behaviour can be due to the high affinity of the DNA-DNA interaction.

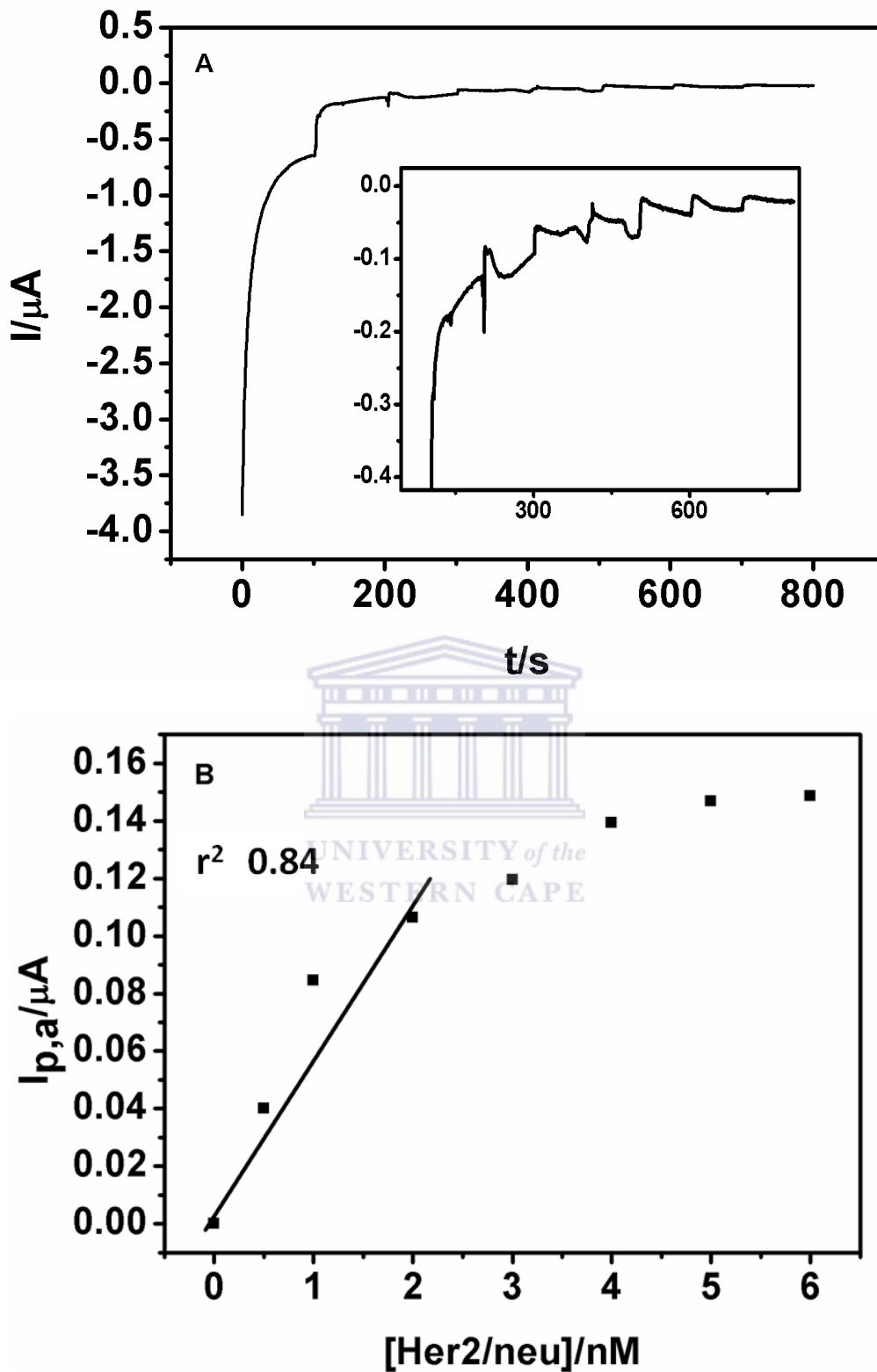


Figure 74. Time-based chronoamperometric plots of Au/3MPA-Ga₂Te₃/ssDNA in 0.1M PBS pH = 7: at different concentration of Her2/oncogene (A) Responses to Her2/oncogene and (B) Calibration curve of Her2/oncogene in 'A'.

Figure 74 B shows the genosensor response which correlates well with the behaviour observed in Figure 74 A. Different additions of ssDNA (0.5 - 4 nM) induced a decrease in the current, which reached to another steady-state current after each 100 s (Figure 74 A). After the fourth addition of the target DNA, the genosensor reached its saturation point showing less binding of the target ssDNA and the capture probe at the electrode interface (Figure 74 B). From Figure 74 B the linear response range of target ssDNA concentration was from 0.5 nM - 4 nM with a correlation coefficient (r^2) of 0.84 ($n = 5$). From the slope of 0.049 nA nM⁻¹ (Figure 75), the lower limit of detection was estimated to be 0.09 pM at a signal to noise ratio of 3. The system confirms the signal response of the DNA-DNA interaction and is comparable with other systems i.e. CV and SWV, evident by a current response and linear range.

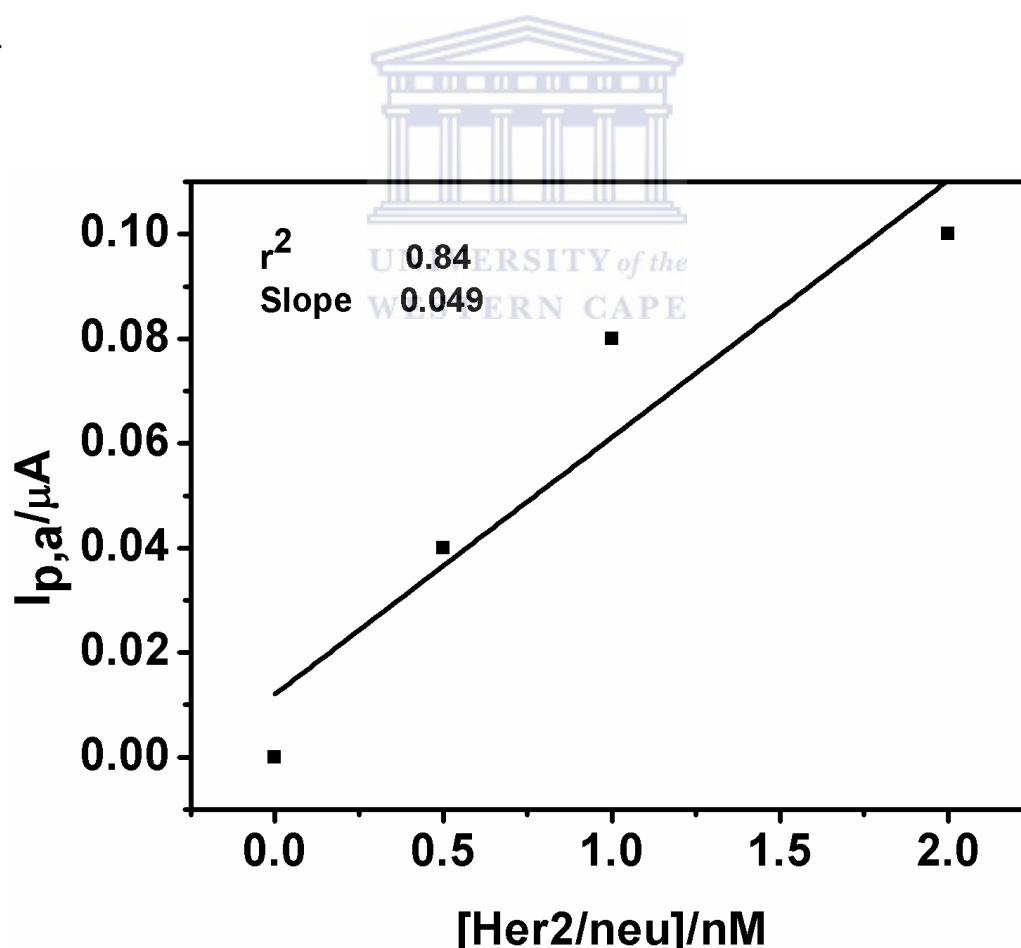


Figure 75. Calibration curve of Her2/oncogene with data from '74 B'.

5.3 Spectroscopic genosensor response

5.3.1 UV-vis responses of Her2/neu oncogene genosensor

UV-Vis was carried out to determine the interaction of the probe DNA and the target DNA in solution. Equimolar concentrations of the quantum dots and probe ssDNA and 3MPA-Ga₂Te₃ were prepared and analysed before the introduction of the target DNA, Figure 76. After acquiring the spectrum of the probe ssDNA at 255 nm, 3MPA-Ga₂Te₃/ssDNA at 257 and 3MPA-Ga₂Te₃ at 220 nm, the interaction of the 3MPA-Ga₂Te₃/ssDNA with the target analyte was carried-out, Figure 77 A.

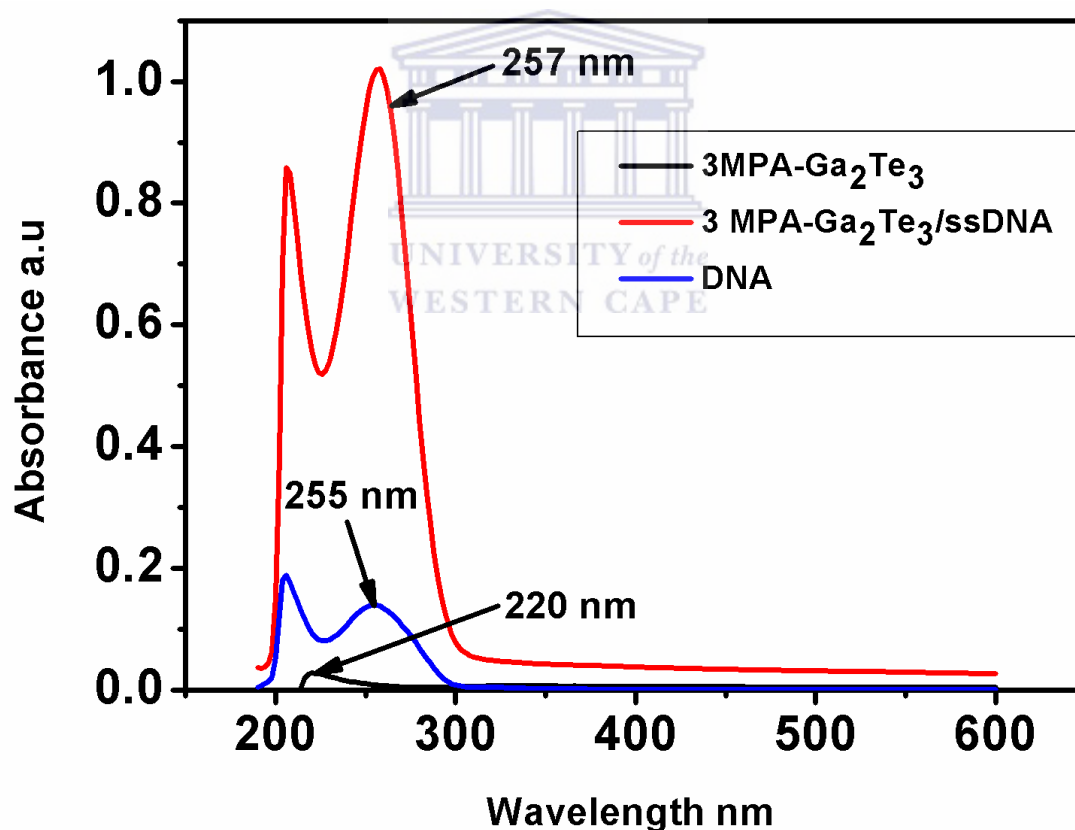
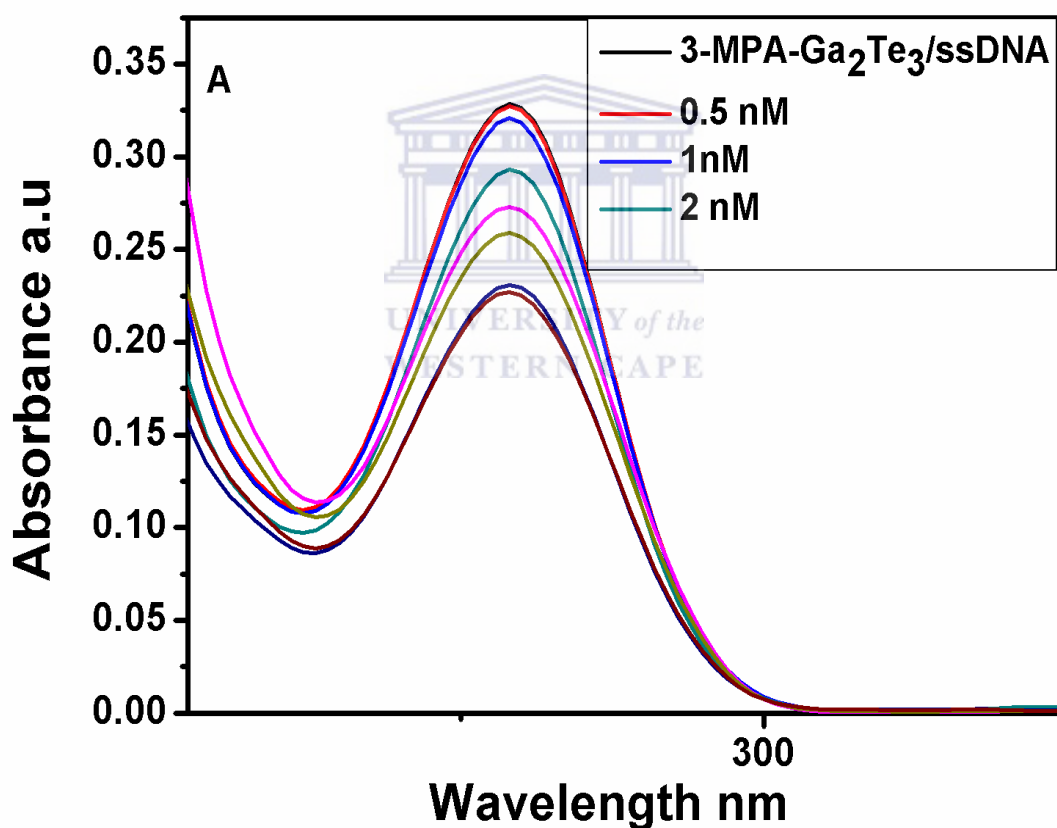


Figure 76. UV/vis plots of (A) DNA, 3MPA- Ga₂Te₃ and Au/3MPA-Ga₂Te₃/ssDNA.

From the absorbance spectrum (Figure 76) it is evident that the quantum dots capped with 3MPA has a catalytic effect evident by an increase in the absorbance peak intensity at 257, when compared with absorption peaks at 220 nm and 255 nm. From the calculated molar absorption coefficient (ϵ) it was evident that the combination of both quantum dots and probe DNA had higher absorptivity. The Beer-Lambard equation (eq. 14) was used for the absorptivity values: $A = \epsilon bc$ and the values were calculated to be 3 MPA-Ga₂Te₃: 149, DNA: 20.8 and 3 MPA-Ga₂Te₃ 7.5.



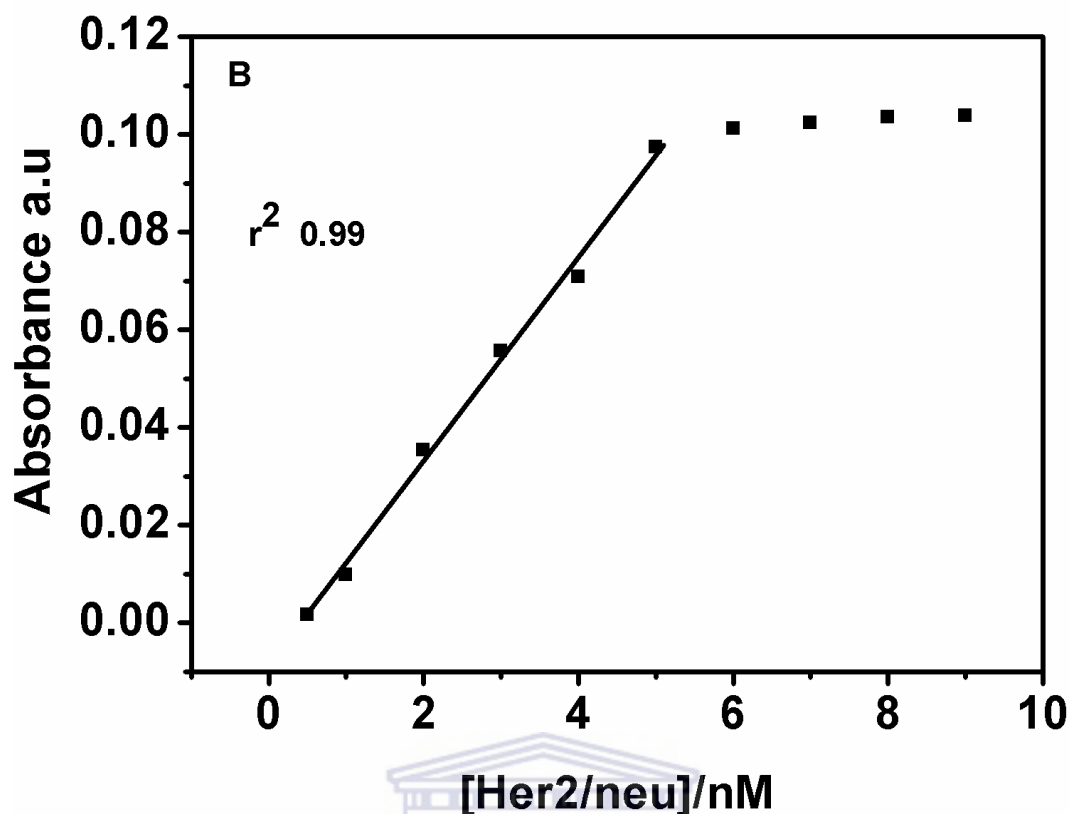


Figure 77. (A) UV/vis plots of 3MPA-Ga₂Te₃/ssDNA at different concentrations of Her2/oncogene (0.5-8 nM) and (B) Calibration curve of Her2/oncogene in 'A'.

The interaction between the probe DNA and the target DNA was studied as shown in Figure 77 A. Introducing different concentrations of the target DNA resulted in a decrease the absorbance peak intensity. This behaviour suggests that the target DNA is acting as an insulator. Figure 77 B shows a calibration curve of the genosensor response in solution. As observed from the spectrum an increase in target DNA concentration resulted in a decrease in the absorbance peak intensity and thus the sensitivity. The linear range and the detection limit of the genosensor were found to be 0.5-5 nM and 0.37×10^{-3} nM. The sensitivity was found to be 0.21 nM with the correlation coefficient (r^2) of 0.99, Figure 78. The results obtained are in good agreement with the obtained electrochemical measurements.

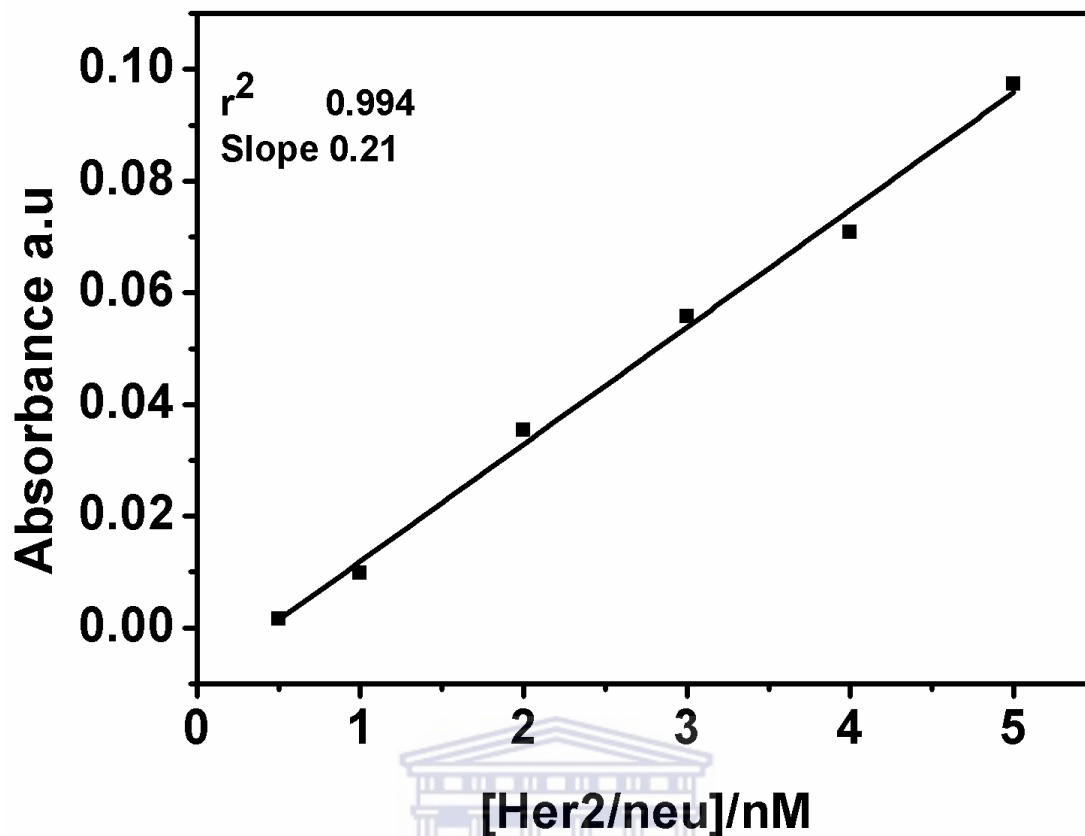


Figure 78. Calibration curve of Her2/oncogene with data from '77B'.

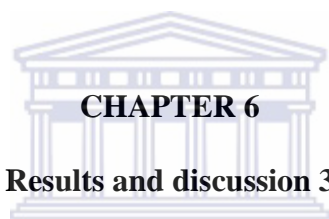
UNIVERSITY of the
WESTERN CAPE

5.4 Sub conclusion

Conclusively the redox properties of the bimetallic-quantum dots were determined and found to possess an irreversible behaviour having both the reduction and oxidation peak currents. Consequently the semiconductors (QDs) were found to have enhanced the conductivity of the used biomolecule, Her2/neu oncogene in this regard. The peak currents of the adsorbed species (3MPA-Ga₂Te₃/ssDNA) were found to be lower than that of 3MPA-Ga₂Te₃ as expected since the ssDNA acts as an insulator and the opposite is true. The binding event of the genosensor was monitored both in solution and on the electrode interface. The results obtained were comparable in both instances, since the current of the measured ssDNA

decreased as we introduced the analyte DNA. The genosensor attained a higher sensitivity with very lower detection limit (pg mL^{-1}). The linear dynamic range with the r^2 ranging from 0.92 - 0.99 was found to be very lower (nM). The viability of the Her2/neu oncogene was also confirmed by UV-vis spectroscopy and it was observed that the DNA was still interacted and can be used for our applications.





CHAPTER 6

Results and discussion 3

EQCM and micro-fluidic responses of Her2/Neu Oncogene genosensor

WESTERN CAPE

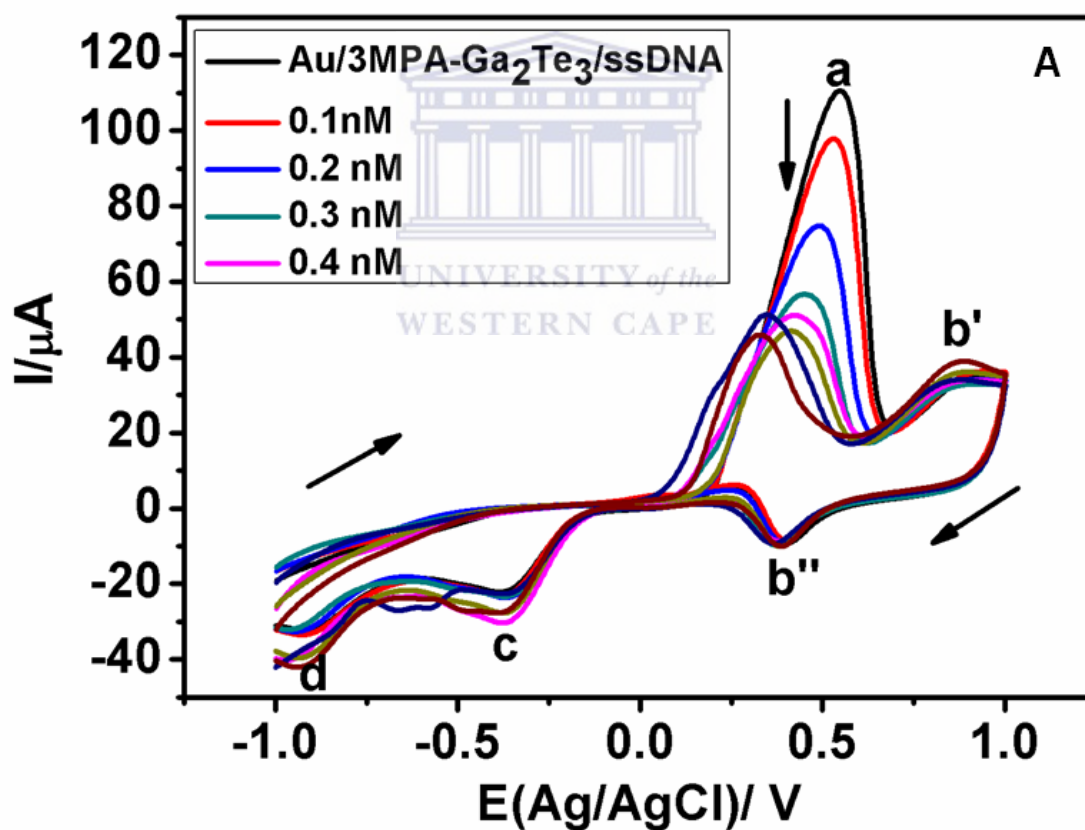
6.1 EQCM of genosensor

6.1.1 Genosensor response of 3MPA-Ga₂Te₃/ssDNA

An EQCM study was carried out in concert with the CV in order to investigate in more detail the electrochemical processes taking place at the electrode interface (3MPA-Ga₂Te₃/ssDNA).

Figure 79 A, shows a change in current while Figure 79 B shows variations in mass as a function of potential (-1.0V/Ag/AgCl < E < 1.0V/Ag/AgCl) for various ssDNA concentrations.

The scan rate used for all the measurements was 25 mV s⁻¹.



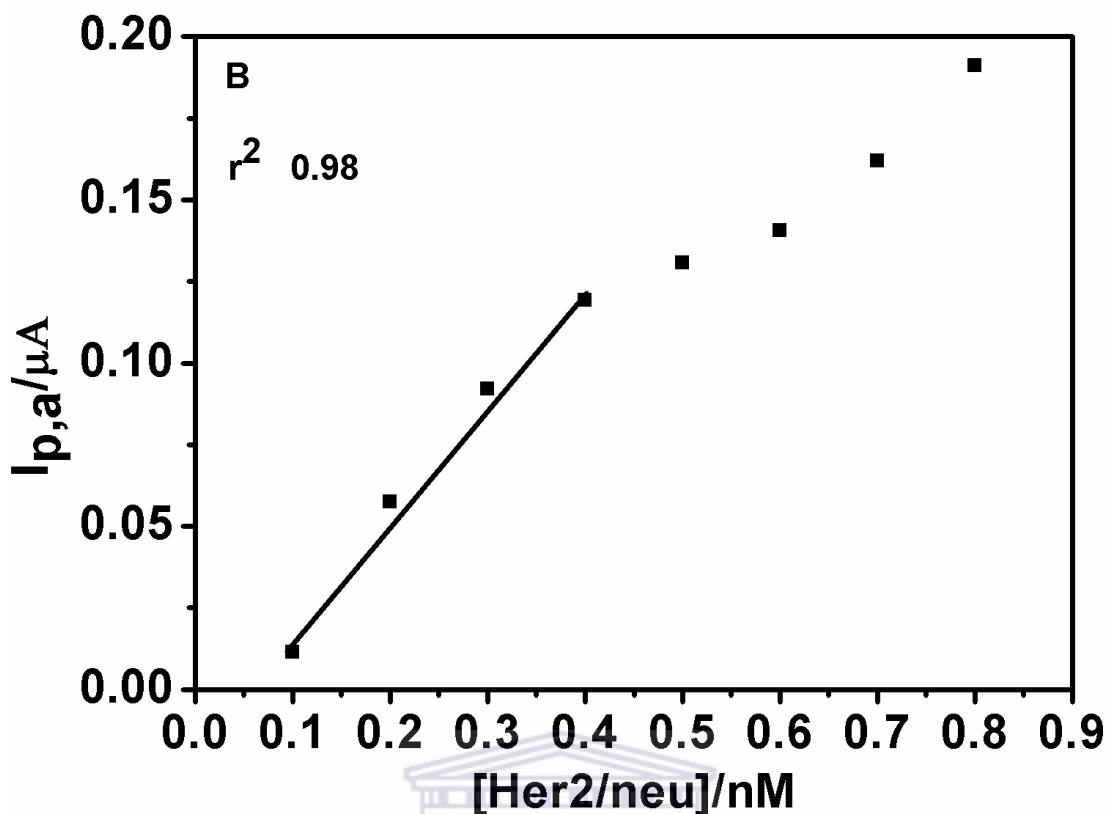


Figure 79. EQCM Voltammetric plots of CE/3MPA-Ga₂Te₃/ssDNA at different concentration of Her2/neu oncogene (0.1→1), (A) CV responses to Her2/oncogene and (B) Calibration curves of Her2/oncogene genosensor in ‘A’.

From cyclic voltammetry the first redox reaction of 3MPA-Ga₂Te₃/ssDNA showed an oxidation peak current ($I_{p,a}$) at $E_p = 0.55$ V (Figure 79 A, a), the peak current observed was denoted as a characteristic of both the 3MPA-Ga₂Te₃/ssDNA with traces of the unreacted bulk Te. And reduction peaks ($I_{p,c}$) at $E_p = -0.4$ V and $E_p = -0.8$ V (Figure 79A, c and d) which are associated with Ga³⁺ and Te²⁻ were also observed. Additional redox peak potential of Au also occurred at $E_p = 0.38$ V and $E_p = 0.88$ V. The genosensor response was monitored at 0.55 V, since both the ssDNA and the catalyst (QDs) occur at this potential range. A decrease in current as a function of Her2/neu oncogene concentrations was observed at 0.55 V, Figure 79 A, a. An introduction of a target ssDNA showed an effect on the electrode

interface of Au/3MPA-Ga₂Te₃/ssDNA, thus hybridisation was concluded. Furthermore, a shift in peak potentials ($E_{p,a}$) at the oxidation peak current ($I_{p,a}$) were observed: 0.55 V, 0.53 V, 0.49, 0.45 V to 0.43 V, Figure 77 A, a. These potential shifts with a potential difference of (≈ 0.004 V) were denoted as a characteristic of electrode reactions having slow electron transfer kinetics but most significantly proves that the genosensor can be employed as the potentiometric sensor. Figure 79 B, shows a genosensor response to Her2/oncogene genosensor. From the calibration curve it was noted that the sensor reached its saturation point at 0.5 nM, proving that the sensor can detect even lower concentrations. The sensitivity of the genosensor calculated from Figure 80, was found to be 0.29×10^{-3} nA M⁻¹ ($r^2 = 0.98$). Its limit of detection was calculated to be 0.04 pM with a linear range of 0.1- 0.5 nM.

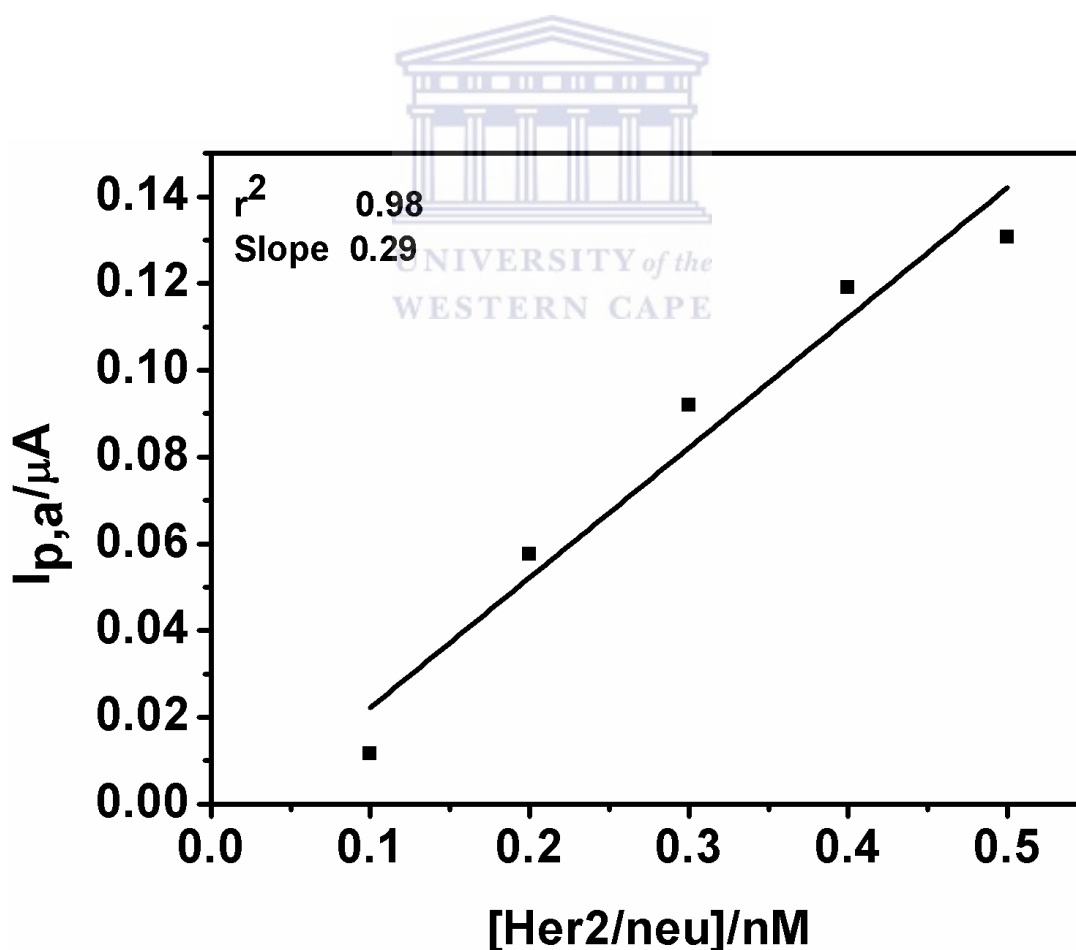
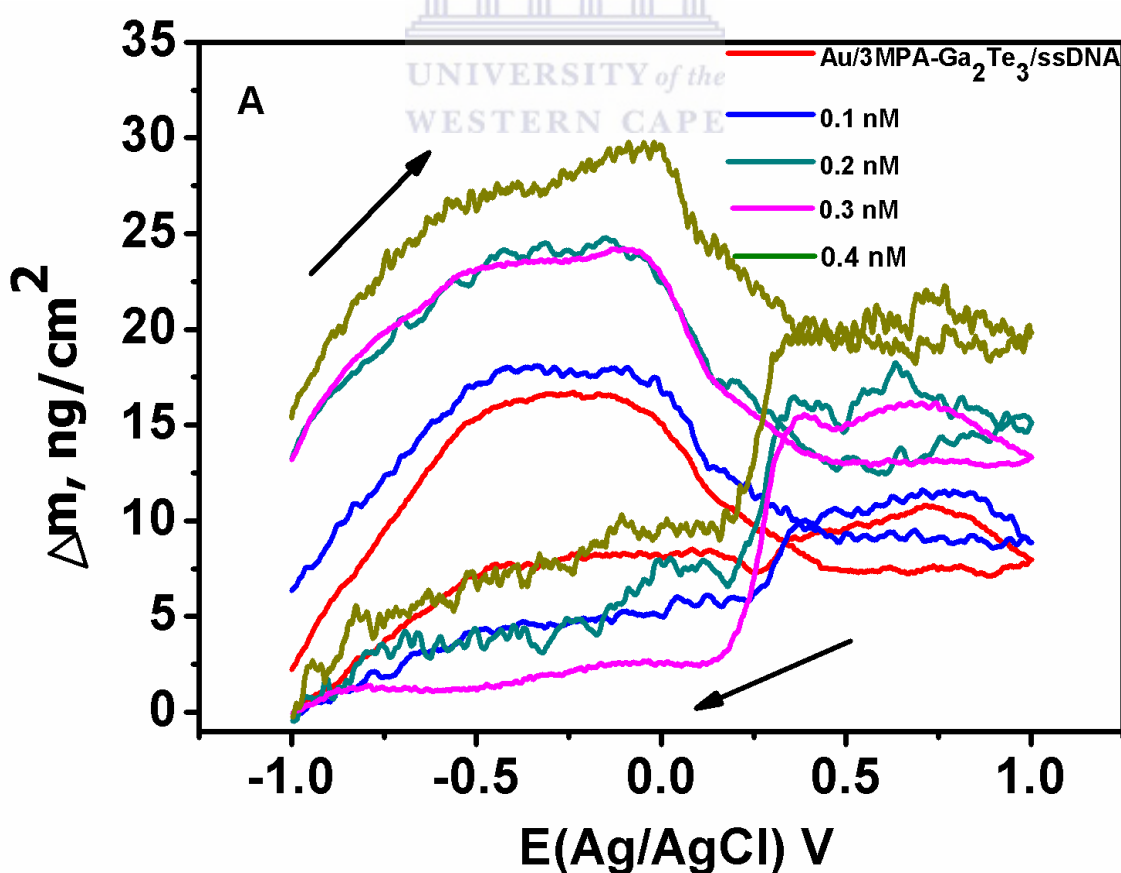


Figure 80. Calibration curves of Her2/oncogene genosensor with data from '79 B'.

From figure 81 A, a total frequency change of 0.38 Hz was observed at first oxidation current at 0.55 V which was due to 3MPA-Ga₂Te₃/ssDNA assembly, at Au electrode interface in the presence of 0.1 nM ssDNA. This frequency change corresponds to gain in mass of 20.5 ng cm⁻² from the electrode surface (see table 5). The EQCM data reveal that mass is gained during the oxidation 3MPA/Ga₂Te₃/ssDNA and the gain in mass means there is an accumulation of the target DNA at electrode interface evident by a decrease in current, Figure 79 A. From figure 81 B it is clear that as we introduce more target DNA the frequency decrease while mass increases (Δf vs. conc.) and the reverse is true for current vs. conc. The sensitivity of the genosensor was found to be 17.7 nM s⁻¹ ($r^2 = 0.92$), Figure 82. These frequency changes have been previously interpreted as indicative of anion or cation loss (or gain) from the monolayer, which is consequent to the injection (or removal) of electrons [311; 312].



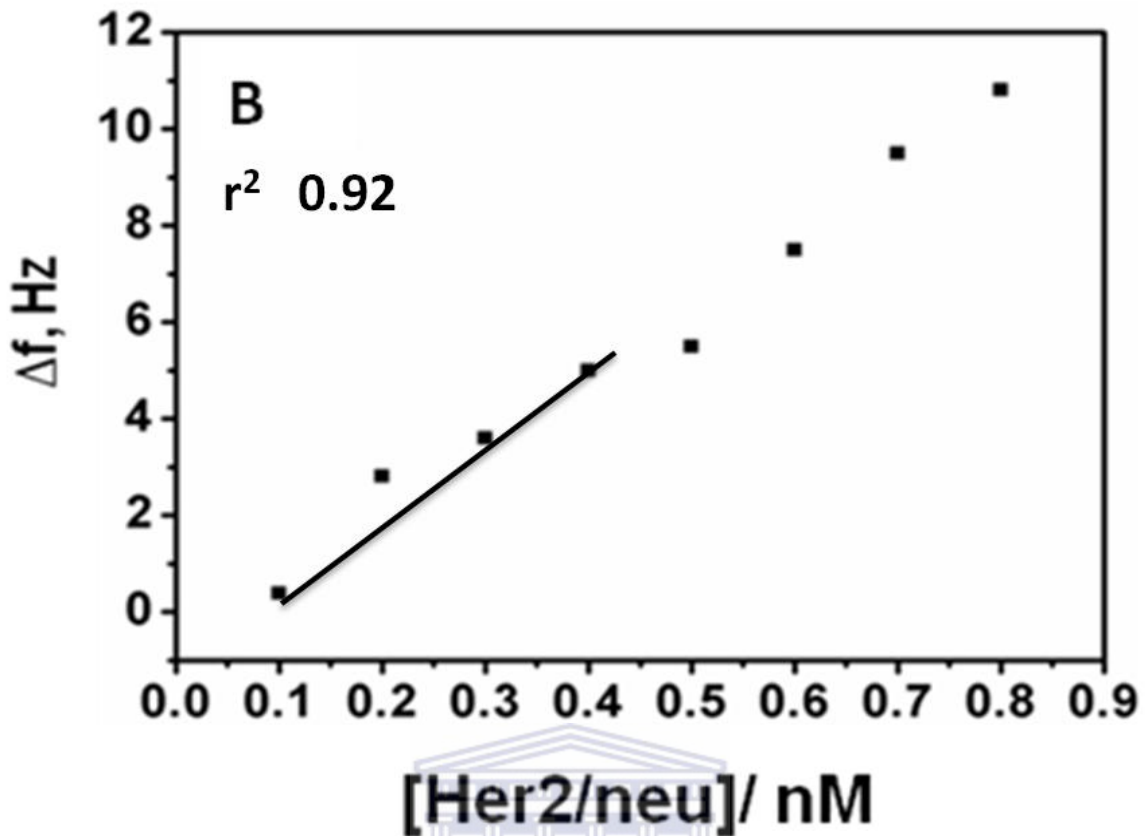


Figure 81. EQCM plots of CE/3MPA-Ga₂Te₃/ssDNA at different concentration of Her2/neu oncogene (0.1→1), (A) EQCM responses to Her2/oncogene and (B) Calibration curves of Her2/oncogene genosensor in ‘A’.

The frequency changes were calculated by using the Sauerbrey’s equation (eq. 11). The EQCM data is in good agreement with the results obtained from both EIS and Chronocoulometry as far as frequency and electro active species at the electrode interface is concern.

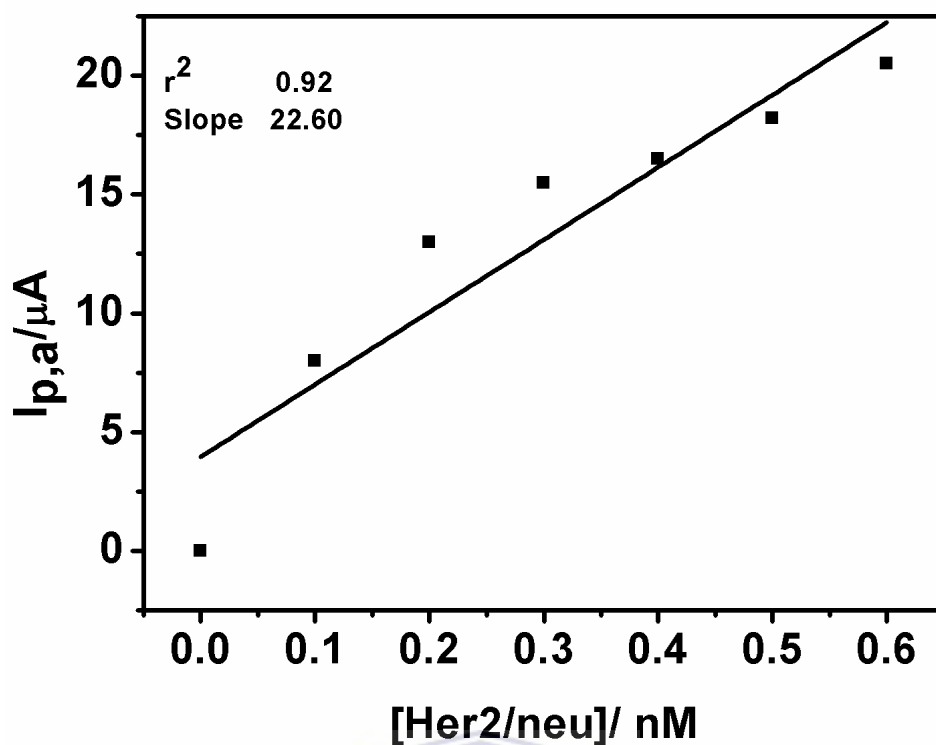


Figure 82. Calibration curves of Her2/oncogene genosensor with data from '81B'.

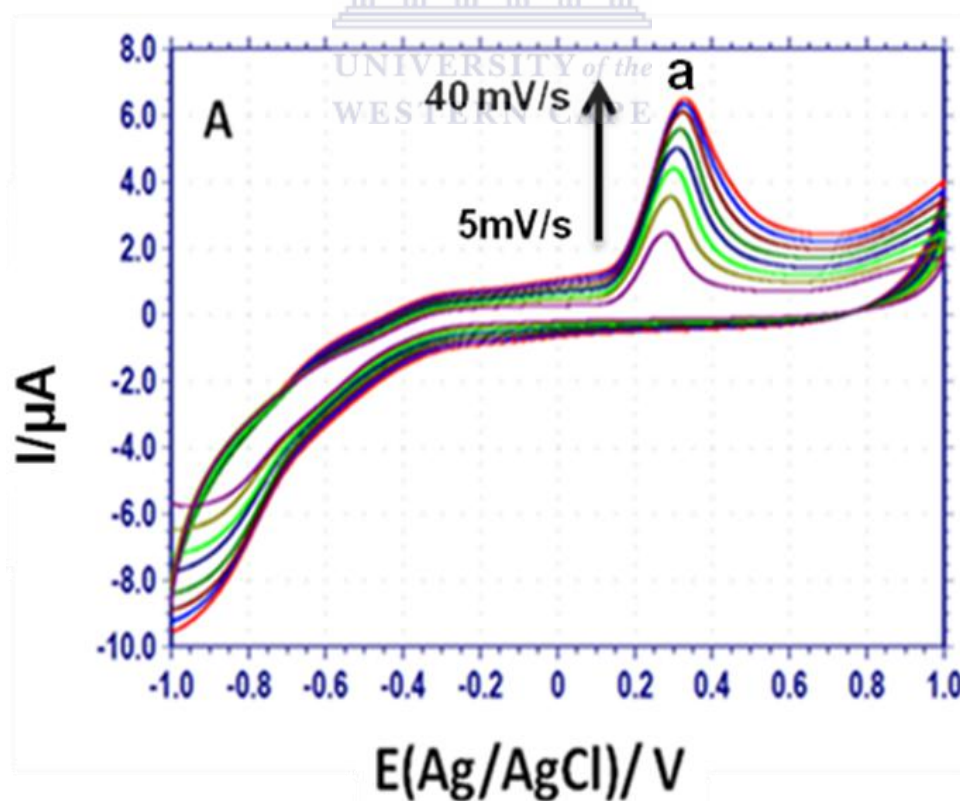
Table 7. Difference in frequency and mass as we introduce target HER2/neu oncogene

Concentration of target DNA, HER2/neu (nM)	Δm (ng cm ⁻²)	Δf (Hz cm ⁻²)
0.00	4.00	12.50
0.10	8.00	7.50
0.20	13.00	5.00
0.30	15.50	4.00
0.40	16.50	2.40
0.50	20.20	0.38

6.2 Micro-Fluidics of genosensor

6.2.1 Scan rate dependence of 3MPA-Ga₂Te₃ and genosensor response of 3MPA-Ga₂Te₃/ssDNA

Our genosensor was moved from the typical bulk electrode to the micro-fluidic system. The sense here was to evaluate and compare the detection systems of the two DNA sensors. Extraction of DNA using PCR method was not done at this stage, the same method applied for the bulk DNA sensor was also employed here. All data are from single experiments with measurements made in triplicate. A carbon paste was used as conducting material or transducer. The sample or quantum dots were immobilised in the form of an injection through an opening onto the transducer. The nanomaterials were left to dry for 2 h since this was a closed system. A scan rate and concentration dependence studies were carried out using cyclic voltammetry.



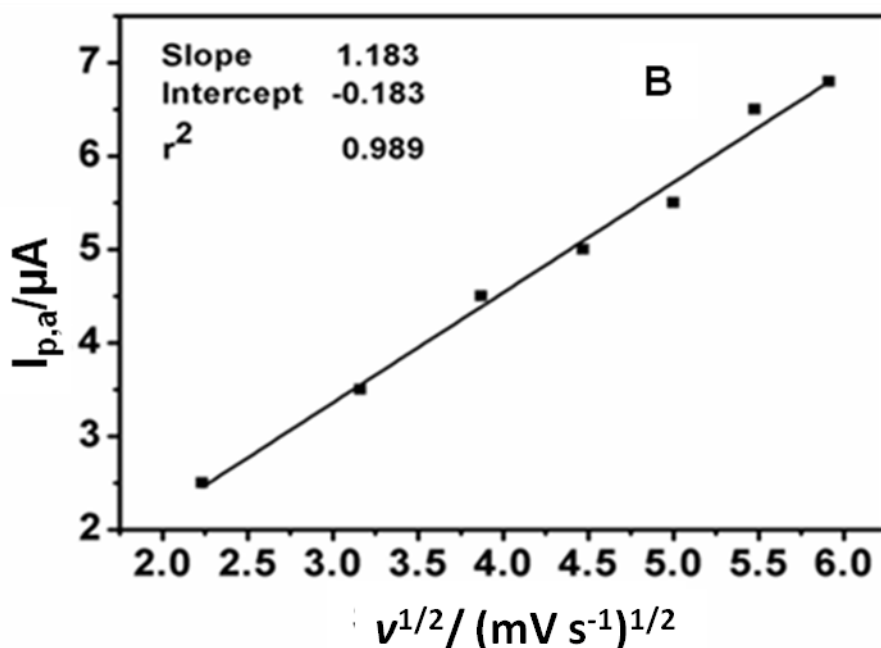


Figure 83. Micro-fluidics voltammetric plots of GC/3MPA-Ga₂Te₃/ssDNA in 0.1M PBS pH = 7: (A) CV plots for 5-30 mV s⁻¹ and (B) Randel-Sevcik plot of data from ‘A’.

The electrochemistry of 3MPA-Ga₂Te₃ was examined using cyclic voltammetry (Figure 83 A). From the cyclic voltammogram of 3MPA-Ga₂Te₃, an oxidation peak current ($I_{p,a}$) was evident at $E_p = 0.40$ V vs. Ag/AgCl which was used to study both the scan rate and concentration dependence studies. No reduction peak currents were observed during the reverse scan at the chosen potential window. The oxidation peak current ($I_{p,a}$) at $E_p = 0.4$ V was found to increase with scan rate from 0.05 - 0.35 V s⁻¹ while E_p at 0.40 V showed a slight shift towards more positive direction, confirming electrochemical irreversibility [29]. A graph of peak current versus the square root of scan rate (Figure 83 B) resulted in a linear relationship ($r^2 = 0.99$) confirming that electrochemical oxidation of 3MPA-Ga₂Te₃ was under diffusion control. The calculated value of $D = 5.0 \times 10^{-6}$ cm² s⁻¹ was used to prove that the system was diffusionally controlled.

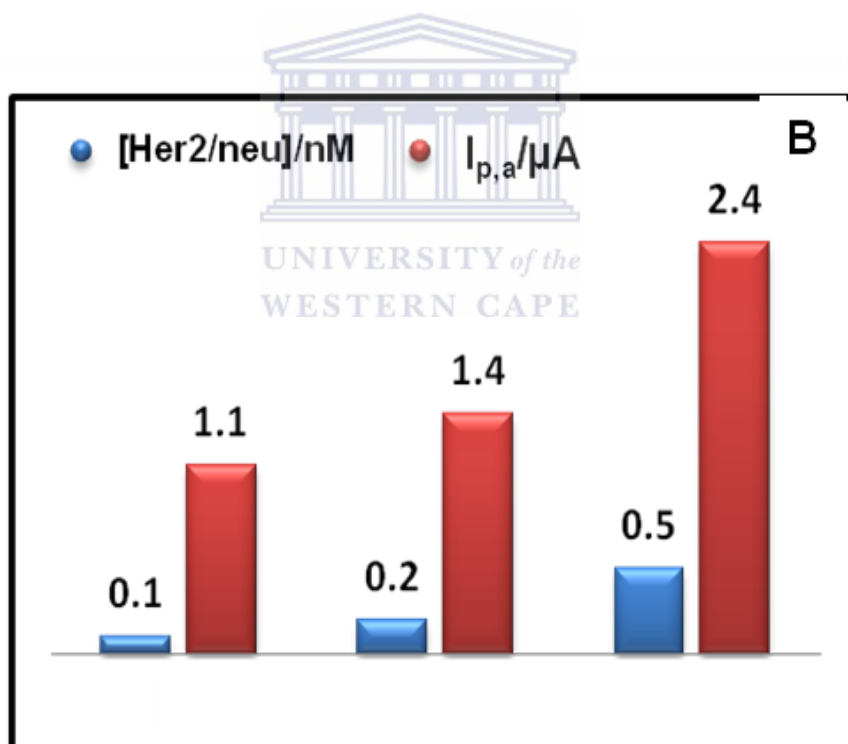
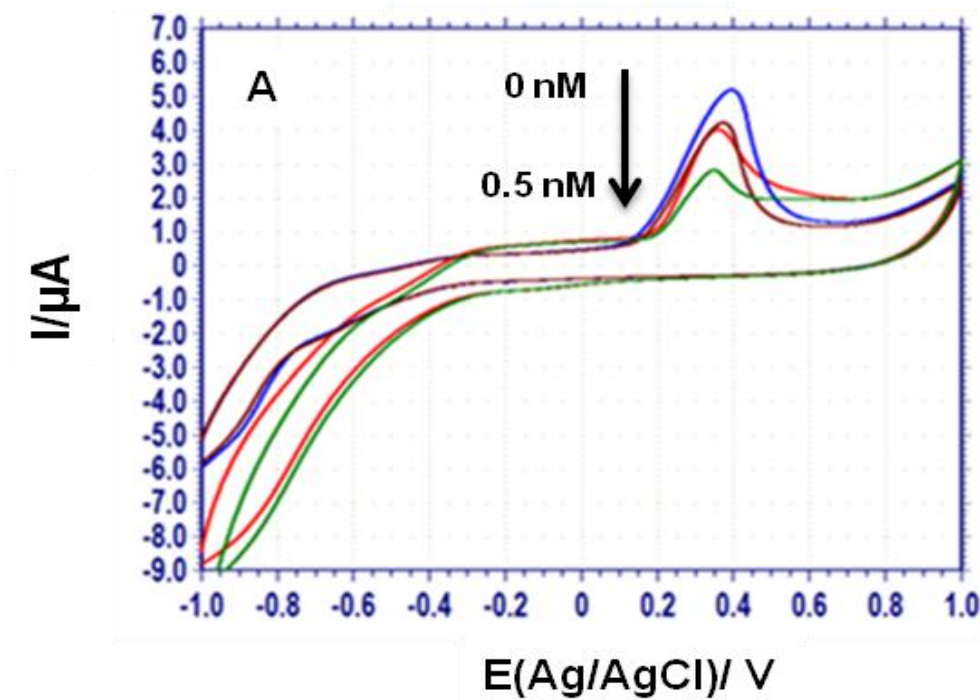


Figure 84. Micro-fluidics voltammetric plots of GC/3MPA- $\text{Ga}_2\text{Te}_3/\text{ssDNA}$ in 0.1M PBS pH = 7: (A) Responses to Her2/ncognen and (B) Bar-chart of the genosensor peak current from 'A'.

The current arising from CE/3MPA-Ga₂Te₃/ssDNA in 0.1 M PBs buffer pH 7.4 was measured using CV (Figure 84 A). A decrease in peak current was observed with introduction of the target analyte (common ssDNA). The genoDot (genosensor) showed binding of the analyte at the electrode interface (Figure 84 B) with a calculated limit of detection (*LOD*) of 0.07 nA M⁻¹.

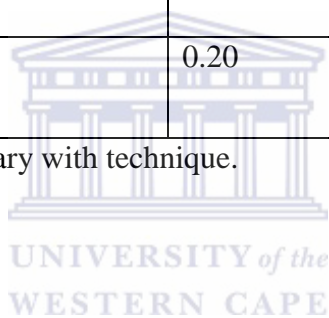
6.3 Sub-conclusion

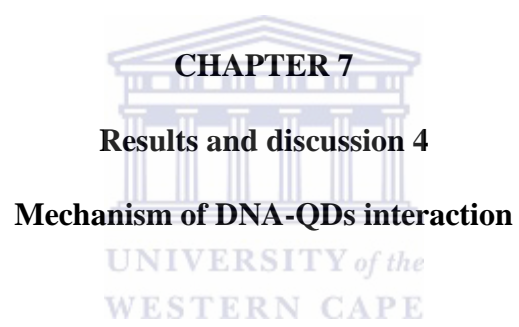
Microfluidic sensor system (**GenoDot Microanalyzer: GDMA**) was successfully developed. This microanalyzer prototype card was used effectively in the construction of DNA sensor which proves that the prototype was effective and can be employed for further analysis. The method applied on normal bulk electrode sensor for detection of Her2/neu oncogene was achieved on this system. On a carbon paste conducting material 3MPA-Ga₂Te₃/ssDNA was immobilised successfully and scan rate dependence studies were carried out in which an increase in current as function of root scan rate was observed. Furthermore detection of Her2/neu oncogene was successfully attained, evident by a decrease in current as we introduce different concentration of the target ssDNA. EQCM technique was able to confirm the hybridisation event of the DNA genosensor to the common DNA. The EQCM data confirmed that the electrons are been hindered as we introduce different concentration of the target analyte. These results are in good agreement with the data obtained from micro-fluidics system.

Table 8. Analytical parameters of the genosensor obtained by various techniques

	<i>LDR</i> (nM)	<i>LOD</i> (pg mL ⁻¹)	Sensitivity*
CV	0.50-3.00	0.07	0.02 $\mu\text{A ng}^{-1} \text{mL}^{-1}$
SWV	0.10-3.00	0.02	0.10 $\mu\text{A ng}^{-1} \text{mL}^{-1}$
EIS	0.50- 4.00	0.05	1.49 $\Omega \text{ nM}^{-1}$
EQCM	0.10- 0.50	0.07	17.7 nM s^{-1}
CC	0.50-4.00	0.12	0.02 $\Omega \text{ nM}^{-1}$
CA	0.50-4.00	0.20	0.16 A nM^{-1}

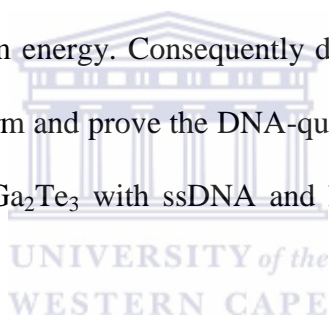
*The unit of sensitivity vary with technique.





7.1 Introduction

This chapter describes/discusses and show the mechanism of DNA-QDs interaction before and after hybridisation. In unison give evidence of the detection signal from both quantum dots and the ssDNA. An important property of quantum dots is that they can easily transfer energy when excited. In our case the nanodots transferred energy in the form of a signal (current, A) when the voltage was passed on the quantum dots. Since quantum dots are semiconductors they passed this energy on to a nearby molecule which is through the capping ligand attached to the quantum dots to the ssDNA-capture probe, which eventual gave a current signal due to the quantum energy. Consequently different experiment/analyses have been carried out in order to confirm and prove the DNA-quantum dots binding event and also pin-pointes the role of 3 MPA-Ga₂Te₃ with ssDNA and how the cations/anions affect the detection-signal (ssDNA-QDs).



7.2 Electrochemical genosensor mechanism

7.2.1 Genosensor response using metal ions as electrolytes

Since the oxidation potential was shown to be dependent to the reduction potential of the quantum dots (the reverse is true), a potential dependence study was carried out to prove that the later is true. Figure 84 shows the behaviour of the peak current and peak potential of the 3MPA-Ga₂Te₃ quantum dots at the same scan rate but different potential windows. An oxidation peak current ($I_{p,a}$) was evident at $E_p = 0.43$ V vs. Ag/AgCl (Figure 85A, b and 86 A, b) and a reduction peak current at ($I_{p,c}$) was observed at $E_p = -0.65$ V vs. Ag/AgCl, Figure 85A, b and 86 A, b. The two redox peaks were used to monitor the potential dependence of 3MPA-Ga₂Te₃.

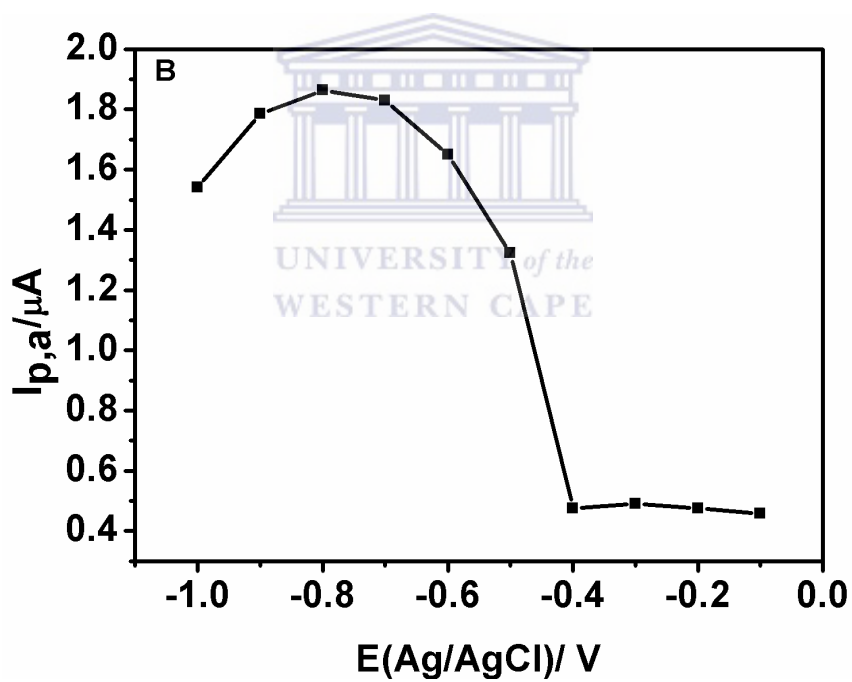
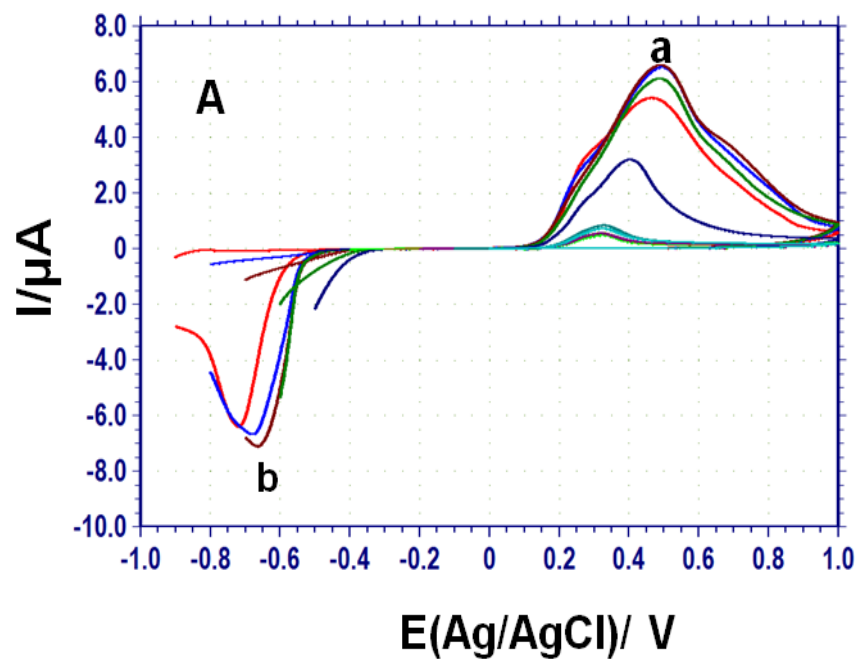


Figure 85. Voltammetric plots of A) GCE/3MPA-Ga₂Te₃/ssDNA at different potential windows (-1.0 V to 1.0 V) and B) Calibration curve of potential windows in 'A'.

From Figure 85 A, it is evident that as we move from higher potentials to lower potentials (-1.0 V to 0 V and 1.0 V to 0 V) the peak current at 0.4 V decreases in intensity. And simultaneously a shift in peak potential was also observed as we move towards lower potentials, confirming an irreversible system. A calibration plot of potential vs. current was used to clearly show this behaviour, Figure 85 B. It is clear from this figure that at higher potentials (-1.0 to -0.5 V), higher peak currents are observed and at lower potentials of -0.4 V to -0.1V the peak currents decreases and are almost constant. Additionally, the behaviour in peak potentials and peak currents proves that both the oxidation and the reduction peaks are dependent to each other. Hence a wider potential window was chosen. From the observed data more experiments had to be carried out in order to account for the peculiar behaviour in peak potentials. At first glance the behaviour in peak potentials was associated with the anions and cations that interacted with the unreacted Te from the quantum dots (3MPA-Ga₂Te₃) surface. From the bimetallic point of view it's common knowledge that when two metals interact to form a compound or a quantum dot in our case, one of the metals tends to move towards the surface of the overall bulk material (some unreacted metals). It is this unreacted nanomaterials on the surface of the quantum dots which are been investigated. The aim here is to determine the effect of quantum dots (3MPA-Ga₂Te₃) which are Te enriched, interacting with the ssDNA whilst studying the overall reaction of genosensor (3MPA-Ga₂Te₃/ssDNA) with the cations. Figure 86, shows the behaviour of different cations with the genosensor (3MPA-Ga₂Te₃/ssDNA) before hybridisation. From Figure 86 A, both lithium ions and cesium ions were two species that clearly showed a good interaction with the genosensor. The ionic radii of Cs⁺ was higher 1.65 (Figure 86 B) compared to other cations showing that there's more steric hindrance. However Li⁺ with the smallest sensitivity and smallest peak current was also noted to have the smallest ionic radii 0.45 (Figure 86 B) thus showing less steric hindrance.

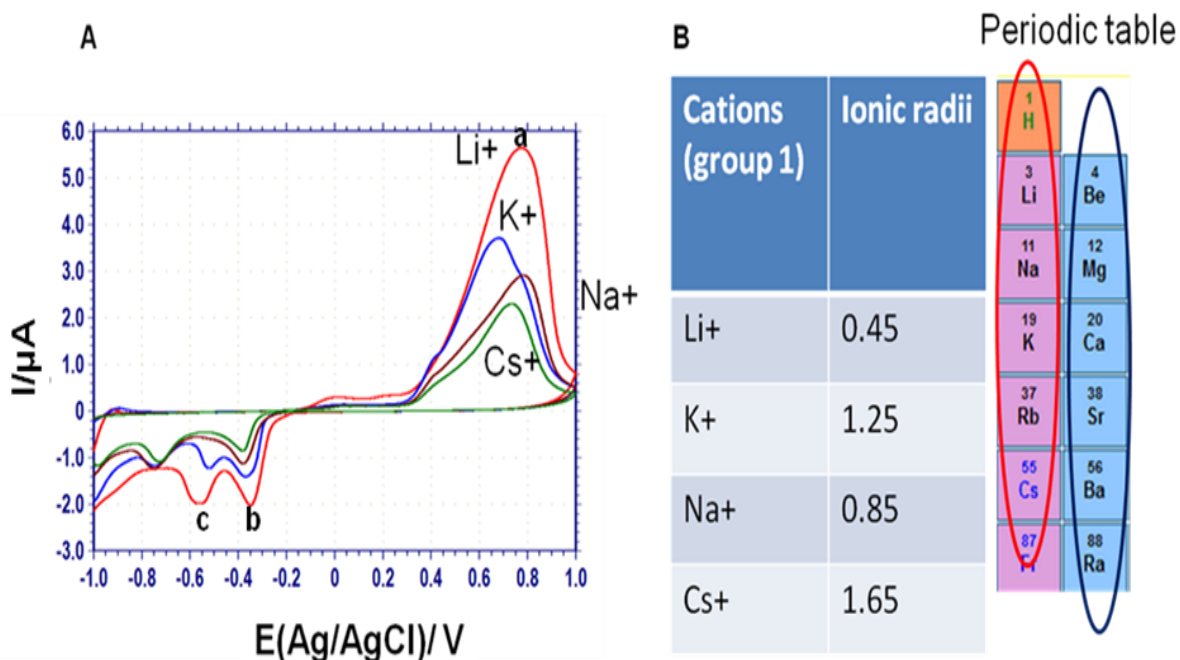


Figure 86. Genosensor response of A) CV of GCE/3MPA- Ga_2Te_3 /ssDNA with different cations but same concentrations (0.1M) and B) Table showing the electronegativity of different cations together with a periodic table with elements from group 1 and 2.

The obtained data suggests that as we go down the period there's higher electronegativity and the opposite is true. Based on these observations further analysis were carried out to investigate the behavior of the two cations with the genosensor (3MSA- Ga_2Te_3) before and during hybridisation. Figure 87 A and 89A, shows the genosensor interaction with different concentrations (0.1 - 8 nM) of target analyte while introducing more cations on the electrode surface. Before introducing the analytes or the electrolyte into the system there were redox peaks observed from both Figure 87 A and 89 A; Cyclic voltammograms with redox properties of GC/3MSA- Ga_2Te_3 -ssDNA were observed with an oxidation peak potential ($I_{p,a}$) at $E_p = 600$ mV (Figure 87 A, a and 89 A, a) and a reduction peak potential ($I_{p,c}$) at $E_p = -500$ mV which was associated with redox properties of Ga^{3+} , Figure 87 A, b and 89 A, b. An additional reduction peak was observed at reduction peak potential ($I_{p,a}$) of $E_p = -700$ mV which can be due to the products of the Te^{2-} .

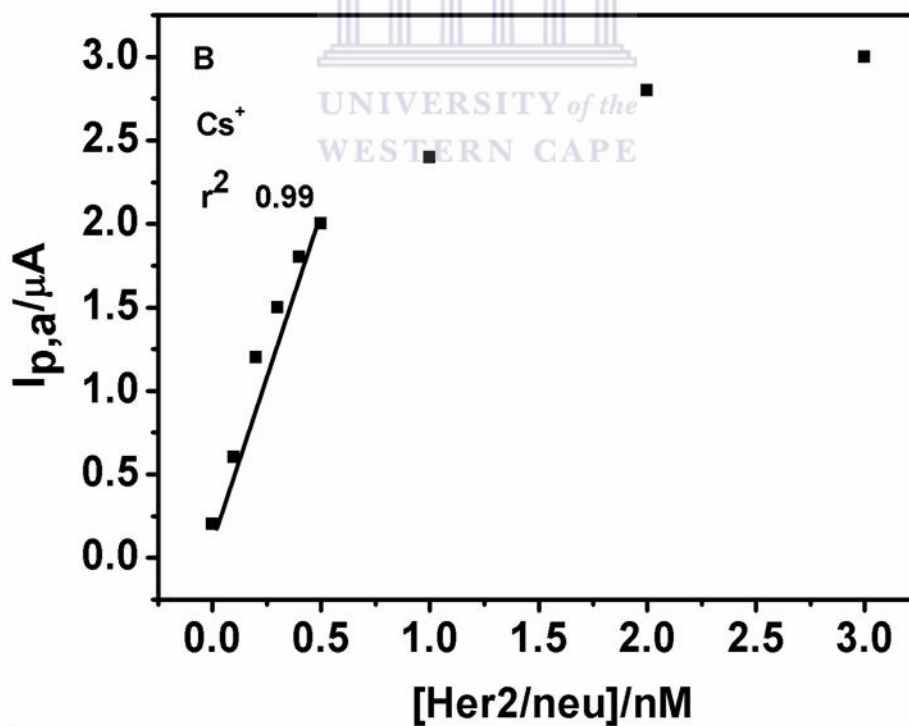
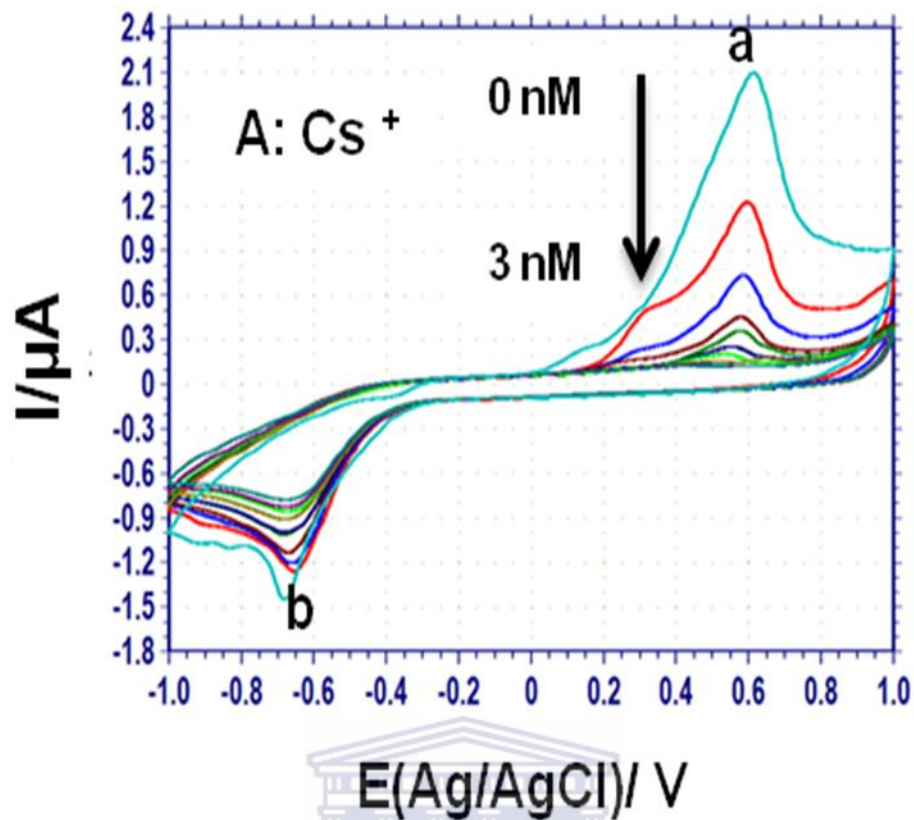


Figure 87. Effect of electrolytes on genosensor responses: (A) CsCl and Calibration curves of Her2/oncogene genosensor in (B) CsCl electrolyte.

The introduction of cations was done by washing the immobilized electrode with 0.1M of Cs^+/Li^+ solutions after each binding or hybridisation with target analyte and also using the aliquots as the electrolytes. Compare to the phosphate buffer (K^+) system the two systems (Cs^+ and Li^+) showed higher sensitivity (2.74 - 3.69 nA M^{-1} ; $r^2 = 0.99$) and very low detection limits (0.0004 pM) with the linear dynamic range starting from 0.1-1 nM), Figure 88 and 90. The genosensor cation interaction showed a decrease in peak current after the first addition of the target analyte (Figure 87 A and 89 A) and reached its point of saturation after adding 1 nM of Her2/neu concentration (Figure 87 B and 89 B). The observed behaviour suggest an interaction between the tellurium enriched 3 MSA- Ga_2Te_3 with cations whilst binding to the target analyte forming a $3\text{MSA-Ga}_2\text{Te}_3/\text{dsDNA}/\text{Cs}^+/\text{Li}^+$.

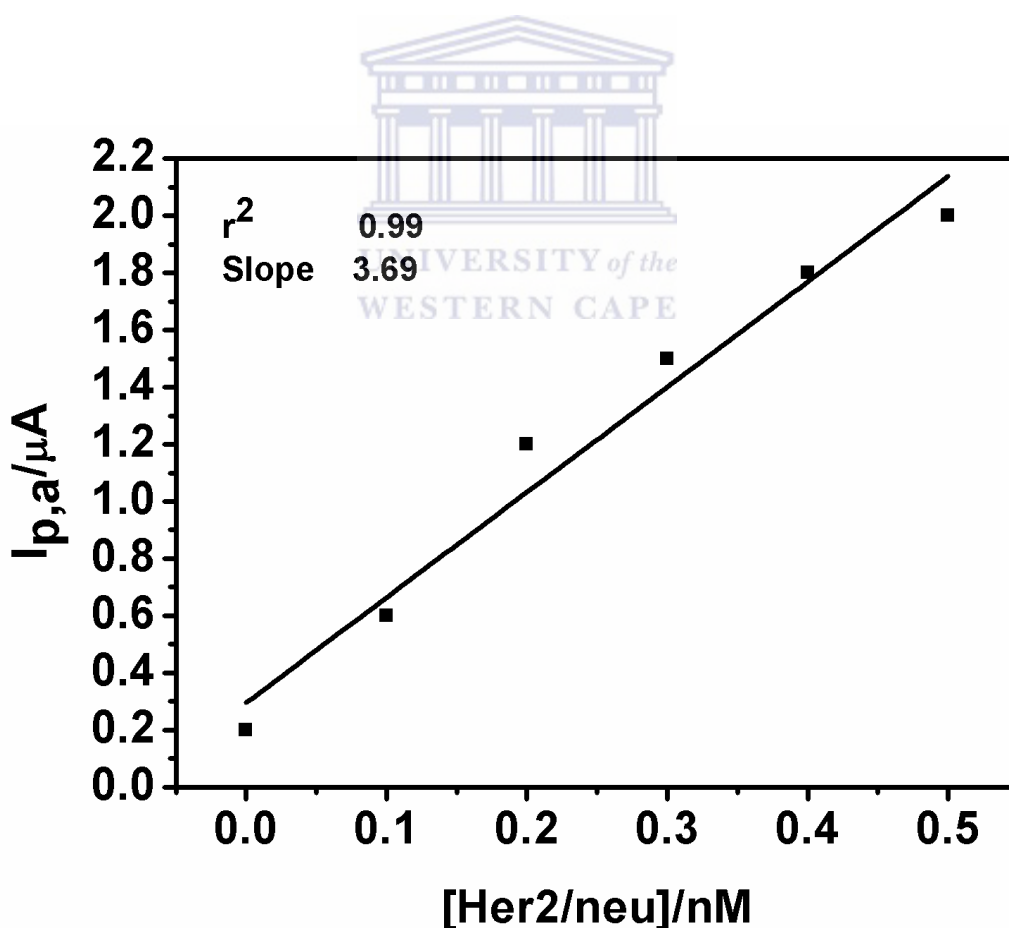


Figure 88. Calibration curve of Her2/oncogene with data from '87 B' CsCl electrolyte.

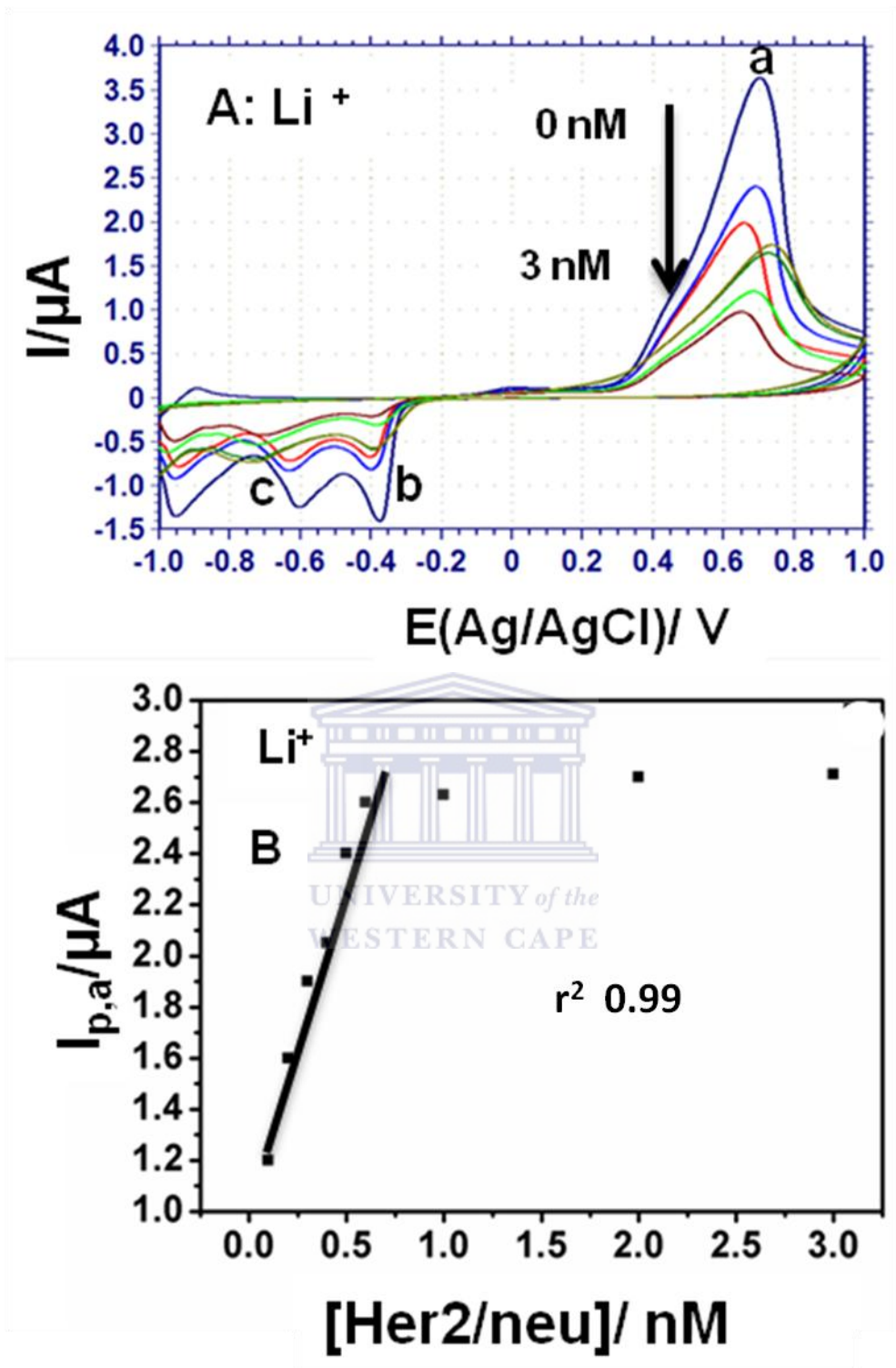


Figure 89. Effect of electrolytes on genosensor responses: (A) LiCl and Calibration curves of Her2/oncogene with data from (B) LiCl electrolyte.

Based on our findings or obtained data a mechanism for the genosensor is proposed, scheme 5 A and B. From our findings it was observed that there was an interaction between the cations and the tellurium nanoparticles on the surface of the quantum dots that caused a shift and a decrease in signal at 400 mV, as we increasing the concentration of the Li^+ . What we are proposing here is that the electrons from the bulk electrode are been pumped to the adsorbed species (3MSA- Ga_2Te_3) into the electrolyte solution and back to the electrode or in between the quantum dots (scheme 5 A and B) giving energy to semiconductor hence a higher signal response. The free electrons from the electrolyte solution (Li^+) interact with the adsorbed species of tellurium that acts as a shell of the core quantum dots. The electrons from Li^+ forces the Te^0 to be reduced back to Te^{2-} (rxn: $\text{Te}^0 + 2\text{e}^- \rightarrow \text{Te}^{2-}$) thus forming an adsorbed complex: $\text{Te}^{2-} + \text{Li}^+ \rightarrow \text{Te}\cdot 2\text{Li}$. This adsorption complex is believed to be behind the genosensor response in which a decrease in peak current was observed after hybridisation due to big ionic radii and steric hindrance of the Li^+ cation.

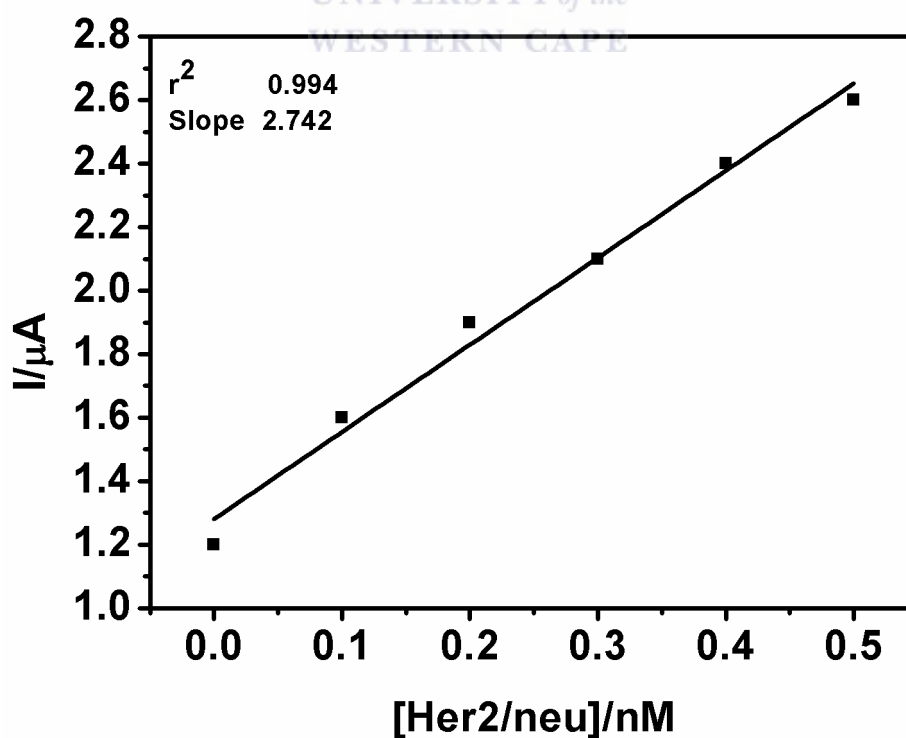
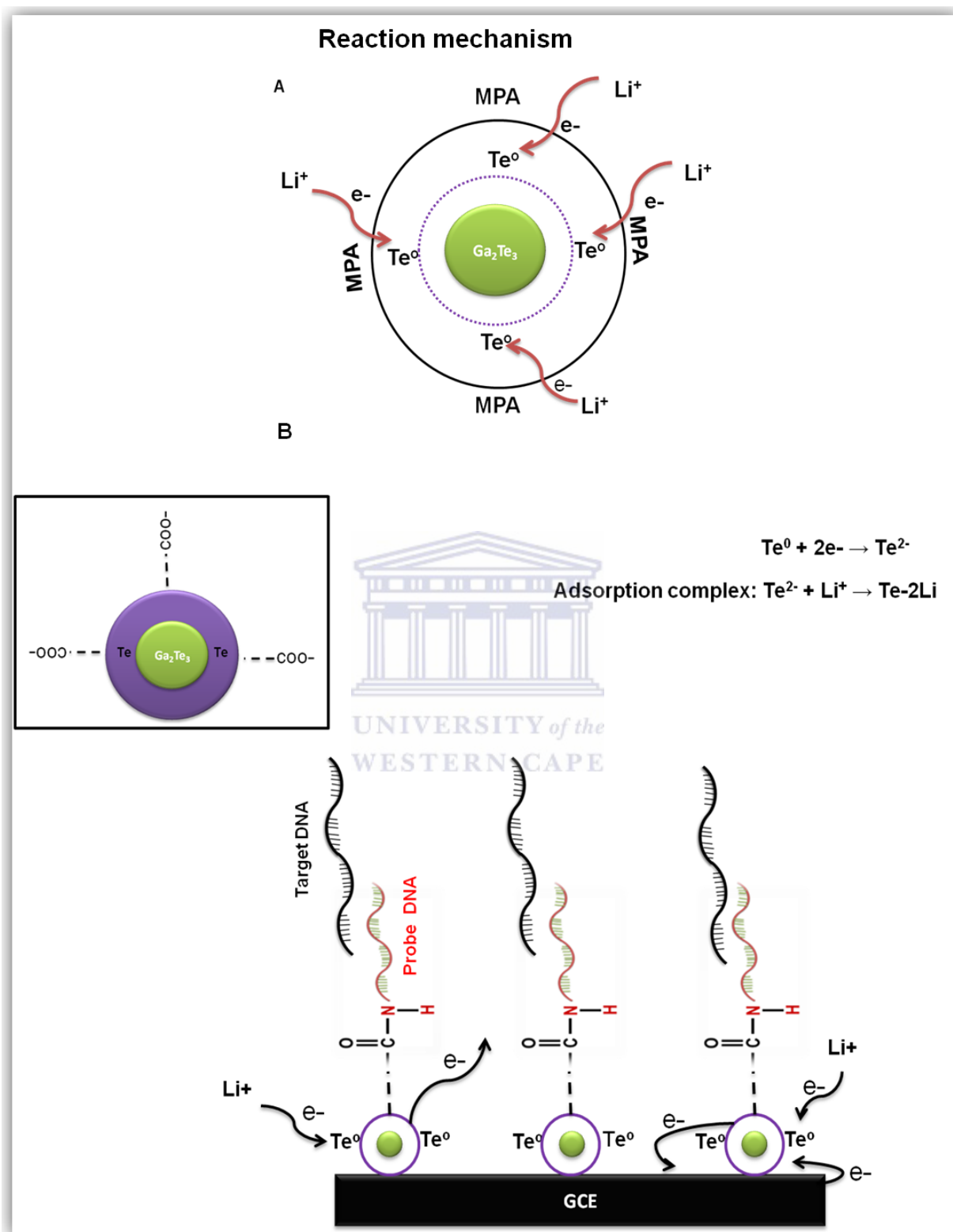


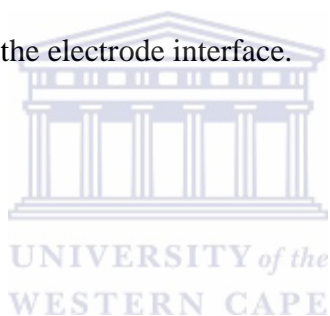
Figure 90. Calibration curve of Her2/oncogene with data from '89 B' LiCl electrolyte.

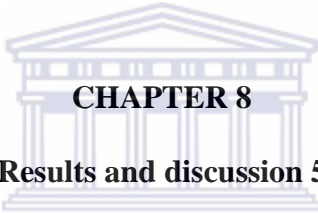


Scheme 5. Reaction mechanism of GC/3 MSA/Ga₂Te₃/dsDNA with cationic species i.e. Li⁺ and Cs⁺.

7.3 Sub-conclusion

Following a detailed investigation of the genosensor signal/detection, it was established that the unreacted telluride on the surface of the quantum dots (3 MPA-Ga₂Te₃) was mostly responsible for the detection signal. Hence the mechanism of the genosensor was designed around this idea. It was believed that upon binding of the genosensor and the target analyte there were pockets available between the quantum dots and the electrode surface in which the unreacted telluride was found to interact with Li⁺ ions. From the interaction an increase in peak current signal was observed. However after hybridisation the current decreased due to high ionic radii and steric hindrance of the Li⁺ and also due to an accumulation of the ssDNA on the immobilised GC electrode. Thus the saturation point of the DNA sensor was reached abruptly due to less active site on the electrode interface.





CHAPTER 8
Results and discussion 5
Cytotoxicity of quantum dots
WESTERN CAPE

8.1 Introduction

QDs are not meant to replace fluorescent dyes and proteins, but rather to be a specialised tool that can augment and complement them. Quantum dots are known to possess advantageous properties compared to conventional dyes. Due to their non-degradation and high photostability quantum dots are more favoured than fluorescent dyes. Internalisation of QDs in the cells can take place in diffusive and active forms [313; 314; 315], which depend dramatically on the type of cell and the biofunctionalisation of the QDs. Among the most referenced methods for a detailed study of this internalisation is confocal microscopy and flow cytometry. This chapter concentrate on the size and toxicity of the nanodots using different electrochemical, microscopic and spectroscopic techniques. Cytotoxicity of quantum dots was carried out using the MTT assay and CC. Lung cell line were used for the study and also the quantum dots delivery/transport was done and characterised with TEM and confocal microscopy. 3MSA-Ga₂Te₃ was used instead of 3MPA-Ga₂Te₃ due to the solubility of the quantum dots. We used 3MSA due to its higher K_{pa} value = 3.41 compared to 3MPA with a K_{pa} value of 3.21. Using the 3MSA ligand helped our quantum dots to be more soluble in water or PBs for this cytotoxicity study.

8.2 Cytotoxicity of quantum dots using 3 MSA-Ga₂Te₃ in cancer cells

8.2.1 Characterisation of 3 MSA-Ga₂Te₃ using electron microscopy and spectroscopy

8.2.1.1 Atomic force and electron microscopy of 3 MSA-Ga₂Te₃

As viewed from literature, size of quantum dots can be of vital importance as far as toxicity is concerned. Arguably the smaller the size of the nanodots the higher the toxicity since there's more penetration of the quantum dots and versa vice.

This theory was put into test in our cytotoxicity study. Before carrying the toxicity study the 3MSA-Ga₂Te₃ quantum dots were characterised. This was done to determining the particle and chemical composition of the nanodots. TEM, HRTEM, STEM, AFM, XPS and XRD were employed to confirm the formation of the as-prepared 3 MSA-Ga₂Te₃ quantum dots. Silicon wafer was used as the sample holder for the distribution of the 3MSA-Ga₂Te₃ nanomaterials.



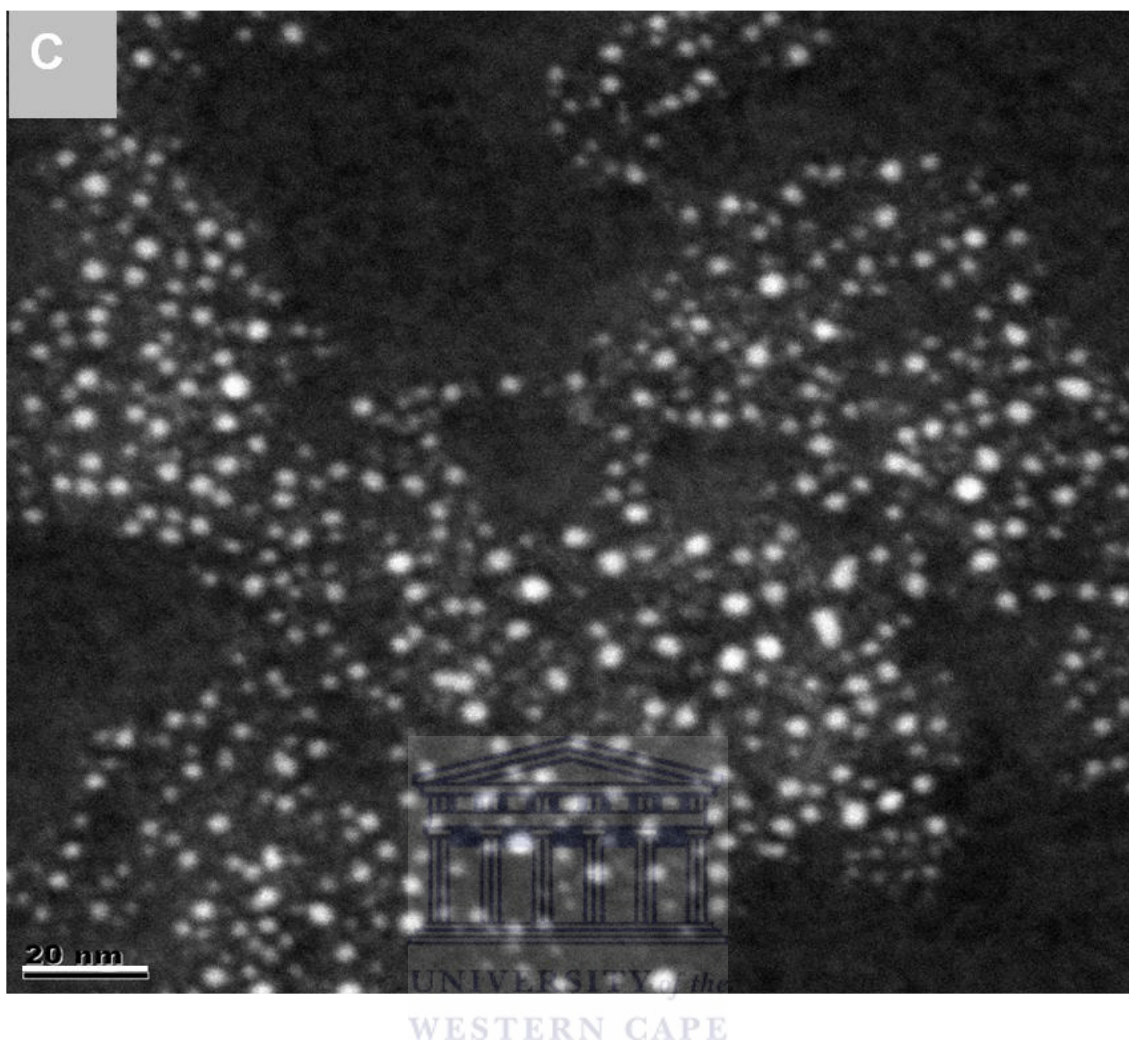
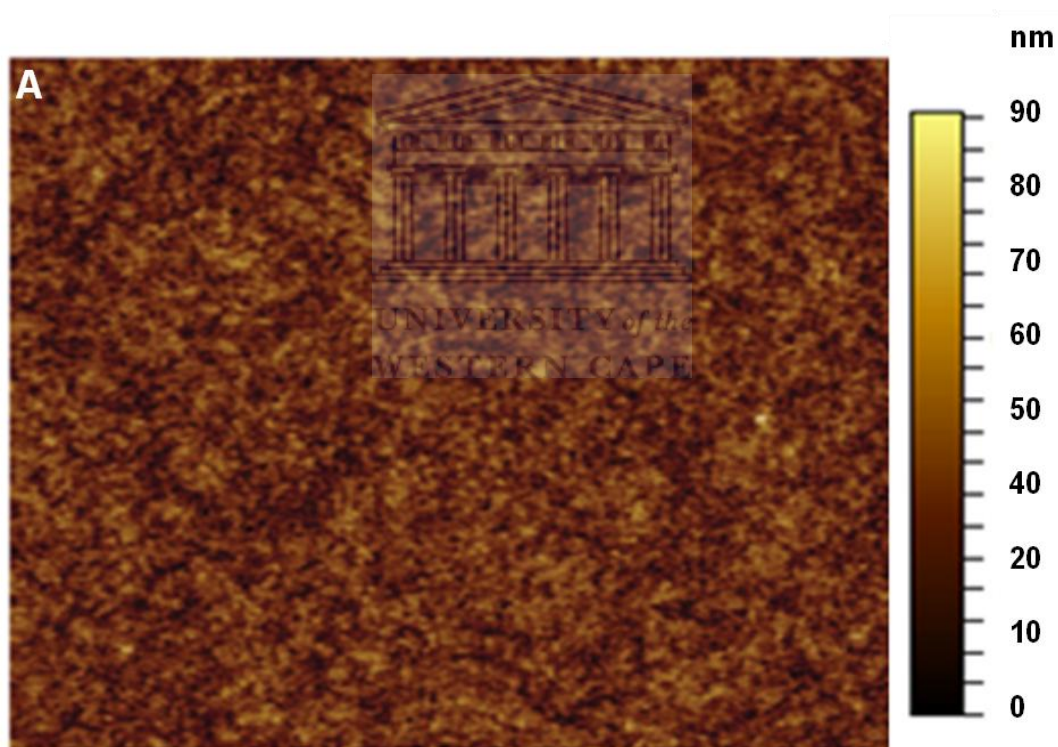


Figure 91. TEM (A), STEM (B) and HRTEM (C:insert) image of Ga₂Te₃-3MSA.

3MSA-Ga₂Te₃ quantum dots with the average particle size of 20 ± 2 nm were evenly distributed on the silicon substrate as shown by the TEM, HRTEM (insert) and STEM images in Figure 91 A and B. The lattice fringe of individual quantum dots with the lattice space (d space) of 0.2 (insert) were found to be in the same direction thus confirming the single-single crystallinity of the nanomaterials and their zinc-blende properties (Figure 91 A). STEM image conform with the results observed in TEM and HRTEM, apparent by the structural morphology and the average particle size of 5 ± 20 nm which is well within range required for the dimensionless quantum dots (Figure 91 C: insert).

8.2.1.2 AFM of 3 MSA-Ga₂Te₃

AFM was also employed in determining the particle size of the 3MSA-Ga₂Te₃ quantum dots. As in other analysis silicon wafer was also used as the sample holder for the immobilisation of the quantum dots. The sample was analysed in air using a non-contact or a tapping mode due to sample softness. Figure 92 A, B and 93 A, B show AFM image of the synthesised 3 MSA-Ga₂Te₃. Images of bare silicon substrate in Figure 92 A showed no particles distribution, confirming that the substrate was not immobilised with the quantum dots (3 MSA-Ga₂Te₃).



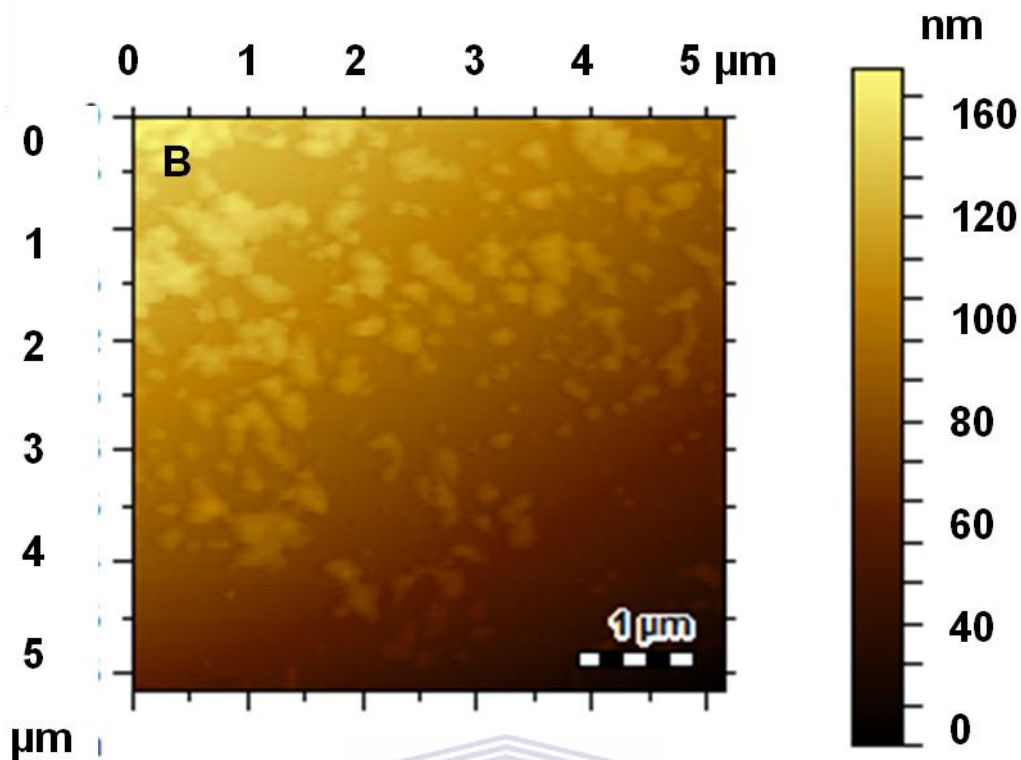


Figure 92. AFM images of 3MSA-Ga₂Te₃ quantum dots.

Compared to bare silicon substrate, the topography image of the quantum dots was found to have a large number of as-prepared quantum dots distributed on the surface of the silicon substrate. However the the QDs were found to be slightly agglomerated; this can be due to improper heating and sonication. Nonetheless, there were more particles size with the average diameter of 20 nm observed. The modified silicon wafer was found to have higher surface roughness (36.9) compared to the unmodified silicon wafer (0.03), Figure 92 A and B. A clear distinction of the nanomaterials was observed from the 3D images, Figure 93 A. The structural morphology of the quantum dots was found to be more globular and oval as is expected to be the nature of the QDs. The results agree well with the TEM, HRTEM, STEM images/data and also with other synthesised quantum dots (e.g. CdTe, CdSe etc.) from literature if morphology and size is concerned.

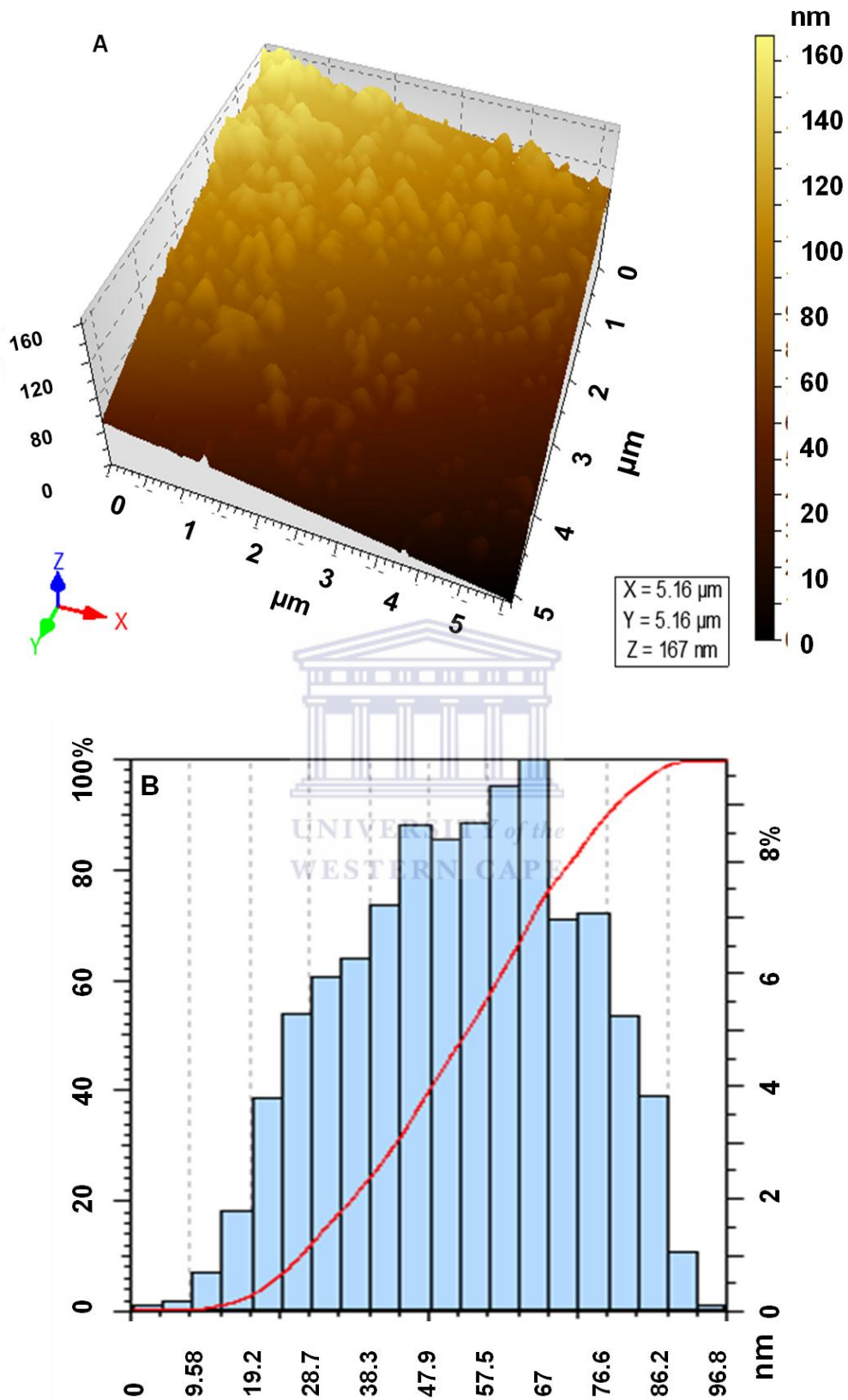


Figure 93. AFM images of 3MSA-Ga₂Te₃ quantum dots.

The distribution of the quantum dots was also confirmed by the histogram image obtained, Figure 93 B. The particle distribution ranged from 19.2 - 76 nm, covering 80% of the substrate surface.

8.2.1.3 XRD analysis of 3 MSA-Ga₂Te₃

XRD and FFT (Figure 94 A, B and C) were employed to explore the crystallinity, the particle size and also the composition of the 3MSA-Ga₂Te₃ quantum dots.

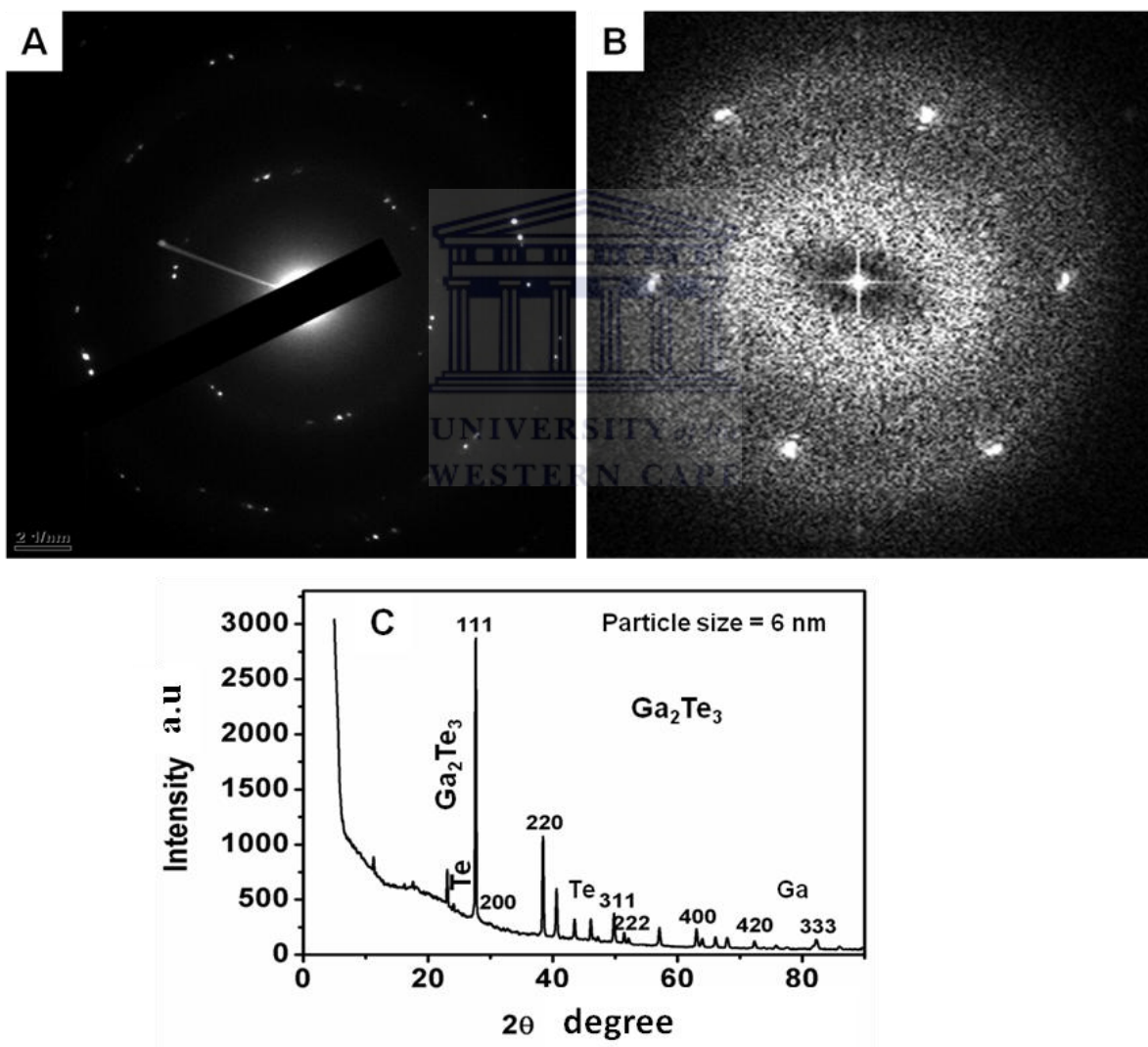


Figure 94. FFT crystallinity of A,B) 3MSA-Ga₂Te₃ and C) X-ray diffraction pattern of 3MSA-Ga₂Te₃ quantum dots.

The images of the FFT observed (Figure 94 A and B) were obtained from TEM instrument in which the fast Fourier transform is coupled. From this technique together with the XRD we were able to determine the crystallinity of our quantum dots. In determining the crystal structure of the quantum dots only one spot or dot was used. From Figure 93 A, it can be seen from the x-ray pattern obtained from TEM that the QDs seem to be of multiple crystalline, however this was found not to be accurate hence further analysis were carried out using FFT with the aim of confirm the true nature of the quantum dots as far as crystallinity is concerned. From the FFT (Figure 94 B) it was clear that the nanodots are of single-single crystallinity, apparent by lattice spacing of the quantum dots. The results obtained from both XRD also showed the 3MSA-Ga₂Te₃ quantum dots were of single crystalline, Figure 94 C. The diffraction peaks observed indicates the nanocrystalite nature. The peaks situated at angles (2θ) of 27.6°, 28.0°, 39.5°, 43.4°, 50.0°, 51.5°, 62.9°, 73.8°, 83.0° corresponds to the reflection from: (111), (200), (220), (311), (222), (400), (420) and (333) crystal planes, respectively. As reviewed in literature the [282; 283] XRD patterns of the nanodots are indexed/associated to the cubic phase (zinc blende) structures with lattice constant, $a = 5.8913$ nm [284]. In the spectrum, plane (111) was found to be very clear and abundant which indicates preferential growth of the crystallites in this particular direction. Based on this observation the average crystal size was calculated based on the width of the peak by using the Scherre's equation (eq. 23) [285]. And it was calculated to be 6 nm, which aggress well with values calculated from other techniques.

8.2.1.4 Structural analysis of 3 MSA-Ga₂Te₃

Modifying the surface of the bimetallic like quantum dots was found to be of great importance in this study. The reason for this was to protect the core shell and avoid the metal ions from leaching out, as this will cause toxicity not only to the environment but also when exposed to the body. Due to this reasons the introduction of the capping agent or ligand to the surface of the quantum dots was investigated. Both FTIR and XPS (Figure 96 and 97) were employed to ensure proper surface capping or coating of the quantum dots. While the EDS and XPS confirmed the components of the as synthesised 3 MSA-Ga₂Te₃ quantum dots, Figure 95 and 97.

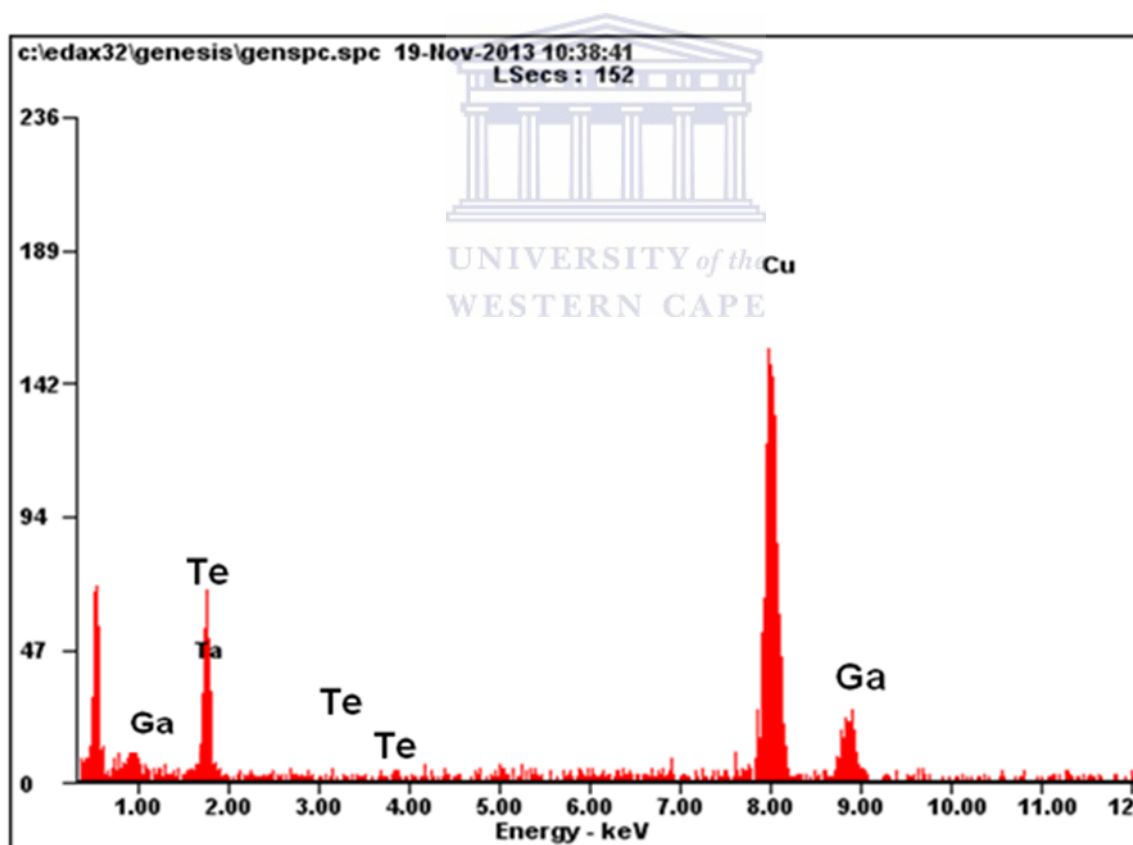


Figure 95. EDS spectra of Ga₂Te₃-3 MSA.

The elemental composition of the prepared quantum dots were observed from the EDS analysis, evident by the presence of Te and Ga peaks in the obtained spectra, Figure 95. The elemental peaks were observed across the spectra at different energies (1 keV – 9 keV). Furthermore the vibration stretches of the capping agent on the surface of the quantum dots were observed from the FTIR spectra, Figure 96. The spectra of 3MSA showed intense vibration stretches at wavenumbers of 1600 cm^{-1} (C=O), 3000 cm^{-1} (OH) and 2500 cm^{-1} (SH). Compared to 3MSA, the capped quantum dots showed less intense vibration stretches with slight shifts in peak positions. The vibration stretches shifted from 1600 to 1550 cm^{-1} (C=O), 3000 to 3500 cm^{-1} (OH) and 2500 to 2450 cm^{-1} (SH). This behaviour suggested that the Ga_2Te_3 quantum dots were well capped with the 3MSA, stable and that there's less chance of the metal ions from leaching out.

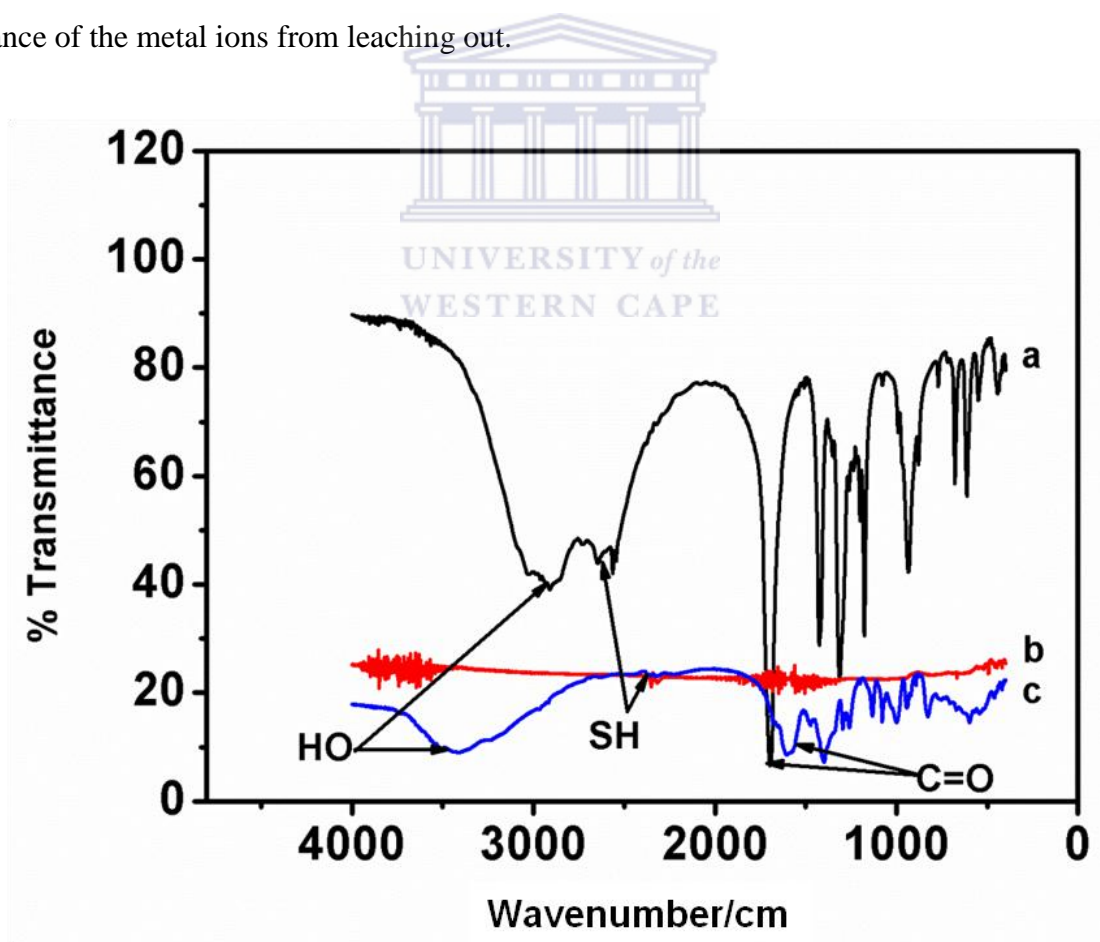


Figure 96. FTIR spectra of a) 3 MPA, b) uncapped Ga_2Te_3 and c) Ga_2Te_3 -3 MSA.

From the XPS analysis the vibrational stretches or vibrational bands and the elemental composition of the 3MSA-Ga₂Te₃ quantum dots were observed (Figure 97). The presence of S, O, C, in the spectra confirmed the capping of the quantum dots while the peaks due to Te and Ga proved the composition of the binary quantum dots. The chemical states of the elements were shown to be in different energy levels and molecular orbitals (Figure 98).

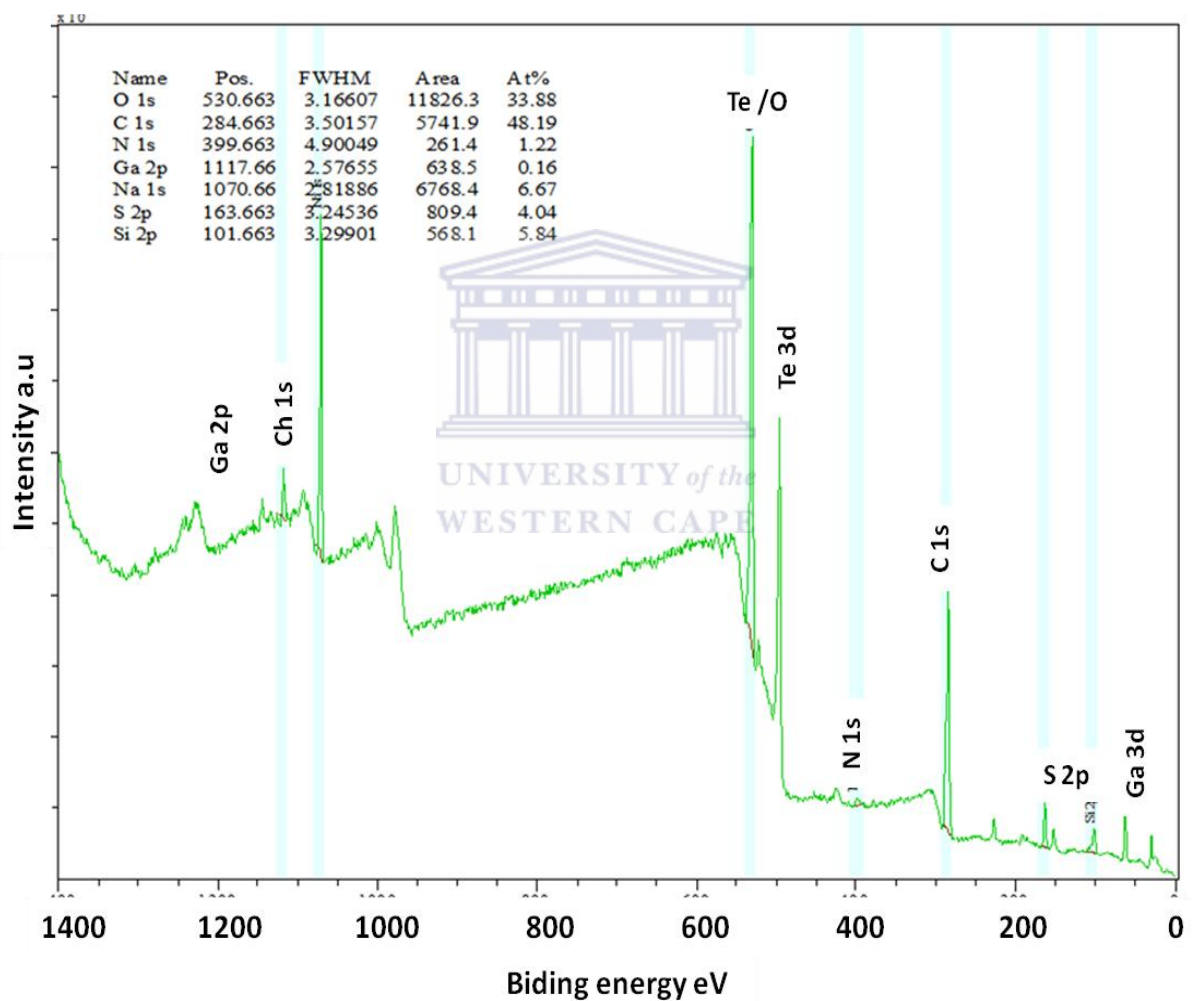


Figure 97. XPS spectra of 3MSA-Ga₂Te₃.

Ga:Te surface concentration was found to be 1:5 which is higher than the expected Ga:Te composition. This indicates that the surface is Te enriched and possibly Ga and Te may be present in more than one oxidation state; Ga₂Te₃ (42.7%), Ga₂O₃ (15%), Ph₂Te₂/Te (35.4%) and TeO₃ (6.8%). There are several factors that may contribute to the difference in composition i.e. surface composition vs. bulk composition, surface is Te enriched, overlapping of O and Ga/Te signal may give rise to variation in composition. There was a substantial amount of oxygen, however, due to co-existing oxygen and oxygenated carbon species, it was difficult to distinguish the contribution from oxidised Ga/Te in the corresponding O 1s spectra. The higher surface composition of Te compared to nominal composition also confirms that Te is present in different oxidation states (elemental tellurium, TeO₃, Ga₂Te₃ etc). So from the bimetallic compositions other than Ga₂Te₃ crystals it is possible that Te is segregated at Ga₂Te₃ surface based upon surface free energy arguments. However, in such cases the bimetallic compositions are notably affected by adsorbates from the surrounding gaseous environment and the metal having the highest affinity for these adsorbates will preferentially segregate to the surface. Figure 98 a and b, show the chemical states or molecular orbitals of the bimetallic. The C-1s spectra consists of peaks arising due to (C-C, C-H, C-O, C-OH, C=O) functionalities arising due to the use of MPA as a capping agent during quantum dots synthesis and interaction with environmental oxygen. Furthermore initial XPS measurements were carried out on the Ga-2p peaks of 3MSA-Ga₂Te₃. The Ga-2p spectra (Figure 98 a) shows two peaks due to a spin (j-j) orbit of Ga 2p_{1/2} and Ga 2p_{3/2} whilst possessing the oxygenated peak Ga-O 1142 eV and Ga-Ga binding at 1117 eV, the observed values are in agreement with the reported values [316; 317; 318].

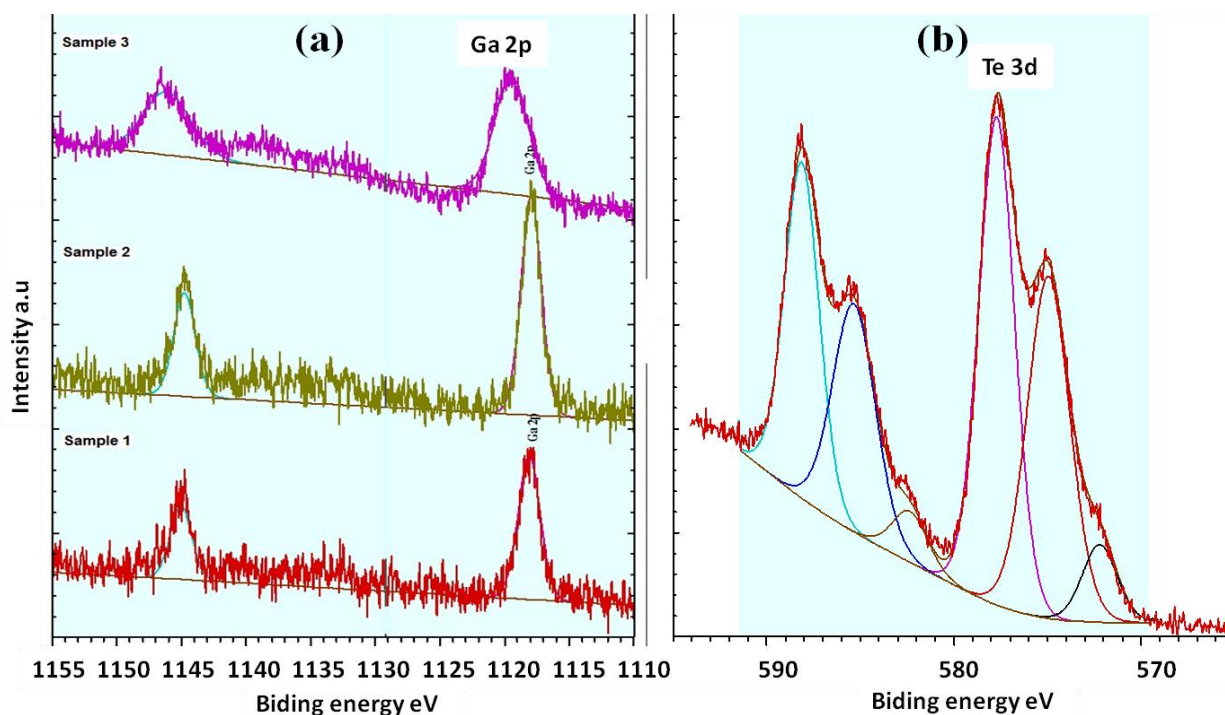


Figure 98. XPS spectra of 3MSA-Ga₂Te₃.

The intensities of O 1s emission, corresponding to gallium oxide (at 1142 eV) and tellurium oxide (at 578 eV) practically coincide with the Ga₂Te₃ stoichiometry, which proves the equal quantity of chemisorbed oxygen on the surface both by gallium and tellurium [319; 320; 321]. XPS peaks of Te 3d for the Ga₂Te₃ sample are shown in Figure 98 b. There are two different overlapping peaks or doublets observed in this figure at binding energies of 590 - 570 eV. Of the two peaks Te 3d_{5/2} peak (576 - 570 eV) is narrower and stronger than Te 3d_{3/2} (585 - 590 eV) and the area of Te 3d_{5/2} peak is greater than that of Te 3d_{3/2} due to spin-orbit ($j-j$) coupling. As explained above both peaks have degeneracy of two states. The peak positions at binding energies of (586 - 573 eV) are associated with Te-O and that of Ga-Te are observed at 578 eV. And a shoulder at 581 eV is due to Te(OH)₂ as reviewed in literature [322] The investigated peaks have been widely explored by many researchers and the values obtained are in good agreement with literature values [319; 322; 323].

8.2.1.6 Toxicity tests of 3 MSA-Ga₂Te₃

This section describes the cytotoxicity of photoactive materials, specifically, quantum dots. The toxicity on photoactive nanomaterials has been developed rapidly and has attracted a great amount of interest. In this study we present the 3MSA-capped Ga₂Te₃ QDs as our photoactive nanomaterials.

It is expected that many novel developments and applications of photoactive nanomaterials will ensue in the near future. Novel 3MSA-Ga₂Te₃ quantum dots have been synthesised and characterised using various methods of preparation and analysis. Figure 99 A, B, C and D, show the cytotoxicity of 3MSA-Ga₂Te₃ quantum dots, using both electrochemical (Figure 99 A and B) and spectroscopic (Figure 99 C and D) methods. The observed results are the average of 3 experiments carried out in triplicate, Figure 99. Error bars $SD\ n = 9$. Data points marked with an asterisk are statistically different from control (Figure 99 A-D) and MTT cytotoxicity data ($\lambda_{max} = 570\text{ nm}$, results are the average of 3 experiments carried out in triplicate. Error bars are $SD\ n = 9$). Several studies have been carried out in determining or investigating the cytotoxicity of the nanomaterials. An example which has been widely reported is the cyto-toxicity of CdTe and CdSe QDs. This was first studied by Derfus *et al.*, [144]. Primary hepatocytes (liver cell) were incubated with CdSe QDs for 24 h following a measurement of cell mitochondrial activity through an MTT viability assay. Severe cytotoxic effects of CdSe QDs were observed even at a low concentration of $62.50\ \mu\text{g mL}^{-1}$ of QDs under certain conditions, such as perturbing the CdSe QDs with UV-light, oxygen or hydrogen peroxide.

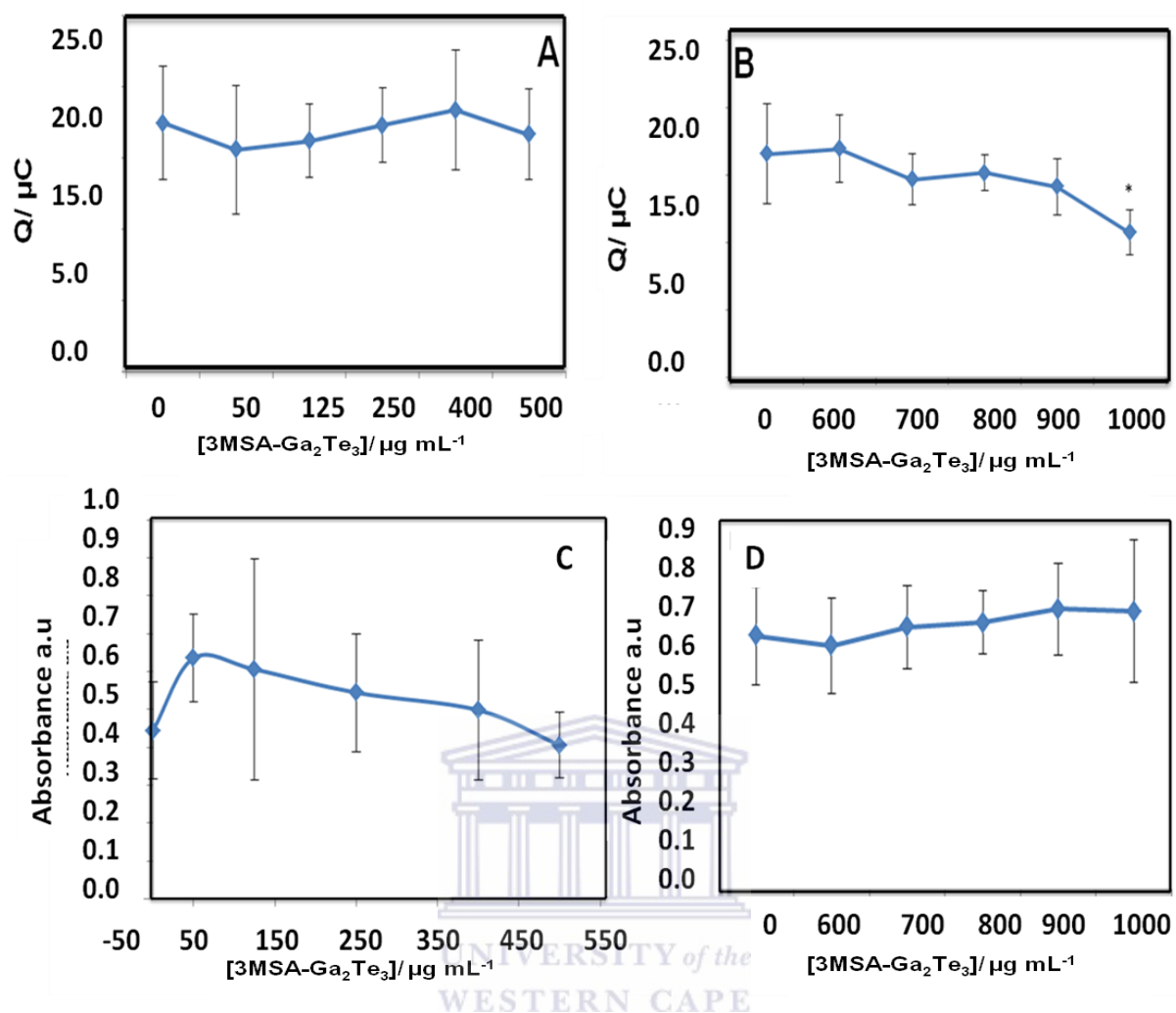


Figure 99. Electrochemical AP cytotoxicity assay.

The release of free Cd²⁺ ions from CdSe QDs after surface oxidation was a key reason for their cytotoxicity. The experiments clearly demonstrated that the extent of cytotoxic effects was correlated with the concentration of the released Cd²⁺. And also this behaviour denotes that the quantum dots were not well capped by the used capping ligand. Compared to the data obtained in the previous studies [144], the as-prepared 3MSA-Ga₂Te₃ quantum dots were found to have no cytotoxic at the observed concentrations of the Ga₂Te₃ quantum dots (Figure 99 C), after 24 h, even though different cell line was used (lung cell- A549 human bronchial lung epithelial cells). However the cytotoxicity of quantum dots was found at higher

concentration of $1000 \mu\text{g mL}^{-1}$ (Figure 99 D) when using CC, the reason for this cytotoxicity of the nanodots at this concentration was due to the quantum dots falling out of suspension and settling on the cells. The data obtained from uv-vis (MTT assay) was compared to one from CC and the two methods were not in agreement due to high sensitivity of the electrochemical method, Figure 99 A and B. The data obtained from both techniques suggest that the coating ligands on the QDs was stable hence the observed results. Additionally the 3 MSA-coated Ga_2Te_3 QDs showed no toxicity compared to previously studied quantum dots (e.g. MUA-CdSe QDs) at the same concentration ($62.50 \mu\text{g mL}^{-1}$). In order to assess 3 MSA- Ga_2Te_3 QDs viability and internalisation, A549 human bronchial lung epithelial cells were incubated for 24 h at 37°C with 3 MSA- Ga_2Te_3 QD at different concentrations of $5.0 - 1000 \mu\text{g L}^{-1}$, washed twice with PBS and then observed under an Light microscopy (X 100) confocal microscope (Hamburg, Germany) at excitation $340\text{--}400 \text{ nm}$ and emission $640\text{--}700 \text{ nm}$ wavelengths. Figure 100 A and B, shows typical confocal microscope images of cells only and exposed to $1000 \mu\text{g mL}^{-1}$ of 3 MSA- Ga_2Te_3 quantum dots. The size effect was also observed during a cytotoxicity study of 3MSA/ Ga_2Te_3 QDs. The green fluorescence 3 MSA- Ga_2Te_3 QDs were found to have a particle size ranging from $2 - 10 \text{ nm}$ in diameter, as reported earlier from the TEM and STEM. From the reported images (Figure 100 B) in which higher concentration exhibited slight cytotoxicity effects of the QDs. The results suggest that there might be very small QDs which were able to penetrate into the nucleus membranes of N9 cells and remained inside the nucleus after 24 h of incubation. Using a fluorescence microscope, the interaction of the 3 MSA- Ga_2Te_3 QDs with cells was monitored in situ. The results suggested that the cytotoxicity of QDs can be reduced by increasing particles size, thus avoiding penetration of smaller QDs from entering the nucleus.

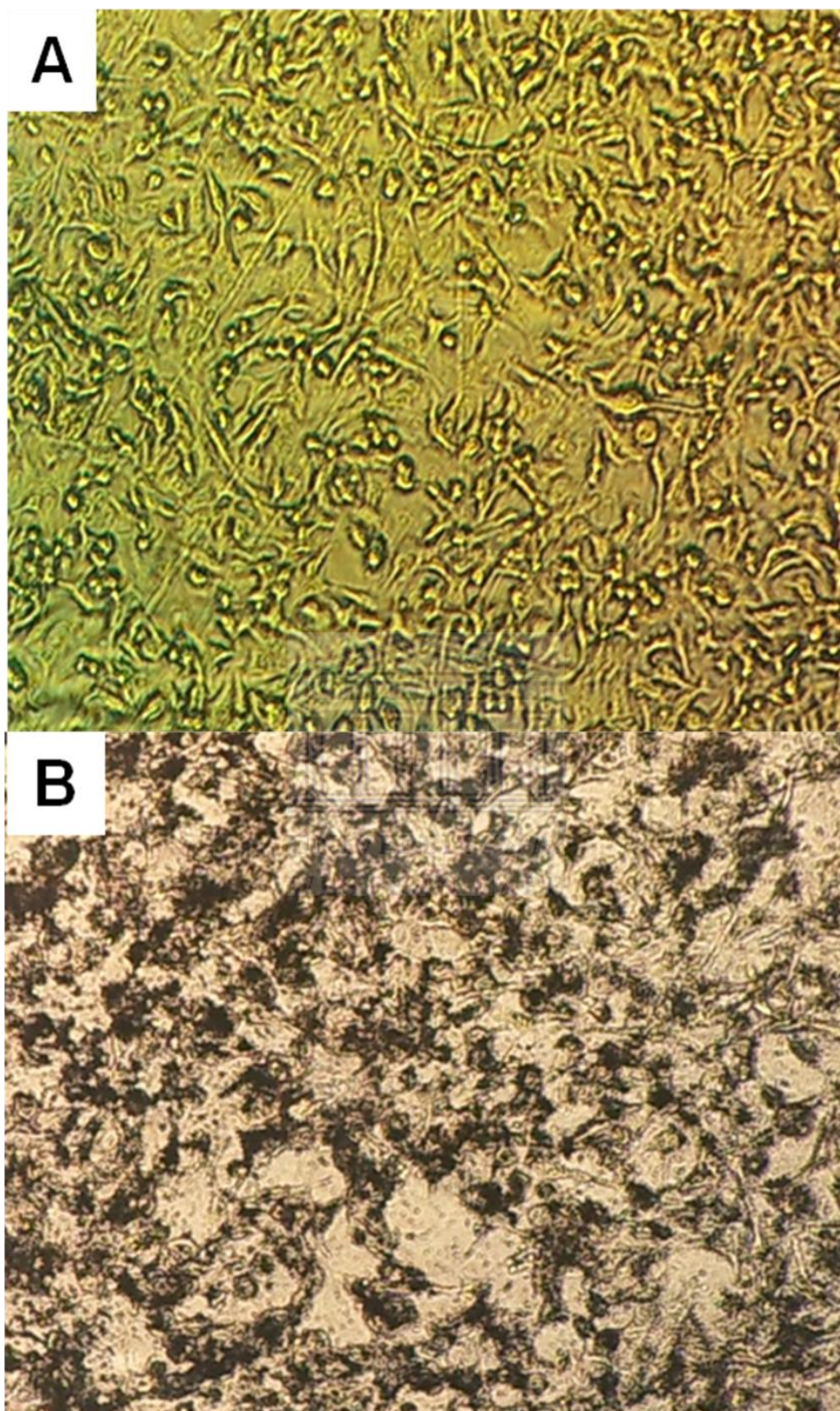


Figure 100. Light microscopy (X100) image of cells after 24 h exposure to (A) medium plus PBS and (B) $1000 \mu\text{g mL}^{-1}$ Ga_2Te_3 3 MSA quantum dots.

Investigation of lung cell exposed to quantum dots (internalization) was carried out using TEM. TEM images of the human lung cells before and after exposure with 3MSA-Ga₂Te₃ quantum dots are as shown in Figure 101.

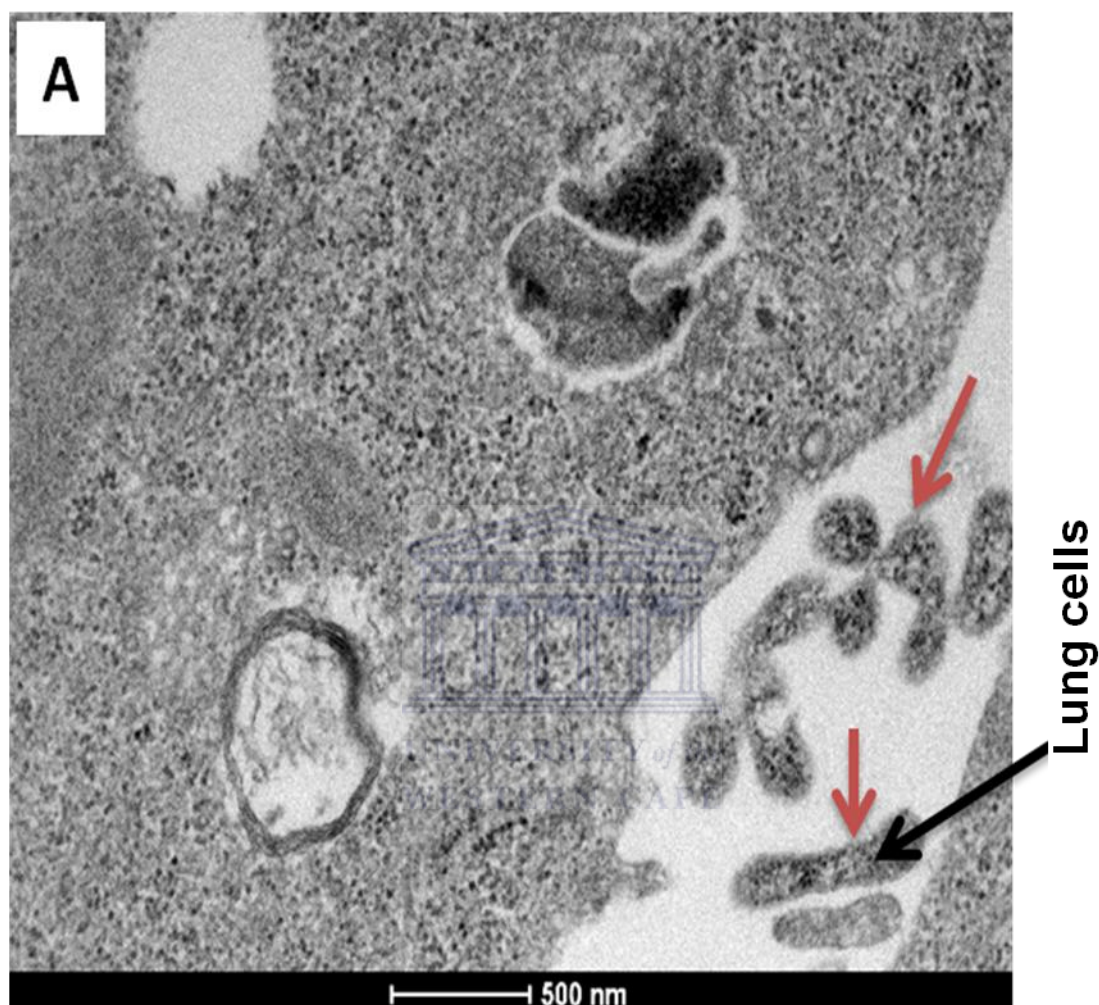


Figure 101. 26500 X TEM images of A549 human lung epithelial cells: (A) in PBS only.

The idea here was to check quantum dots internalisation into the cells. Compared to cell exposure to PBs (Figure 101 A: black arrows), TEM confirmed that the 3MSA-Ga₂Te₃ QDs were not internalised by the cells but they were rather aligned on the vacuolar lining/wall of the cells (Figure 102 A and B: red arrows). The obtained results suggest that the quantum dots were big enough not to enter the nucleus as it was the case from data obtained using confocal microscope and electrochemical methods.

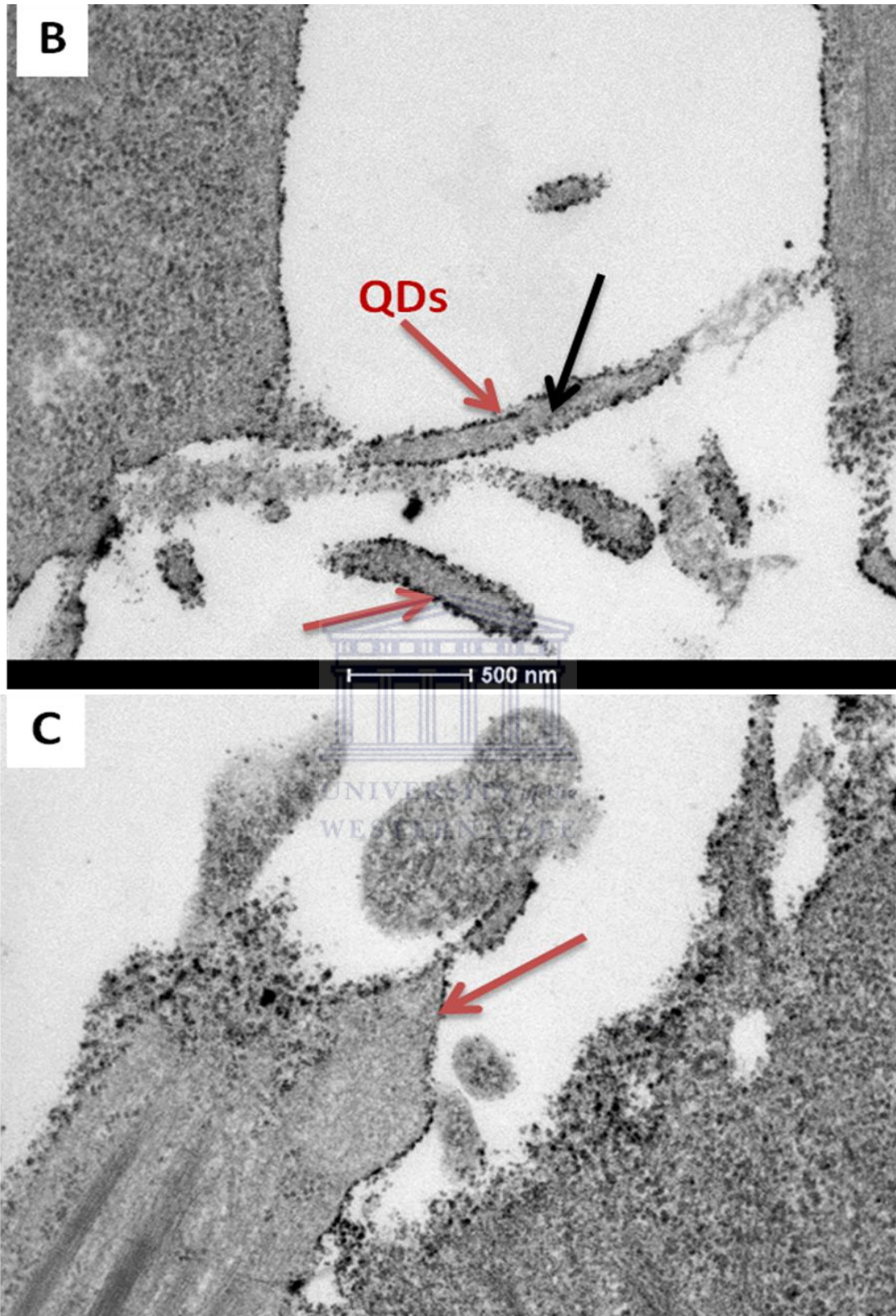
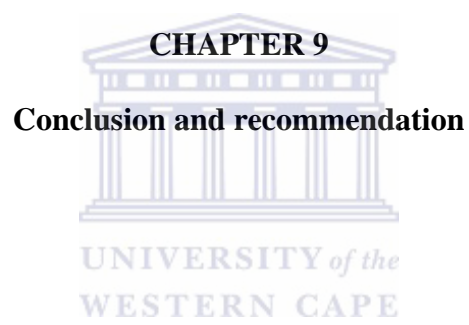


Figure 102. 26500 X TEM images of A549 human lung epithelial cells: (B, C) in PBS solution of 3MSA-Ga₂Te₃.

8.3 Sub-conclusion

From the obtained data and literature reports, it is clear that size, concentration and quantum dots preparation are very important, specifically capping of the nanomaterials. Avoiding the cation e.g. Ga^{2+} from leaching out into the nucleus like Cd^{2+} in previous studies is crucial. Leaching of cation causes cytotoxicity; a stable coating ligand proves to be a priority for quantum dots functionalisation. Electrochemical methods and microscopic methods proved to be more sensitive than spectroscopic methods since the toxicity of the quantum dots were observed when using the latter methods.





9.1 Conclusion

The fast progression of DNA-based biosensors highlights their future applications in various scientific fields. The major impacts of such technologies appear to be in early detection of diseases, pathogens, genetic mutations and bio-targets. Of these applications, early detection of cancer seems to present an interesting approach for the development of novel target-based sensors/therapies. In this study, novel biocompatible and water soluble Gallium telluride quantum dots (3 MPA-Ga₂Te₃ and 3MSA-Ga₂Te₃) were successfully synthesised and the redox properties and structural morphology of the quantum dots were successfully determined by microscopic and electrochemical methods. The composition of the quantum dots was verified by EDS and XPS, in which the constituents in Ga, Te, S and O were observed. The chemical states, crystallinity and molecular orbital of the as-synthesised quantum dots were successfully achieved by XPS, XRD and FFT. UV-visible, electrochemical impedance and fluorescence technique were able to determine the conductivity of the quantum dots, which was found to be that of a semiconductor. From both UV-visible and fluorescence technique it was possible to calculate the band gap energies (3 - 3.5 eV) which increased with refluxing time but was still within the required range of the semiconductor. The bifunctional amphiphilic molecule (3-mercaptopropionic acid and 3-mercaptosuccinic acid) used as capping agents rendered the quantum dots biocompatible, soluble and stable. Electrostatic repulsion arising from dehydrogenated carboxyl groups on the surface of the quantum dot particles kept them non-agglomerated. Retention of the capping agent on the quantum dot surface was successfully confirmed by FTIR and Raman studies, which showed characteristic vibrational stretches and bands related to C-H, C=O, -SH as well as -O-H groups. The hydrophilic nature of the capped quantum dots were confirmed by contact angle measurements, evident by contact angle of 12.2° which showed

good wetting compared to that of uncapped quantum dots 79.9° . The as-synthesised MPA-capped Ga_2Te_3 quantum dots proved to have better quantum yield in comparison with organic dye, rhodamine 6G. Since high quantum yield is desirable in most imaging applications, the obtained data confirmed the photostability of the MPA-capped Ga_2Te_3 quantum dots and that they can be considered as an alternative to fluorescent dyes, notably in biological uses. In other study a breast cancer genosensor was successfully developed and characterised using electrochemical and spectroscopic methods. The techniques used to monitor hybridisation events between the probe DNA and different targets were i.e. SWV, EQCM, EIS, CC and UV-vis.). It was generally observed that all analytical techniques exhibited good linearity, presenting linear correlation coefficients superior to 0.99. The linear range of the sensor was found to range from 1.8 - 740.00 ng mL^{-1} . And from both electrochemical and spectroscopic detection methods these values were found to be significantly lower than reported literature values (28 - 46250 ng mL^{-1}). Furthermore, the detection limit and sensitivity of the genosensor from SWV and EQCM were calculated to be 0.0002 - 0.0006 ng mL^{-1} and 0.028 - 0.18 ng mL^{-1} , respectively. The calculated *LOD* values for the genosensor were significantly lower than reported literature values (0.06 - 100 ng mL^{-1}) and most importantly were far below physiological limits (FDA approved guidelines) for Her2/neu detection (2 - 15 ng mL^{-1}). The study also involved application of the synthesised quantum dots in fabrication of sensing platform for selected analytes or cross-reactivity studies (complimentary, 1-base mismatch, 3-base mismatch and non-complimentary). Compared to other analytes, the sensor proved to be more specific to the complimentary analyte. Additionally, a genosensor that is efficient, effective and capable of detecting analytes (target DNA) in small concentrations was developed successfully. While conversely the genosensor proved to be significantly stable after being used for several measurements. The calculated percentage from statistical analysis for the sensor was found to be exceptionally small, suggesting that the genosensor

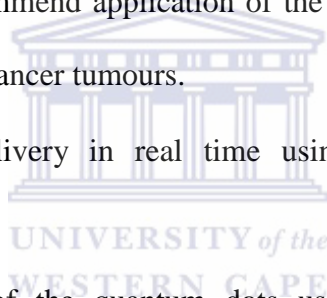
can be used for several measurements without being depleted. The genosensor was compared to traditional methods such as IHC, FISH, ELISA and PCR; PCR will serve as an example in this regard. It was reported that traditional PCR requires prolonged sample preparation prior to detection (minutes-hours) whilst the genosensor is less time consuming; it takes (seconds-minutes) in detection. In addition, the PCR is known to have low detection limit (0.06 ng mL^{-1}) and has high specificity compare to other traditional methods. However, based on the data presented in our work the genosensor was found to have very low *LOD* ($0.0002 \text{ ng mL}^{-1}$). Furthermore, the genosensor was found to be highly specific when introduced to different analytes thus proving ones more that it surpasses the traditional methods which are prone to errors. The genosensor is very promising and have the potential for the high sensitive detection of transgenes or biomarkers for breast cancer. Additionally the device can be used as a tool for monitoring disease progression in a low-cost sensing setup. This experimental success with analytical (buffer-based) samples should encourage future work with clinical (serum-based) samples. Furthermore, the results also denotes that the classical use of quantum dots as DNA labels can be substituted with “use of quantum dots as platforms for probe DNA immobilisation”, thus reducing the number of genosensor fabrication procedures, time of fabrication as well as the cost. Successful detection of the studied analytes on the binary quantum dot platforms widens the scope of biocompatible nanostructured platforms upon which other biomolecules of interest can be immobilised for a wide range of analytical purposes. The mechanism of the genosensor system was established based on metal ion (Li^+) interaction with the $\text{Au}/3\text{MPA-Ga}_2\text{Te}_3/\text{dsDNA}$. The sensing mechanism attributed a strong effect of Li^+ counterions on the electronic response, thus suggesting a charge-based mechanism of DNA detection using $\text{Au}/3\text{MPA-Ga}_2\text{Te}_3/\text{dsDNA}$. TOXOR was recently developed as a simple and highly sensitive tool for the toxicity assessment of 3MSA-capped Ga_2Te_3 quantum dots. Despite significant interest in developing quantum dots for biomedical

applications, many researchers are convinced that QDs will never be used for treating patients because of their possible toxicity. The perception that QDs are toxic is sourced in the assumption of cadmium-containing QDs that are believed to kill cells in culture. Many researchers then assume that because other QDs are toxic to the cells, they classify QDs as a homogeneous group of materials. Though unsubstantiated, these assumptions continue to drive QDs research. Additionally, QDs are not uniform: each design is a unique combination of physicochemical properties that influence biological activity and toxicity. In this account, we summarise key findings from our cytotoxicity studies, explore the causes of the divergency in QD toxicological data and provide our view of the future path of the field. Concentration-dependent cytotoxicity studies on lung cells were carried out, toxic effects of 3MSA-capped Ga_2Te_3 quantum dots on human lung cancer cells were measured by chronocoloumetry and classic MTT assay method. Compared to CC, Conventional MTT assay did not show toxicity of 3MSA-capped QDs at low and higher concentrations (5 - 1000 $\mu\text{g mL}^{-1}$). However toxicity of the capped quantum dots was observed at concentrations of 1000 $\mu\text{g mL}^{-1}$ when using electrochemical method (CC). And this cytotoxicity of 3MSA-capped quantum dots at this particular concentration was confirmed using both confocal microscope and TEM techniques. From the observed images it was assumed that the particles might have fallen out of suspension and settled on the cells, hence a slight toxicity. IC_{50} values for the QDs were not calculated since the quantum dots did not show 50% reduction in cell viability by either assay. Compared to other reviewed capped quantum dots i.e. CdTe and CdSe, the 3MSA-capped Ga_2Te_3 QDs proved to be significant since there were no cytotoxicity observed to the cancer cell lines at the same concentrations (5 - 62.50 $\mu\text{g mL}^{-1}$). There are several factors known to contribute to the cyto-toxicity of the quantum dots such as concentration, particle size and mainly the surface coating of the QDs. This physicochemical parameter affects their biological and toxicological effects. However, based on our findings it

can be concluded that the 3MSA-capped quantum dots were not affected by the mentioned parameters since no toxicity was observed. Considering the various aspects studied, these results suggest that the as-prepared water soluble 3MSA-capped Ga₂Te₃ quantum dots produced in an environmentally friendly manner and at low temperatures have the potential to be used for toxins and contaminants in the environment. Such environmental contaminants include e.g. persistent organic pollutants (POP) and polychlorinated biphenyl (PCBs). Since quantum dots for environmental monitoring purposes have not been extensively tested, but biological uses are currently being tested. The same kind of dots used for biological tests (in our case 3MSA-capped Ga₂Te₃) would be needed for environmental tests. This means water soluble quantum dots are required, meaning cheaper, environmentally friendly aqueous growth methods will probably work best. The results of the present study also hold promise in the biomedical application (e.g. clinical diagnosis, pathogen and drug delivery) and in the future design of biologically safe quantum dots. Other areas in which quantum dots can be explored are in (a) Anti-counterfeiting capabilities: inject dots into liquid mixtures, fabrics, polymer matrices, and the ability to specifically control absorption and emission spectra to produce unique validation signatures and (b) Defense applications: Integrate quantum dots into dust that tracks enemies. The unique and attractive properties of quantum dots present new opportunities for the design of highly sophisticated electroanalytical DNA sensing devices. Due to their high surface area, nontoxicity, biocompatibility and charge-sensitive conductance of nanomaterials they act as effective transducers in nanoscale biosensing and bioelectronic devices.

9.2 Recommendations

- Synthesise ternary Ga₂Te₃ quantum dots with the incorporation of iron (Fe) in the systems.
- Investigate the attachment of EDC/NHS and DNA onto quantum dots using gel electrophoresis method
- Investigate the binding event or attachment of quantum dots to DNA or other biomolecules using AFM technique
- Using nanodot technique as a means of detection for DNA sensor
- A comparative study between genosensor and ELISA method
- I would also highly recommend application of the genosensor for detection of other oncogene from different cancer tumours.
- Study quantum dots delivery in real time using TEM and other microscopic techniques
- Enhance the solubility of the quantum dots using several capping short chain biomolecules for toxicity assays and bio-imaging applications
- Further studies on the GenoDot microanalyser preferably using the PCR method.



References

- [1] M.P. Bray and D.M. Parkin., The changing global patterns of female breast cancer incidence and mortality. *Breast Cancer Research* 6 (2004) 229–239.
- [2] C. Shih, L. Padhy, M. Murray and R.A. Weinberg., Transforming gene of carcinomas and neuroblastomas introduced into mouse fibroblasts. *Nature* 290 (1981) 261-264.
- [3] M.C. Hung, A.L. Schechter, L. Vaidyanathan, D. Stern and R.A. Weinberg., Isolation of the molecular clone of the neu oncogene from the B103 rat neuro/glioblastoma cell line. *Molecular Epidemiol Cancer* 40 (1986) 391-395.
- [4] N.C. Popescu, C.R. King and M.H. Kraus., Localization of the human erbB-2 gene on normal and rearranged chromosomes 17 to bands q12-21.32. *Genomics* 4 (1989) 362-366.
- [5] D.H. Yu., Overexpression of ErbB2 in cancer and ErbB2-targeting strategies. *Oncogene* 19 (2000) 6115–6121.
- [6] K.F. Lee, H. Simon, H. Chen, B. Bastes, M.C. Hung and C. Hauser., Requirement for neuregulin receptor erbB2 in neural and cardiac development. *Nature* 378 (1995) 394-398.
- [7] D.H. Yu., In: *Molecular Basis of Oncology* 1st ed., Blackwell Scientific Publication, Cambridge, (1995) 131-162.
- [8] J.Y. Jiang, R. Greenlee, Y. Shen, H. Duan, X. Chen., Effects of silencing of HER2/neu gene in anti-BPDE-transformed cells. *Toxicology In Vitro* 23 (2009) 53-59.
- [9] B.T. Chuanga, J.Y. Liuc, C.T. Lind, W.L. Su-Chien., Change, H, M.C. Kaoe, Human manganese superoxidizedismutase suppresses HER2/neu-mediated breast cancer malignancy. *Nano Letters* 581 (2007) 4443-4449.

- [10]G. Cornolti, M. Ungari, M. Morassi, F. Facchetti, E. Rossi, D. Lombardi, P. Nicolai., Amplification and overexpression of HER2/neu gene and HER2/neu protein in salivary duct carcinoma of the parotid gland. Archives of Otolaryngology – Head & Neck Surgery 133 (2007) 1031-1036.
- [11]J. Fu, Y. Jiang, Y. Zou, Y. Shen, A. Gartel, E.S. Kandel., Effect of anti-BPDE on expression of HER2/neu gene in the human bronchial epithelial cell line. Biomolecular Engineering 23 (2007) 17-34.
- [12]E. Verri, P. Guglielmini, P. Puntoni, M. Perdelli, L. Papadia, A. Lorenzi, P. Rubagotti, R. Boccardo., HER2/neu oncoprotein overexpression in epithelial ovarian cancer: evaluation of its prevalence and prognostic significance: Clinical study. Oncology 68 (2005) 154-161.
- [13]C. Lottner, S. Schwarz, S. Diermeier, A. Hartmann, R. Knuechel, Hofstaedter, G. Brockhoff., Simultaneous detection of HER2/neu gene amplification and protein overexpression in paraffin-embedded breast cancer. Pathology 205 (2005) 577-584.
- [14]H.K. Koeppen, B.D. Wright, A.D. Burt, P. Quirke, A.M. McNicol, N.O. Dybdal, M.X. Sliwkowski, K.J. Hillan., Overexpression of HER2/neu in solid tumours: an immunohistochemical survey. Histopathology 38 (2001) 96-104.
- [15]T.E. Seeman., Allostatic load as a marker of cumulative biological risk: Macarthur studies of successful aging. Proceedings of the National Academy of Science 98 (2001) 4770-4775.
- [16]B.S.Dohrenwend, Overview of biological markers. In: Biological markers in epidemiology 4th ed., Oxford University Press, New York, (1990) 45-74.
- [17]S. Naylor., Biomarkers: current perspectives and future prospects. Expert Review of Molecular Diagnostic 3 (2003) 525-529.

- [18]T.L. Gruenewald., Combinations of biomarkers predictive of later life mortality. Proceedings of the National Academy of Science 103 (2006) 14158-14263.
- [19]C. Ding, Q. Zhang, J. Lin, and S. Zhang., Electrochemical detection of DNA hybridization based on bio-bar code method. Biosensors and Bioelectronics 24 (2009) 3140-3143.
- [20]T.G. Drummond, M.G. Hill, and J.K. Barton., Electrochemical DNA sensors. Nature Biotechnology 21 (2003) 1192-1199.
- [21]C. Burda, X. Chen, R. Narayanan, and M.A. El-Sayed., Chemistry and properties of nanocrystals of different shapes. Chemical Reviews 105 (2005) 1025-1102.
- [22]R.R. Naik, S.J. Stringer, G. Agarwal, S.E. Jones., Stone biomimetic synthesis and patterning of silver nanoparticles. Nature Materials 1 (2002) 69-172.
- [23]A. Ghadimi, C. Ludovico., Molding flexible nanocrystal solids into multifunctional architectures. Journal of the American Chemical Society 7 (2007) 3864-3868.
- [24]P. Alivisatos., The use of nanocrystals in biological detection. Nature Biotechnology 22 (2004) 52-47.
- [25]A.V. Drbohlavova, R. Kizek., Quantum dots - characterization, preparation and usage in biological systems. International Journal of Molecular Sciences 10 (2009) 656-673.
- [26]T. Franzl, J. Müller, T.A. Klar, A.L. Rogach, J. Feldmann, D.V. Talapin, and H. Weller., CdSe:Te Nanocrystals: Band-edge versus Te-related emission. Journal of Physical Chemistry C 111 (2007) 2974-2979.
- [27]R.E. Bailey., Alloyed semiconductor quantum dots: Tuning the optical properties without changing the particle size. Journal of the American Chemical Society 125 (2003) 7100-7106.

- [28]N. Pradhan, D. Goorskey, J. Thessing, and X.G. Peng., An alternative of CdSe nanocrystal emitters: Pure and tunable impurity emissions in ZnSe nanocrystals. *Journal of the American Chemical Society* 127 (2005) 17586-17587.
- [29]W.C. Chan., Quantum dot bioconjugates for ultrasensitive nonisotopic, p-detection. *Science* 281 (1998) 2016-2018.
- [30]J. Aldana, Y.A. Wang, and X. Peng., Photochemical instability of cdse nanocrystals coated by hydrophilic thiols. *Journal of the American Chemical Society* 123 (2001) 8844-8850.
- [31]M. Liu, G. Shi, L. Zhang, Y. Cheng, and L. Jin., Quantum dots modified electrode and its application in electroanalysis of hemoglobin. *Electrochemistry Communications* 8 (2006) 305-310.
- [32]M.J. Giz, B. Duong, and N.J. Tao., In situ STM study of self-assembled mercaptopropionic acid monolayers for electrochemical detection of dopamine. *Journal of Electroanalytical Chemistry* 465 (1999) 72-79.
- [33]J. Li, G. Zou, X. Hu, and X. Zhang., Electrochemistry of thiol-capped CdTe quantum dots and its sensing application. *Journal of Electroanalytical Chemistry* 625 (2009) 88-91.
- [34]J. Wang., Nanoparticle-based electrochemical DNA detection. *Analytica Chimica Acta* 500 (2003) 247-257.
- [35]Z.S. Huang, H. Qiu, Q. Xiao, Q. Zhou, W. Su, B. Hu., A sensitive quantum dots-based "OFF-ON" fluorescent sensor for ruthenium anticancer drugs and ctDNA. *Colloids and Surfaces B-Biointerfaces* 117 (2014) 240-247.
- [36]J. Hopkins., New nanosensors uses quantum dots to detect DNA 6 (2005) 453-461.

- [37]A.O. Morten, L. Jepsen, Birgitta R. Knudsen and Yi-Ping Ho., Quantum dot based DNA nanosensors for amplification-free detection of human topoisomerase I. *RSC Advances* 4 (2014) 2491-2494.
- [38]Z.S. Qian, X.Y. Shan, L.J. Chai, J.J. Ma, J.R. Chen, H. Feng., DNA nanosensor based on biocompatible graphene quantum dots and carbon nanotubes. *Biosensors and Bioelectronics* 60 (2014) 64-70.
- [39]Z. Xu, Chapter 12 - Genomics and molecular profiling of lung cancer, in: G. Dellaire, J.N. Berman, R.J. Arceci, 1st ed., *Cancer Genomics*, Academic Press, Boston (2014) 193-211.
- [40]P.M. F. Bray, D.M. Parkin., The changing global patterns of female breast cancer incidence and mortality. *Breast Cancer Research* 6 (2004) 229–239.
- [41]M. Corbex, S. Bouzbid, P. Boffetta., Features of breast cancer in developing countries, examples from North-Africa. *European Journal of Cancer* 50 (2014) 1808-1818.
- [42]S.H. Ferlay, F. Bray, D. Forman, C. Mathers, D.M. Parkin., Cancer incidence and mortality worldwide. *International Agency for Research on Cancer* 2 (2010) 253-260.
- [43]C.C. Devilee., Somatic genetic changes in human breast cancer. *Biochimica et Biophysica Acta* 1198 (1994) 113-130.
- [44]S.H. Lewis, D. Margaret, *Medical/surgical nursing* 2nd ed., Mosby, Lippincott, (2000) 452-470.
- [45]B.W. Cohen., *Memmler's structure and function of the human body* 7th ed., Williams & Wilkins Lippincott, Philadelphia (2000).
- [46]W.W. Gibbs., Untangling the roots of cancer. *Scientific American* 11 (2003) 57-65.
- [47]R.W. Memmler., *The human body in health and disease*, Williams & Wilkins Lippincott, (2000) 93-95.
- [48]C. Bahls, and M. Fogarty., Reining in a killer disease. *The Scientist* 6 (2000) 16-33.

- [49]O.I. Angeletti S, Jimenez., Molecular aspects of breast cancer. In: García-Foncillas. Genetic Diagnosis in Medicine, Pamplona, Spain, (1998) 61-82.
- [50]J. Kling., Put the blame on methylation. *The Scientist* 16 (2003) 27–28.
- [51]A.J. Rayl, R. Lewis., In cancer research, diet and exercise roles strengthen. *The Scientist* 15 (2001) 17-35.
- [52]S.H. Ferlay, Bray, F. Forman, Mathers, M.D. Parkin., Cancer incidence and mortality worldwide. *International Agency for Research on Cancer* 2 (2008) 10-44.
- [53]S.B. Corbex, P. Boffetta., Features of breast cancer in developing countries, examples from North-Africa. *European Journal of Cancer* 50 (2014) 1808–1818.
- [54]S. Veggeberg., Fighting cancer with angiogenesis inhibitors. *The Scientist* 16 (2002) 41-57.
- [55]W.E. Ruddy., Male breast cancer: risk factors, biology, diagnosis, treatment, and survivorship. *Annals of Oncology* 24 (2013) 1434-1443.
- [56]T.K. Goodman, M.T. Wilkens., Comparative epidemiology of breast cancer among men and women in the US, 1996 to 2000. *Cancer Causes and Control* 17 (2006) 127-136.
- [57] V.D Vijver, M.J. He, H. Dai, V. Hart., Molecular genetic changes in human breast cancer. *Advance in Cancer Research* 61 (1993) 25-56.
- [58]L.R. Bieche., Genetic alterations in breast cancer. *Genes Chromosomes Cancer* 14 (1995) 227-251.
- [59] J. Ferlay., HER2-positive breast cancer an aggressive type of breast cancer. *International Journal of Cancer* 127 (2010) 2893-2917.
- [60]L.A. Hameed., Human epidermal growth factor receptor 2 testing in breast cancer: 30% versus 10% cut-off for immunohistochemistry. *Journal of Clinical Oncology* 131 (2007) 18-43.

- [61]T.S. Latta EK, Parkes, R.K. O'Malley., The role of HER-2/neu overexpression/amplification in the progression of ductal carcinoma in situ to invasive carcinoma of the breast. *Modern Pathology* 15 (2002) 1318-1325.
- [62]K.N. Semba K, Toyoshima., A v-erbB-related proto-oncogene, c-erbB-2, is distinct from the c-erbB-1/epidermal growth factor-receptor gene and is amplified in a human salivary gland adenocarcinoma. *Proceeding of the National Academy of Science* 82 (1985) 6497-6501.
- [63]R.N. Carney, A. Lipton, K. Leitzel, S. Ali and C. Price., Potential clinical utility of serum her-2/neu oncoprotein concentrations in patients with breast cancer. *Clinical Chemistry* 49 (2003) 1579–1598
- [64]E.K. Rowinsky., Cell signal transduction and its inhibition in cancer. *The Oncologist* 8 (2003) 5-17.
- [65]K.C. Popescu NC, Kraus., Localization of the human erbB-2 gene on normal and rearranged chromosomes 17 to bands q12-21.32. *Genomics* 4 (1989) 362-366.
- [66]J.J. Nielsen KV, Schonau., Human epidermal growth factor receptor 2 testing in breast cancer. *Archives of Pathology and Laboratory of Medicine* 131 (2007) 1330-1341.
- [67]J.C. Albanell, J. Rovira, A. Mellado, B. Gascón., Mechanism of action of anti-HER2 monoclonal antibodies: scientific update on trastuzumab and 2C4 new trends in cancer for the 21st century. *Advances in Experimental Medicine and Biology* 532 (2003) 253-268.
- [68]T.H. Holbro., ErbB receptors: Directing key signalling networks throughout life. *Annual Review of Pharmacology and Toxicology* 44 (2004) 195-217.
- [69]A.C. Wolff, J.N. Schwartz., American society of clinical oncology/college of American pathologists guideline recommendations for human epidermal growth factor receptor

- 2 testing in breast cancer. *Archives of Pathology and Laboratory of Medicine* 131 (2007) 18-43.
- [70]C.O. Hameed, A. Adams., Does using a higher cutoff for the percentage of positive cells improve the specificity of HER2 immunohistochemistry in breast carcinoma. *American Journal of Clinical Pathology* 128 (2007) 825-829.
- [71]P.M. Brandt-Rauf, P.W. Carney., The c-erbB-2 protein in oncogenesis: molecular structure to molecular epidemiology. *Critical Reviews in Oncogenesis* 5 (1994) 313–329.
- [72]H.M. Schechter, A.L. Vaidyanathan., The neu gene: an erbB-homologous gene distinct from and unlinked to the gene encoding the EGF receptor. *Science* 229 (1985) 976-978.
- [73]H.M. Bargmann, R.A. Weinberg., The neu oncogene encodes an epidermal growth factor receptor related protein. *Nature* 319 (1986) 226–230.
- [74]Y.L. Coussens, Y.C. Liao, E. Chen, A. Gray, J. McGrath., Tyrosine kinase receptor with extensive homology to EGF receptor shares chromosomal location with neu oncogene. *Science* 230 (1985) 1132–1139.
- [75]A. SA., Growth factors and cancer. *Science* 254 (1991) 1146-1153.
- [76]F.S. Daniel A. Vorobiof, and G.Vorobiof. Breast cancer incidence in South Africa. *Journal of Clinical Oncology* 19 (2001) 125-127.
- [77]W.B. Walker, J. Ncongwane., Age of menopause in black women in South Africa. *British Journal of Obstetrics and Gynecology* 91 (1984) 797-801.
- [78]P.H. Hoffman M, Cooper., Breast cancer incidence and determinants of cancer stage in the Western Cape. *South African Medical Journal* 90 (2000) 1212-1216.
- [79]N.D. Pegoraro, J.V. Bryer., Clinical patterns of presentation of breast cancer of different racial groups in South Africa. *South African Medical Journal* 68 (1985) 808-810

- [80]W.B. Walker AR, Tshabalala., Low survival of South African urban black women with breast cancer. *British Journal of Cancer* (1984).
- [81]X.Z. Mingfeng Zhang¹, Abrar A. Qureshi, A. Heather Eliassen, Susan E. Hankinson, J. Han., Association between cutaneous nevi and breast cancer in the nurses' health study: A prospective cohort study. *PLOS Medicine* 11 (2014) 100-115.
- [82] S.E. Hankinson, J.E. Manson, G.A. Colditz, D.J. Hunter., Plasma sex steroid hormone levels and risk of breast cancer in postmenopausal women. *Journal of the National Cancer Institute* 90 (1998) 1292-1299.
- [83]C. D. Karley, D. Gupta, A. Tiwari., Contribution of oncoproteomics to cancer 2. biomarker discovery. *Molecular Cancer* 6 (2007) 25-33.
- [84]K.B. Srinivas, P.R. Srivastava., Trends in biomarker 1. Research for cancer detection. *Lancet Oncology* 2001 2 (2001) 698-704.
- [85]D.L.Henrya., Cancer biomarkers. *Molecular Oncology* 6 (2012) 140-146.
- [86]B.A. Jaenisch., Epigenetic regulation of gene expression: how the genome integrates intrinsic and environmental signals. *Nature Genetics* 33 (2003) 245-254.
- [87]J.A. Ludwig., Weinstein biomarkers in cancer staging, 6. Prognosis and treatment selection. *Nature Review Cancer* 5 (2005) 845-856.
- [88]D.C. Allred., hormone receptor testing in breast cancer: a distress signal from Canada. *Oncologist* 13 (2008) 797-801.
- [89]P.M. Bossuyt, J.B. Reitsma, D.E. Bruns, C.A. Gatsonis, P.P. Glasziou, Irwig, L.M. Moher, D. Rennie, D. de Vet, J.G. Lijmer., The STARD statement for reporting studies of diagnostic accuracy: explanation and elaboration. *Annals of Internal Medicine* 138 (2003) 1-12.
- [90]M. Cristofanilli, G.T. Budd, M.J. Ellis, A. Stopeck, J. Matera, M.C. Miller, J.M. Reuben, G.V. Doyle, W.J. Allard, L.W. Terstappen, D.F. Hayes., Circulating tumor cells,

- disease progression, and survival in metastatic breast cancer. *New England Journal of Medicine* 351 (2004) 781-791.
- [91]B. Freidlin, L.M. McShane, E.L. Korn., Randomized clinical trials with biomarkers: design issues. *Journal of the National Cancer Institute* 102 (2010) 152-160.
- [92]L. Harris, H. Fritsche, H. Mennel, R. Norton, L. Ravdin, P. Taube, M.R. Somerfield, D.F. Hayes, M.C. Bast., Update of recommendations for the use of tumor markers in breast cancer. *Journal of Clinical Oncology* 25 (2007) 5287-5312.
- [93]J.M. Hall, M.K. Lee, B. Newman, J.E. Morrow, L.A. Anderson, B. Huey, M.C. King., Linkage of early-onset familial breast cancer to chromosome 17q21. *Science* 250 (1990) 1684-1689.
- [94]D.F. Hayes, Bast, R.C., Desch, C.E., Fritsche Jr., H., Kemeny, N.E., J.M. Jessup, M. Locker, G.Y. Macdonald, J.S, Mennel, L. Norton, R. Ravdin, P. Taube, S. Winn., Tumor marker utility grading system: a framework to evaluate clinical utility of tumor markers. *Journal of the National Cancer Institute* 88 (1996) 1456-1466.
- [95]F. Innocenti, M.J. Ratain., Pharmacogenetics of irinotecan: clinical perspectives on the utility of genotyping. *The Pharmacogenomics Journal* 7 (2006) 1211-1221.
- [96]H. Lodish, *Molecular cell biology* 4th ed., W.H. Freeman., New York, (1999) 1–1084.
- [97]R.E. Dickerson., The DNA helix and how it is read. *American Journal of Science* 249 (1983) 94-111.
- [98]F.H. Watson., *Molecular structure of nucleic acids: A structure for deoxyribonucleic acids*. *Nature* 171 (1953) 737-738.
- [99]R.G. Franklin., *Molecular configuration in sodium thymonucleate*. *Nature* 171 (1953) 740–741.
- [100]A. Rich, B. Nordheim, J. Wang., *The chemistry and biology of left-handed Z DNA*. *Annual Reviews of Biochemistry* 53 (1984) 791-846.

- [101]J.D. Watson., Genetical implications of the structure of deoxyribonucleic acids. *Nature* 171 (1953) 964–967.
- [102]M.H.F. Wilkins, A.R. Stokes and H.R. Wilson., Molecular structure of deoxyribose nucleic acids. *Nature* 171 (1953) 738–740.
- [103]A.Z. Milosavljevi, M. Zeremski, D. Grujic, T. Paunesku and R. Crkven., Clone clustering by hybridization. *Genomics* 27 (1995) 89-111.
- [104]W.B. Smith., Novel method for nucleic acid sequence determination. *Journal of Theoretical Biology* 135 (1988) 307-329.
- [105]O.C. Uhlenbeck, A. Pardi, and J. Feigon., RNA structure comes of age. *Cell* 90 (1997) 833–840.
- [106]E. Palecek., Oscillographic polarography of highly polymerized deoxyribonucleic acid. *Nature* 188 (1960) 656-657.
- [107]M.H. Pournaghi-Azar, M.S. Hejazi, and E. Alipour., Developing an electrochemical deoxyribonucleic acid (DNA) biosensor on the basis of human interleukine-2 gene using an electroactive label. *Analytica Chimica Acta* 570 (2006) 144-150.
- [108]E. Komarova, M. Aldissi, and A. Bogomolova., Direct electrochemical sensor for fast reagent-free DNA detection. *Biosensors and Bioelectronics* 21 (2005) 182-189.
- [109]K. Wu, J. Fei, W. Bai, and S. Hu., Direct electrochemistry of DNA, guanine and adenine at a nanostructured film-modified electrode. *Analytical and Bioanalytical Chemistry* 376 (2003) 205-209.
- [110]C.N.R. Rao, Muller, A., and A.K. Cheetham, *Chemistry of Nanomaterials* 1st ed., Wiley-VCH, Weinheim (2004) 199-203.
- [111]W.H Qi., Size effects on the cohesive energy of nanoparticles. *Journal of Material Science Letters* 21 (2002) 1743–1745.

- [112]M.A. Nanda K.K, Krus F.E, Fissan H, and Strappert S, Strappert., Higher surface energy of free nanoparticles. *Physical Review Letters* 91 (2003) 106-102.
- [113]I.L. Berger., *Semiconductor Materials*, 1st ed., CRC PRESS, USA, (1996) 15-18.
- [114]R.S. Quimby., *Photonics and lasers: An introduction* 1st ed., John Wiley & Sons, New Jersey, USA (2006) 55-178.
- [115]M. Hoffman, S. Choi, W. Bahnemann., Environmental applications of semiconductor photo catalysis. *Chemical Reviews* 95 (1995) 69-96.
- [116]D.S. Neamen., *An introduction to semiconductor devices* 1st ed., McGraw-Hill, USA, (2006) 1-5.
- [117]N.M. Cutler., Observation of anderson localization in an electron gas. *Physical Review* 181 (1969) 1336.
- [118]J.W. Allen., Gallium Arsenide as a semi-insulator. *Nature* 187 (1960) 403-405.
- [119]R. M. Reed., Electron transport in quantum dots. *Scientific American* 268 (1993) 118.
- [120]P. Kluson, H. Bartkova, and I. Budil., Welcome in the nanoworld. *Chemicke Listy* 101 (2007) 262-272.
- [121]A. Merkoci, M. Aldavert, S. Marin, and S. Alegret., New materials for electrochemical sensing V: Nanoparticles for DNA labeling. *Trends in Analytical Chemistry* 4 (2005) 341-349.
- [122]E.P. Kawasaki., Nanotechnology, nanomedicine, and the development of new, effective therapies for cancer. *Nanomedicine: Nanotechnology, Biology and Medicine* 1 (2005) 101-109.
- [123]X. Michalet, F.F. Pinaud, L.A. Bentolila, J.M. Tsay, S. Doose, J.J. Li, G. Sundaresan, A.M. Wu, and S. Weiss., Quantum dots for live cells, in vivo imaging, and diagnostics. *Science* 307 (2005) 538-544.

- [124]F.B. Aldeek, L. Lambert, J. Schneider., The influence of capping thioalkyl acid on the growth and photoluminescence efficiency of CdTe and CdSe quantum dots. *Nature Nanotechnology* 19 (2008) 9-22.
- [125]A.P. Alivisatos., Semiconductor clusters, nanocrystals, and quantum dots. *Science* 271 (1996) 933-937.
- [126]C.S.V. Suzete, D. Diogo and R. Jacenir., CdTe and CdSe quantum dots cytotoxicity: A Comparative study on microorganisms. *Sensors* 11 (2011) 11664-11678.
- [127]V.A. Jana Drbohlavova, R. Kizek, J. Hubalek., Quantum dots -characterization, preparation and usage in biological systems. *International Journal of Molecular Science* 10 (2009) 656-673.
- [128]A.J. Ferancova., DNA biosensors based on nanostructured materials. In nanostructured materials in electrochemistry 1st ed., Wiley-VCH: Weinheim, Germany, (2008) 1-40.
- [129]S.M. Reiman., Electronic structure of quantum dots. *Reviews of modern physics* 74 (2002) 1285.
- [130]A.P. Alivisatos., Semiconductor clusters, nanocrystals, and quantum dots. *Science* 271 (1996) 933-937.
- [131]X. Michalet, F.F. Pinaud, L.A. Bentolila, J.M. Tsay, S. Doose, J.J. Li, G. Sundaresan, A.M. Wu, and S. Weiss., Quantum dots for live cells, in vivo imaging, and diagnostics. *Science* 307 (2005) 538-544.
- [132]M.A. Walling, J.A. Novak, J.R.E. Sheppard., Quantum dots for live cell and in vivo imaging. *International Journal of Molecular Science* 10 (2009) 441-491.
- [133]K. Fujioka, M. Hiruoka, K. Sato, N. Manabe, R. Miyasaka, S. Hanada, A. Hoshino, R.D., Y.M. Tilley, K. Hirakuri, K. Yamamoto., Luminescent passive-oxidized silicon, luminescent passive-oxidized silicon quantum dots as biological staining labels and

- their cytotoxicity effects at high concentration. *Nanotechnology* 19 (2008) 415102-415109.
- [134]A. Merkoci, M. Aldavert, S. Marin, and S. Alegret., New materials for electrochemical sensing V: Nanoparticles for DNA labeling. *Trends in Analytical Chemistry* 4 (2005) 341-349.
- [135]A.P. Kawasaki., Nanotechnology, nanomedicine, and the development of new, effective therapies for cancer. *Nanomedicine: Nanotechnology, Biology and Medicine* 1 (2005) 101-109.
- [136]A.P. Alivisatos, W. Gu, and C. Larabell., Quantum dots as cellular probes. *Annual Review of Biomedical Engineering* 7 (2005) 55-76.
- [137]X. Michalet, F.F. Pinaud, L.A. Bentolila, J.M. Tsay, S. Doose, J.J. Li, G. Sundaresan, A.M. Wu, and S. Weiss., Quantum dots for live cells, in vivo imaging, and diagnostics. *Science* 307 (2005) 538-544.
- [138]T. Jin, F. Fujii, Y. Komai, J. Seki, A. Seiyman, and Y. Yoshioka., Preparation and Characterization of Highly Fluorescent, Glutathione-coated Near Infrared Quantum dots for in Vivo Fluorescent Imaging. *International Journal of Molecular Science* 9 (2008) 2044-2061.
- [139]W.C.W. Chan, D.J. Maxwell, X. Gao, R.E. Bailey, M. Han, and S. Nie., Luminescent quantum dots for multiplexed biological detection and imaging. *Current Opinion in Biotechnology* 13 (2002) 40-46.
- [140]L.C. Mattheakis, J.M. Dias, Y.J. Choi, J. Gong, M.P. Bruchez, J. Liu, E. Wang., Optical coding of mammalian cells using semiconductor quantum dots. *Analytical Biochemistry* 327 (2004) 200-208.

- [141]X. Gao, L. Yang, J.A. Petros, F.F. Marshall, J.W. Simons, and S. Nie., In vivo molecular and cellular imaging with quantum dots. *Current Opinion in Biotechnology* 16 (2005) 63-72.
- [142]M.G. Galian., The use of quantum dots in organic chemistry. *Trends in Analytical Chemistry* 28 (2009) 279-291.
- [143]H. Li, W.Y. Shih, and W.H. Shih., Non-heavy-metal ZnS quantum dots with bright blue photoluminescence by a one-step aqueous synthesis. *Nature Nanotechnology* 18 (2007) 205604-205609.
- [144]A.M. Derfus, S.N. Bhatia., Probing the cytotoxicity of semiconductor quantum dots. *Nano Letters* 4 (2004) 11-18.
- [145]J. Lovrić, H.S. Bazzi, Y. Cuie, G.R. Fortin, D. Maysinger., Differences in subcellular distribution and toxicity of green and red emitting CdTe quantum dots. *Journal of Molecular Medicine* 83 (2005) 377-385.
- [146]A. Hoshino, K. Fujioka, T. Oku, M. Suga, Y.F. Sasaki, T. Ohta, M. Yasuhara, K. Suzuki, K. Yamamoto., Physicochemical properties and cellular toxicity of nanocrystal quantum dots depend on their surface modification. *Nano Letters* 4 (2004) 2163-2169.
- [147]E. Chang, N. Thekkek, W.W. Yu, V.L. Colvin, and R. Drezek., Significance of evaluating quantum dot cytotoxicity based on intracellular uptake. *Small* 12 (2006) 1412-1417.
- [148]J. Zou, R.K. Baldwin, K.A. Pettigrew, S.M. Kauzlarich., Solution synthesis of ultrastable luminescent siloxane-coated silicon nanoparticles. *Nano Letters* 4 (2004) 1181-1186.
- [149]R.E. Burch, H.K.J. Hahn, and J.F. Sullivan., Newer aspects of the roles of zinc, manganese and copper in human nutrition. *Clinical Chemistry* 21 (1975) 501-520.

- [150]N. Pradhan, D.M. Battaglia, Y.C. Liu, X.G. Peng., Efficient, stable, small, and water-soluble doped ZnSe nanocrystal emitters as non-cadmium biomedical labels. *Nano Letters* 7 (2007) 312-317.
- [151]E.B. Garon, L. Marcu, Q. Luong, O. Tcherniantchouk, G.M. Crooks, and H.P. Koeffer., Quantum dot labeling and tracking of human leukemic, bone marrow and cord blood cells. *Leukemia Research* 31 (2007) 643-651.
- [152] K.P. Narayanan., Aggregated CdS quantumdots: Host of biomolecular ligands. *Journal of Physical Chemistry B* 110 (2006) 24403-24409.
- [153]M. Dahan, T. Laurence, F. Pinaud, D.S. Chemla, A.P. Alivisatos, M. Sauer and S. Weiss., Time-gated biological imaging by use of colloidal quantum dots. *Optics Letters* 26 (2001) 825-827.
- [154]S. Pathak, S.K. Choi, N. Arnheim, M.E. Thompson., Hydroxylated quantum dots as luminescent probes for in situ hybridization. *Journal of the American Chemical Society* 123 (2001) 4103-4104.
- [155]S.J. Rosenthal, I. Tomlinson, E.M. Adkins, S. Schroeter, S. Adams, L. Swafford, J., Y.W. McBride, L.J. DeFelice, and R.D. Blakely., Targeting cell surface receptors with ligand-conjugated nanocrystals. *Journal of the American Chemical Society* 124 (2002) 4586-4594.
- [156]L.Q. Debasis Bera, Teng-Kuan Tseng and Paul H. Holloway., Quantum dots and their multimodal applications. *Journal of Materials* 3 (2010) 2260-2345. 232
- [157]V.I. Klimov., Mechanisms for photogeneration and recombination of multiexcitons in semiconductor nanocrystals: Implications for lasing and solar energy conversion. *Journal of Physical Chemistry* 110 (2006) 16827-16845.

- [158]C.B.N. Murray, D.J. Bawendi., Synthesis and characterization of nearly monodisperse CdE (E = S, Se, Te) semiconductor nanocrystallites. *Journal of American Chemical Society* 115 (1993) 8706-8715.
- [159]L.I. Medintz, H. Mattoussi., Quantum dot-based resonance energy transfer and its growing application in biology 45. *Physical Chemistry Chemical Physics* 11 (2009) 17-45.
- [160]Y.H. Wang., Nanometer-sized semiconductor clusters—materials synthesis, quantum size effects and photophysical properties. *Journal of Physical Chemistry* 95 (1991) 525-532.
- [161]M.G.W. Bawendi, W.L. Rothberg, L. Carroll, P.J. Jedju, T.M. Steigerwald, M.L. Brus., Electronic-structure and photoexcited-carrier dynamics in nanometer-size CdSe clusters. *Physical Review Letters* 65 (1990) 1623–1626.
- [162]A.L.R. Efros, M. Kuno, M. Nirmal, M. Norris, D.J. Bawendi., Band-edge exciton in quantum dots of semiconductors with a degenerate valence band: Dark and bright exciton states. *Physical Review B* 54 (1996) 4843–4856.
- [163]M.F. Kuno, D.P. Hamann, H.F. Gallagher, A. Nesbitt., Nonexponential "blinking" kinetics of single CdSe quantum dots: A universal power law behavior. *Journal of Chemical Physics* 112 (2000) 3117-3120.
- [164]T.H. Gfroerer., *Photoluminescence in analysis of surface and interfaces*, John Wiley & Sons Ltd, Chichester 1st ed, UK, (2000) 9209-9231.
- [165]R.C.Viswanatha, S. Basu, S. Sarma., Blue-emitting copper-doped zinc oxide nanocrystals. *Journal of Physical Chemistry B* 110 (2006) 22310-22312.
- [166]X.Y. Xiu, Z. Mandalapu, L.J. Liu, J.L. Beyermann., p-Type ZnO films with solid-source phosphorus doping by molecular-beam epitaxy. *Applied Physics Letters* 88 (2006) 105-106.

- [167]R. Williams, *Luminescence and the light emitting diode* 1st ed., Pergomon Press, New York, USA, (1977) 2320-2322.
- [168]A.A. Klimov, D.W. Leatherdale, M.G. Bawendi., Quantization of multiparticle Auger rates in semiconductor quantum dots. *Science* 287 (2000) 1011-1013.
- [169]A.L.R. Efros., Random telegraph signal in the photoluminescence intensity of a single quantum dot. *Physics Review Letters* 78 (1997) 1110–1113.
- [170]T. Franzl, J. Müller, T.A. Klar, A.L. Rogach, J. Feldmann, D.V. Talapin, and H. Weller., CdSe:Te Nanocrystals: Band-edge versus Te-related emission. *The Journal of Physical Chemistry C* 111 (2007) 2974-2979.
- [171]C.B.K. Murray, M.G. Bawendi., Self-organization of CdSe nanocrystallites into 3-dimensional quantum-dot superlattices. *Science* 270 (1995) 1335-1338.
- [172]V.L.G. Colvin, A.P. Alivisatos., Semiconductor nanocrystals covalently bound to metal-surfaces with self-assembled monolayers. *Journal of American Chemical Society* 114 (1992) 5221-5230.
- [173]M.D. Nirmal, B.O. Bawendi, M.G. Macklin, J.J. Trautman, J.K. Harris, T.D. Brus., Fluorescence intermittency in single cadmium selenide nanocrystals. *Nature* 383 (1996) 802–804.
- [174]M.G. Empedocles., Quantum-confined stark effect in single CdSe nanocrystallite quantum dots. *Science* 278 (1997) 2114-2117.
- [175]M.A. Walling, J.A. Novak, J.R.E. Sheppard., Quantum dots for live cell and in vivo imaging. *International Journal of Molecular Science* 10 (2009) 441-491.
- [176]R.M. Penner., Hybrid electrochemical/chemical synthesis of quantum dots. *Accounts of Chemical Research* 33 (2000) 78-86.

- [177]A.F.E. Hezinger, J. TeBmar, A. Gopferich., Polymer coating of quantum dots-A powerful tool toward diagnostics and sensorics. *European Journal of Pharmaceutics and Biopharmaceutics* 68 (2008) 138-152.
- [178]J. Ma, K.M. Stewart, S.O. Kelley., DNA-passivated CdS nanocrystals: Luminescence, bioimaging, and toxicity profiles. *Langmuir* 23 (2007) 12783–12787.
- [179]Q.K. Wang, Y.C. Wang, Y.W. Shin, G. Ruengruglikit, C. Huang., Luminescent properties of water-soluble denatured bovine serum albumin-coated CdTe quantum dots. *Journal of Physical Chemistry and Materials* 110 (2006) 16860–16866.
- [180]S.X. Santra, J.S.Wang, K.M. Tan., Luminescent nanoparticle probes for bioimaging. *Nanoscience and Nanotechnology* 4 (2004) 590–599.
- [181]H.M. Alireza Valizadeh, M. Samiei, S M. Farkhani, N. Zarghami, M. Kouhi., Quantum dots: synthesis, bioapplications, and toxicity. *Nanoscale Research Letters* 7 (2012) 48.
- [182]P.H.Y. Holloway, H. Lee, H. Seo, S. Santra, S. Qian, L. Bera., In nanophosphor: PL, EL, and biological markers. *Proceeding International Display Workshops* 2 (2006) 6-8.
- [183]P.P. Ghasemi, Y. Afifi., Quantum dot: magic nanoparticle for imaging, detection and targeting. *Acta Biomedica* 80 (2009) 156-165.
- [184]E.P. Chason, S.T. Poate, J.M. Borland, J.O Current, M.I. delaRubia, T.D. Eaglesham, D.J. Holland, M.E, Magee, C.W, Mayer, J.W. Melngailis, A.F. Tasch., Ion beams in silicon processing and characterization. *Journal of Applied Physics* 81 (1997) 6513-6561.
- [185]K.H. Tsutsui, E.L. Wilkinson., Reactive ion etched II-VI quantum dots–dependence of etched profile on pattern geometry. *Japan Journal of Applied Physics Part 1* 32 (1993) 6233–6236.

- [186]T.P. Trindade, N.L Pickett., Nanocrystalline semiconductors: Synthesis, properties, and perspectives. *Journal of Materials Chemistry* 13 (2001) 3843–3858.
- [187]A. Henglein., Small-particle research-physicochemical properties of extremely small colloidal metal and semiconductor particles. *Chemical Reviews* 89 (1989) 1861–1873.
- [188]C.C. Burda, X.B. Narayanan, R. El-Sayed, M.A., Chemistry and properties of nanocrystals of different shapes. *Chemical Reviews* 105 (2005) 1025–1102.
- [189]C.C. Burda, Narayanan R, El-Sayed MA., Chemistry and properties of nanocrystals of different shapes. *Chemical Reviews* 105 (2005) 1025–1102.
- [190]J.H Bang, P.H.Holloway., Enhanced and stable green emission of ZnO nanoparticles by surface segregation of Mg. *Nature Nanotechnology* 17 (2006) 973-986.
- [191]Q.L. Bera, D. Sabui, S Santra., Photoluminescence of ZnO quantum dots produced by a sol–gel process. *Optical Materials* 30 (2008) 1233-1239.
- [192]Y.A. Xin SH, Kim C, Dobrowolska M, Merz., Formation of selfassembling CdSe quantum dots on ZnSe by molecular beam epitaxy. *Applied Physics Letters* 69 (1996) 3884-3886.
- [193]M.M. Małgorzata Geszke-Moritz., Quantum dots as versatile probes in medical sciences: Synthesis, modification and properties. *Materials Science and Engineering* 33 (2013) 1008-1021.
- [194]J.M. Costa-Fernández, R. Pereiro, A. Sanz-Medel., The use of luminescent quantum dots for optical sensing. *Trends in Analytical Chemistry* 25 (2006) 207-218.
- [195]M. Geszke-Moritz, M. Moritz., Quantum dots as versatile probes in medical sciences: Synthesis, modification and properties. *Materials Science and Engineering: C* 33 (2013) 1008-1021.

- [196]E.M.R. L.M. Maestro, F.S. Rodríguez, M.C.I. de la Cruz., A. Juarranz, R, F.V. Naccasche, D. Jaque, J.A. Capobianco, J.G. Solé., High-sensitivity fluorescence lifetime thermal sensing based on cdte quantum dots. *Nano Letters* 10 (2010) 5109-5115.
- [197]L.Z. Li, Y. Fang, Z. Chen, D. Pan, M. Wu., Observation of growth of metal nanoparticles. *Journal of Physical Chemistry* 80 (2011) 1333-1336.
- [198]Q.W. Luo, M. Zhang, P. Li, Y. Ding., Changes of CdTe QD fluorescence intensity during the growth of E-coli. *Colloid Interface Science* 362 (2011) 100-106.
- [199]D.Y Tan, Maity, C.X. Yong, K.-H. Chuang, Y. Zhao, S., J.D. Wang, S.S. Feng., multimodal tumor imaging system based on magnetic resonance imaging (MRI) and the fluorescence imaging. *Biomaterials* 32 (2011) 2969-2978.
- [200]K.A. Liu, Q. Yuan, L. Lu., Bimodal fluorescence and MRI nanoprobes. *Biomaterials* 32 (2011) 1185-1192.
- [201]W.Y. Au, S.J. Tseng, W.H. Shih., Near-infrared-emitting QDs to medicine and pharmacy. *Nanotechnology* 23 (2012) 275-601.
- [202]R.C. Gu, Z.-L. Zhang, Z.X. Xie, D.W. Pang, J. Am., Synthesis of water-dispersible AgSe quantum dots with near-infrared photoluminescence emission at 820 nm and their application for the living nude mouse imaging. *Journal of American Chemical Society* 134 (2012) 79-82.
- [203]J.Q. D. Wang, F. Cai, S. He, S. Han, Y. Mu., Synthesised near-infrared emitting PbS quantum dots application for in vivo sentinel lymph node mapping of mice. *Nanotechnology* 23 (2012) 245-701.
- [204]J. wang, *Analytical electrochemistry* 2nd ed., Wiley-VCH, USA, (2000) 278-282.
- [205]S. Rodriguez-Mozaz, M.J.L.d. Alda, M.-P. Marco, D. Barceló., Biosensors for environmental monitoring: A global perspective. *Talanta* 65 (2005) 291-297.

- [206]Y. Fu, R. Yuan, L. Xu, Y. Chai, X. Zhong, D. Tang., Indicator free DNA hybridization detection via EIS based on self-assembled gold nanoparticles and bilayer two-dimensional 3-mercaptopropyltrimethoxysilane onto a gold substrate. *Biochemical Engineering Journal* 23 (2005) 37-44.
- [207]S. Marko, K. Johannes, B. Matthias, T. Alexander., Electronic and optical properties of ZnO/(Mg,Zn)O quantum well with and without a distinct quantum-confined Stark effect. *Journal of Applied Physics* 111 (2012) 63701-63709.
- [208]M.P. Bruchez., Turning all the lights on: quantum dots in cellular assays. *Current Opinion in Chemical Biology* 9 (2005) 533-537.
- [209]J.K. Jaiswal, S. M. Simon., Potentials and pitfalls of fluorescent quantum dots for biological imaging. *Trends Cell Biology* 14 (2004) 497-504.
- [210]A.M. Smith, S. M. Nie., Chemical analysis and cellular imaging with quantum dots. *Analyst* 129 (2004) 672-677.
- [211]O. Salata, Applications of nanoparticles in biology and medicine. *Journal of Nanobiotechnology Review* 2 (2004) 1-6.
- [212]L. Ding, Zhou, P. J. Li, S. Q. Shi, G. Y., Spectroscopic studies on the thermodynamics of L-cysteine capped CdSe/CdS quantum dots—BSA interactions. *Journal of Fluorescence* 21 (2011) 17-24.
- [213]M. De, C. You, C. Srivastava, V.M. Rotello., Biomimetic interactions of proteins with functionalized nanoparticles: a thermodynamic study. *Journal of American Chemical Society* 129 (2007) 10747-10753.
- [214]D. Leckband., Measuring the forces that control protein interactions. *Annual Review of Biophysics and Biomolecular Structures* 29 (2000) 1-26.
- [215]J.Y. Jie, J. Zhang., structures containing quantum dots for electrochemiluminescence detection of adenosine triphosphate. *Biosensor and Bioelectronics* 31 (2012) 69-76.

- [216]J.Y. Jie., structures containing quantum dots for electrochemiluminescence detection of adenosine triphosphate and thrombin. *Analytical Chemistry* 84 (2012) 2811-2817.
- [217]B. M. Gui, Y. Xia, C. Wei, S. Zhang, C. Zhu., l-cysteine capped CdTe quantum dots to monitor physiological pH changes in fixed and living cells by means of pH-dependent fluorescence emission color of quantum dots. *Biosensor and Bioelectronics* 30 (2011) 324-327.
- [218]C.H. Li., CdSe/ZnS quantum dots coated with cyclodextrins for the determination of phenols in water. *Chemistry of Materials* 20 (2008) 6053-6059.
- [219]Y. Chen, He, H. Lin, P. Sheng, C. Liu, S. Luo, Q. Cai., Synthesis of l-cysteine-capped CdTe QDs and their application as fluorescent probe for selective trinitrotoluene (TNT) detection. *Nanotechnology* 21 (2010) 125-502.
- [220]F.R. Algarra, Aquiar, J.E. Rodriguez-Borges, J.E. de Silva., CdTe QDs coupled with 11-[(ethoxycarbonyl)mercapto]undecanoyl- β -cyclodextrin showing fluorescence enhancement after acetylsalicylic acid (ASA) addition. *Material Science and Engineering C* 32 (2012) 799-803.
- [221]Z.Y. Yang, J. Zhang, J. Hao, Q. Hu, X.G. Chen., Thioglycolic acid-capped core/shell CdTe/CdSe QDs have been successfully used as pH-sensitive fluorescent probe for a simple and rapid determination of ascorbic acid in commercial tablets. *Journal of Fluorescence* 21 (2011) 1123-1129.
- [222]T.F. R. Freeman, I. Willner, W. Angew., Electrochemical immunosensor for the detection of prostate specific antigen (PSA) being the cancer biomarker. *Chemie International* 48 (2009) 7818-7821.
- [223]Y.T Tu, H.Y Kang, P. Chang., Immunosensor based on CdSe/ZnS quantum dots for detection of human serum albumin (HSA). *Biosensor and Bioelectronics* 34 (2012) 286-290.

- [224]L.J. Tian, Y. Zhao, Y. Wang, Y. Peng, S. Zhao., CdTe quantum dots were used for detection of human serum alpha fetoprotein and carcinoembryonic antigen. *Talanta* 92 (2012) 72-77.
- [225]X.Q. Yang, T. Song, J. Yang, S. Zhu, Y. Li, Y. Cui, Y. Li, B. Zhang, J. Chang., Developed immunochromatography test strip based on quantum dots for detection of already mentioned alpha fetoprotein being a valuable marker for diagnosis of primary hepatic carcinoma. *Biosensor and Bioelectronics* 30 (2011) 145-150.
- [226]H.Z. Zhai, N. Du, B. Chen, H. Huang, Y. Wu, D. Yang., One-pot synthesis of biocompatible cdse/cds quantum dots and their applications as fluorescent biological labels. *Nanoscale Research Letters* 6 (2011) 31-45.
- [227]D.L. Erbo Ying, S. Guo, S. Dong., Synthesis and bio-imaging application of highly luminescent mercaptosuccinic acid-coated cdte nanocrystals. *Small* 2 (2006) 476-480.
- [228]V. Barbu., Molecular hybridization techniques of nucleic acids. *Innovative Romanian Food Biotechnology* 1 (2007) 1-12.
- [229]R.E. Cheng., In situ PCR/RT-PCR coupled with in situ hybridization for detection of functional gene and gene expression in prokaryotic Cells 1st ed., Academic Press, San Diego, California, USA, (2001) 129-41.
- [230]D. Wang., Synthesis of some neutral, water-soluble carbodiimides and their use in the formation of peptide bonds. *Scientica Sinica Series B* 30 (1987) 449-459.
- [231]A. Darr., Synthesis and characterization of tyramine based hyaluronan hydrogels. *Journal of Material Science* 20 (2009) 33-44.
- [232]N. Nakajima., Mechanism of amide formation by carbodiimide for bioconjugation in aqueous media. *Bioconjugate Chemistry* 6 (1995) 123-130.
- [233]D. Sehgal., A method for the high efficiency of water-soluble carbodiimide-mediated amidation. *Analytical Biochemistry* 218 (1994) 87-91.

- [234]J.V.Staros., Enhancement by N-Hydroxysulfosuccinimide of watersoluble carbodiimide-mediated coupling reactions. *Analytical Biochemistry* 156 (1986) 220-226.
- [235]P.J. Park, S.N. Kim, J.M. Song H. Suh., Characterization of porous collagen/hyaluronic acid scaffold modified by 1-ethyl-3-(3-dimethylaminopropyl) carbodiimide cross-linking. *Biomaterials* 23 (2002) 1205-1212.
- [236]G.J. Grabarek., Zero-length crosslinking procedure with the use of activate esters. *Analytical Biochemistry* 185 (1990) 131-135.
- [237]P. Bulpitt., New strategy for chemical modification of hyaluronic acid: Preparation of functionalized derivatives and their use in the formation of novel biocompatible hydrogels. *Journal of Biomedical Materials Research* 47 (1999) 152-169.
- [238]A. Darr., Synthesis and characterization of tyramine based hyaluronan hydrogels. *Journal of Material Science* 20 (2009) 33-44.
- [239]A. Skoog, F. Holler, R. Crouch, *Fundamentals of analytical 8th ed Chemistry*, New York, (2004) 694-699.
- [240]F. Holler, *Fundamentals of analytical chemistry 8th ed. Chemistry: David Harris, USA*, (2004) 676-687.
- [241] A. Skoog, F. Holler, R. Crouch, *Fundamentals of analytical chemistry 8th ed.*, David Harris, New York, (2004) 631-641.
- [242]A.J. Bard, *Electrochemical methods: Fundamentals and applications 2nd ed.*, John wiley & sons, inc, New Yorke Chichester Weinheim, (2000) 293-298.
- [243]S.P. Kounaves, *Voltammetric techniques: Handbook of instrumental techniques for analytical chemistry, 1st ed.*, staff.tanta.edu.eg, USA, (1997) 709-725.
- [244]A.J. Bard, *Electrochemical methods: Fundamentals and applications 2nd ed.*, John wiley & sons, inc., New Yorke Chichester Weinheim, (2001) 163-430.

- [245]D.A. Ward, Physical electrochemistry: principle, methods and applications 1st ed., Marcel Dekker, New York, (1995) 775-793.
- [246]D.A. Buttry, In electroanalytical chemistry: A series of advances 1st ed., Marcel Dekker: New York, New York, (1991) 1-12.
- [247]V.E. Gileadi., In electroanalytical chemistry: A series of advances; A. J. Bard, I. Rubinstein, Eds. 1st ed., Marcel Dekker, New York, (2003) 1-99.
- [248]M.H. A, In interfacial electrochemistry: Theory, experiment, and applications, 1st ed., marcel dekker, New York, (1999) 559–576.
- [249] E.A. Skoog, Principles of instrumental analysis 6th ed., Thomson Brooks/Cole, New York, (2007) 522-525.
- [250]J. Peuravuori, R. Koivikko, and K. Pihlaja., Characterization, differentiation and classification of aquatic humic matter separated with different sorbents: synchronous scanning fluorescence spectroscopy. Water Research 36 (2002) 4552-4562.
- [251]J.R. Lakowicz, Principles of fluorescence spectroscopy 3rd ed., Springer, USA, (2006) 954-1255.
- [252]B. Valeur, Molecular fluorescence: Principles and applications 2nd ed., Wiley-VCH, New York, (2001) 69-80.
- [253]E. Wehry, Modern fluorescence spectroscopy 1st ed., Plenum Press, New york, (1976) 410-459.
- [254]A. Baker., Fluorescence excitation–emission matrix characterization of some sewage-impacted rivers. Environmental Science & Technology 35 (2001) 948-953.
- [255]C.M. Sharpless., Effects of aluminum-induced aggregation on the fluorescence of humic substances. Environmental Science & Technology 33 (1999) 3264-3270.
- [256]S.A. Williams., Relative fluorescence quantum yields using a computer controlled luminescence spectrometer. Analyst 108 (1983) 1067.

- [257]G. Dhimi., Rumbles, S. M. Bishop, D. Phillips and A. Beeby., Phthalocyanine fluorescence at high concentration: dimers or reabsorption effect? *Journal of Photochemistry and Photobiology* 61 (1995) 341.
- [258]X.M. Kang, Z. Zou, X. Cai, P. Mo, M. Jinyuan., A novel glucose biosensor based on immobilization of glucose oxidase in chitosan on a glassy carbon electrode modified with gold-platinum alloy nanoparticles/multiwall carbon nanotubes. *Analytical Biochemistry* 369 (2007) 71-79.
- [259]S. Schlücker., Design and synthesis of Raman reporter molecules for tissue imaging by immuno-SERS microscopy. *Journal of Biophotonics* 6 (2011) 453-463.
- [260]G.R. Ellis., Metabolic fingerprinting in disease diagnosis: biomedical applications of infrared and Raman spectroscopy. *Analyst* 131 (2006) 875-885.
- [261]K. Raman., A new type of secondary radiation. *Nature* 121 (1928) 501-502.
- [262]B.E. Warren, X-ray Diffraction, 1st ed., General Publishing Company, USA, (1990) 94720-4767.
- [263]C.G. M. Birkholz, T. Jung., X-ray diffraction study on residual stress and preferred orientation in thin titanium films subjected to a high ion flux during deposition. *Journal of Applied Physics* 96 (2004) 7202-7253.
- [264]S.R. Stock, Elements of x-ray diffraction 3rd ed., Prentice Hall, New Jersey, (2001) 256-270.
- [265]J.B. Brady, and Boardman, Shelby J., Introducing mineralogy students to x-ray diffraction through optical diffraction experiments using lasers. *Journal of Geological Education* 43 (1995) 471-476.
- [266]S. Ray., Quantitative analysis of adsorbed proteins by x-ray photoelectron spectroscopy. *Analytical Chemistry* 83 (2011) 8659-8666.

- [267]J.F. Wolstenholme., An introduction to surface analysis by XPS and AES by 1st ed., John Wiley & Sons, Chichester England, (2003) 62-67.
- [268]S.B. Paul, Eugene, S. Ilton, Connie, J. Nelin., The interpretation of XPS spectra: Insights into materials properties. Surface Science Report 68 (2013) 273-304.
- [269]M.A. O'Keefe, P. R. Buseck and S Iijima., Computed crystal structure images for high resolution electron microscopy. Nature 274 (1978) 322–324.
- [270]P.D. Geuens, D., The S-state model: a work horse for HRTEM. Ultramicroscopy 3 (2002) 179-198.
- [271]H. Lichte., Optimum focus for taking electron holograms. Ultramicroscopy 38 (1991) 13-22.
- [272]J.M. Buseck, and L. Eyring., High-resolution transmission electron microscopy and associated techniques 1st ed., Oxford University Press., New York, (1988) 477–490.
- [273]E. Suzuki., High-resolution scanning electron microscopy of immunogold-labelled cells by the use of thin plasma coating of osmium. Journal of Microscopy 3 (2002) 153–157.
- [274]C.R. Hall, Electron microscopy of plant cells, 1st ed., Academic Press, London, (2002) 1-66.
- [275]C.Y. Martin, H.K. Wickramasinghe., Atomic force microscope-force mapping and profiling on a sub 100-e scale. Journal of Applied Physics Letters 61 (1987) 4723-4739.
- [276]J.R. Young, F. Scire., The topografiner: An instrument for measuring surface microtopography. Review of Scientific Instruments 43 (1982) 999-116.
- [277]N.M. Tsukada., Theory of atomic-force microscopy. Scientific Reports 44 (1997) 1-15.
- [278]R.F. Gould, Contact angle wettability and adhesion 1st ed., American Chemical Society, USA, (1964) 1-4.

- [279]A. Seibold, Nardin M, Schultz. J, Walliser, A. and M Oppliger., Effect of dynamic contact angle on capillary rise phenomena. *Colloids and Surfaces A: Physicochemical and Engineering Aspects* 161 (2000) 81-87.
- [280]A.L. Rogach., Aqueous synthesis of thiol-capped CdTe nanocrystals. *Physical Chemistry* 111 (2007) 14628-14637.
- [281]P.T. Tran., Use of luminescent CdSe-ZnS nanocrystal bioconjugates in quantum dot-based nanosensors. *Physica Status Solidi B-Basic Research* 229 (2002.) 427-432.
- [282]Y. Otaki, Y. Yanadori, Y. Seki, M. Tadano, S. Kashida., X-ray study of the modulated structure in as-grown Ga₂Te₃ crystals with the defect zinc-blende lattice. *Journal of Solid State Chemistry* 182 (2009) 1556-1562.
- [283]Y. Otaki, Y. Yanadori, Y. Seki, K. Yamamoto, S. Kashida., X-ray study of the modulated structure in quenched Ga₂Te₃ with a defect zinc-blende lattice. *Acta Materialia* 57 (2009) 1392-1398.
- [284]K. George, C.H.d. Groot, C. Gurnani, A.L. Hector, R. Huang, M. Jura, W. Levason, G. Reid., Low pressure chemical vapour deposition of crystalline ga₂te₃ and ga₂se₃ thin films from single source precursors using telluroether and selenoether complexes. *Physics Procedia* 46 (2013) 142-148.
- [285]U.I. Kalsoom, S. Bashir, N. Ali., SEM, AFM, EDX and XRD analysis of laser ablated Ti in nonreactive and reactive ambient environments. *Surface and Coatings Technology* 235 (2013) 297-302.
- [286]M.R. Castro, J. F. Arenas and J. C. Otero., Surface-enhanced Raman scattering of 3-mercaptopropionic acid adsorbed on a colloidal silver surface. *Journal of Raman Spectroscopy* 35 (2004) 997-1000.
- [287]J. Creighton, In spectroscopy of surfaces, 1st ed., Wiley, Chichester, (1988) 91-101.

- [288] V.I. Vinogradov., Kucherenko, N. N. Mel'nik, P. Fernandez, Chai, Lu Jing., Raman spectra of structures with cdte-, znte-, and cdse-based quantum dots and their relation to the fabrication technology. *Fizika Tverdogo Tela* 50 (2008) 159-162.
- [289] C.A. Munder, M. G. Berger, and H. Liith., A Raman study of Au/Te/Au/GaAs (100) ohmic contacts. *Journal of Applied Physics* 71 (1992) 15-31.
- [290] R. Alam, M.M. Maye., Asymmetric quantum dot growth via temperature cycling. *Inorganica Chimica Acta* 380 (2012) 114-117.
- [291] A.J. Bard, *Fundamentals and applications of electrochemical methods* 2nd ed., Wiley, London, (2000) 589-608.
- [292] R.G. Aulich., Electrochemical study of gold electrodes with anodic oxide films-II. Inhibition of electrochemical redox reactions by monolayers of surface oxides. *Journal of Electroanalytical Chemistry* 18 (1968) 295-315.
- [293] M.K. P. Zuman, *Progress in polarography* 2nd ed., Interscience, New York, (1962) 426-427.
- [294] P. Delahay, *New instrumental methods in electrochemistry* 1st ed., Interscience, New York, (1954) 180.
- [295] F.E. Zittel., A glassy-carbon electrode for voltammetry. *Analytical Chemistry* 37 (1965) 200-203.
- [296] A.J. Bard, *Electrochemical methods: Fundamentals and applications* 2nd ed., Wiley New York, (2000) 590-593.
- [297] A.J.P. Theuwissen., CMOS image sensors: State-of-the-art, solid state electronic. *Microelectronics Journal* 52 (2008) 1401-1406.
- [298] L.C. Mattheakis, J.M. Dias, Y.J. Choi, J. Gong, M.P. Bruchez, J. Liu, E. Wang., Optical coding of mammalian cells using semiconductor quantum dots. *Analytical Biochemistry* 327 (2004) 200-208.

- [299]E.C. M. Bigas, J. Forest and J. Salvi., Review of CMOS image sensors. *Microelectronics Journal* 37 (2006) 433-451.
- [300]L.J. Kozolowski., Noise minimization via deep submicron system-on-chip integration in megapixel CMOS imaging sensors. *Journal of Opto-Electronics* 14 (2006) 11-18.
- [301]S.P. Pack, N.K. Kamisetty, M. Nonogawa, Kamakshaiyah, C. Devarayapalli, K. Ohtani, Y.K. Yamada, T. Kodaki, and K. Makino., Direct immobilization of DNA oligomers onto the amine-functionalized glass surface for DNA microarray fabrication through the activation-free reaction of oxanine 10. *Nucleic Acids Research* 35 (2007) 1-10.
- [302]P.D. Tam, T. Trung, M.A. Tuan, and N.D. Chien., Electrochemical direct immobilization of DNA sequences for label-free herpes virus detection. *Journal of Physics* 187 (2009) 1-8.
- [303]M. Dufva., Fabrication of high quality microarrays. *Biomolecular Engineering* 22 (2005) 173-184.
- [304]J. Wang, G. Liu, R.M. Jan, and Q. Zhu., Electrochemical detection of DNA hybridization based on carbon -nanotubes loaded with CdS tags. *Electrochemistry Communications* 5 (2003) 1000-1004.
- [305]J.A. Capobianco, W.Y. Shih, G.P. Adams, W.H. Shih., Label-free Her2 detection and dissociation constant assessment in diluted human serum using a longitudinal extension mode of a piezoelectric microcantilever sensor. *Sensors and Actuators B: Chemical* 160 (2011) 349-356.
- [306]S.W. Alexandra, F.H. Jim, C. Simon, S. Valerie, S. Jacqui, E. Stephen, A.F. Carole, J.S. Daniel., Comparison of microfluidic digital PCR and conventional quantitative PCR for measuring copy number variation. *Nucleic Acids Research* 40 (2012)1-12.
- [307]D. Lüftner, C. Lüke, K. Possinger., Serum HER-2/neu in the management of breast cancer patients. *Clinical Biochemistry* 36 (2003) 233-240.

- [308]P.E. Sias, C.E. Kotts, D. Vetterlein, M. Shepard, W.L.T. Wong., ELISA for quantitation of the extracellular domain of p185HER2 in biological fluids. *Journal of Immunological Methods* 132 (1990) 73-80.
- [309]Q.A.M. Al-Khafaji, M. Harris, S. Tombelli, S. Laschi, A.P.F. Turner, M. Mascini, G. Marrazza., An electrochemical immunoassay for HER2 Detection. *Electroanalysis* 24 (2012) 735-742.
- [310]L.M. Rossi, L. Shi, N. Rosenzweig, Z. Rosenzweig., Fluorescent silica nanospheres for digital counting bioassay of the breast cancer marker HER2/nue. *Biosensors and Bioelectronics* 21 (2006) 1900-1906.
- [311]S.A. John, T. Ohsaka., Electrochemical and EQCM studies on the assembly of asymmetric viologen on bare and alkanethiol-coated Au electrodes. *Journal of Electroanalytical Chemistry* 477 (1999) 52-61.
- [312]D.A. Buttry, *Electroanalytical chemistry* 1st ed., 17 Marcel Dekker, New York, (1991) 1-85.
- [313]M.J. Raúl J. Martín-Palma., Optical biosensors based on semiconductor nanostructures. *Sensors* 9 (2009) 5149-5172.
- [314]C.M. Walther, K. Rennert., Quantum dot-carrier peptide conjugates suitable for imaging and delivery applications. *Bioconjugate Chemistry* 19 (2008) 2346–2356.
- [315]S.L. Rajan, H.Y. Vu, T.Q., Ligand-bound quantum dot probes for studying the molecular scale dynamics of receptor endocytic trafficking in live cells. *Journal of American Chemical Society* 2 (2008) 1153–1166.
- [316]H.D. Zhernokletov, B. Brennan, M. Yakimov, V. Tokranov., Surface and interfacial reaction study of half cycle atomic layer deposited HFO₂ on chemically treated GaSb surfaces. *Applied Physics Letters* 102 (2013) 131-140.

- [317]J.E.B. M. Rei Vilar, F. Debontridder, R. Artzi, R. Naaman, A. M. Ferraria, A.Rego.,
Characterization of wet-etched GaAs (100) surfaces. *Surface and Interface Analysis*
37 (2005) 673-682.
- [318]G.A. Gamala, M.I. Ashraf, H.J. Eman., Ferroelectric phase transition in Ga₂Te₃ single
crystals. *Journal of Physics and Chemistry of Solids* 66 (2005) 1-4.
- [319]B.A. Gillan EG., Chemical vapor deposition of hexagonal gallium selenide and telluride
films from cubane precursors: understanding the envelope of molecular control.
Chemistry of Materials 9 (1997) 3037-3048.
- [320]F.M. Pohle R, Meixner H., In situ infrared emission spectroscopic study of the
adsorption of H₂O and hydrogencontaining gases on Ga₂O₃ gas sensors. *Sensors and
Actuators B: Chemical* 68 (2000) 151-156.
- [321]B. OA., Gallium oxide crystallization during Ga₂Se₃ oxidation. *Physics of the Solid
State* 2 (2001) 267-271.
- [322]V.P. Balitskii., Peculiarities of Ga₂Te₃ thermal oxidation. *Materials Science In
Semiconductor Processing* 10 (2007) 124-127.
- [323]P.H. Toru Yamashita., Analysis of XPS spectra of Fe²⁺ and Fe³⁺ ions in oxide materials.
Applied Surface Science 254 (2008) 2441-2449.